

Ultrafast Charge Transfer Dynamics in Dye-Metal and Semiconductor Material

By
Jayanta Dana
CHEM01201304028

Bhabha Atomic Research Centre, Mumbai-400085

A thesis submitted to the
Board of Studies in Chemical Sciences
In partial fulfillment of requirements
for the Degree of
DOCTOR OF PHILOSOPHY
of
HOMI BHABHA NATIONAL INSTITUTE

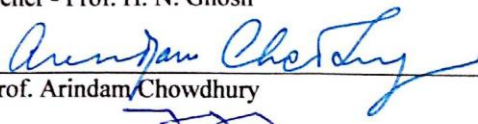
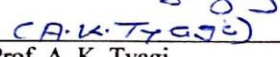
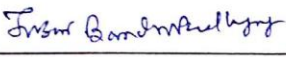


August, 2017

Homi Bhabha National Institute¹

Recommendations of the Viva Voce Committee

As members of the Viva Voce Committee, we certify that we have read the dissertation prepared by Jayanta Dana entitled " Ultrafast Charge Transfer Dynamics in Dye-Metal and Semiconductor Material" and recommend that it may be accepted as fulfilling the thesis requirement for the award of Degree of Doctor of Philosophy.

 Chairman - Prof. H. Pal	23/11/17 Date:
 Guide / Convener - Prof. H. N. Ghosh	23/11/17 Date:
 Examiner - Prof. Arindam Chowdhury	23/11/17 Date:
 Member 1- Prof. A. K. Tyagi	23/11/2017 Date:
 Member 2- Prof. T. Bandyopadhyay	23-11-17 Date:
 Member 3- Prof. S. Nath	23.11.17 Date:

Final approval and acceptance of this thesis is contingent upon the candidate's submission of the final copies of the thesis to HBNI.

I/We hereby certify that I/we have read this thesis prepared under my/our direction and recommend that it may be accepted as fulfilling the thesis requirement.

Date: 23.11.17

Place: Mumbai

<Signature>

Co-guide (if applicable)



<Signature>

Guide

¹ This page is to be included only for final submission after successful completion of viva voce.

STATEMENT BY AUTHOR

This dissertation has been submitted in partial fulfillment of requirements for an advanced degree at Homi Bhabha National Institute (HBNI) and is deposited in the Library to be made available to borrowers under rules of the HBNI.

Brief quotations from this dissertation are allowable without special permission, provided that accurate acknowledgement of source is made. Requests for permission for extended quotation from or reproduction of this manuscript in whole or in part may be granted by the Competent Authority of HBNI when in his or her judgment the proposed use of the material is in the interests of scholarship. In all other instances, however, permission must be obtained from the author.



Jayanta Dana

DECLARATION

I, hereby declare that the investigation presented in the thesis has been carried out by me. The work is original and has not been submitted earlier as a whole or in part for a degree / diploma at this or any other Institution / University.



Jayanta Dana

List of Publications arising from the thesis

Journal

1. "Restriction of Molecular Rotation and Intramolecular Charge Distribution in The Photo-Excited State of Coumarin Dyes on Gold (Au) Nanoparticle Surface.", **Jayanta Dana**, Tushar Debnath, Partha Maity and Hirendra N. Ghosh, *J. Phys. Chem. C*, **2015**, *119*, 2046-2052.
 2. "Enhancement of Charge Separation in Epitaxial Metal- Semiconductor Nanohybrid Material Anchored with an Organic Molecule". **Jayanta Dana**, Tushar Debnath, Partha Maity and Hirendra N. Ghosh. *J. Phys. Chem. C*. **2015**, *119*, 22181-22189.
 3. "Involvement of Sub-Bandgap States in Subpicosecond Exciton and Bi-exciton Dynamics of Ternary AgInS₂ Nanocrystals". **Jayanta Dana**, Tushar Debnath and Hirendra N. Ghosh *J. Phys. Chem. Lett.* **2016**, *7*, 3206–3214.
 4. "Hot Electron Transfer from Semiconductor to Metal Domain in CdSe@CdS{Au} Hetero-structure". **Jayanta Dana**, Partha Maity, and Hirendra N. Ghosh. *Nanoscale*, **2017**, *9*, 9723-9731.
 5. "Inhibiting Interfacial Charge Recombination for Boosting Up Power Conversion Efficiency in CdSe{Au} Nano-hybrid Sensitized Solar Cell". **Jayanta Dana**, Pranav Anand, Sourav Maiti, Farazuddin Azlan and Hirendra N. Ghosh. *JPC C (DOI: 10.1021/acs.jpcc.7b08448)*
 6. "Direct Correlation of Excitonics with Efficiency in Core Shell Quantum Dot Solar Cell". **Jayanta Dana**, Sourav Maiti, V. S. Tripathi and Hirendra N. Ghosh. *J. Phys. Chem. C (Communicated)*.
 7. "Concurrent Ultrafast Electron and Hole Transfer Dynamics in CsPbBr₃ Perovskite and Quantum Dots". **Jayanta Dana**, Partha Maity, Biswajit Jana, Sourav Maiti, and Hirendra N. Ghosh. *J. Phys. Chem. C (Communicated)*.
 8. "Extraction of Electron and Enhancement of Charge Separation By Gold Nano Core in Non-Epitaxial Metal-Semiconductor nanohybrid and Organic Molecule Triad System". **Jayanta Dana**, Partha Maity, Tushar Debnath, and Hirendra N. Ghosh. *(To be communicated)*.
 9. "Shell Thickness Dependent Charge Separation in CdSe@CdS{Au} Nanohybrid Materials". **Jayanta Dana**, Sourav Maiti, Srijon Ghosh and Hirendra N. Ghosh. *(To be communicated)*.
-

Other Publications Associated in research work:

1. “Restriction of Molecular Twisting on Au nanoparticle Surface”. Tushar Debnath, **Jayanta Dana**, Partha Maity, , Hyacintha Lobo, Ganapati S. Shankarling, and Hirendra N. Ghosh. *Chem. Eur. J*, **2015**, *21*, 5704 – 5708.
 2. “Effect of Molecular Coupling on Ultrafast Electron Transfer and Charge Recombination Dynamics in Charge Transfer Complex formed by Tri Phenyl Methane Dye Adsorbed on Wide Gap ZnS Nano Aggregate Surface”. Tushar Debnath, Partha Maity, **Jayanta Dana**, Hirendra N. Ghosh. *Chem Phys Chem*, **2016**, *17*, 724-730.
 3. “Multiple Charge Transfer Dynamics in Colloidal CsPbBr₃ Perovskite Quantum Dots Sensitized Molecular Adsorbate”. Partha Maity, **Jayanta Dana** and Hirendra N. Ghosh *J. Phys. Chem. C*. **2016**, *120* , 18348-18354.
 4. “Photoinduced Ultrafast Charge Separation in Colloidal 2-Dimensional CdSe/CdS-Au Hybrid Nanoplatelets and Corresponding Application in Photocatalysis”. Himani Chauhan, Yogesh Kumar, **Jayanta Dana**, Biswarup Satpati, Hirendra Ghosh, Sasanka Deka, *Nanoscale*, **2016**, *8*, 15802-15812.
 5. “Intraband Electron Cooling Mediated Unprecedented Photocurrent Conversion Efficiency of CdS_xSe_{1-x} Alloy QDs: Direct Correlation between Electron Cooling and Efficiency”. Partha Maity, Sourav Maiti, Tushar Debnath, **Jayanta Dana**, Sourav K. Guin and Hirendra N. Ghosh . *J. Phys. Chem. C*.**2016**, *120* , 21309-21316.
 6. “Proton Couple Electron Transfer Processes in Ultrafast Time Domain: Evidence for H-Bonded Water as Proton Acceptor”. Ananta Dey, **Jayanta Dana**, Sunil Aute, Partha Maity, Amitava Das and Hirendra N. Ghosh, *Chem. Eur.J*. **2017**, *23*,3455 –3465.
 7. “Electrochemical Evaluation of Dopant Energetics and the Modulation of Ultrafast Carrier Dynamics in Cu-Doped CdSe Nanocrystals”. Sourav Maiti, **Jayanta Dana**, Yogesh Jadhav, Tushar Debnath, Santosh K. Haram and Hirendra N. Ghosh. *J. Phys. Chem. C* (DOI: [10.1021/acs.jpcclett.6b00348](https://doi.org/10.1021/acs.jpcclett.6b00348)).
 8. “Manipulating the charge extraction efficiency in ZnSe/CdS nanoheterostructures for photocatalytic hydrogen production. Mona Mittal, **Jayanta Dana**, Franziska Lübke, Hirendra N. Ghosh, Nadja C. Bigall and Sameer Sapra”. *Chem. Mater* (Submitted)
-

9. “Manipulation of Optical Band and Improving Charge Separation through In-situ Alloying of Graded Cd_xZn_{1-x}Se Nanocrystals”. Partha Maitya, **Jayanta Dana**, and Hirendra N. Ghosh *J. Phys. Chem. C (Submitted)*

Conferences

1. “Energy Transfer Dynamics between Twisted Intramolecular Charge Transfer (TICT) and Intramolecular Charge Transfer (ICT) States of Coumarin Dyes on Au Nanoparticle surface” **Jayanta Dana**, Tushar Debnath, Partha Maity and Hirendra N. Ghosh, TSRP-2014, BARC, Mumbai, India.
2. “Plasmon Induced Enhancement of Charge Separation in Au/CdS Metal-Semiconductor Nano-Composite Sensitized with Dye Molecule” **Jayanta Dana**, Tushar Debnath, Partha Maity, and Hirendra N. Ghosh. APC-2014, IISER-TVM & CSIR-NIIST, Trivandrum, India.
3. “Ultrafast Charge Transfer dynamics in Au/CdSe/Br-PGR Tri-composite System” **Jayanta Dana**, Tushar Debnath, Partha Maity, and Hirendra N. Ghosh. ISMC-2014, BARC, Mumbai, India.
4. “Restriction of Molecular Rotation and Intramolecular Charge Distribution in the Photo-Excited State of Coumarin Dyes on Gold (Au) Nanoparticle Surface” **Jayanta Dana**, Tushar Debnath, Partha Maity, and Hirendra N. Ghosh. ISMC-2014, BARC, Mumbai, India.
5. “Enhancement of Surface Plasmon of Gold Nano Rod Appended with Organic Molecule”. **Jayanta Dana**, Partha Maity and Hirendra N. Ghosh*, TSRP-2014, BARC, Mumbai, India.
6. “Ultrafast Charge Carrier Dynamics in Metal Deposited CdSe@CdS Quasi Type II Core Shell Material and Its Photocatalytic Behavior” **Jayanta Dana**, Partha Maity and Hirendra N. Ghosh*, ICONSAT-2016, IISER Pune, India.
7. “In-Ag Antisite Defect Dependent Bi-exciton in AgInS₂ Ternary Quantum Dots” **Jayanta Dana**, Tushar Debnath and Hirendra N. Ghosh*. IPS-2016, St. Petersburg, Russia.
8. “Optimisation of CdS Shell Thickness of CdSe@CdS Core-Shell in Higher Efficient QDs Solar Cell.” **Jayanta Dana**, Sourav Maity, V. S. Tripathi and Hirendra N. Ghosh*. UFS-2016, BARC, Mumbai, India.

Jayanta Dana

Dedicated to My Beloved Parents

ACKNOWLEDGEMENTS

I take this opportunity to acknowledge and appreciate some associated peoples who helped me to accomplish this journey successfully and made it memorable too. Without their precious help I couldn't able to complete my thesis work.

First and foremost I would like to express a sincere gratitude and thanks to my Ph. D supervisor Prof. Hirendra Nath Ghosh for giving me a golden opportunity to work with him in such a never ending exciting field of research. I am greatly thankful to him for his continuous support, advice, encouragement and inspiration in every moment throughout the tenure of my Ph.D. His relentless advice, direction, hopes have always been there whenever the things weren't going right with me. His thinking style and quality of work always impressed me. I learnt a lot at the time of scientific discussion with him during my research. He opened a door for me how to create a new problem and how to tackle the problem. I will be grateful to him for introducing me this amazing research direction. Apart from excellent scientific carrier, he is also an honest and real human being. I have been delighted by him as a good character and researcher too. Thank you very much sir for being a friend, philosopher and guide of mine.

A very special thanks goes to Dr. Amitava Das (CSMCRI, Bhavnagar, India), Dr. Sashanka Deka (Delhi University), Dr Santosh Haram (Pune University) for their excellent support. My research work was greatly benefitted by scientific discussion with them. I wish to express my deepest gratitude for their crucial contribution in improving the quality of my research work.

I am sincerely grateful to Dr. P. D. Naik, (Director, chemistry group and Head, Radiation and Photochemistry Division, BARC, India) and Dr. Awadhesh, Kumar (Head,

Environmental & Interfacial Spectroscopy Section, BARC, India) for providing me the opportunity which are conductively favourable for carrying out my research work.

I am also thankful to CSIR, Government of India for providing me the research fellowship. Without their financial support this work would not have been possible. A special thank goes to Homi Bhabha National Institute (HBNI), and Bhabha Atomic Research Centre (BARC), Government of India for providing the huge research facilities. I must thank to the all faculties and staff members of HBNI for their kind help during my one year course work in the training school. Without their support I could not able to complete my research.

My sincere thank goes to Dr. Narayan Pradhan (IACS, Kolkata) Dr. Anindya Datta (IITB, India), Dr. Divesh Srivastava (CSMCRI, Bhavnagar, India), Dr. V. S. Tripathi (BARC, Mumbai), Dr. S. K. Guin (BARC, Mumbai) for providing me the facilities at their laboratories.

I would like to thank to all of my Doctoral Committee (DC) members for their important advice during the annual meeting which assist me to be success in my dissertation.

I am grateful to Dr. S. Kaniyankandy, Dr. S. Verma and Dr. P. Singh for their valuable help at the periods of my dissertation.

I express deepest sense of my gratitude's to all of my beloved lab mates, and all the RPCD members. Especially I would like to mention the names Partha da, Tushar da, Pallavi di, and Sourav da for their co-operation and discussions which substantially contribute in my extended research life. Sunil, Ananta, Pranab, Farhaz, Uday, Deepa, Biswajit, Srijon and Kausturi all you people made daily work enjoyable and fun. I learnt a lot from you all. Thank you very much to all.

I would like to thank to Minakshmi Paramanik (Dey), Soumen Dey, Pavita V.K, Prachi Verma, Minakshmi Sinde, Avinash Singh, Doddipatla Srinivas, Saukat Sekh, Raman Khurana, Samu Naidu, Ganga Babu, Shitaljit Sharma, Neha Paraswani for being a source of constant energy and inspiration for me.

Last but not least, I am deeply and forever indebted to my parents for their love, blessing and encouragement throughout my entire life. Words fail me to express my appreciation to my beloved elder brother whose love, dedication, support, has taken the load off my shoulder. Without his critical caring I would not have finished my dissertation. I also express to immense gratitude to my other family member and all cousin brothers and sisters for their love and constant support.

Finally, I also wish to thank to all the BARC members including the administrative and security stuffs for cooperation in my research life.

B. A. R. C., Mumbai

Jayanta Dana

August, 2017

Contents

Synopsis	1
Abbreviations	12
List of Figures	16
List of Schemes	28
List of Tables	31
CHAPTER-1	35
INTRODUCTION	35
1.1. General Introduction:	37
1.2. Quantum Dots (QDs)	37
1.3. Electronic Structure of the QDs: Theoretical Framework	38
1.3.1. Quantum Confinement	38
1.3.3. Particle-in-a-Sphere Model	40
1.3.2. Effective Mass Approximation:	41
1.3.4. Band Structure	42
1.3.5. Electronic Structure of Quantum Dots:	43
1.3.6. Exciton Fine Structure	45
1.3.7. Dark exciton and Stoke shift	46
1.4. Density of States (DOS) in Different Size NCs.	48
1.5. Carrier Relaxation	49
1.5.1. Phonon-Assisted Intraband Electron Relaxation: Phonon bottleneck	50
1.5.2 Augur Recombination and Multi Exciton Generation (MEG).	51
1.5.3 Relaxation Through Electronic to Vibrational Energy Transfer Processes.	52
1.5.4 Trapping and Recombination:	53
1.6 Heterostructure: Core-Shell Nanocrystal	54
1.7 Metal Nanoparticles.	55
1.8. Surface Plasmon Resonance (SPR).	59
1.9 Metal-Semiconductor Nanohybrid Material (Exciton-Plasmon Coupling)	60
1.10 Synthesis of Colloidal Quantum Dots.	62
1.11 Interfacial Electron Transfer	64
1.12. Photovoltaic QDSC	65
1.13. Overview and scope of the thesis	68

CHAPTER-2	72
EXPERIMENTAL TECHNIQUES	72
2.1. Introduction.	74
2.2. High Resolution-Transmission Electron Microscopy (HR-TEM).	74
2.3. X-Ray Diffraction (XRD)	78
2.4 Ultraviolet-Visible (UV-Vis) Absorption Spectroscopy	80
2.5 Emission spectroscopy	81
2.6 Time Correlated Single Photon Counting (TCSPC) technique:	81
2.7 Time Resolved Absorption Measurements: Pump-Probe technique	84
2.8. Photovoltaic Measurement (IPCE and IV):	95
2.9. Synthesis of Nanostructures and Solar Cell Fabrication:	96
2.10. Preparation of Solar Cell Assembly:	102
CHAPTER-3	106
PHOTOPHYSICAL BEHAVIOR OF TWO STRUCTURALLY SIMILAR COUMARIN DYES ON GOLD NANOPARTICLE SURFACE	106
3.1. Introduction:	108
3.2. Results and Discussion:	110
3.2.1. Solvatochromic Behaviour of C343 and D1421.	110
3.2.2. Characterisation of Au NP.	112
3.2.3. Interaction of C343 and D1421 with Au Nanoparticle.	113
a) Steady State Absorption Spectroscopy of C-343 and D-1421 on Au NP Surface:	113
b) Steady State Emission Spectroscopy of C-343 and D-1421 on Au NP Surface:	116
c) Time-Resolved Emission Spectroscopy of C-343 and D-1421 on Au NP Surface:	119
d) Restriction of Molecular Rotation and Charge Distribution in the Excited States of Coumarin Dyes on Au NP Surface.	123
3.3. Conclusions:	125
CHAPTER-4	128
CHARGE (HOLE AND ELECTRON) CARRIER DYNAMICS OF SEMICONDUCTOR NANOCRYTALS AND ITS SOLAR CELL APPLICATION	128
4.1 Introduction.	130
4.2. Results and Discussion.	134
4.2.1 Optimisation of Shell Thickness in Highest Efficiency CdSe@CdS Core Shell Quantum Dots Solar Cell	134

a. Characterisation of Materials.	134
b. IV and IPCE Measurement.	137
c. TA Measurement.	139
e. Discussions	144
4.2.2 Charge transfer in QDs and CPB perovskite composite system..	147
a. Characterisation.	147
b. Interaction of CdSe QDs with CPB Perovskite.	148
c. Interaction of CdSe@CdS Core Shell with CPB Perovskite.	151
e. TA Spectroscopy Measurement of CdSe QDs and CPB Perovskite mixture.	155
f. TA Spectroscopy Measurement of CdSe@CdS Core Shell and CPB Perovskite mixture.	159
4.3 Conclusion:	161
CHAPTER-5	165
ULTRAFAST EXCITON AND BI-EXCITON DYNAMICS OF TERNARY AgInS ₂ NANOCRYSTALS	165
5.1. Introduction:	167
5.2. Results and Discussions:	169
A. Characterisation of AIS NCs.	169
B. Steady State Optical Absorption and Emission Studies.	170
C. Femto Second Transient Absorption Studies.	174
5.3. Conclusion:	189
CHAPTER-6	191
CORRELATION OF ENHANCED PHOTOVOLTAIC AND PHOTOCATALYTIC EFFICIENCY OF THE METAL–SEMICONDUCTOR NANOHYBRID MATERIALS WITH ULTRAFAST SPECTROSCOPY.	191
6.1. Introduction.	193
6.2 Results and Discussions.	197
6.2.1 Enhancement of Power Conversion Efficiency (PCE) of CdSe{Au} QDSC.	197
A. Characterization and Optical Properties of CdSe{Au} HS:	197
B. Transient Absorption Study of CdSe{Au} HS:	199
C. Photovoltaic Measurement of CdSe/Au Nanohybrid materials.	203
D. Electrochemical Impedance Spectroscopy Measurement.	207

6.2.2 Size Dependent Hot Carrier Dynamics of CdSe@CdS{Au} Nanohybrid Materials.	210
A. Characterization and Optical Properties of CdSe@CdS{Au} HS:	210
B. TA Spectroscopy Measurement of CdSe@CdS{Au}	214
C. Photocatalytic Study of CdSe@CdS{Au} NHM.	224
6.2.2 Shell Thickness Dependent Carrier Dynamics of CdSe@CdS{Au} Nanohybrid Materials.	226
A. Characterization and Optical Properties of CdSe@CdS{Au} NHM with Different Shell Thickness:	226
B. TA Studies of CdSe@CdS{Au} NHM with Different Shell Thickness:	228
6.3 Conclusions.	237
CHAPTER-7	240
ENHANCEMENT OF CHARGE SEPARATION IN METAL-SEMICONDUCTOR NANOHYBRID MATERIAL BY SENSITISATION WITH DYE MOLECULE	240
7.1 Introduction:	241
7.2. Results and Discussion:	244
7.2.1 Charge Separation in CdSe{Au} HS and BrPGR Triad System.	244
A. Characterization and Optical Properties of CdSe{Au} HS:	244
B. Transient Absorption Study of CdSe{Au} HS:	248
C. Sensitization of CdSe{Au} HS by BrPGR Molecule:	252
7.2.2 Charge Separation in Au@CdS core shell and DBF Triad System.	258
A. Characterization and Optical Properties of Au@CdS core shell:	258
B. Carrier Dynamics of Au@CdS Core Shell.	260
C. Electron and Hole Transfer Dynamics in Au/CdS Core Shell Nanohybrid After Sensitization with DBF Molecule:	263
7.3. Conclusions:	268
CHAPTER-8	271
SUMMARY and OUTLOOK	271
8.1. Summary.	273
8.2 Outlook.	278
REFERENCES	283

Synopsis

Synopsis

It is time to finding out the alternative of non-renewable energy sources such as coal, oil, natural gas, bio-fuels, nuclear fuels etc which are going to shrink.¹ By means of renewable energy sources such as solar energy is the best option for renewable energy sources, which is unending source of energy. Photocatalysis and Photovoltaic's are the process by which solar light the renewable energy source can be harvested.² Photovoltaic's cells have emerged from silicon based solar cell to dye sensitized solar cell (DSSC) over the years.³ Maximum 13% efficiency have been achieved in DSSC using specially designed porphyrin molecule endowed with D- π -A push pull groups.² However there is a challenge to make a stable dye molecule towards solar radiation which absorbs maximum portion of solar light. Hence considerable attention has been focussed on Semiconductor nanocrystals (NCs) (e.g. quantum dots, QDs) which show its size tuneable optoelectronic properties.³ The semiconductor NCs with size less than Bohr radius (Bohr radius is a material property i.e. mean free path of an exciton in a particular crystal lattice) show quantised energy level, is called QDs.⁴ The QDs are zero dimensional and the exciton is confined in all three dimensions.⁴ The QDs show the size tuneable band gap, i.e. the band gap increases with decreasing size and vice versa.⁴ This unique property control the electronic property of QDs which make it promising material for light emitting devices. The dye sensitised solar cell (DSSC) is termed as quantum dot solar cell (QDSC) when the dye is replaced by QDs, show considerable promise in photovoltaic's.⁵ The QDs show Multiple exciton generation, i.e more than one exciton can be generated if the absorbed photon energy is more than double of its band gap.⁶ Theoretically maximum 32 % efficiency (Queisser-Shockley limit) can be achieved by this property. The small particle size of QDs enhances the electron-hole coulomb interaction which facilitates the recombination through Auger process.⁷ This process limits

Synopsis

the efficiency of QDSC. The Auger recombination can be minimized by the architecting the band alignment of the core shell. Most commonly two types of core-shell nanostructure i.e. the Type I & Type II can be architected by considering the band gap of core and shell. In type I, The photo excited carriers (exciton) are confined in the core and no such interaction is there with surface. Hence the quantum yield is increased due to diminishing of surface states (e.g. CdSe/CdS, CdS/ZnS). However, there is better charge separation in Type II alignment. These types of hetero structures have great importance in case of solar cells (e.g. CdSe/CdTe, CdSe/ZnTe). The photovoltaic and photocatalytic properties of semiconductor QDs can be significantly improved when metal NPs spatially contact with semiconductor QDs.^{8,9} The metal NPs shows the strong surface plasmon resonance property when interact with light.¹⁰ The surface plasmon of metal NP is also a size tunable property.¹¹ The optoelectronic properties of metal and semiconductor are changed from its individual when they form the nanohybrid materials.¹² The photocatalytic and photovoltaic efficiency of the nanohybrid material can be enhanced than the metal and semiconductor by formation of charge separated state or modification of local electric field of the semiconductor.^{13,14} The charge separation of the nanohybrid also can be improved by adsorbing the nanohybrid material by the some organic dye molecule. The adsorbed dye molecule improves the charge separation either by injecting electron into the QDs or extracting the hole from QDs as well.

In the present thesis work, we focused mainly on synthesis, characterization and ultrafast charge transfer dynamics of quantum dot core, core-shell, metal-semiconductor nanostructure materials. Electron and hole transfer dynamics was also monitored using suitable adsorbate molecule on metal-semiconductor nanohybrid materials using femtosecond

Synopsis

transient absorption spectrometer. Finally we discussed the photovoltaic efficiency of DQs and hybrid materials.

CHAPTER 1: GENERAL INTRODUCTION

This chapter explains the brief introduction of photovoltaics involving different semiconductor materials. The fundamental introduction of semiconductor nanocrystals (especially QDs) and metal nanoparticles have been discussed briefly. The general physics and electronic structure of QD are discussed by the effective mass approximation. The band structure in semiconductor QD also has been explained by outline diagram. The charge carrier relaxation in semiconductor QDs has been demonstrated briefly. The fundamental of surface Plasmon of resonance has also been discussed. The basic of exciton Plasmon coupling in metal semiconductor nanohybrid material explained briefly. We discussed the electron transfer in different systems, i.e. dye-semiconductor, semiconductor-semiconductor and metal-semiconductor NHM by Marcus theory.

CHAPTER 2: EXPERIMENTAL TECHNIQUE

A general outline of transmission electron microscope (TEM), X-ray diffraction (XRD) were used for characterization of newly synthesized materials, are described in this chapter. For optical characterization used steady state UV-Vis absorption and photoluminescence spectroscopy have been discussed in detail in this chapter. The instrumentations and technique of time correlated single photon counting (TCSPC) have been explained in brief. Broad band femtosecond transient absorption spectroscopy was used for measure the Ultrafast phenomena in different nano materials. The details of femtosecond transient absorption spectroscopy, i.e. the Generation and power amplification of ultrashort

pulses, second harmonic generation (800 nm to 400 nm) and white light continuum of probe pulse (450-1000nm) are discussed.

CHAPTER 3: PHOTOPHYSICAL BEHAVIOR OF TWO STRUCTURALLY SIMILAR COUMARIN DYES ON GOLD NANOPARTICLE SURFACE

In this chapter, we investigated the different photophysical behavior of the two structurally similar coumarin dyes namely coumarin 343 (C-343) and 7-diethyl amino coumarin 3-carboxylic acid (D-1421) on the Au metal NP surface. In non-polar solvent both the coumarin dyes exist as locally excited (LE) state, but in polar solvent C-343 exists as intramolecular charge transfer (ICT) state and D-1421 predominantly exists as twisted intramolecular charge transfer (TICT) state. After photo excitation the energy transfer is occurred from photoexcited C 343 to Au NP in aqueous medium. But there is no energy transfer from photoexcited D1421 to Au NP due to lack of overlap between the emission band of D1421 and absorption band of Au NP. On the other hand the quantum yield of the D1421 tremendously enhances in presence of Au NP due to restriction of TICT state convert TICT state to ICT state on the surface of Au NP.

CHAPTER 4: CHARGE (HOLE AND ELECTRON) CARRIER DYNAMICS OF SEMICONDUCTOR NANOCRYTALS AND ITS SOLAR CELL APPLICATION

This chapter explores the ultrafast charge transfer dynamics has been demonstrated in CdSe quantum dot (QD) and CdSe@CdS core shell with CsPbBr (CPB) perovskite NCs. The measured electron transfer time from CPB NCs to CdSe QDs and hole transfer time from CdSe QDs to CPB NCs were found to be 550 fs and 750 fs respectively. But the charge transfer process is restricted in CPB/CdSe@CdS core shell system where electron transfer

from CPB NCs to core-shell has taken place within 450 fs. However the hole transfer from core shell to CPB restricted due to CdS shell which made the process thermodynamically nonviable. Additionally we measured the carrier dynamics of CdSe@CdS core shell with different CdS shell thickness and correlated with the measured power conversion efficiency (PCE). We optimised the CdS shell thickness in core shell by observing the carrier dynamics to have maximum PCE by CdSe@CdS core shell QDSCs. The maximum 3.88 % PCE has been measured by the CdSe@CdS 4ML where the CdSe shell thickness is 4 monolayer (ML).

CHAPTER 5: ULTRAFAST EXCITON AND BI-EXCITON DYNAMICS OF TERNARY AgInS₂ NANOCRYSTALS

This chapter deals with the stoichiometry dependent exciton and bi-exciton Dynamics of defect oriented ternary AgInS₂ (AIS) nanocrystals, which is unexplored in literature. We synthesised the three AIS NCs with different Ag and In ratio and characterised. The Ag induced sub band gap state (S-state) is generated with increasing the Ag ratio. Two types of emission are originated from AIS NCs, which are due to Ag-related S-state and antisite states (donor states), depending on the stoichiometric ratio of Ag and In in AIS NCs. The luminescence due to S-state was increased and antisite state was decreases with increasing the Ag ratio. Carrier dynamics in AIS QDs which involve multiple states like higher excited state, conduction band edge, S- States and antisite (donor) states are varied with the Ag/In stoichiometry ratio. The probe induced bi-exciton featured was observed in AIS NCs even at low pump fluency. The bi-exciton feature and carrier cooling at bi-exciton wavelength increased with increasing the Ag ratio and pump fluency as well.

CHAPTER 6: CORRELATION OF ENHANCED PHOTOVOLTAIC AND PHOTOCATALYTIC EFFICIENCY OF THE METAL–SEMICONDUCTOR NANOHYBRID MATERIALS WITH ULTRAFAST SPECTROSCOPY.

In this chapter we explored the enhancement of photovoltaic and photocatalytic efficiency of metal-semiconductor nanohybrid materials compared to semiconductor by femtosecond transient absorption spectroscopy study. We have synthesised the CdSe{Au}, CdSe@CdS{Au} nanohybrid material and characterised by the HR-TEM and steady state optical studies. First we measured the PCE of CdSe{Au} NHM and compared with CdSe QDs. The measured PCE of CdSe{Au} was found to be 4.39 % which is enhanced from the CdSe QDs 3.37 % efficiency. The enhancement of PCE of NHM has been explained by the TA spectroscopy studies. The electron transfer is occurred from photoexcited CdSe QDs to Au NPs, results a long lived charge separated state is generated which enhanced the PCE. The induced photon to current conversion efficiency (IPCE) by CdSe{Au} NHM also enhanced tremendously than the CdSe QDs. Then we investigated the hot and thermalised electron transfer dynamics from CdSe@CdS core shell to different size of Au NPs followed by its photo catalytic activity. The hot electron transfer from core shell to Au NP becomes faster in larger size of Au NP. The measured hot and thermalised electron transfer time from core shell to larger size Au NPs were 150 fs and 300 fs respectively, whereas these time were 300 fs and 550 fs respectively. This faster hot electron transfer in larger Au NP enhances the photo degradation of rhodamin dye. i.e. the photo catalytic activity of CdSe@CdS{Au} nanohybrid material was more efficient in attached larger Au compared to smaller one. We also investigated the charge carrier dynamics of CdSe@CdS{Au} nanohybrid material after varying the thickness of CdS shell in CdSe@CdS core shell. We observed that the charge

transfer rate gradually decreased with increasing the shell thickness of CdS but the back recombination becomes slows down with CdS thickness. The life time of the charge separated state is also increases with the CdS shell thickness.

CHAPTER 7: ENHANCEMENT OF CHARGE SEPARATION IN METAL-SEMICONDUCTOR NANOHYBRID MATERIAL BY SENSITISATION WITH DYE MOLECULE

This chapter explores the enhancement of charge separation in metal semiconductor NHM by appended with the dye molecule. In previous chapter we discussed the charge separation in CdSe{Au} NHM. For enhance the charge separation in CdSe{Au} NHM more, we sensitised this NHM by bromo-pyrogallol red (Br-PGR) dye. The measured electron transfer time from photo-excited CdSe to Au NP was ~ 270 fs, whereas the hole-transfer time from photo-excited CdSe to Br-PGR was measured to be ~ 500 fs. Therefore after photo excitation the electron transfer from Br-PGR to CdSe followed by Au NP and hole transfer from CdSe to Br-PGR. However the long lived charge separated state was generated between CdSe{Au} NHM and Br-PGR where all the electrons are localised in Au and all the holes are in Br-PGR. Additionally we investigated the charge separation between Au@CdSe core shell and dibromo-fluorscene (DBF) dye molecule. The synthesised Au@CdSe core shell was sensitised with DBF molecule and a strong charge transfer (CT) complex was formed between these two. The electron transfer time from HOMO of DBF to CB of CdS was found to be <100 fs (pulse width limited) and hole transfer time from VB of CdS to the HOMO of DBF was 400 fs. i.e the electron transfer is occurred from LUMO of DBF to the Au nano core through the CB of CdS shell and hole transfers from VB of CdS to the HOMO of DBF molecule. Therefore after photo excitation of the triad system all electrons and holes would

be localised at the Au nano core and LUMO of DBF respectively. As a result the charge separation in this triad system (Au@CdS/DBF) is higher than the charge separation in CdS/DBF system.

CHAPTER 8: SUMMERY AND OUTLOOK

To summarize, present thesis work revealed the effect of molecular structure on the photophysical behaviour of structurally similar coumarin dyes on the gold NP surface. The charge separation of (II-VI semiconductor) QDs and core shell with perovskite NCs which can be better light harvesting material. The power conversion efficiency of solar cell of Cde@CdS core shell increases with CdS shell and at a certain thickness the efficiency becomes maxima. The change of bi-exciton feature of ternary system with cation ratio explained. The Ag generated sub band gap state also generated which depends on the Ag ratio. The bi-excitonic feature and carrier cooling time increase with the Ag ratio. The PCE of the nanohybrid material is enhanced compared to QDs due to ultrafast charge separation from QDs to metal NP. The hot electron transfer and photo catalytic efficiency of the CdSe@CdS{Au} NHM depends on the size of the Au NP. With increasing the size of the Au NP enhances the hot electron transfer and photo catalysis efficiency of CdSe@CdS{Au} NHM. The electron transfer rate from cores shell to Au NP and back electron transfer is also affected by the CdS shell thickness in CdSe@CdS{Au} NHM system. The shell thickness slows down the electron transfer from core shell to metal NP and the back recombination from metal NP to core shell as well. The charge separation between metal semiconductor nano hybrid and dye molecule has also been investigated. The charge separation of NHM improves in presence of dye molecule and the electron and hole transfer time also has been

Synopsis

measured by TA study. This metal-semiconductor-dye tri-compoite material should be better material for photo voltaic.

REFERENCES:

1. Bartlett, A. A. Sustained availability: A management program for nonrenewable resources. *American Journal of Physics* **1986**, *54*, 398-402.
2. Dresselhaus, M. S.; Thomas, I. L. Alternative energy technologies. *Nature* **2001**, *414*, 332-337.
3. O'Regan, B.; Gratzel, M. A low-cost, high-efficiency solar cell based on dye-sensitized colloidal TiO₂ films. *Nature* **1991**, *353*, 737-740.
4. . Alivisatos, A. P. Semiconductor Clusters, Nanocrystals, and Quantum Dots. *Science* **1996**, *271*, 933-937
5. Kamat, P. V. Meeting the Clean Energy Demand: Nanostructure Architectures for Solar Energy Conversion. *J. Phys. Chem. C* **2007**, *111*, 2834-2860.
6. Beard, M. C.; Luther, J. M.; Semonin, O. E.; Nozik, A. J. Third Generation Photovoltaics based on Multiple Exciton Generation in Quantum Confined Semiconductors. *Acc. Chem. Res.* **2013**, *46*, 1252-1260.
7. Klimov, V. I. Spectral and Dynamical Properties of Multiexcitons in Semiconductor Nanocrystals. *Annu. Rev. Phys. Chem.* **2007**, *58*, 635-673.
8. Mokari, T.; Rothenberg, E.; Popov, I.; Costi, R.; Banin, U. Selective Growth of Metal Tips onto Semiconductor Quantum Rods and Tetrapods. *Science*. **2004**, *304*, 1787–1790.
9. Song, H. Metal Hybrid Nanoparticles for Catalytic Organic and Photochemical Transformations *Acc. Chem. Res.* **2015**, *48*, 491–499.

Synopsis

10. Xingyou, L.; Lihua, Q.; Pengfei, G.; Jian, Z.; Mingwei C. Localized surface plasmon resonance of nanoporous gold. *APPLIED PHYSICS LETTERS*, **2011**, *98*, 093701.
11. Xiong, L.; Mark, A.; Wang, J.; Qun H. Extinction coefficient of gold nanoparticles with different sizes and different capping ligands. *Colloids and Surfaces B: Biointerfaces*, **2007**, *58*, 3–7.
12. Elmalem, E.; Saunders, A. E.; Costi, R.; Salant, A.; Banin, U. Growth of Photocatalytic CdSe–Pt Nanorods and Nanonets. *Adv. Mater.* **2008**, *20*, 4312–4317.
13. Gao, N.; Liu, C.; Jeong, H. E.; Yangnopillars, P.; Plasmon-Enhanced Photocatalytic Activity of Iron Oxide on Gold. *ACS Nano*. **2012**, *6*, 234–240.
14. Li, P.; Wei, Z.; Wu, T.; Peng, Q.; Li, Y. Au_ZnO Hybrid Nanopyramids and Their Photocatalytic Properties. *J. Am. Chem. Soc.* **2011**, *133*, 5660–5663

Abbreviations

MNP	Metal nanoparticles
NCs	Nanocrystals
QDs	Quantum Dots
1D	One dimension (1D)
2D	Two dimension
EVET	Electronic to vibrational energy transfer
TOPO	Trioctyl phosphine oxide
HS	Heterostructure
CB	Conduction band
VB	valence band
LUMO	Lowest unoccupied molecular orbital
ET	Electron transfer
BET	Back electron transfer
HOMO	highest occupied molecular orbital
QDSC	Quantum dot sensitized solar cell
PCE	power conversion efficiency
NHM	Nanohybrid material
Br-PGR	Bromo-pyrogallol red
DBF	Dibromo-fluorscene
CT	Charge transfer
HR-TEM	High Resolution-Transmission electron microscopy
SAED	Selected area electron diffraction
XRPD	X-ray powder diffraction
XRD	X-Ray Diffraction

PMT	Photomultiplier tube
TCSPC	Time Correlated Single Photon Counting
TAC	Time-to-amplitude converter
MCA	Multi channel analyser
PD	Photodiode
CFD	Constant fraction discriminator
IRF	Instrument-photo response function
TIS	Ti-sapphire
DPSS	Diode pumped solid state
KLM	Kerr lens mode
GVD	Group velocity dispersion
BBO	β -barium borate
SHG	Second harmonic generation
WLG	White Light Generation
SPM	Self phase modulations
CdO	Cadmium oxide
DDA	Dodecylamine
DDAB	Didodecylammonium bromide
OA	Oleic acid
TOP	Trioctylphosphine
DDT	Dodecanethiol
OAm	Olylamine
ODE	1-octadecene
MPA	Mercaptopropionic acid
FRET	Forster Resonance Energy Transfer
SET	Surface energy transfer

ICT	Intramolecular charge transfer
TICT	Twisted intramolecular charge transfer
LE	Locally excited
CPB	CsPbBr ₃
SILAR	Successive ion layer absorption and reaction
CBD	Chemical bath deposition technique
FF	Fill factor
QY	Quantum yield
PL	Photoluminescence
AIS	Silver indium sulfide
TA	Transient Absorption
EIS	Electrochemical impedance spectroscopy
MEG	Multiple exciton generation

List of Figures

Figure 1.1: Change of energy gap from the molecular system to bulk via cluster and quantum dots.

Figure 1.2: Band diagram of (A) direct and (B) indirect bulk semiconductor.

Figure 1.3: Splitting of Valence band (VB) of the bulk CdSe in diamond (A) and wurtzite (B) like structure at $k = 0$ point.

Figure 1.4: Optical absorption spectrum of colloidal CdSe QDs and assignment of different excitonic states for different optical transition. Development of energy levels diagram from bulk semiconductor to the QDs. The optical transitions occur from different discrete CB (hole) to the VB (electron). levels arising from the valence band and conduction band respectively

Figure 1.5. (A) Sub bangap exciton fine structure and energy level diagram for e-h exchange interaction and size anisotropy.

Figure 1.6: Schematic electron-hole exchange interaction and anisotropy associated with crystal field in the wurtzite lattice structure. Optical absorption is in bright state and photoluminescence (PL) is due to dark state transition. The energy difference between the lowest absorption and emission energy levels is assigned as Stoke's shift.

Figure 1.7: Change of density of states with changing the carrier confinement.

Figure 1.8: Schematic diagram of intraband electron cooling through phonon emission.

Figure 1.9: Schematic diagram of intraband electron cooling through Auger process.

Figure 1.10: Schematic diagram of (a) Auger assisted multiple exciton generation and (b) Auger recombination process.

Figure 1.11: Schematic diagram of intraband electron cooling through electronic to vibrational energy transfer (EVET) process.

Figure 1.12. Schematic diagram of (A) electron and (B) hole trapping in different surface states.

Figure 1.13. Schematic Band alignment of core-shell heterostructures. (Type-I, Type-II and Quasi Type-II).

Figure 1.14. Schematic Band alignment of Metal NP with respect to bulk.

Figure 1.15. Plasmon Oscillation in Elongated Au NP. i.e. Oscillation in different direction of the NP.

Figure 1.16. Different relaxation processes of hot carriers at different time scale in Metal NP.

Figure 1.17. Oscillation of plasmon resonance.

Figure 1.18. Schematic interaction of exciton with Plasmon.

Figure 1.19. La Mer's growth model for Nucleation and growth stage for monodisperse colloidal nanoparticle.

Figure. 1.20. Schematic diagram of QDSC.

Figure. 2.1 Schematic Layout of TEM.

Figure 2.2. Schematic Layout of powder XRD.

Figure 2.3. Schematic diagram of TCSPC instrument.

Figure 2.4. Block diagram of Pump-Probe Transient Absorption spectroscopy.

Figure 2.5. Schematic block diagram of Ti-Sapphire Oscillator.

Figure 2.6. Optimal layout of femtosecond pulse stretcher.

Figure 2.7. Schematic diagram of multipass amplification process in our used setup.

Figure 2.8. Schematic layout of two grating compressor.

Figure 2.9. Optical layout of Excipro pump-probe setup.

Figure 3.1: Panel-A: a and a' are the absorption and emission spectrum of C343 in water, b and b' are the absorption and emission spectrum of C343 in cyclohexane respectively. **Panel-B:** c and c' are the absorption and emission spectrum of D1421 in water, d and d' are the absorption and emission spectrum of D1421 cyclohexane respectively.

Figure 3.2: Panel-A: Time resolved emission decay traces of (a) C343 dye in water and (b) C343 dye in cyclohexane, probed at emission maxima after 406 nm excitation. **Panel-B:** Time resolved emission decay traces of (c) D1421 in water and (d) D1421 in cyclohexane probed at emission maxima after 406 nm excitation.

Figure 3.3 (A): High resolution TEM image of citrate stabilized Au NP. Inset: SAED pattern of citrate stabilized Au NP. **(B):** Extinction spectra of Au Nanoparticles in aqueous medium.

Figure 3.4: Panel-A: Steady state optical absorption spectra of (a) Au [40nM] (b) C343 [70 μ M] (c) C343 [70 μ M] and Au [40nM] in H₂O (d) addition of a and b. Panel-B: Steady state optical absorption spectra of (e) Au [100nM] (f) D1421 [100 μ M] (g) D1421 [100 μ M] and Au [100nm] in H₂O. (h) addition of e and f.

Figure 3.5: Steady state emission spectra of C-343 at different concentration (a) 0.0 nM (b) 10 nM (c) 20 nM (d) 30 nM (e) 40 nM of Au nanoparticles in water. [C-343] = 70 μ M.

Figure 3.6: Steady state emission spectra of D1421 at different concentration (a) 0.0 nM (b) 40 nM (c) 60 nM (d) 80 nM (e) 100 nM of Au nanoparticles in water. [D-1421] = 100 μ M.

Figure 3.7: Time resolved emission decay traces of C-343 on Au NP surface at 500 nm at different concentration (a) 0.0 nM (b) 10 nM (c) 20 nM (d) 40 nM of Au nanoparticles in water. **Inset:** Emission of C-343 on 100 nM Au NP surface at 448 nm. Excitation wavelength was kept at 406 nm. **L** stands for Lamp profile of 406 nm laser excitation source.

Figure 3.8: Time resolved emission decay traces of D-1421 on Au NP surface at 475 nm at different concentration (a) 0.0 nM (b) 20 nM (c) 60 nM (d) 100 nM of Au nanoparticles in water. Excitation wavelength was kept at 406 nm.

Figure 4.1: (A) HR-TEM images of CdSe (a), CdSe@CdS 2ML (b), CdSe@CdS 4ML (c) and CdSe@CdS 6ML (d). (B) Powder X-ray diffraction pattern of (a) CdSe QD, (b) CdS/CdSe 2ML, (c) CdS/CdSe 4ML and (d) CdS/CdSe 6ML core-shell respectively. (C) UV-Visible absorption and luminescence spectrum of CdSe (a'), CS 1 (b'), CS 2 (c') and CS 3 NCs (d'). (D) Graphical plots of Quantum Yields (QY) Vs CdS shell thickness.

Figure 4.2. A: a, b, c, d and a', b', c', d' are the UV-Visible absorption spectra of CdSe, CS 1, CS 2 and CS 3 in Chloroform and Water respectively. **B:** a, b, c, d and a', b', c', d' are the UV-Visible luminescence spectra of CdSe, CS 1, CS 2 and CS 3 in Chloroform and Water respectively.

Figure 4.3. Left Panel. Current density (mA/cm^2) Vs Voltage (Volts) plot of (a) CdSe, (b) CS 1 (c) CS 2 and (d) CS 3. **Right Panel:** Incident photon to current conversion efficiency Spectra of (a') CdSe, (b') CS 1 (c') CS 2 and (d') CS 3.

Figure 4.4. TA spectra of (a) CdSe, (b) CS 1, (c) CS 2 and (d) CS 3 core-shell NCs at different time delay. (All TA measurements have been carried out after 400 nm Laser excitation).

Figure 4.5: Bleach dynamics of (a) CdSe at 570 nm, (b) CS 1 at 578 nm (c) CS 2 at 588 nm and (d) CS 3 at 600 nm. **In Inset.** Early scale bleach dynamics of a, b, c and d. **B.** Bleach dynamics of (a') CdSe at 570 nm, (b') CS 1 at 578 nm (c') CS 2 at 588 nm and (d') CS 3 at 600 nm on TiO_2 film. (All TA measurements have been carried out after 400 nm Laser excitation)

Figure 4.6. (A) HR-TEM image **(B)** XRD pattern and **(C)** UV-Visible absorption (olive solid line) and photoluminescence spectra (red dotted line) of CPB NCs. **In inset** of figure A shows the single particle of CPB.

Figure 4.7: Steady state **(A)** UV-Vis absorption and **(B)** photoluminescence spectra of (a) CPB, (b) CdSe QDs, and (c) colloidal mixture of CPB and CdSe QDs. Spectrum (d) shows simple addition of spectra a and b. **(C, D)** Up-conversion luminescence decay traces of (a') CPB at 487 nm, (b') CdSe at 570 nm, (c' and c'') mixture of CPB and CdSe at 487 nm and 570 nm, respectively. For Up-conversion luminescence measurements the samples were excited at 400 nm.

Figure 4.8: Steady state **(A)** UV-Vis absorption and **(B)** photoluminescence spectra of (a) CPB, (b) CdSe/CdS, and (c) colloidal mixture of CPB and CdSe/CdS. Spectrum (d) shows simple addition of spectra a and b. **(C, D)** Luminescence up-conversion decay traces of (a')

CPB at 487 nm, (b') CdSe/CdS at 600 nm, (c' and c'') mixture of CPB and CdSe/CdS at 487 nm and 600 nm, respectively.

Figure 4.9: TA spectra of (a) CPB perovskite, (b) CdSe QDs, and (c) mixture of CPB and CdSe at different time delay after 400 nm pulse excitation in toluene.

Figure 4.10: TA bleach dynamics of (a, b) CPB NCs and CPB/CdSe QD system at 477 nm, and (c,d) CdSe QDs and CPB/CdSe QD system at 555 nm after 400 nm excitation..

Figure 4.11: comparison of upconversion decay dynamics (a) and bleach decay dynamics (b) of CPB nanocrystals. These figures show the luminescence decay and bleach decay dynamics is almost matches.

Figure 4.12: TA spectra of (A) CdSe QDs and (B) mixture of CdSe@CdS and CPB at different time delay after 400 nm pulse excitation in toluene.

Figure 4.13: TA bleach dynamics of (a) CPB at 477 nm (b) CdSe@CdS/CPB at 477 nm (c) CdSe@CdS core shell at 590 nm and (d) CdSe@CdS/CPB at 590 nm after 400 nm excitation.

Figure 5.1.A: HR-TEM image of AIS 3 QDs. **B.** XRD pattern of AIS 1, AIS 2 and AIS 3 NCs.

Figure 5.2. Left panel: Steady state optical absorption and luminescence spectra of (a, a') AIS 1 ($\text{Ag}_{0.25}\text{InS}_2$) (b, b'') AIS 2 ($\text{Ag}_{0.5}\text{InS}_2$) and (c, c') AIS 3 (AgInS_2) respectively. Spectra in dotted line are the de-convoluted emission spectra of AIS 3 (Figure 2 c'). Deconvolution of c' to two Gaussians (peaking at 630nm and 727nm) also have been shown. **Inset.** Time-resolved luminescence spectra of AIS 3 monitored at (d) 630 nm and (e) 727 nm after 445 nm laser excitation. **L** is the lamp profile of 445 nm laser. **Right panel:** Schematic diagram of photoinduced processes, which shows that the electron is trapped either in lower lying Ag

related S-States or donor state (D) and the hole is trapped in internal defect (acceptor state, A). The straight arrows show radiative recombination.

Figure 5.3.A: Graphical plot of (a) Emission QY Vs Ag/In (b) Emission life time at peak wavelength Vs Ag/In (c) FWHM of luminescence Vs Ag/In and (d) Stokes shift Vs Ag/In ratio. **B.** Deconvoluted PL spectra of AIS 1 and AIS 2 and the time resolved PL kinetics of AIS 1 and AIS 2 at the respective peak wavelength after exciting at 445 nm wavelength.

Figure 5.4. Left Panel. Early time scale (100fs to 1.5 ps) TA spectrum of (A) AIS 1 (B) AIS 2 and (C) AIS 3. **Right panel.** Longer time scale TA spectrum of (D) AIS 1 (E) AIS 2 and (F) AIS 3 after 400 nm laser excitation in the toluene solvent.

Figure 5.5: Deconvoluted TA spectrum of AIS 1, AIS 2, and AIS 3 NCs after 1 ns time delay.

Figure 5.6: TA bleach recovery kinetics of (a) AIS 1 at 475 nm (b) AIS 2 at 485 nm and (c) AIS 3 at 535 nm after 400 nm laser excitation in toluene solvent. **Inset:** Bleach recovery kinetics at early time scale of a, b and c.

Figure 5.7. Left panel: TA bleach recovery kinetics of AIS 3 (a) at 455 nm (b) at 535 nm, (c) at 610 nm and (C) at 690 nm after 400 nm laser excitation in toluene solvent. **Right Panel:** Pictorial representation of electron transition from higher excited state to band edge, band edge to Ag related S-States followed by antisite state. Finally recombination takes place through donor acceptor pair.

Figure 5.8: The bi-exciton dynamics of the of the AIS 3 at the 690 nm in pump energy of (a) 0.2 μJ (b) 0.35 μJ (c) 0.45 μJ and (d) 0.8 μJ . **e.** The graphical representation of change of $\Delta A_{\text{max}}^+/\Delta A_{\text{max}}^-$ with changing the pump energy.

Figure 5.9: The bi-exciton dynamics of (a) AIS 1 at 520 nm (b) AIS 2 at 600 nm and (c) AIS 3 at 690 nm with pump energy 0.45 μ J. d) The graphical representation of change of $\Delta A^+_{\max}/\Delta A^-_{\max}$ with changing the ratio of Ag and In.

Figure 6.1-A: HR-TEM image of CdSe NH material. **B:** Steady state optical absorption and luminescence spectra of CdSe quantum dot (a and a') and CdSe⁴³ HS (b and b') in chloroform. **In Inset.** The luminescence decay traces of (a'') CdSe and (b'') CdSe{Au} NH at 586 nm after 406 nm excitation. **(L is lamp profile)**

Figure 6.2: TA spectrum of (a) CdSe quantum dot and (b) CdSe{Au} HS at different time delay on the film after exciting the samples at 400 nm.

Figure 6.3: The decay kinetics of (a) CdSe quantum dot at 560 nm, (b) CdSe{Au} HS at 552 nm and (c) CdSe{Au} HS at 650 nm after exciting the samples at 400 nm.

Figure 6.4. (A) Jsc-V curves of (a) CdSe QDs and (b) Au/CdSe nanohybrid material under 1 sun illumination. **(B)** IPCE spectra of (a') CdSe QDs and (b') Au/CdSe nanohybrid material. **Inset.** The magnified curves of a' and b' beyond 600 nm.

Figure 6.5. A. Nyquist plots for (a) CdSe NCs and (b) CdSe{Au} NHM at -0.5 V forward bias. **B.** Bode phase diagram for CdSe NCs and CdSe{Au} NHM.

Figure 6.6: HR TEM image of **(A)** CdSe@CdS{Au}-1 and **(B)** CdSe@CdS{Au}-2. **(C)** UV-Visible steady state optical absorption spectra of (a) CdSe@CdS core shell (b) HS 1 and (c) HS 2 nanohybrid material in chloroform. **Inset:** Graphical plot of ratio of absorption at 450 nm and absorption at 1S excitonic wavelength versus radii of attached Au NPs. **(D)** Scheme of charge transfer transition within CdSe@CdS{Au} nanohybrid material. **Inset:** Optical absorption band of the CT transition. **(E)** Photoluminescence spectra of (a') CdSe@CdS core

shell (b') HS 1 and (c') HS 2 hetero-structure after 400 nm excitation. **(F)** Time-resolved luminescence decay traces of (a'') CdSe@CdS core shell (b'') HS 1 hetero nanostructure and (c'') HS 2 hetero-structure monitoring at 596 nm after 445 nm laser excitation. **L** is the excitation lamp profile.

Figure 6.7: Transient Absorption spectra of (A) CdSe@CdS core shell nanoparticles (B) HS 1 and (C) HS 2 hetero-structure materials in chloroform at different time delay after 400 nm laser excitation.

Figure 6.8: **(A)** Normalised bleach recovery kinetics at 1S excitonic wavelength (a) CdSe@CdS core shell at 580 nm (b) HS 1 at 570 nm and (c) HS 2 hetero-structure at 570 nm in chloroform after 400 nm laser excitation. **Inset:** Un-normalised bleach recovery kinetics at shorter time scale at same concentration to monitor the change of intensity after coupling with different sizes of Au NP. **(B)** Normalised bleach recovery kinetics at 1P excitonic wavelength of (d) CdSe@CdS core shell (e) HS 1 and (f) HS 2 hetero-structure at 480 nm in chloroform after 400 nm laser excitation. **Inset:** Un-normalised bleach recovery kinetics at shorter time scale at same concentration to monitor the change of intensity after coupling with different sizes of Au NP.

Figure 6.9: **(A)** Transient decay kinetics at 620 nm for (a) CdSe@CdS{Au}-1 (HS-1) and (b) CdSe@CdS{Au}-2 (HS-2) hetero-structure; **(B)** Transient decay kinetics at 510 nm for (c) CdSe@CdS{Au}-2 hetero-structure in chloroform after 400 nm laser excitation. **Inset:** Early time scale transient kinetics.

Figure 6.10: **(A)** Absorption spectra of rhodamin B (RhB) dye in presence of (a) CdSe/CdS core shell (b) HS 1 and (c) HS 2 at different time scale under 1 sun light illumination. **(B)** Plot of C_t/C_0 Vs time of RhB dye in presence of different materials under 1 sun light illumination.

Figure 6.11: (A) UV-Visible absorption and of (a, a') CS 1 and HS 1(dotted line), (b, b') CS 2 and HS 2 (dotted line), (d) CS 3 NCs and HS 3. (B) Steady state luminescence spectra of (a, a') CS 1 and HS 1, (b, b') CS 2 and HS 2 (dotted line), (d) CS 3 NCs and HS 3. (C) Graphical diagram of QY Vs CdS Shell thickness.

Figure 6.12. Transient absorption spectra of (a, a') CS 1 and HS 1, (b, b') CS 2 and HS 2, (c, c') CS 3 and HS 3 at different time delay after 400 nm laser excitation.

Figure 6.13. Exciton Bleach dynamics of (a) CdSe at 570 nm, (b) CS 1 at 578 nm (c) CS 2 at 587 nm and (d) CS 3 at 600 nm after 400 nm excitation. **In Inset.** Early time scale dynamics of a, b, c and d.

Figure 6.14. Bleach kinetics of (a,a') CdSe@570 nm and CdSe/Au@565 nm, (b,b') CS 1 and HS 1@575 nm, (c,c') CS 2 and HS 1@588 nm (d,d') CS 3 and HS 3 @600 nm.

Figure 6.15. Bleach kinetics of (a,a') CS 1 and HS 1@480 nm, (b,b') CS 2 and HS 1@480 nm (c,c') CS 3 and HS 3 @480 nm.

Figure 6.16. Photoinduced absorption dynamics of (a) HS 1 (b) HS 1 (c) HS 3 at 680 nm. **In Inset.** Early time scale dynamics of a,b and c.

Figure 7.1 A: HR-TEM picture of CdSe{Au} HS material. (In Inset magnified image of Au/CdSe). **B:** Steady state optical absorption spectra of (a) CdSe quantum dot, (b) Au NP and (c) CdSe{Au} HS in chloroform.

Figure 7.2: Steady state photoluminescence spectra of (a) CdSe quantum dot (b) CdSe{Au} HS. **Inset:** Time resolved luminescence decay trace of (c) CdSe quantum dot and (d) CdSe{Au} HS at 580 nm after exciting the samples at 406nm. (L is the lamp profile of 406nm laser)

Figure 7.3: Transient absorption spectrum of (A) CdSe quantum dot and (B) CdSe{Au} HS (C) isolated Au NPs in chloroform solvent after exciting the samples at 400 nm.

Figure 7.4: Bleach recovery kinetics at 560 nm for (a) CdSe quantum dot and (b) CdSe{Au} HS; and (c) transient absorption kinetics at 650 nm for CdSe{Au} HS in chloroform after 400 nm laser excitation. Inset: Bleach recovery kinetics for trace a and trace b after normalizing at 5 ps.

Figure 7.5: Steady state optical absorption spectra of (a) Br-PGR dye (10 μ M) (b) CdSe{Au} HS and (c) Br-PGR sensitize CdSe{Au} HS in chloroform. **Inset:** Molecular structure of Br-PGR.

Figure 7.6: The transient absorption spectra of (A) CdSe{Au}/Br-PGR tri-composite system and (B) Br-PGR molecule at different time delay after exciting the samples at 400 nm in chloroform.

Figure 7.7-Panel A: Bleach recovery kinetics of (a) CdSe{Au} HS and (b) CdSe{Au}/Br-PGR tri-composite system at 555nm. **Panel B:** Bleach recovery kinetics of CdSe{Au}/Br-PGR tri-composite system at 655nm.

Figure 7.8: HR TEM image of **Left Panel:** Au NP and **Right Panel:** Au@CdS core shell nano hybrid structures.

Figure-7.9: Steady state UV-Vis absorption spectra of (a) Au nano particles and (b) Au@CdS core shell nano particles in Chloroform.

Figure 7.10. (A) TA spectrum of Au NP after 400 nm laser excitation and **(B)** TA spectrum of Au/CdS core shell nanohybrid after 400 nm laser excitation in chloroform solvent.

Figure 7.11: Bleach recovery dynamics of (a) Au NP at the wavelength of 525 nm and (b) Au/CdS core shell nanohybrid at the wavelength of 570 nm in chloroform solution after 400 nm laser excitation.

Figure 7.12. A: Steady state optical absorption spectra of (a) DBF dye molecule (b) Au@CdS core shell nanohybrid material and (c) After sensitization of Au@CdS core shell with DBF dye molecule. **B.** Steady state UV-Vis luminescence spectra of (a') DBF molecules and (c') Au/CdS-DBF triad system in chloroform after 480 nm excitation. **In Inset:** Time resolved luminescence spectra of (a'') DBF molecule and (c'') Au@CdS/DBF triad system at 570 nm after excitation of 445 nm laser. C is the lamp profile of the **445 nm** laser. All of these spectrum are at the same concentration in chloroform solvent.

Figure 7.13: TA spectrum of Au/CdS-DBF triad system in chloroform solvent after 400 nm laser excitation.

Figure 7.14: Bleach recovery dynamics of (a) CdS-DBF and Au@CdS-DBF triad system at (b) 500 nm at and (c) 530 nm after 400 nm laser excitation.

List of Schemes

Scheme 3.1: Schematic Diagram Showing Photoexcitation to LE States of Both C-343 and D-1421, Followed by De- Excitation to ICT States and Emission from Both LE and ICT States^a.

Scheme 4.1. This scheme represents the carrier cooling, carrier transfer and various type of recombination which are responsible for efficiency of the core shell QDSC.

Scheme 4.2: Schematic representation of electron from CB of CPB to CdSe and hole transfer from VB of CdSe to CPB QDs, respectively.

Scheme 4.3: Allowed electron and restricted hole transfer processes from CPB to CdSe/CdS core shell and CdSe/CdS to CPB NCs, respectively.

Scheme 5.1. Pictorial representation of carrier cooling in antisite state with different pump energy~ 0.2 and 0.8 μJ in AIS 3 NCs. The electron cooling slows down with increasing the pump energy.

Scheme 5.2: Schematic representation of electron cooling and bi-excitonic feature of AIS 1 and AIS 3. Longer electron cooling time in antisite state and higher bi-excitonic feature are shown in AIS 3 than AIS 1.

Scheme. 6.1. Schematic diagram of the role of Au NP in Au/CdSe NHM in enhancement of PCE. Various recombination processes are restricted by the Au NP.

Scheme 6.2: Photo-excited hot and thermalized electron transfer processes in the CdSe@CdS{Au}hetero-structure with different sizes of Au. It shows the photoexcitation of the hetero-structure electrons and holes are generated where the electrons are transferred to the Fermi level of Au NP and the holes are localized in the CdSe core.

Scheme 7.1: Schematic diagram showing electron transfer from semiconductor domain to the metal domain in CdSe{Au} nanohybrid material.

Scheme 7.2: Schematic diagram illustrating the electron and hole transfer processes in CdSe{Au}/Br-PGR tri-composite system. It shows photo-excitation of QD electron and hole are generated where electron is transferred to the Fermi level of Au NP and hole is captured by Br-PGR molecules. On the other hand photo-excited Br-PGR injects electron into the CB of CdSe QD and finally transferred to Au NP. The dashed line indicates the charge recombination reaction between electron in Au NP and hole in Br-PGR.

Scheme 7.3: This Schematic diagram shows after photoexcitation the electron is transferred from LUMO of DBF to fermi level of Au NP via the the CB of CdS shell and simultaneously the hole is transferred to the HOMO of DBF from VB of CdS shell.

List of Tables

Table 3.1: Emission life times of C-343 and D-1421 in absence and in presence of Au NP of different concentrations after exciting the samples at 406 nm.

Table 4.1: The measured J_{SC} , V_{OC} , Fill factor and PCE of CdSe and all core shells.

Table 4.2: The exponential fitted parameter of bleach kinetics of CdSe QD and all core shell.

Table 4.5: Fitted parameter of bleach dynamics of CPB, CdSe and mixture of CPB-CdSe at mentioned wavelength (λ).

Table 4.6. Fitted parameter of bleach dynamics of CPB, CdSe/CdS core shell and mixture of CPB-CdSe/CdS at mentioned wavelength (λ).

Table 5.1. Exponentially fitted parameter of time resolved luminescence decay traces of AIS NCs at different wavelengths after exciting the samples at 445 nm.

Table 5.2: Exponential fitted parameter for bleach recovery kinetics of AIS 1, AIS 2 and AIS 3 NCs at their bleach maxima.

Table 5.3: Multiexponential Fitting Time Constants for the Bleach Kinetics of AIS 3 NCs at Different Wavelengths after Exciting the Sample at 400 nm.

Table 5.4. The exponential fitted parameter of single and bi-exciton dynamics of AIS 3 at 690 nm at different Laser fluency.

Table 5.5. The exponential fitted parameter of single and bi-exciton dynamics of AIS 1, AIS 2 and AIS 3 with laser energy~ 0.45 μ J.

Table 6.1: Multi exponential fitted parameter of luminescence decay traces of CdSe and CdSe/Au after exciting the samples at 406 nm and monitoring at 586 nm.

Table 6.2: The multi-exponential fitted parameters of bleach decay kinetics of CdSe and CdSe/Au hetero-structures.

Table 6.3. The measured solar cell parameters in terms of short circuit current (J_{SC} , mA/cm²), open circuit voltage (V_{OC} , V) and fill factor (FF, %) for CdSe NC and Au/CdSe NHM with and without Cu_xS layer.

Table 6.4. The Fitted Parameters for electrochemical impedance spectroscopy for CdSe NCs and CdSe{Au} NHM.

Table 6.5: Multi exponential fitted parameter of luminescence decay traces of CdSe@CdS, CdSe@CdS{Au}-1 and CdSe@CdS{Au}-2 after exciting the samples at 445 nm and monitoring at 596 nm.

Table 6.6: Multi-exponential fitted parameters of the decay kinetics at 1S and 1P excitonic bleaches of CdSe@CdS core shell, CdSe@CdS{Au}-1 and CdSe@CdS{Au}-2 hetero-structures.

Table 6.7: The multi-exponential fitted parameters of decay kinetics of CdSe@CdS{Au}-1 and CdSe@CdS{Au}-2 hetero-structures.

Table 6.8: Multi-exponential fitted parameters for bleach dynamics of all core shell and heterostructure at different wavelength.

Table 6.9: Multi-exponential fitted parameters for bleache dynamics of all core shell and heterostructure at 480 nm wavelength.

Table 7.1: Multi exponential fitted parameter of TA kinetics of CdSe and CdSe{Au} HS at different wavelengths after exciting the samples at 400 nm.

Table 7.2: Multi-exponential fitted parameters for the TA bleach recovery dynamics of CdSe{Au}/Br-PGR tri-composite system at 555nm and 655nm.

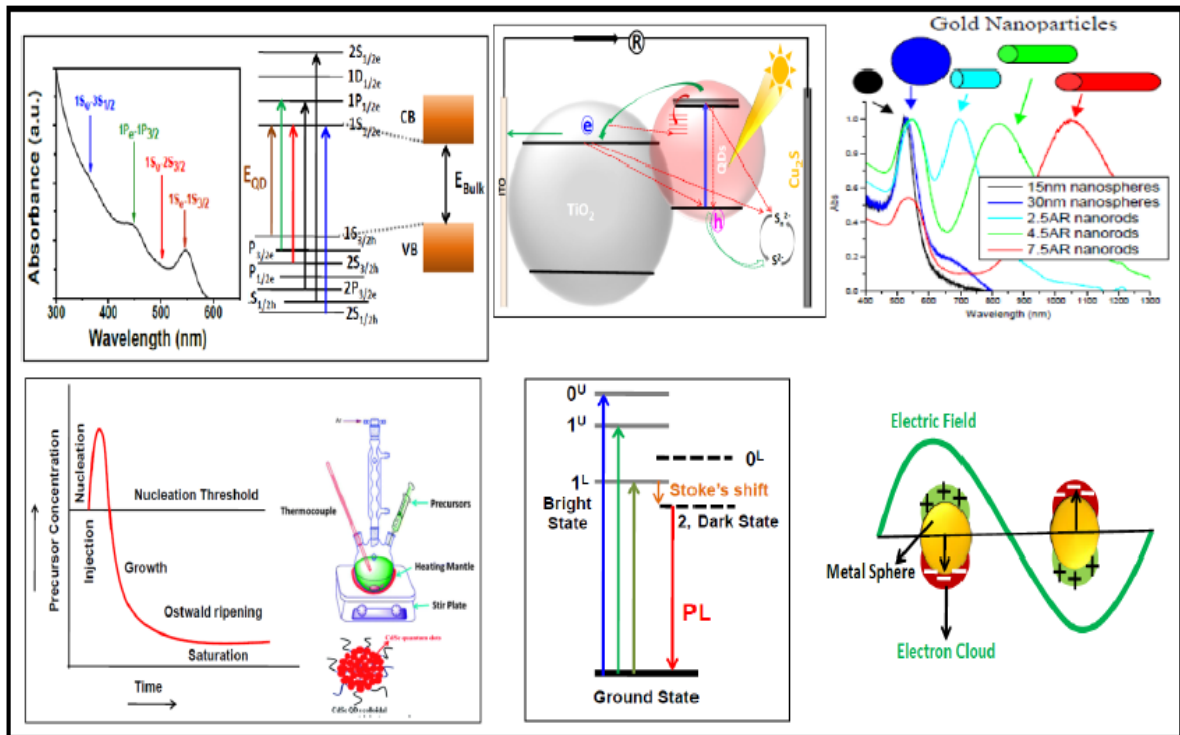
Table 7.3: Multi exponential fitted value for bleach recovery of Au NP and Au@CdS core shell after 400 nm laser excitation.

Table 7.4: Multi exponential fitted value for bleach recovery of Au@CdS core shell and DBF tricomposite at different key wavelength.

CHAPTER 1

CHAPTER-1

INTRODUCTION



CHAPTER 1

1.1. General Introduction:

The time has come to find out the alternative non-renewable energy sources which are going to shrink due to consumption of energy by the people for various purposes.¹ The solar light the unending source of energy is the best option for this non-renewable energy sources² and the semiconductor and metal nanoparticles (MNP) are the best harvester for the solar light.³ The knowledge about metal and semiconductor is very essential to enhance the performance of the light harvesting system with reducing the cost. Since last decades the various important fields of colloidal nanocrystals have been grown rapidly due to its several important properties. The semiconductor nanocrystals, metal nanoparticles and metal semiconductor nanohybrid materials are investigated in this thesis work. In this chapter we are demonstrating the principles of the QDs and MNP, motivation of the work, theoretical aspects of their structural properties, colloidal synthesis method, and its application in photovoltaic.

1.2. Quantum Dots (QDs)

One of the most important NCs of this decades is the QDs. The QDs are emerging materials for photocatalytic and photovoltaics materials due to its unique electronic and photophysical behaviour.^{4, 5 6-9} The quantum dots are the nanocrystals (NCs) where the exciton (electron-hole pair) is confined in all three dimensions.^{10, 11} The exciton confinement makes the QDs size quantised. All the QDs are the NCs, but all NCs are not QDs as the QDS are size quantised but NCs always does not show the size quantization. The assembly of hundreds or thousands of atoms form the QDs and the electronic properties of the QDs follow the quantum mechanics. The QDs are NCs not the large molecules as the electronic properties of the QDs do not change if significant numbers of atoms is changed, where the properties of the molecules become change with number of atoms. The accumulation of well

CHAPTER 1

defined numbers of atoms but less than QDs called the cluster. The electronic property of QDs is different from the molecules and clusture. The band gap of the QDs is in between the cluster and NCs, which is shown in Fig 1.1. The shifting the luminescence compared to absorption first was observed in CdS colloidal solution in 1920. But the shifting of luminescence respect to absorption was not explored. In 1960, the breakthrough of research on nano science was occurred after discovery of the Molecular Beam Epitaxy (MBE).¹² First 2-D quantum well was invented by using the MBE. First Ekimov and Efros started to explore the size quantisation of different semiconductor theoretically in 1980. Murray et al. first synthesised the dimensionless QDs based on CdX (X=S, Se) in 1993 by using the organometallic reagent.¹³ The theoretical knowledge and different synthesis protocol of QDs open multidirectional platform of research field in the current science.

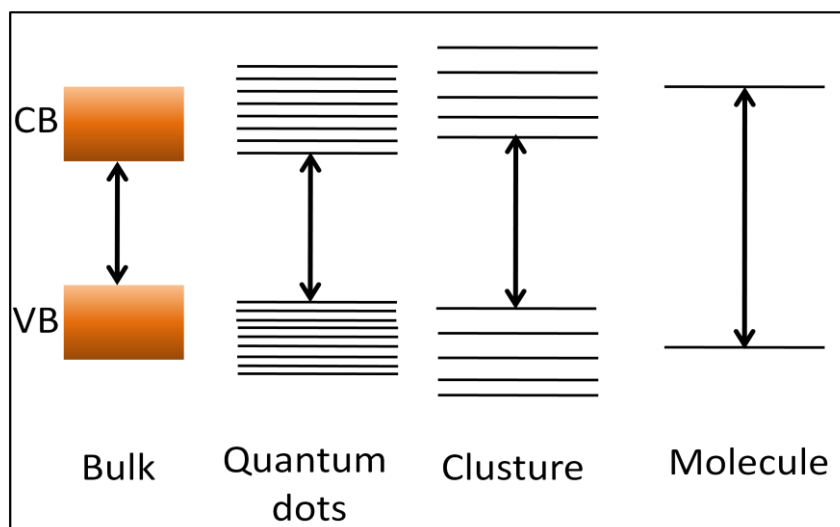


Figure 1.1: Change of energy gap from the molecular system to bulk via cluster and quantum dots.

1.3. Electronic Structure of the QDs: Theoretical Framework

1.3.1. Quantum Confinement

CHAPTER 1

In modern science, the contribution of NCs is excellent, therefore it is very important to know the electronic structure of the QDs. Earlier of this chapter we already discussed that the QDs are dimensionless due to three dimensional confinement of the carrier. On the other way it is also possible to charge confinement in one dimension (1D) or two dimension (2D) and the 1D and 2D charge confinements are referred as quantum wire and quantum well, respectively. In QDs the electron and holes are bound by strong columbic attraction and acts as a single particle with reducing the mass, called exciton. The exciton has well defined mean free path, which is less than the de-Broglie wavelength of the carrier and termed as exciton Bohr radius (a_b). The QDs follow the quantum size effect only when the size of the QDs is less than its exciton Bohr radius. The expression of the Bohr radius is shown below,¹⁴

$$a_b = \epsilon_r \frac{m}{\mu} a_H \quad 1.1$$

Where, a_H = Bohr radius of hydrogen atom (0.052 nm), ϵ_r = size dependent dielectric constant, m = mass of electron, μ = reduced mass of the exciton.

The QDs shows the different type of confinement depending on the size of the QDs. If the radius of QDs is less than the radius of electron (a_e), hole (a_h) and exciton (a_{exc}) i.e. $a < a_e, a_h, a_{exc}$, shows strong confinement where the electron and hole are bound very strongly and termed as *strong confinement regime*. In this regime, the exciton shows quantization of exciton levels. When radius (a) is smaller than both electron and hole but larger than the exciton Bohr radius (i.e. $a_e, a_h < a < a_{exc}$) the confinement energy is less than its columbic or exciton energy and termed as *weak confinement regime*.{Klimov, 2010 #679} The band gap in this case can be given as,

$$E_{QD} = E_B - E_c + \frac{\hbar^2 \pi^2}{2(m_e + m_h)a^2} \quad 1.2$$

The other confinement regime is intermediate confinement regime where only one carrier either hole or electron will be confined. Therefore the confinement of QDs depends upon the size of the NCs. The Bohr radius of CuCl is 0.7 nm which is very small compared to NCs size, shows weak confinement regime. The Bohr radius of III-V semiconductor InAs shows strong confinement regime due its larger Bohr radius ~36 nm which is very larger than the NCs size.¹⁵ But the II-VI semiconductors CdSe, CdS and CdTe whose Bohr radius is at intermediate range 4-7 nm, show either strong or intermediate confinement regime depending upon their NCs size.

1.3.3. Particle-in-a-Sphere Model

The QDs show the size quantisation due to strong carrier confinement in all three dimensions. To explain the size quantisation by quantum mechanically we are adopting the particle-in-a-sphere model.¹⁶ According to the quantum mechanics model, if the particle with mass " m " confined in a sphere of radius " a " can be explained as following equation,

$$V = \begin{cases} 0, & r < a \\ \infty, & r > a \end{cases} \quad 1.6$$

The obtained wave function after solving the Schrödinger equation is shown below:

$$\varphi(r, \theta, \varphi) = C \frac{J_l(k_{nl}r)Y_l^m(\theta, \varphi)}{r} \quad 1.7$$

Where, C is a normalization constant, $J_l(k_{nl}r)$ is the l^{th} order spherical Bessel function, $Y_l^m(\theta, \varphi)$ is known as spherical harmonic, and where

$$K_{nl} = \frac{\alpha_{nl}}{a} \quad 1.8$$

Where, α_n is the n^{th} zero of the J_l . Now, the energy of the particle can be determined from Eigen value of the Schrödinger equation by the following energy equation:

$$E = \frac{a_n^2 \hbar^2}{2ma} \quad 1.9$$

The potential energy is zero within the sphere in Shordinger's wave model. Hence the total energy is only contributed by the kinetic energy of the electron which strongly depends on the size of the QDs. As the Eigen functions are same as atoms, therefore the quantised state can be defined by the different quantum numbers like n (1, 2, 3...), l ($s, p, d...$), and m . Still there is some limitation as the QD was assumed as a blank sphere, but in practical the QDs are not blank sphere, many atoms are there. This limitation can be overcome by Effective Mass Approximation.¹⁷

1.3.2. Effective Mass Approximation:

The Effective Mass Approximation model is used to solve the Schrödinger equation of electronic wave function of bulk semiconductor. From Bloch's theorem the electronic wave functions in a bulk semiconductor crystal can be shown by the equation below,

$$\psi_{nk}(\mathbf{r}) = u_{nk}(\mathbf{r}) e^{i\mathbf{k} \cdot \mathbf{r}} \quad 1.3$$

Where " u_{nk} " is the function of periodicity in the crystal lattice and " n " is label ($n = c$ for conduction band and $n = v$ for valence band) for the band index for the wave function and " k " is the wave vector. The E Vs K band diagram in figure 1.2 shows the energy level of the wave function. To simplify the effective mass approximation, assumption of parabolic shape of band is taken into consideration. According to this approximation the semiconductors can be classified into two types, i.e. direct band gap and indirect band gap semiconductor. In direct semiconductor both the conduction band minima and the valence band maxima point occur at $k = 0$ (Figure 1.2 A), whereas in indirect band gap semiconductor the conduction band minima is away from $k = 0$ (Figure 1.2 B). Therefore the electronic transitions from valence band to conduction band involve phonons instead of following the Frank-Condon

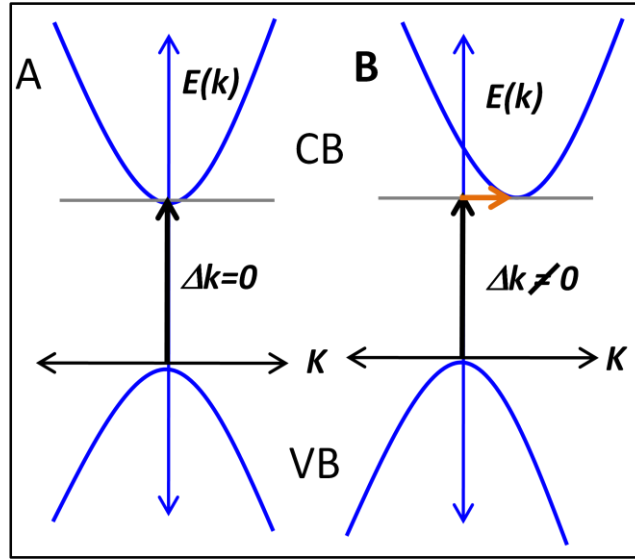


Figure 1.2: Band diagram of (A) direct and (B) indirect bulk semiconductor.

principle. According to effective mass approximation¹⁸ the energy of valence and conduction band can be given as:

$$E_k^c = \frac{\hbar^2 k^2}{2m_{eff}^c} + E_g \quad 1.4$$

$$E_k^v = -\frac{\hbar^2 k^2}{2m_{eff}^v} \quad 1.5$$

Where, E_g represents the bulk semiconductor band gap and the superscript “c” and “v” stand for conduction and valence band, respectively. According to this approximation, the charge carriers act as free particles with an *effective mass*, m_{eff}^c and m_{eff}^v for electron in conduction band and hole in valence band, respectively.

1.3.4. Band Structure

In our previous discussion we have seen that the band structure is parabolic in nature and non degenerate. But in reality this is seldom parabolic and degenerate. This complexity of the band structure can be discussed by discussing the band formation of CdSe QDs. The CB of CdSe is formed by the 5s orbital of the Cd which is two folds degenerate at $k=0$, Where as the VB is formed by 4p orbital of the Se atom which is six fold degenerate at $k=0$.

CHAPTER 1

The CdSe QDs shows two different lattice structures (i.e. diamond and wurtzite) and the valence band degeneracy of these two structure is shown in figure 1.3. In diamond like structure the VB is two fold degenerate, i.e. $p^{3/2}$ and $p^{1/2}$ at $k=0$ due to strong spin orbit ($\Delta = 0.42$ eV) coupling. The subscript 3/2 and 1/2 represent the angular momentum ($J = l+s$). The

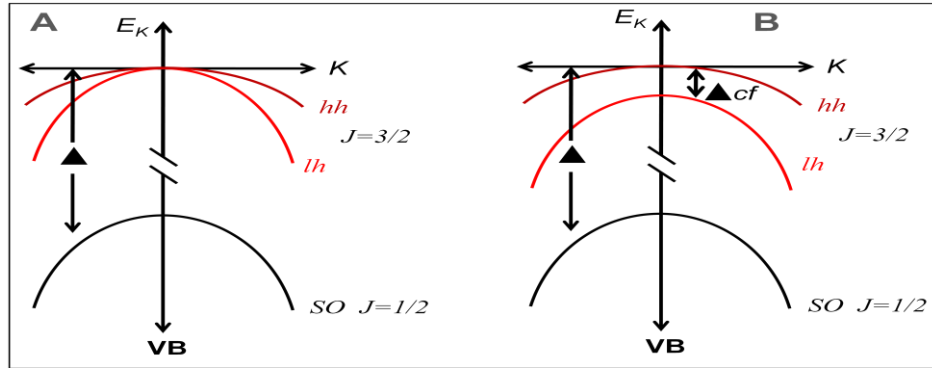


Figure 1.3: Splitting of Valence band (VB) of the bulk CdSe in diamond (A) and wurtzite (B) like structure at $k = 0$ point.

4p orbital of Se has 4 electrons, hence the angular and spin contributions are $l=1$ and $s=1/2$, respectively. The band $p^{3/2}$ again splits into two sub bands $J_z = \pm 3/2$ and $J_z = \pm 1/2$ at away from $k=0$, where J_z is the projection of J . These three bands are generally termed as heavy-hole (hh , $J = 3/2$ and $J_z = \pm 3/2$), light-hole (lh , $J = 3/2$ and $J_z = \pm 1/2$) and split-off-hole (sh , $J = 1/2$). For wurtzite CdSe heavy and light hole bands are no longer split at $k = 0$ due to crystal field asymmetry. The effective masses are $m_{hh} = 1.14m_0$, $m_{lh} = 0.31m_0$, and $m_{so} = 0.49m_0$, respectively.

1.3.5. Electronic Structure of Quantum Dots:

The VB and CB band of QDs are discrete and the discreteness decreases with increasing the size of QDs. The total energy states of CB and VB can be assigned by the angular momentum of the charge carrier at the particular state.¹¹ The total angular momentum

CHAPTER 1

of the electron and hole is contributed by the two types of angular momentum named as (a) a “unit cell” contribution (J) due to the underlying atomic basis, which forms the bulk bands and (b) an envelope function contribution (L) due to the particle-in-a-sphere orbital. It can be

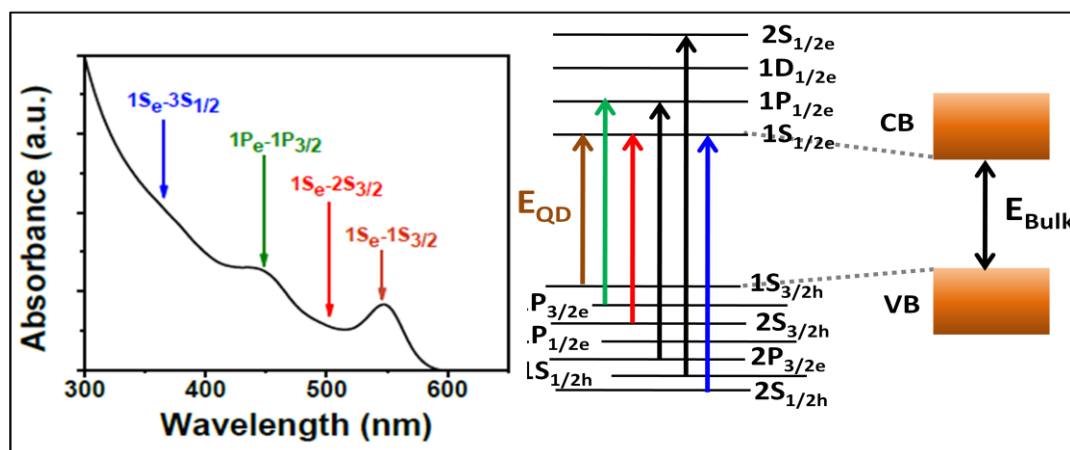


Figure 1.4: Optical absorption spectrum of colloidal CdSe QDs and assignment of different excitonic states for different optical transition. Development of energy levels diagram from bulk semiconductor to the QDs. The optical transitions occur from different discrete CB (hole) to the VB (electron). levels arising from the valence band and conduction band respectively.

expected that the quantum number of each valence sub band (J_h) and each envelope function (L_h) are conserved. But due to band mixing, these two are not conserved. So the VB of the QDs is the mixture of all three sub bands. The nL_e and nL_h are used as angular momentum of electron and hole states arising due to the envelope wave function. Where, L values are S, P, D etc for $L=0, 1, 2$ etc. and n value varies as 1, 2, 3 etc. Therefore the electron states are defined as $1S_e, 1P_e, 1D_e$ etc. while the hole states are as $1S_h, 1P_h, 1D_h$ etc. The valence band of the QDs are complicated due to mixing of different sub bands. The lowest energy hole states are calculated after considering the mixing of different energised hole, i.e heavy hole,

light hole and split off hole. Therefore, for CdSe the lowest energy transition can be represented as $1S_e1S_h^{3/2}$ (1S), $1S_e2S_h^{3/2}$ (2S) and $1P_e1P_h^{3/2}$ (1P)¹⁹ showing in Figure 1.4, which are correlated with the optical absorption spectra of CdSe in figure 1.4. The fine structure of CdSe QDs is explained in next section.

1.3.6. Exciton Fine Structure

Earlier of this chapter, we have discussed about the band structure and energy levels of small QDs by the particle in a sphere model, however there are several other factors which also changes the energy levels.¹⁹ The deviation from the spherical shape of the CdSe QDs (wurtzite,¹⁷ actual shape is prolate¹⁴ like) splits the valence band into different sub bands.¹¹ In case of spherical cubic (zinc blend) CdSe, the electron and hole states are highly degenerate.²⁰ In smaller NCs QDs the interband exchange interaction increases with increasing the electron hole wave function overlap. Therefore the energy states become more degenerates. The $1S_h^{3/2}-1S_e$ state of the CdSe QDs becomes eight fold degenerates. In figure 1.5 illustrates the exciton fine structure and energy levels of spherical and wurtzite shaped CdSe QDs. The energy structure can be demonstrated by considering the two limiting condition. Due to non-spherical shape of wurtzite CdSe, the excited state $1S_h^{3/2}1S_e$ is split into two states with 4-folds degenerate states and assign as $M_n = \pm 3/2$ and $M_n = \pm 1/2$ in the left side of the Figure 1.5. The $\pm 3/2$ or $\pm 1/2$ represents the projection of the total angular momentum of the lowest energy electron and hole in the CB and VB, respectively. In small sized QDs the electron hole exchange interaction increases due to overlap of electron hole wave function. Hence the band splits again in subband gap stated and shown in figure 1.5. Due to strong e-h exchange interaction the lowest energy $1S$ electron and $1S^{3/2}$ hole cannot be considered independently and treated as an exchange-correlated exciton with a total angular momentum N having value either 1 or 2. The exchange interaction splits these two states, one

is high-energy, optically active $N = 1$ bright exciton and lower-energy, optically passive $N = 2$ dark exciton. The size deviation from spherical to prolate further splits the bright ($n=1$) and the dark ($N = 2$) excitonic states into five energy levels having 5-fold and 3-fold degenerate states, respectively. This is shown in figure 1.5 and N_m refers as quantum number i.e. the projection of N along with unique crystal axis. Each energy state are two folds degenerate except energy level $N_m = 0$, resulting eight fold degenerate band-edge exciton split into five subband.²¹

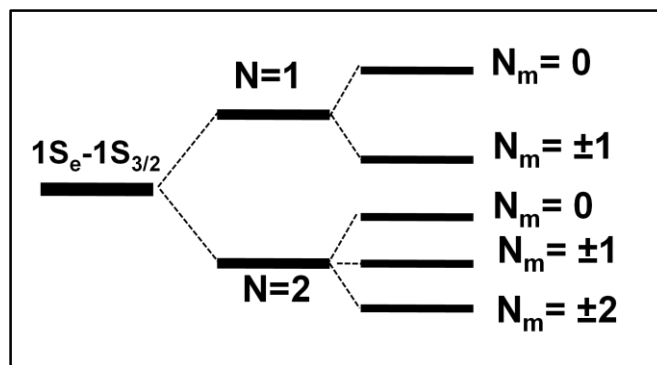


Figure 1.5. (A) Sub bangap exciton fine structure and energy level diagram for e-h exchange interaction and size anisotropy.

1.3.7. Dark exciton and Stoke shift

The e-h recombination time for bulk semiconductor is 1 ns, whereas this time extends from several ns to μ s for NCs.^{22, 23} The longer excited state life time of the NCs is due to trap state which decouples the e-h. But the longer lifetime for high quality QDs can't be explored. This longer life time can be explained by dark exciton. Earlier the fine structure of the exciton is explained through electron hole exchange interaction and deviation from spherical shape.²³ We have discussed that the fine structure of the $1S^{3/2}$ - $1S_e$ excitonic state splits into five different sub levels having same N_m value can be labelled as "U" for upper and "L" for lower states (Figure 1.6). The lowest state ($|Nm| = 2$) remains optically passive after

CHAPTER 1

splitting. On the basis of fine structure and dark exciton transition, the emission behaviour of the QD was first proposed by Calcott et al. The electron-hole radiative recombination from the lowest excitonic state ($|Nm| = 2$, dark excitonic) to the ground state is responsible for photoluminescence of the QDs (red solid line in the Figure 1.6), termed as *dark exciton* and this is forbidden in terms of electric dipole approximation.²³ This transition is one-photon forbidden as for the angular momentum conservation two photons return to the ground state from the $|Nm| = 2$ sub level. On the otherhand, in QDs the lowest optically allowed transition

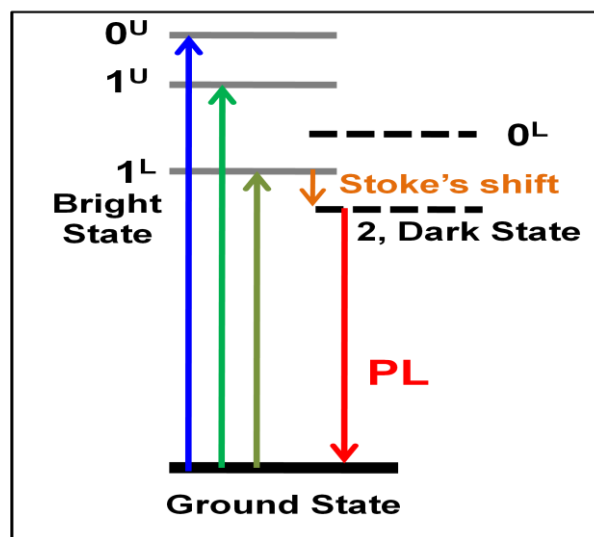


Figure 1.6: Schematic electron-hole exchange interaction and anisotropy associated with crystal field in the wurtzite lattice structure. Optical absorption is in bright state and photoluminescence (PL) is due to dark state transition. The energy difference between the lowest absorption and emission energy levels is assigned as Stoke's shift.

is from the ground state to the 1^L state, which is active state. The broad optical absorption spectrum of the QDs (Figure 1.6 right side) can be explained by the transition from ground state to the 1^U and 0^U state. The photo excited charge carriers thermalize to the dark state from the higher excitonic state. The energy gap between the dark state and the first allowed

state (1L) is higher than the $k_B T$ (where, k_B is Boltzmann constant) and emission is occurred due to recombination of the dark state to the ground state, which is lower energy as compare to energy gap between the lower allowed energy state and ground state. Hence the energy difference between the lowest bright state (allowed transition) and the dark state (forbidden transition) is termed as the resonant Stoke's shift (ΔS_r).¹¹ The ΔS_r value depends on the size of the NCs.

1.4. Density of States (DOS) in Different Size NCs.

The Density of States (DOS) of NCs represent the number of energy states in per unit energy interval.²⁴ The Steady state absorption, carrier relaxation dynamic and charge carrier trapping processes in NCs strongly depend on the involved DOS of the semiconductor NCs. The number of DOS is determined by the charge carrier confinement. The density of states can be represented below,

$$g(E) = \frac{1}{V} \frac{dN}{dE} \quad 1.10$$

In bulk semiconductor, considering the energy distributions are isotropic parabolic in nature and the DOS can be represented as,

$$g(E)^{3D} = \frac{\sqrt{2Em^3}}{\pi^2 \hbar^3} \quad 1.11$$

Therefore the DOS in bulk state strongly depends on the energy (Fig. 1.7).

The DOS of two dimensional quantum well system is independent of energy and represented as,

$$g(E)^{2D} = \frac{m}{\pi \hbar^2} \quad 1.12$$

Therefore here the particles are independent of energy. In 1-dimension quantum wire the DOS is as,

$$g(E)^{3D} = \frac{m}{\pi\hbar} \sqrt{\frac{2m}{E}} \quad 1.13$$

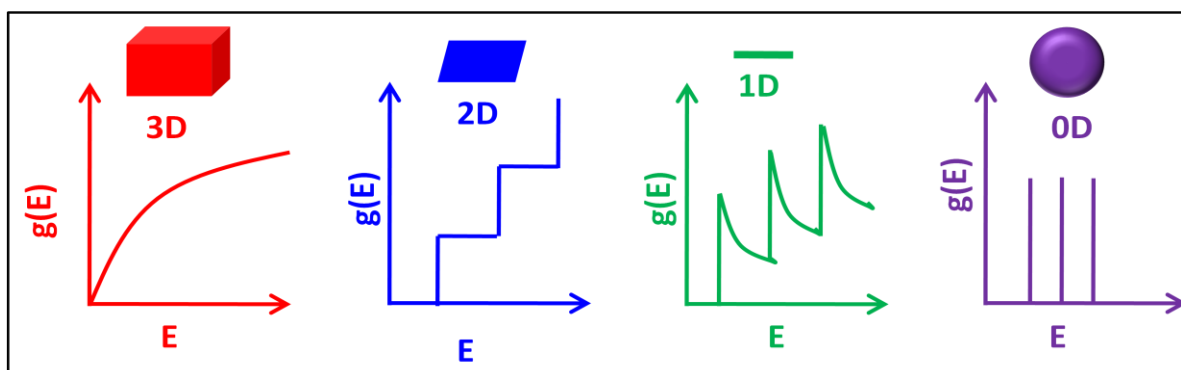


Figure 1.7: Change of density of states with changing the carrier confinement.

i.e. the DOS decreases with increasing the energy (Fig.1.7). In zero dimensional QDs the carriers are strongly confined in three dimensions, hence the energy states are completely discrete. Therefore the DOS can be expressed as simply delta function. The figure 1.7 shows the diagram of DOS with decreasing the confinement.

1.5. Carrier Relaxation

In this thesis the synthesised QDs are passivated by the surface ligand. The discussed energy quantisation of QDs plays a significant role in Charge carrier relaxation. Hot exciton (electron-hole pair) is generated when quantum dots absorbs photon having energy more than the band gap energy of the semiconductor. However the hot hole or electron relaxes to the corresponding band edge state through different pathways. Due to lesser energy gap between the intraband state compared to thermal energy, in bulk semiconductor the carrier relaxes through phonon emission. But the quantised energy gap between two intraband state is larger

as compared to thermal energy, therefore the hot carrier relaxes through different ways such as phonon-assisted relaxation (i.e. phonon modes of the crystal lattice), Auger recombination, and electronic to vibrational energy transfer (EVET) from QD to ligand.^{25, 26}

1.5.1. Phonon-Assisted Intraband Electron Relaxation: Phonon bottleneck

In bulk semiconductor the carrier relaxation is very fast through continuous intraband by emitting the phonon. But in QDs the quantised intraband gap is thousands order of meV, whereas the phonon energy is sub tens of meV. Hence multiphonon emission is necessary for intraband cooling (Fig. 1.8). Therefore the phonon mediated carrier relaxation becomes slows down and the relaxation time (τ) can be expressed as,

$$\tau = \frac{1}{\omega_{LO}} e^{\frac{\Delta E}{k_B T}} \quad 1.14$$

Where, ω_{LO} is the frequency of the longitudinal optical (LO) phonon and ΔE is the energy spacing between the sub band states of the CB.

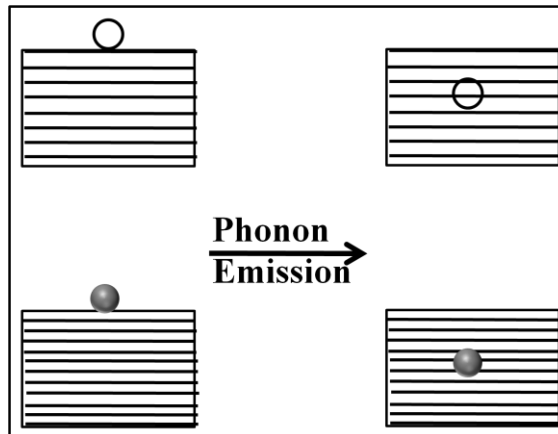


Figure 1.8: Schematic diagram of intraband electron cooling through phonon emission.

Thus the intraband electron cooling mediated through electron-LO phonon coupling slows down with decreasing the NCs size due to restriction imposed by momentum and energy

conservation,^{27, 28} this is termed as ‘*Phonon bottleneck*’.^{25, 29} As the intra band energy spacing for hole state is less than the electron state, the “phonon bottleneck effect” for hole cooling is less compared to the electron.

1.5.2 Auger Recombination and Multi Exciton Generation (MEG).

In our previous discussion, we have seen that the hot electron relaxation decreases with decreasing the size of QDs. Hence the hot carrier relaxes through electron-hole energy transfer processes, termed as Auger recombination (Figure 1.9).³⁰ The CB and VB energy levels of II-VI semiconductor NCs are discrete and the more degeneration of VB than CB makes the less intraband spacing of hole state compare to electron. Within the small regime of NCs there is strong columbic interaction between electron and hole and couple each other. The hot electron relaxes after fast energy transfer to the hole nonradiatively.^{31, 32} Therefore this relaxation mechanism is the fast energy transfer from hot electron followed by the fast hole relaxation process.^{20, 32-34} If the photon energy (i.e. $h\nu \gg E_g$) is more than the band gap

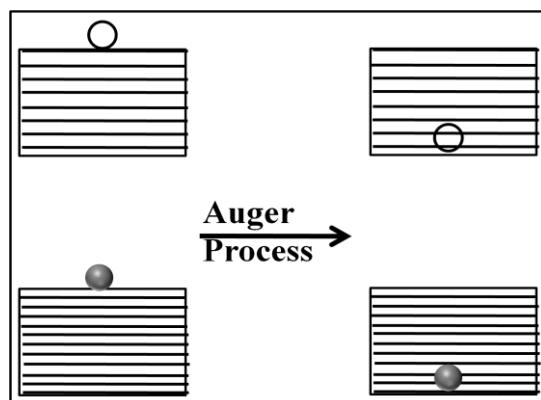


Figure 1.9: Schematic diagram of intraband electron cooling through Auger process.

of the semiconductor, the relaxed excess energy of the hot carrier generates other exciton, called bi-exciton (Figure 1.10). The photon energy having two times more than the band gap of the semiconductor generates the more than two exciton, referred as multi-exciton^{6, 35-37} and

this is efficient for the low band gap NCs (such as PbS, PbSe etc.). Sometimes the excess relaxation energy of the hot carrier produces other exciton, termed as impact ionisation.

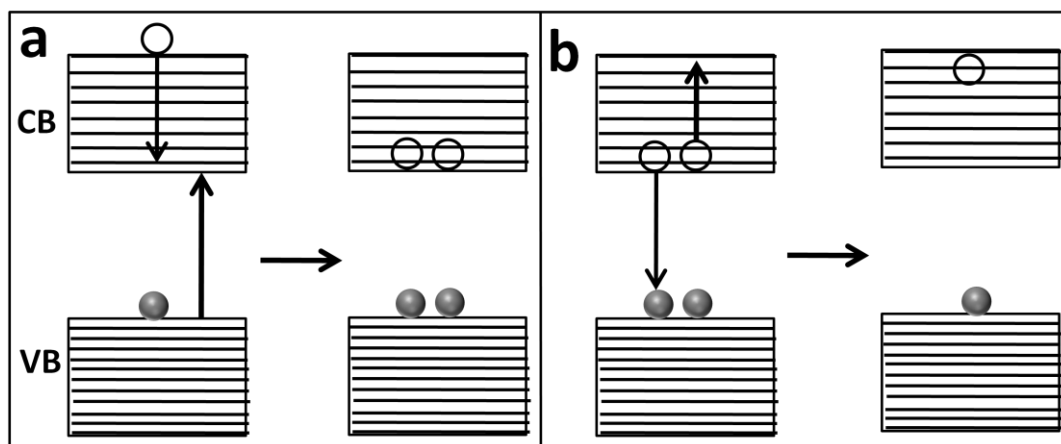


Figure 1.10: Schematic diagram of (a) Auger assisted multiple exciton generation and (b) Auger recombination process.

1.5.3 Relaxation Through Electronic to Vibrational Energy Transfer Processes.

Additional to this above discussed relaxation processes, one more cooling processes are there, where the vibrational levels of ligands are involved and termed as electronic to vibrational energy transfer (EVET).³⁸⁻⁴⁰ In this processes (Fig. 1.11) the excess energy

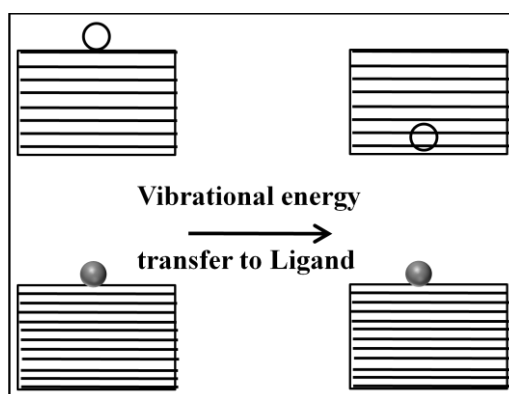


Figure 1.11: Schematic diagram of intraband electron cooling through electronic to vibrational energy transfer (EVET) process.

transferred from electronic state of the QDs to vibrational state of the surface ligand which passivates small QDs. In this thesis work oleic acid, trioctylphosphine, trioctyl phosphine oxide (TOPO) etc. are used for surface capping agent. The hot carrier relaxes through non-radiative energy transfer to the ligand, only when the intraband gap matches with the vibrational state of the ligand molecule

1.5.4 Trapping and Recombination:

Very high surface to volume ratio of quantum dots leads to surface defects in their structure. The surface defect arises in the QDs due to capping agent, dangling bond, crystal mismatch etc.^{41, 42} If energy level of this defect lies within the band gap of the semiconductor, then charge carrier (either electron or hole, depending on the energy levels of defect site) fast transfer to the trap state nonradiatively (Fig. 1.12). The carrier relaxation processes change after the carriers are trapped.^{43 44} The cooling process of the hot carrier becomes faster due to fast trapping and the recombination through trap state slows down due to decoupling of the electron and hole.

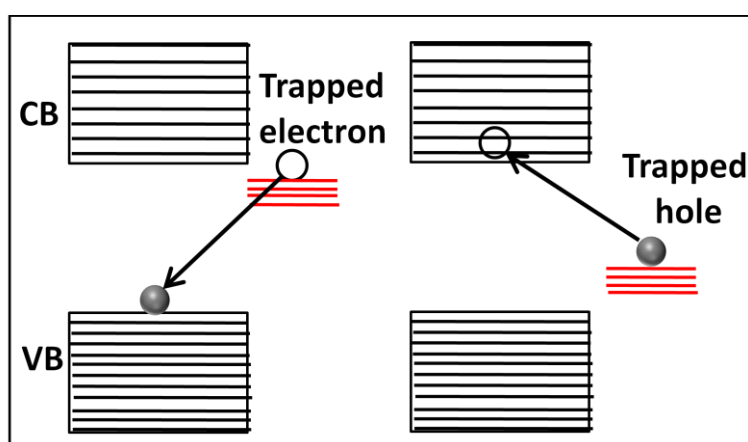


Figure 1.12. Schematic diagram of (A) electron and (B) hole trapping in different surface states.

1.6 Heterostructure: Core-Shell Nanocrystal

The trapped states in QDs decrease the luminescence quantum yield. To improve the quality of luminescence and to alter the electronic structure of the semiconductor QDs often core/shell nano-architecture are introduced. In a single core/shell nanostructure more than one semiconductor is present, which is termed as heterostructure (HS). Considering the band alignment of the semiconductor NCs, the core shells are generally two types such as type I and type II (Fig 1.13).⁴⁵⁻⁴⁸ In type I core shell the wide band gap shell passivates the low band gap core, leading to improvement of QY. Both the carriers (electron and hole) are confined within the core. If the band alignment is reverse, i.e. the smaller band gap shell passivates the wider band gap core named as inverted type I. The core shell CdSe/ZnS, CdSe/ZnSe etc show the type I semiconductor.⁴⁹ In the type II core shell the band alignment of the core and shell is considered in such a way that the one carrier is localised in the core and other is in shell.⁵⁰ CdSe/CdTe, CdS/ZnSe show the type II semiconductor due to their such band alignment.

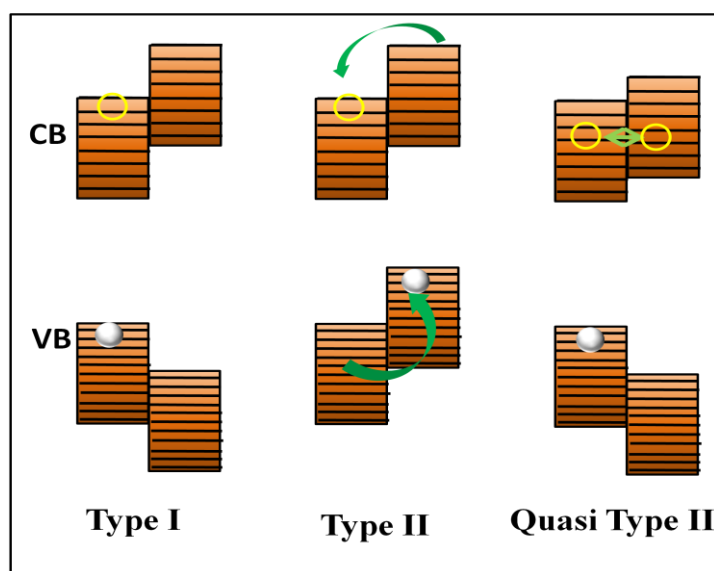


Figure 1.13. Schematic Band alignment of core-shell heterostructures. (Type-I, Type-II and Quasi Type-II).

Therefore the charge separated state between core and shell is generated after photo excitation. Other than these two types of core shell one more class of semiconductor is established after considering the band alignment of core and shell known as quasi type II (CdSe/CdS).⁵¹⁻⁵⁶ Here the one carrier is localised in the core and the other one is delocalised through the core and shell due to minimum band off set between core and shell. This type of semiconductor is very useful in photocatalysis and photovoltaic application.

1.7 Metal Nanoparticles.

The metal particle in nanometer size shows strong and fascinating colour.⁵⁷⁻⁶⁰ Free electrons (i.e. d-orbital for Au and Ag) can travel through the metal nanoparticles (MNP) surface. The mean free path of the metal nanoparticles (MNP) is 10-100 nm.⁶¹ The charge carriers are confined in metal NP (in Figure 1.14). The most important property of the metal nanoparticles (MNP) is surface Plasmon resonance which makes the MNP strong coloured.⁶²⁻⁶⁷ Hence the colour of the MNP strongly depends on the size, shape and dielectric constant of the medium.^{9, 60, 61, 68, 69} To describe the interaction between light and MNP, quasi-static approximate has been used, where the particle size has to be very smaller than the interacting light wavelength.^{59, 70, 71} This interaction is based on particle in an electrostatic

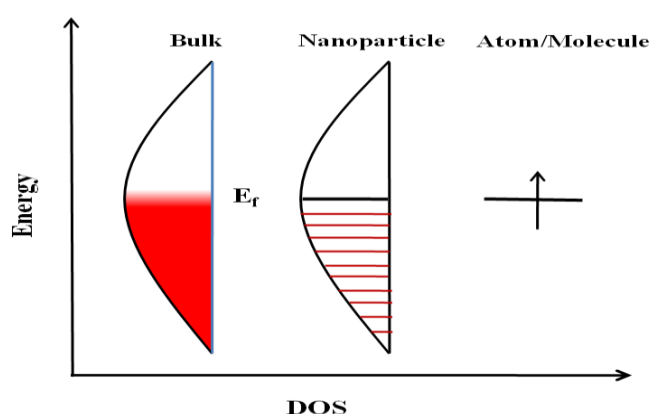


Figure 1.14. Schematic Band alignment of Metal NP with respect to bulk.

CHAPTER 1

field where the field variation is constant through the MNP surface. To explain the molecular polarizability (α) of the MNP of spherical shape, the Clausius-Mossotti relation is used, showing in equation below,^{72,73}

$$\alpha = 3V\epsilon_0 \frac{\epsilon - \epsilon_m}{\epsilon + 2\epsilon_m} \quad 1.15$$

Where, V represents the volume of the particle and ϵ_0 , ϵ and ϵ_m are the dielectric of the vacuum, MNP and medium, respectively. The dielectric constant of the MNP can be expressed as complex form as a function of wavenegth, i.e.

$$\epsilon(\lambda) = \epsilon_1(\lambda) + i\epsilon_2(\lambda) \quad 1.16$$

By using the above equation, we can calculate the absorption and scattering spectra for spherical MNP. In MNP, the imaginary part (ϵ_i) of the dielectric function is varying slowly with the frequency and the real part (ϵ_r) mainly contributed to the dielectric function ($\epsilon \approx \epsilon_r$). The ϵ_i indicates how much light being absorbed in the medium and the ϵ_r determines the resonance frequency of the MNP. To fulfil the resonance condition, the polarisability has to be maximum and from equation 1.15 we can deduce,

$$\epsilon_r + 2\epsilon_m = 0 \quad 1.17$$

Therefore the ϵ_r should be negative. The absorption (C_{abs}) and scattering (C_{sca}) cross-sections [88] can be represented in terms of the dipolar polarizability, i.e.

$$C_{abs} = kIm(\alpha) = 4\pi k a^2 Im \frac{\epsilon_1 - \epsilon_m}{\epsilon_1 + 2\epsilon_m} \quad 1.18$$

CHAPTER 1

$$C_{Scat} = \frac{k^6}{4\pi} |\alpha|^6 = \frac{8\pi}{3} k^4 a^6 \left[\frac{\epsilon_1 - \epsilon_m}{\epsilon_1 + 2\epsilon_m} \right]^2 \quad 1.19$$

For sub-nm fine small MNP, the extinction is dominated by the absorption over the scattering.

The dielectric constant of the medium changes the resonance frequency by varying the ability to accommodate the charge density from the MNP.^{68, 74, 75} The nature of the capping agent also plays an important role in the resonance frequency due to local nature of its effect on the surface of MNP.

The plasmon resonance strongly depends on the geometry of the MNP.^{9, 59, 75-77} In rod MNP, two types of resonance are observed, e.g. transverse and longitudinal resonance (Fig. 1.15). The transverse mode corresponds to oscillation through the width and the longitudinal mode corresponds to the resonance frequency through the length. According to the discrete dipole approximation (DDA) methods,⁷⁸ the transverse Plasmon resonance does not depend on the aspect ratio (=length divided by width), but the frequency and intensity of longitudinal resonance frequency strongly depends on the aspect ratio. The longitudinal wavelength maxima and intensity both are increased with aspect ratio, leading to enhancement of electric field.

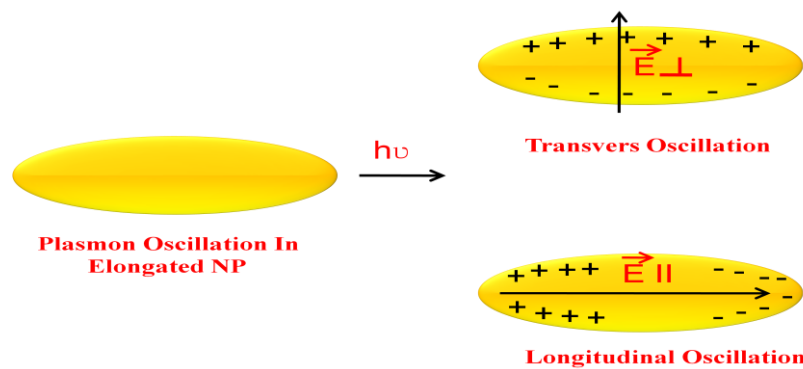


Figure 1.15. Plasmon Oscillation in Elongated Au NP. i.e. Oscillation in different direction of the NP.

a. Electron Dynamics

The electron dynamics of excited MNP plays an important role in electron transfer reaction involved with some adsorbate molecule or semiconductor. The photo excitation and relaxation of the electron in MNP can be discussed in various processes,^{61, 79-83} shown in Fig. 1.16. First, after absorbing the photon the electron from below Fermi level excites to the above Fermi level and creates an electron-hole pair. Second, the hot electron relaxes very fast through electron-electron scattering which is very fast within ~ 10 fs and it depends on the hot electron energy. Third, the hot electron relaxes by 100 fs-1ps by quasi thermal distribution among distinct electron. Fourth, the hot electron further relaxes by electron-phonon coupling in a moderately slower 1 ps-100 ps time scale. The slowest relaxation process is the interaction of electron with the environment as releasing the heat energy. Figure 1.16 represents all the relaxation processes of the excited electron with different time scale.

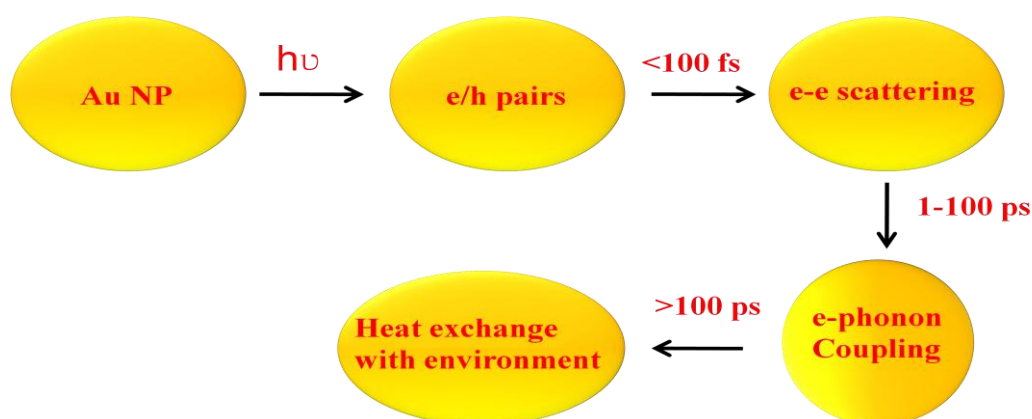


Figure 1.16. Different relaxation processes of hot carriers at different time scale in Metal NP.

1.8. Surface Plasmon Resonance (SPR).

Collective Oscillation of free electron in the conduction band of metal is termed as ‘*Plasmon*’.^{57, 58, 84, 85} Due to interaction between electromagnetic wave with free electron, the electron clouds becomes polarised and starts to oscillate at a resonance frequency of the external electric wave and is called *Plasmon resonance*. If the Plasmon resonance is located on the surface termed as ‘*surface Plasmon resonance*’.^{62, 68, 75, 86} In SPR the electron and hole are oscillating and propagating through the parallel to the metal/dielectric interface showing in Fig 1.17. The oscillating frequency can be expressed by the equation below,

$$\omega = \sqrt{\frac{Ne^2}{\epsilon_0 m_e}} \quad 1.20$$

Where, ω is Plasmon frequency, e is electronic charge, m_e effective mass of electron, N is the electron density in CB of metal NP and ϵ_0 is dielectric constant of the medium. The resonance condition depends on the geometry of the metal, size and dielectric constant of the medium and metal both. The geometry changing causes the change of electric field density on the surface, resulting frequency change of plasmon which alters the absorption and scattering cross section.

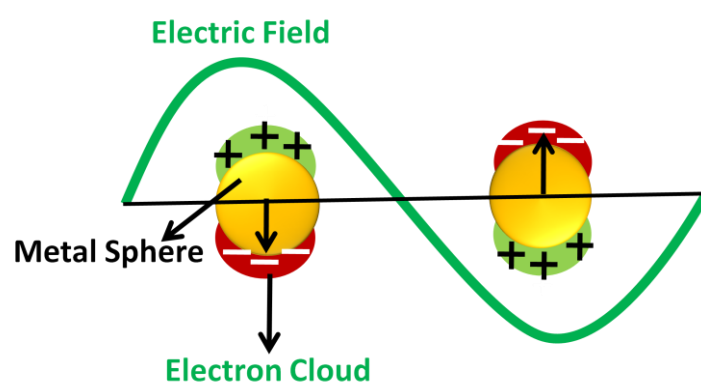


Figure 1.17. Oscillation of plasmon resonance.

1.9 Metal-Semiconductor Nanohybrid Material (Exciton-Plasmon Coupling)

Earlier of this chapter we discussed the details photophysical properties of the metal and semiconductor individually. But it is very important to investigate the change of photophysical behaviour of metal and semiconductor when they are spatially contact. The surface Plasmon resonance of MNP and exciton of semiconductor lose its real properties when they are spatially coupled.⁸⁷⁻⁸⁹ After photo excitation the photo-excited electrons are transferred from semiconductor domain to metal domain in sub picoseconds time scale, resulting luminescence quenching of semiconductor.^{51, 90, 91} Due to spatial contact between metal and semiconductor, the potential barrier decreases to allow the electron transfer, leading to the mixing the electronic state of metal and semiconductor (Fig 1.18).⁸⁷ Hence a long lived charge separated state is generated between semiconductor and MNP. Due to fast electron transfer from semiconductor to MNP, the exciton dissociation is occurred. The multiexciton generation and Auger recombination is minimised due to electron transfer from semiconductor to MNP.⁹² These hybrid materials can harvest the solar light and convert the photon energy to a long lived charge separated state in a single architecture, leading to efficient materials for photocatalytics and photovoltaics. The charge separation is occurred through two ways, first the photo excited electron transfer from semiconductor to Au NP or the hot Plasmon transfer from MNP to semiconductor.⁹³⁻⁹⁵ This electron transfer depends upon the band alignment of the semiconductor. Sometimes the metal and semiconductor both acts as co-sensitizes and generates the more efficient light harvester, where both metal and semiconductor absorbs solar light. A new charge carrier state is generated at the interface of

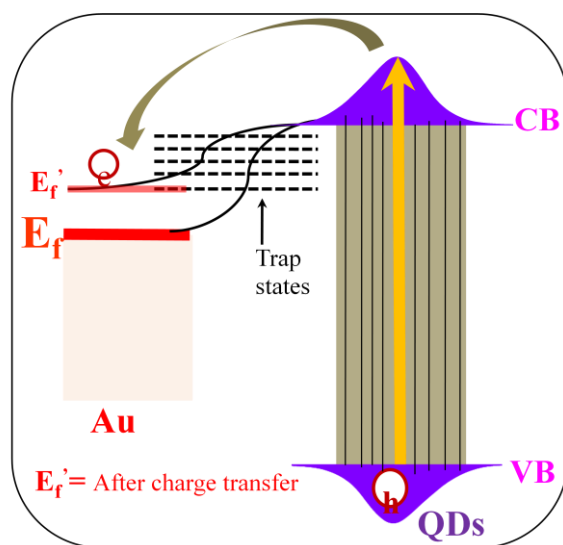


Figure 1.18. Schematic interaction of exciton with Plasmon.

metal and semiconductor in nanohybrid. After electron transfer to Fermi level of MNP, the level goes up towards more negatively charge and reach the equilibrium state of electron transfer from semiconductor to MNP. Hence it makes partly overlap between the energy states of exciton and Plasmon at the interface, leading to mixing of states and modifies the density of states. According to Mie theory, the dielectric function is changed due to mixing of exciton and Plasmon. Therefore the suppression of Plasmon is more in smaller size of Au NP due to more surface contact between metal and semiconductor. The exciton dipole is altered due to local electromagnetic dipole of the Plasmon. The local electric field of exciton is modified due to local electromagnetic field of plasmas, which alters the carrier dynamics of exciton. The charge separation of metal-semiconductor NHM can be enhanced by band engineering concept. The charge separation of type II material like ZnSe@CdS core shell is increased when metal NP attached on the surface, where the electron is localised in MNP and hole is localised in core, leading to enhance the photocatalytic performances.⁹¹

1.10 Synthesis of Colloidal Quantum Dots.

Two major methods have been developed to synthesis the semiconductor NCs like *top down* and *bottom up* approaches.^{96 22, 97} In top down method starting material is bulk and size of bulk is reduced to form NCs by laser ablation, lithographic or ion beam etching etc. But In bottom up approach the precursor and capping agent are taken together and control the synthesis. All the chemical synthesis methods, e.g. sol gel, metal organic colloidal route, chemical vapour deposition and molecular beam epitaxy (MBE) are under the bottom up method.⁹⁸

In this thesis we use only the colloidal quantum dots and to investigate the carrier dynamics of the QDs of the QDs has to be very high quality with monodisperse size. In this thesis we adopted the colloidal synthesis protocol. But in the colloidal synthesis nucleation, growth and precipitation take place simultaneously, leading to poor size distribution. This problem can be solved by the separate nucleation and growth process.⁹⁹ The narrow size distribution of the NCs can be achieved by controlling precursor concentration (self focusing) and a capping ligand during synthesis.⁹⁸ The capping agent binds with the NCs and prevents the agglomeration. The capping agent is chosen after considering the binding efficiency with the NCs. Stronger binding between surfactant (capping agent) and nanocrystal leads to smaller particle size and vice versa. The growth of the NCs can be controlled by the size of the capping ligand. Larger ligand makes steric hindrance which prevents from larger growth. The other important role of the capping agent is the surface passivation. Due to strong binding with the NCs the capping agent reduce the surface trap state. One of the most well defined methods for synthesis of colloidal quantum dots is arrested precipitation technique. It is hot injection method, where the cation precursor is in high temperature in non coordinating solvent and the anion precursor is injected within this at that temperature. After injection fast

nucleation followed by the rapid growth is occurred at that temperature. The growth becomes slow down by Ostwald ripening method (La Mer model, Figure 1.19)¹⁰⁰ and monodisperse QDs is formed. In general phosphine, alkyl phosphine oxide, alkyl amine, alkyl thiol, long chain fatty acid etc are used as surfactants in colloidal synthesis. The high barrier for start to nucleation can be overcome by the high super-saturation and temperature. The

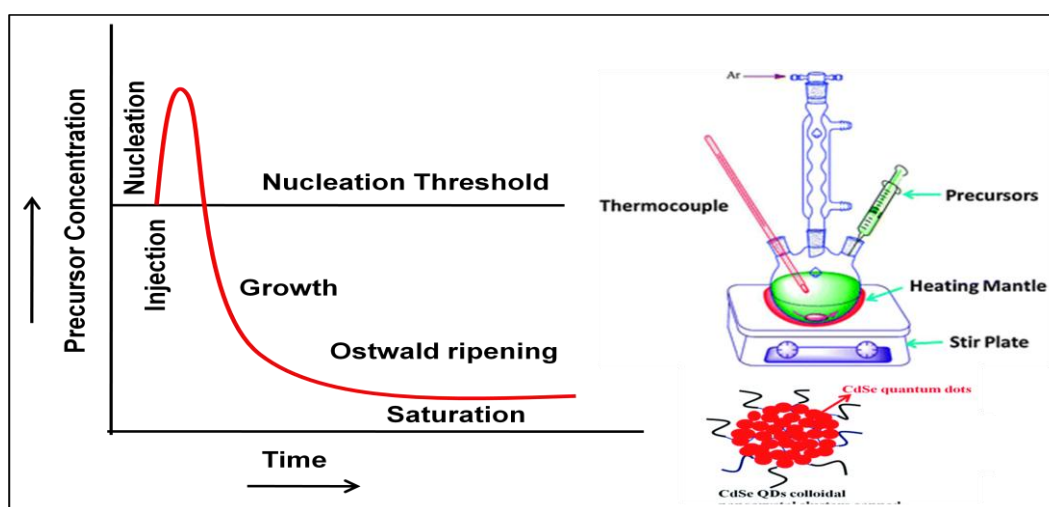


Figure 1.19. La Mer's growth model for Nucleation and growth stage for monodisperse colloidal nanoparticle.

high monodispersity of NCs is achieved by the separate nucleation and growth processes. After following the La Mer's model, the overall nucleation and growth process can be controlled in terms of using precursor concentration and reaction time. The La Mer's model in Figure 1.19 shows the nucleation starts as soon after injecting the precursor and continue until the precursor concentration is above the nucleation threshold. No nucleation is formed after commencing the growth. Extremely slow growth during the nucleation is responsible for sharp size distribution. The monodispersity also controlled by the growth processes. The NCs growth is the fast growth followed by the slow rate. In fast growth processes the smaller

particle grow fast with reacting with unreacted nuclei to minimise the surface energy. After depletion of the nuclei in fast growth process, the nuclei grow in slow rate and termed as Ostwald ripening.

In our synthesis process the excellent size distribution (standard deviation, $\sigma < 10\%$) can be achieved by controlling precursor concentration, reaction time and temperature of the reaction mixture. To clean the synthesised QDs, i.e. to remove the unreacted precursor and excess ligand the NCs are precipitated by the polar solvent like ethanol, methanol or acetone.

1.11 Interfacial Electron Transfer

To explain the electron transfer rate within heterostructure (semiconductor-dye or semiconductor-metal), we follow The Marcus-Hush theory model.^{101, 102} In this thesis the interfacial electron transfer occurs between the semiconductor and dye molecules or metal nanoparticles. Generally the electron transfer occurs due to coupling between the conduction band (CB) of the semiconductor nanocrystal and the lowest unoccupied molecular orbital (LUMO) of the adsorbate molecules or Fermi levels of metal NPs. In dye-semiconductor system the forward electron transfer (ET) takes place from LUMO of the dye molecule to the conduction band of the semiconductor whereas the back electron transfer (BET) occurs from the CB of the semiconductor to the highest occupied molecular orbital (HOMO) of the dye molecule. Analogously in metal-semiconductor nanohybrid system the electron transfer occurs from CB of semiconductor to the Fermi level of metal NPs. The reverse process can't be ruled out. i.e. the hot Plasmon also can be transferred from metal NP to the CB of semiconductor. In semiconductor to metal electron transfer process, the reactant state is mostly localized on semiconductor CB while product consists of continuous states of Fermi level of metal NPs. On the other hand in, in dye semiconductor system the reactant state is

mostly localized on HOMO of dye and product consists of continuous states of CB of semiconductor. Therefore the interfacial ET rate increases with increasing the value of

$$-\Delta G_{ET}^o \quad \text{Where,} \quad -\Delta G_{ET}^o = E_{CB} - E_{LUMO} \dots \dots \dots 1.22.$$

Similarly, the BET (from CB of the semiconductor to the HOMO of the dye molecule) takes place in Marcus inverted region because $-\Delta G_{BET}^o$ (where, $-\Delta G_{ET}^o = E_{CB} - E_{HOMO}$) is greater than the value of reorganization energy. Therefore the more free energy change slows down the BET process.

1.12. Photovoltaic QDSC

Quantum dot sensitized solar cell (QDSC) is one of the promising low cost third generation devices which serve as solar to electrical energy conversion.^{103, 104} The general diagram of the QDSC is shown in figure 1.20. In QDSC the QDs are adsorbed on the small size mesoporous TiO₂ film. After absorbing the solar light the photoexcited electron is injected to the CB of TiO₂. Finally this electron transfer to the FTO glass from TiO₂ and the hole of the QDs gets neutralised by the redox couple of electrolyte to regenerate the neutral QDs. Finally the electron comes to the Cu₂S counter electrolyte to regain the system in its initial state.

The mechanism of QDSC is quite similar to the DSSC. Various processes are responsible for higher efficient solar cell shown in Figure 1.20. After photo excitation the electron is transferred from CB of QDs to CB of TiO₂, leading to increase the flux in CB of TiO₂, which lifts the CB of TiO₂ towards the CB of QDs.^{105, 106} Then this electron flux transfer towards the FTO and simultaneously the hole is neutralised by the electrolyte without changing the redox potential of the electrolyte. The photo excitation energy is stored in terms

of photovoltage and photocurrent. There is some limitation in the QDSC. The main limitation of the solar cell efficiency is the recombination termed as $e^-(\text{TiO}_2)-h^+(\text{VB of QDs})$, $e^-(\text{CB of QDs})-h^+(\text{electrolyte})$ and $e^-(\text{TiO}_2)-h^+(\text{electrolyte})$. Many research groups are trying to minimise the above mentioned recombination to optimise the highest PCE.^{107, 108}

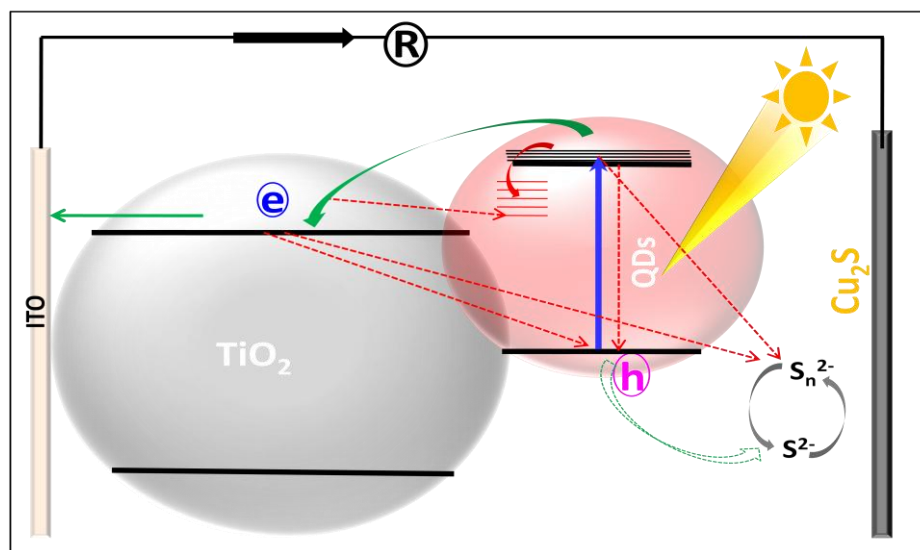


Figure. 1.20. Schematic diagram of QDSC.

Good quality loading of QDs on TiO₂ and control the trap state play an important role in higher efficient QDSC. Several methods are there for loading the QDs on TiO₂ film. One of the QDs loading process is Direct growth technique which includes chemical bath deposition (CBD)¹⁰⁹⁻¹¹¹ and successive ion layer absorption and reaction (SILAR). In direct growth technique the size distribution, i.e. quantum confinement and surface trap state which limits the solar cell efficiency, can't be controlled. Other important method for deposition is post synthesis technique where the size quantized states, high crystallinity, optical properties, band gap and surface state of the sensitizer QD can be controlled. Electrophoretic technique and by ligand assisted assembly method belong to this post deposition technique. Ligand assisted assembly method is more superior compared to electrophoretic technique for QDs

deposition.

1.13. Motivation of the Thesis.

It is very important to find out the alternative source of non-renewable energy source and solar energy is the best option as a renewable unending source of energy. The metal nanoparticles, semiconductor QDs and nanohybrid material are the best solar light harvestor through photocatalysis and photovoltaics. Since last decades this material attracted researcher potentially due to their excellent optoelectronic properties. Most important optical properties of the above material are tunable band gap which can be tuned from visible to NIR by changing the size and shape. The main limitations of the third generation solar cell are the limited absorption of the solar radiation by the QD materials, very fast exciton recombination, less charge separation, photoanode corrosion etc. To overcome the above limitation we need to find out the fundamental aspects of the QDSC by different spectroscopic investigation. It is very important to correlate the excitonics with PCE of the QDSC, which is unexplored in literature. To improve the charge separation of the QDs the metal semiconductor nanohybrid has been introduced. The main goal of my dissertation is the investigation of charge transfer and charge recombination processes in NHM by ultrafast processes to reach maximum PCE. It is unexplored in literature how the charge carrier dynamics is directly correlated with PCE or photovoltaic efficiency. The hot and thermalised electron transfer processes in NHM material has not been discussed in the literature. Therefore main endeavour of my thesis is to investigate the hot and thermalised electron transfer dynamics in metal semiconductor NHM by ultrafast technique. To make more charge separation which is desired for solar energy material, we need to photosensitise the NHM with some organic molecule and in literature it has not been reported the charge transfer

dynamics of metal-semiconductor–dye tricomposite system which can be used as better light harvesting material.

1.14. Overview and scope of the thesis

In this thesis we demonstrated the charge carrier dynamics of metal-semiconductor NHM and metal-semiconductor-dye tricomposite system by ultrafast spectroscopy followed by their photocatalytic and photovoltaic applications. Hence we synthesised the Au NP, different QDs and core shell like CdSe, CdS, CdSe@CdS and metal semiconductor nanohybrid (CdSe/Au and CdSe@CdS/Au) by using different synthesis protocol. The morphology of all the synthesised materials have been characterised by the HR-TEM and X-Ray diffraction techniques. The optical characterisations have been carried out by steady state and time resolved absorption and luminescence spectroscopy studies. The photo physical interaction of two structurally similar coumarin dyes namely coumarin 343 (C-343) and 7-diethyl amino coumarin 3-carboxylic acid (D-1421) on the Au metal NP surface has been investigated. After photo excitation the energy transfer is occurred from photoexcited C 343 to Au NP in aqueous medium. But there is no energy transfer from photoexcited D1421 to Au NP due to lack of overlap between the emission band of D1421 and absorption band of Au NP. On the other hand the quantum yield of the D1421 tremendously enhances in presence of Au NP due to restriction of TICT state and convert TICT state to ICT state on the surface of Au NP. The charge carrier dynamics of CdSe@CdS core shell with varying the shell thickness have been investigated by TA spectroscopy and optimised the shell thickness to reach maximum power conversion efficiency (PCE) 3.88%. To extent the charge separation we sensitised the CdSe and CdSe@CdS core shell with CsPbBr₃ perovskite NCs and charge transfer dynamics have been monitored through ultrafast absorption and luminescence studies. The exciton and bi-exciton dynamics of the AgInS₂ NCs with varying Ag and In ratio

CHAPTER 1

have been discussed and it was found to increase the bi-exciton feature and slow carrier cooling processes with Ag ratio.

The main endeavour of my thesis is to correlate the charge transfer dynamics of metal-semiconductor NHM with photo catalytic and photo voltaic application. In metal semiconductor NHM the electron transfer is occurred from semiconductor to metal NP, leading to formation of charge separated state. To extent the charge separation the NHM was sensitise by a dye molecule and charge separation investigated by ultrafast transient absorption spectroscopy. We found the maximum PCE of CdSe{Au}¹⁹ NHM is 4.39% which is significantly higher than the CdSe QDs alone as monitored through TA and impedance spectroscopy measurement. Then we investigated the hot and thermalised electron transfer dynamics from CdSe@CdS core shell to different size of Au NPs followed by its photo catalytic activity. The hot electron transfer from core shell to Au NP became faster in larger size of Au NP. This faster hot electron transfer in larger Au NP enhances the photo degradation of rhodamin dye. We also investigated the charge carrier dynamics of CdSe@CdS{Au} nanohybrid material after varying the thickness of CdS shell in CdSe@CdS core shell. We observed that the charge transfer rate gradually decreased with increasing the shell thickness of CdS, but the back recombination became slow down with CdS thickness.

Finally this thesis explores the enhancement of charge separation in metal semiconductor NHM by appended with the dye molecule. We investigated the charge separation of CdSe{Au} NHM sensitised by bromo-pyrogallol red (Br-PGR) dye. The long lived charge separated state was generated between CdSe{Au} NHM and Br-PGR where all the electrons are localised in Au and all the holes are in Br-PGR. Additionally we investigated the charge separation between Au@CdSe core shell and dibromo-fluorscene

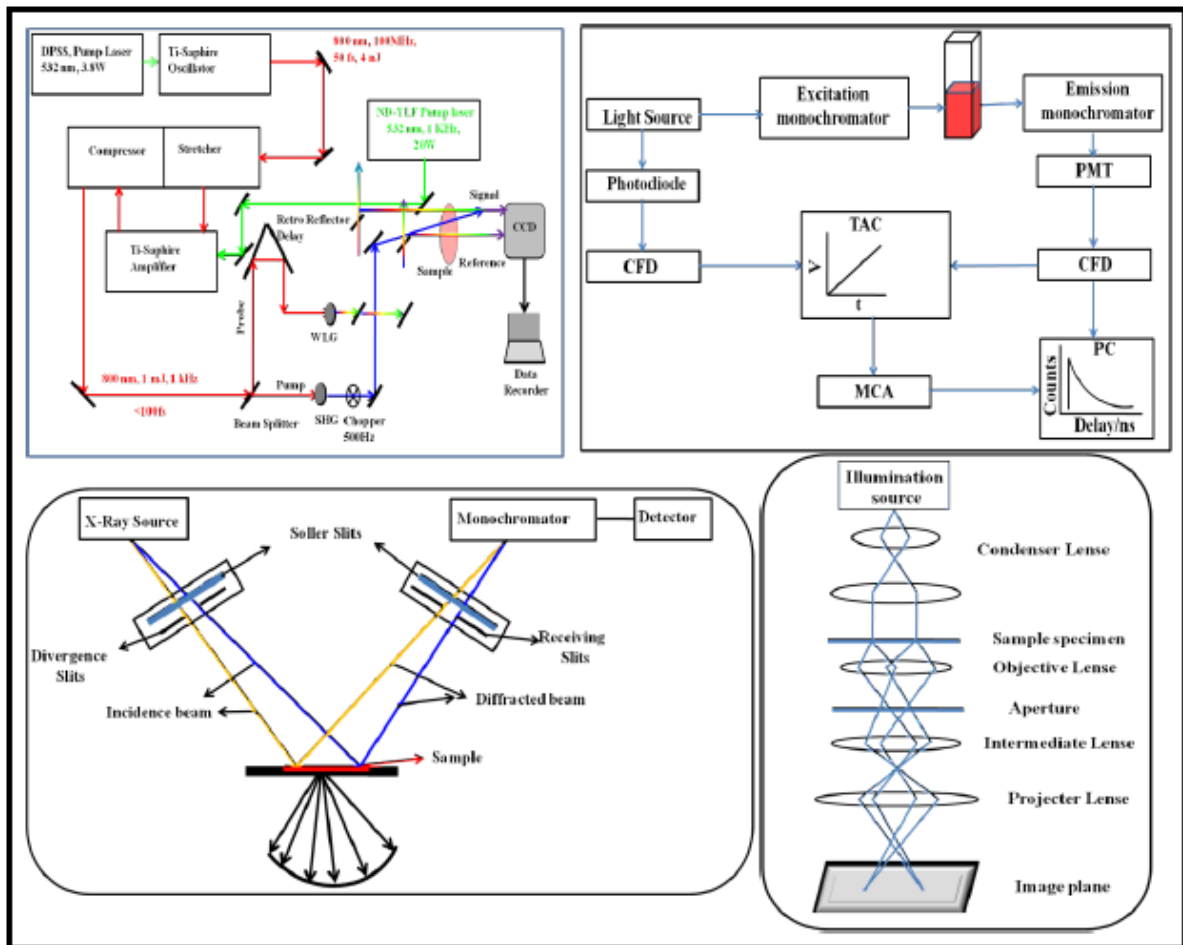
CHAPTER 1

(DBF) dye molecule where a strong charge transfer (CT) complex was formed. Therefore after photo excitation of the triad system all electrons and holes would be localised at the Au nano core and LUMO of DBF, respectively. Therefore, the total investigation of charge transfer dynamics in different hybrid NCs and its application in QDSC and photocatalysis sufficiently contribute in nanoscience research both in fundamental as well as in applications.

CHAPTER 2

CHAPTER-2

EXPERIMENTAL TECHNIQUES



CHAPTER 2

2.1. Introduction.

The investigation of charge carrier dynamics of semiconductor, metal-semiconductor nanohybrid and nanohybrid-dye interface are the main thrust of this present thesis work. Before going to the charge carrier dynamics by various spectroscopic techniques, it is very important to characterise the crystal structure of all the synthesised material. The transmission electron microscopy and X-ray diffraction were appointed for structural characterisation of the synthesized material. Where the UV-Vis optical absorption and emission spectroscopy were used for optical characterization of the materials. To monitor the charge carrier dynamics the nanosecond time resolved luminescence (TCSPC) and broadband femtosecond pump-probe transient absorption spectroscopic techniques were employed. To investigate the photovoltaic performances, we measure the PCE and IPCE. In this chapter we are going to discuss all these above mentioned techniques in brief.

2.2. High Resolution-Transmission Electron Microscopy (HR-TEM).

a. Introduction.

High Resolution-Transmission electron microscopy (HR-TEM) is one of the versatile unique techniques for structural characterisation of nanometer sized crystal. The TEM is unique for characterisation of the nanocrystal (NC) because it is with atomic scale space imaging with 1 nm spatial resolution. The single NC can be identified by HR-TEM with chemical identity. In HR-TEM, the lattice planes of specimen crystal diffract the incident electron beam in different direction and the resolution of HR-TEM is limited by wavelength of diffracted electron wave. The resolution of the TEM follows the Raleigh criteria. After interaction of incident beam with specimen sample, it changes the phase and amplitude with respect to undiffracted or incident beam. The phase contrast mode generates the high resolution image and the reduction of amplitude is the cause of the image contrast.

b. TEM Layout.

The layout of TEM has been shown in figure 2.1. It consist an illumination source, sample specimen, objective lens, magnification system and detector and optional chemical analysis system. Electron gun and condenser lens are the main constituent of the illumination source. The electron gun might be thermionic emission or field emission source. Tungsten filaments or lanthanum hexaboride (LaB_6) crystals (more common) are used as thermionic

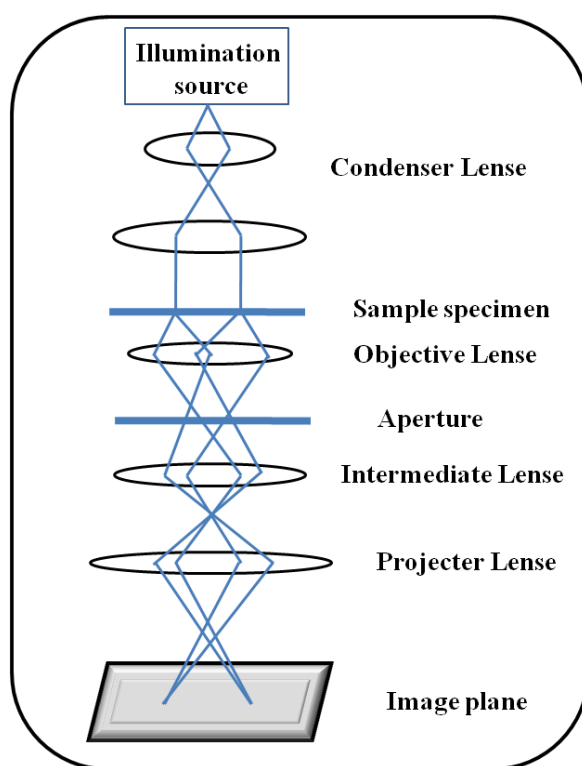


Figure 2.1. Schematic Layout of TEM.

source, whereas the sharp tungsten needle is used as field emitter after applying high voltage. The Field emission source is superior than the thermionic source due to its better coherent nature. In thermionic emission the low work function LaB_6 material reduces the problem arising due to filament heating. A condenser lens is used in illumination system before sample specimen to generate a fine electron probe. The carbon coated Cu grid is used in

CHAPTER 2

sample specimen where the incident electrons interact with sample and diffraction is occurred. After diffraction the objective lens converge the diffracted beam to reconstruct the enlarged image on the image plane. This lens should have small focal length. Depending on the specimen investigation, the rear focal plane or image plane placed as virtual objective plane on detection window. The magnification component consists of intermediate lens and projector lens by which the image is magnified by $\sim 10^6$ orders. Finally the data is recorded by charge coupled device (CCD). To minimise the electron gun oxidation in thermionic electron gun or to get pristine surface in FEG the whole components are in highly vacuum column. To get real image contrast of nano-materials the TEM image mode is used whereas, to identify the crystal and the relative orientation the selected area electron diffraction (SAED) mode is used in DP mode. The main feature of the HR-TEM is the focal length of the objective lens. The focal length of the objective lens has to be very small with high converging ability to form magnified image. This lens minimise the aberrations of largely scattered electron. The aberration reduces the resolution of the instrument and this is generally two types, e.g. spherical and chromatic. The spherical aberration is represented by the equation,

$$r_s = C_s \alpha^3 \quad 2.1$$

Where, r_s , C_s and α represent the radius of disc produced by spherical aberrations, spherical aberration coefficient and lens aperture, respectively. By using the strongly focussing mirror we can minimise this type of aberration.

On the other hand the kinetic energy variation of electrons is responsible for chromatic aberration. The kinetic energy variation is occurred due to fluctuation in

accelerating voltage and inelastic scattering with sample. This chromatic aberration can be expressed by equation below,

$$r_c = \alpha C_C (\Delta E_0 / E_0) \quad 2.2$$

Where, C_C , E_0 and ΔE_0 represent the chromatic aberration coefficient, energy and the spread in energy, respectively. The chromatic abbreviation can be minimized by using the high focusing power laser.

c. Image Formation.

The contrast between bragg's diffracted electron waves with respect to incident wave makes the TEM image. The diffracted electron wave after elastic collision with specimen is focussed by the objective lens to generate the spot or ring pattern which form the magnified image on the image plane. The angular distribution of the elastically scattered electrons produces diffraction pattern, whereas the spatial distribution leads to "image contrast".

d. Selected Area Electron Diffraction (SAED) and Electron Energy Loss Spectroscopy (EELS).

Other than TEM image formation, this instrument is also used for other spectroscopy measurement, like SAED and EELS. Different type of interaction is occurred between the electron wave and specimen. After elastic scattering, the scattered wave produces the ring or spot after constructive interference. The crystalline structure or symmetry can be determined from angular position of spots or rings. Several ring or spots are placed radially from the central point or un-diffracted beam for the crystalline sample. The spots or rings signify the particular plane of the crystal and the radial distance from the centre is related to the lattice spacing and TEM parameters.

The Electron Energy Loss Spectroscopy (EELS) is based on the energy loss of the diffracted electron wave due to inelastic collision with the matter. When the incident wave electrons (E_i) inelastically collide with the matter, lose its specific energy (ΔE) due to excitation of the matter from K-shell to M-shell. The lost energy can be calculated from the scattered electron wave (E_s). For particular sample this specified energy loss is defined. We often use the diagram intensity versus energy loss to calculate the elemental mapping of the specimen.

2.3. X-Ray Diffraction (XRD)

a. Introduction.

X-ray powder diffraction (XRPD) is a versatile techniques to characterise the crystal structure in powder form. By XRPD we can identify the crystallinity and lattice parameter of the sample qualitative and quantitatively. In XRPD, the X-Ray is diffracted in different angle by the different planes of the powder sample. The diffracted angle of the X-ray depends on the inter planner distance (d) and wavelength of the X-ray (λ). The d-spacing can be determined by the popular Bragg's equation,

$$n\lambda = 2d\sin \theta \quad 2.3$$

Where, n is the order of diffraction, λ is wavelength of incident X-ray, θ is the diffraction angle and d is the inter planner distance. The intensity of the diffracted X-ray depends on the scattering factor and miller indices of the planes. The scattering factor depends on electron density of the atoms and increases with increasing the electron density.

The other important application of the XRPD is the determination of the size of the crystal and can be calculated by the broadening of the diffracted X-ray peak by using the Scherrer's formula. The Scherrer's formula is given below,

CHAPTER 2

$$d = \frac{K\lambda}{\beta \cos \theta} \dots\dots\dots 2.4$$

Where, d ~mean size of crystalline domain (in Å), K is shape factor, λ is wavelength of the X-ray, β is FWHM (full width at half maxima) of the peak in radians and θ is Bragg's angle.

The value of shape factor is 0.9-1 and it varies according to the crystal shape. The FWHM of the peak (line broadening, β) can be measured by using Warren formula,

$$\beta^2 = \beta_M^2 - \beta_s^2 \dots\dots\dots 2.5$$

Where, β_M^2 is measured FWHM in radians and β_s^2 is the measured FWHM for standard material. The Scherrer's equation can apply only on grain size lesser than 0.1 μ m.

b. Instrumentation.

The layout of the XRPD has been represented in Figure 2.2. The X-ray is generated by bombarding the metal target by high energy electron. Generally the used metals for X-ray generation are copper, iron, cobalt, molybdenum and chromium. The emitted X-rays are in all direction and to have in same direction, these are allowed to pass through beryllium and nickel window during the measurement. Before fall on the sample, the background of X-rays is passed through divergence slit and soller. The sample for XRPD is prepared by adhering the powder on glass slide by a binder like amyl alcohol. After diffraction the diffracted beam passed through soller, divergence and receiving slits in diffractometer. Before detection, the diffracted beam passes through a monochromator. In detection counter the gas filled tube or scintillation counter are commonly used. In gas filled tube the gas is ionised by the diffracted X-ray and collected by applying the high voltage across the two electrodes. The diffracted X-ray is scanned by detector by sweeping from one angle to other. The some diffracted beams among many are constructed interference at an angle θ and show a sharp peak at that angle

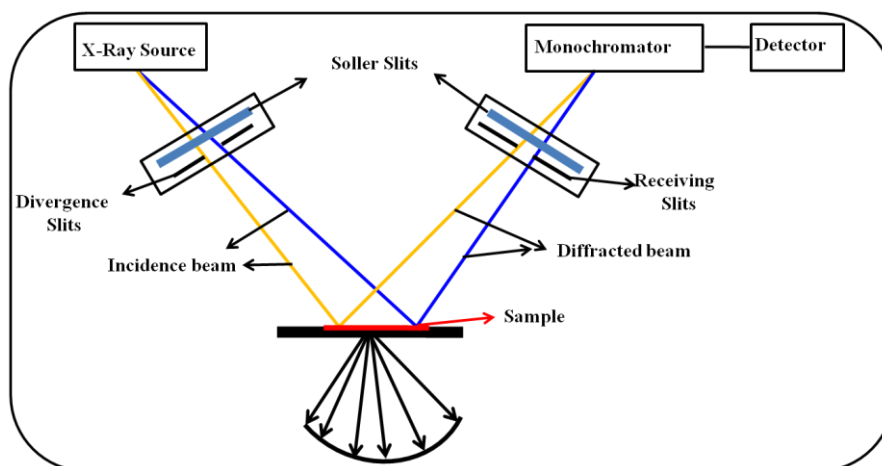


Figure 2.2. Schematic Layout of powder XRD

which follows the Brag’s law. The peak position are appeared at the final plot of intensity versus scattering angle and these peak positions are specific for all material, by which the crystal lattice can be identified.

2.4 Ultraviolet-Visible (UV-Vis) Absorption Spectroscopy

To investigate the electronic transition from ground state to excited state of the molecule and semiconductor, the steady state optical absorption spectroscopy is used. After absorbing the photon the atom or molecule show the electronic transition from ground state to excited state. The absorption (A) of the atom or molecule follow the “Beer-Lambert’s law”,

$$A = \log\left(\frac{I_0}{I}\right) = \epsilon_{\lambda} Cl \dots\dots\dots 2.6$$

where, C represents the concentration (mol L^{-1}) of chromophore and l is optical path length (typically 1cm, quartz cell). ϵ_{λ} is the molecular extinction coefficient which is wavelength dependent property and depends on electronic transitions. In our thesis work we have used the JASCO-640 spectrophotometer. The quantitative and qualitative analysis can be done by absorption spectroscopy, e.g. concentration, size of the semiconductor colloidal particle, polarity dependent electronic transition etc.

2.5 Emission spectroscopy

After absorbing the photon the molecule go to higher vibrational level of electronic excited state directly and relaxes to its lowest vibrational level (i.e. $v = 0$ of excited state) following the Frank-Condon principle and again returns to ground state by emitting photon or non-radiative way. Only radiative recombination is the responsible for emission phenomena. In semiconductor the emission shows due to radiative recombination between lowest vibrational level of CB and VB both, is called band edge emission. The emission in semiconductor is also shown by its trap state recombination, termed as trap state emission. The emission peak maxima and width of the spectra are very important to characterise the sample.^{112, 113} The Excitation Spectra can also be measured by varying the excitation wavelength after keeping fixed luminescence wavelength. In my thesis work, the HORIBA (Canada) luminescence spectrometer has been used. It consist the Xe lamp as excitation source, monochromator for different excitation source and photomultiplier tube (PMT) as detector. This spectrometer covers the spectral range from 300-850 nm. Right angle geometry for excitation beam line and PL beam line is maintained for measurements. The luminescence quantum yield can be calculated by the equation below,

$$\phi(\text{sample}) = \frac{A(\text{sample})}{A(\text{standard})} * \frac{OD(\text{standard})}{OD(\text{sample})} * \phi(\text{standard}) \dots \dots \dots 2.7$$

Where, ϕ , A and OD represent the luminescence QY, area of the luminescence curve and optical density of the corresponding sample or standard, respectively.

2.6 Time Correlated Single Photon Counting (TCSPC) technique:

The time dependent luminescence study is an important technique to measure the luminescence intensity as a function of time after creating the excited state.¹¹⁴ To measure the time dependent luminescence intensity, the commonly used technique is Time Correlated Single Photon Counting (TCSPC).^{115, 116} The various intra and intermolecular photo physical

CHAPTER 2

processes can be resolved by this technique, such as intra and inter molecular energy and electron transfer processes, photosensitisation etc. The excitation source of this technique is short pulse mode locked laser (diode laser-70ps, LED laser-750ps) and photo multiplier tube (PMT) used as detector for TCSPC measurement. The high speed micro plate in the TCSPC improves the time resolution of this technique. This technique is very sophisticated because only 2% counts of the excitation source are necessary for detection. The resolution of the TCSPC does not depend on the width and tail of the PMT.

a. Instrumentation

The Figure 2.3 represents the working layout of the TCSPC instruments. It consists excitation source (pulse laser), monochromator, PMT for emission recording, constant fraction discriminator (CFD) and “time-to-amplitude converter (TAC)” for photon counting, multi channel analyser (MCA) for event histogram generation and finally, a computer for data generation and analysis. In TCSPC the delta pulse is generated from the excitation source and divided into two parts, one illuminate the sample and simultaneously the other part goes to photodiode (PD). The PD generates the start electronic signal and the sample starts to emit the photon. The electronic signal generated from PD goes through “constant fraction discriminator (CFD)” which creates “START” trigger for “time-to-amplitude converter (TAC)”. The TAC consist a capacitor and starts charging as soon as the start signal comes. The other part of the excitation source excites the sample and starts to emit emission photon. After monochromatization the emission photon is sent to PMT detector which is placed at the right angle of the excitation source to detect the emission counts and generates the stop signal. This stop signal passes to TAC through the CFD (second) and the capacitor stop the charging. The TAC runtime Δt , i.e time difference between start and stop trigger

represents the electronic delay of the photon counting. This TAC output signal processed by

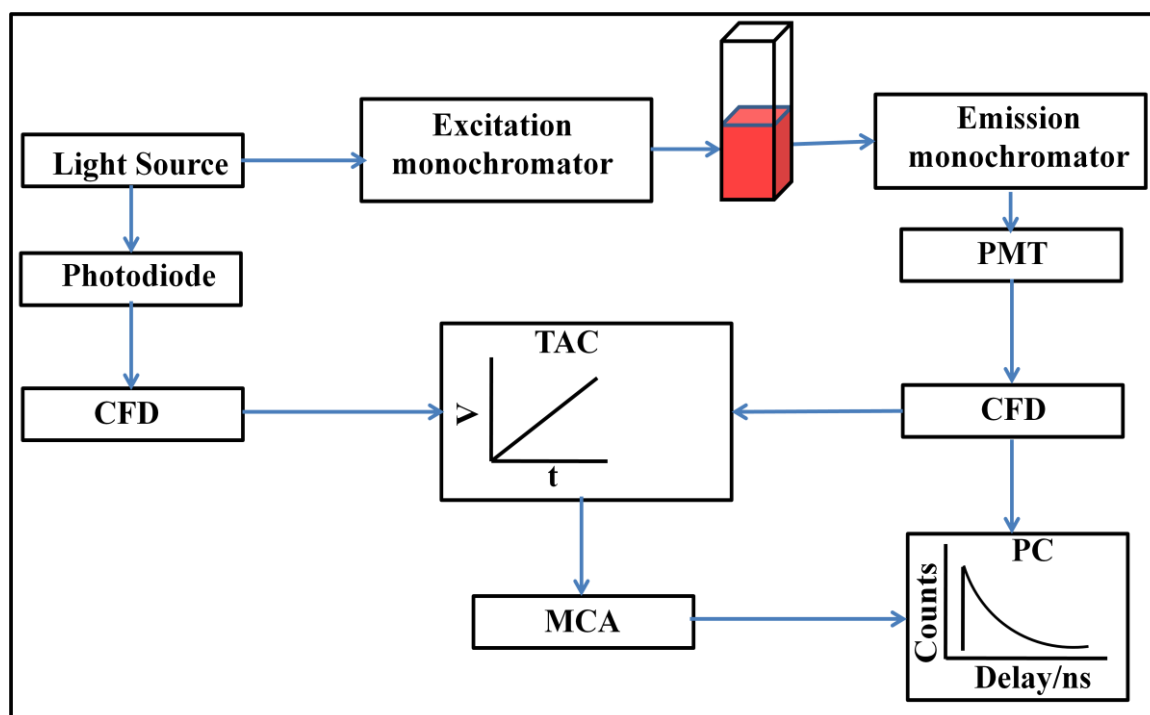


Figure 2.3. Schematic diagram of TCSPC instrument.

analogue to Digital Converter and feed to Multi Channel Analyser (MCA). The electronic delay is adjusted for scattering sample which gives fastest STOP triggering due to its fastest instrument-photo response function (IRF). The 'Window Discriminator' discards the false reading by nullifying the "TAC" readout when voltage is crossed its limit. The counts are registered by the different channel of the MCA and the total 1 to 2400 channel numbers are in order. The width of the channel is the electronic resolution of the TCSPC and the total sum of the channel is the total range of the delay time. The 5000-10000 counts from 1 MHz pulse repetition rate generates a histogram which show the profile of the luminescence decay at very low emission counts as collected data statistics is made by poisson distribution. Therefore the excitation source and counts detection have been maintained at right angle geometry. To avoid the anisotropy effect of the luminescence the emission polariser light was kept at magic

angle (54.5) with respect to excitation polariser. The histogram was deconvoluted by IRF to show the real emission decay kinetics and feed to data software.

To fulfil my thesis work, I used IBH made TCSPC instrumental set-up. The used various excitation source (*viz.* 406nm, 463nm, 589nm) were diode laser with 70 ps pulse width and vertically polarised. The luminescence decay traces is fitted by least square analysis which is instrument set up program. The fluorescence decay $I(t)$ can be represented as,

$$I(t) = \sum_{i=1}^n \alpha_i e^{-t/\tau_i} \dots\dots\dots 2.8$$

Where, τ is intrinsic function of particular emission events, the order “i” stands for many photophysical processes happening in the system.

2.7 Time Resolved Absorption Measurements: Pump-Probe technique

a. Introduction:

The time resolved luminescence technique is restricted only on luminescent sample. The non radiative processes cannot be justified by this technique. The Time Resolved Absorption technique is a versatile technique to monitor the kinetics of various photoinduced radiative and non radiative processes, such as cation formation, intermediate of free radical, regeneration of ground state, electron cooling, charge transfer and recombination, trapping etc.^{112, 117} The two colour pump probe set up is a universal technique to monitor the kinetics of different photo induced processes.^{118, 119} In this pump probe system the sample is first excited by the pump (t=0) and the excited state can be monitored by the probe at different time delay. To do so it is very essential to spatial overlap between pump and probe on the sample. The delay between pump and probe can be generated either by lengthening the optical path distance of the probe light or by shortening the pump path. The used pump probe

CHAPTER 2

set up has been figured out in figure 2.4. The kinetics of the different optical processes can be investigated by the probe pulse intensity before and after the pump excitation.

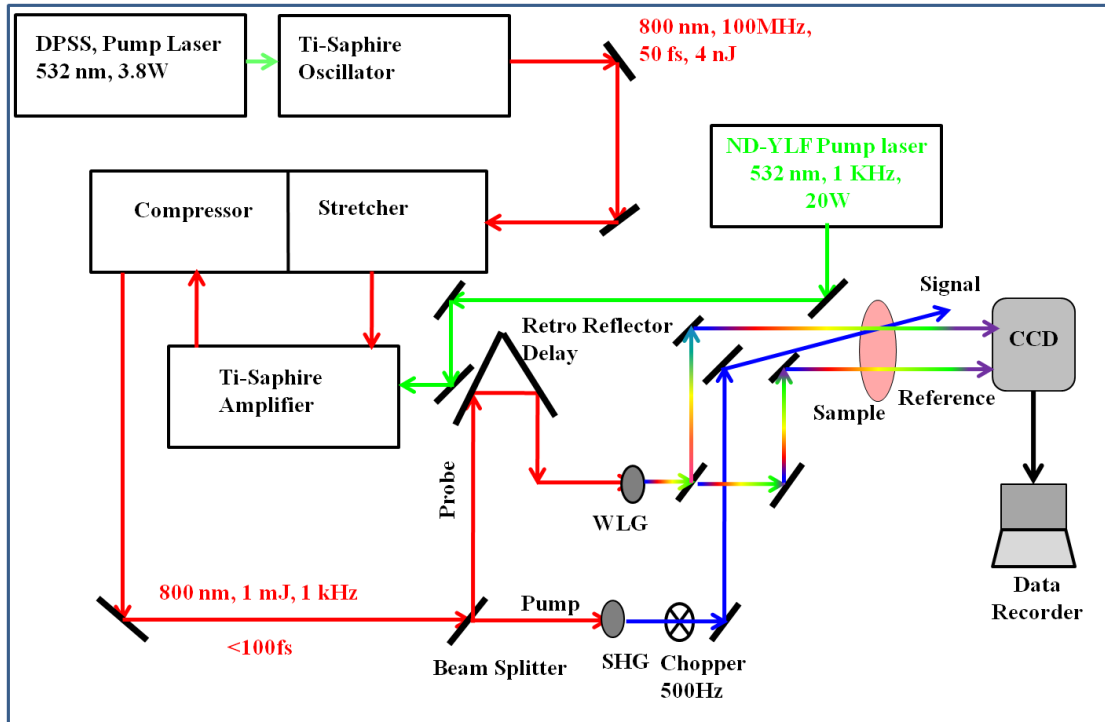


Figure 2.4. Block diagram of Pump-Probe Transient Absorption spectroscopy.

If the probe pulse intensity before ($t=0$) and after the pump excitation ($t=\Delta t$) are $I_{\lambda,0}$ and $I_{\lambda,\Delta t}$ respectively, then from the Beer-Lambert law:

$$I_{\lambda,\Delta t} = I_{\lambda,0} \times 10^{-N\Delta t l} \quad \dots\dots\dots 2.9$$

The absorbance (A) is defined as,

$$A(\Delta t) = \log(I_{\lambda,0}/I_{\lambda,\Delta t}) = N\Delta t l \dots\dots\dots 2.10$$

Assuming an exponentially decay of transient species

$$\ln A(\Delta t) = \ln O.D.(\Delta t) = \ln \varepsilon_{\lambda} N_{(0)} l - \frac{\Delta t}{\tau} \dots\dots\dots 2.11$$

Thus, the population dynamics at a specific wavelength (λ) can be probed by the change of optical density with respect to time delay (Δt).

In pump-probe transient absorption technique, the pump pulse excites the molecules to hot vibrational state after depleting the ground state. The probe wavelength which matches with the absorption spectra shows more transmission due to depletion of ground state ($I_{\lambda,0} > I_{\lambda,\Delta t}$). Hence it shows the negative absorption change and named as ground state bleach. The similar observation can also be possible when the probe wavelength matches with the luminescence and termed as stimulated luminescence. The excited state transition beyond excited state is named as excited state absorption (ESA). However the excited dynamics of any system can be analysed by the bleach recovery, ESA decay and stimulated emission decay at different probe wavelength.

b. Amplified Transient Absorption Spectrometer.

The amplified femtosecond transient absorption system is the combination of various subsequent steps, i.e ultra short pulse generation, pulse stretching, multipass amplification, pulse compressing and finally pump-probe generation.

i) Ti-sapphire Oscillator: Ultra-short Pulse Generation

In this present pump probe system, the 50 fs seed pulse is generated by the Ti-sapphire (TIS) oscillator.¹²⁰ In this oscillator, the diode pumped solid state (DPSS) laser with high power (~3.8W, 532 nm) focussed on the Ti-sapphire crystal which is placed in the focus of a spherical mirror. The broad luminescence band in 660-1050 nm region is emitted from Ti^{+3} ions in sapphire (Al_2O_3) matrix. The Ti-crystal is sustained in this high pump due to its high optical damage threshold (8-10 J/cm²) and high thermal conductivity (46 W/mK at 300 K). The operated cavity of this laser is in TEM₀₀ mode. The refractive index of Ti-sapphire crystal is non linear with lasing intensity, i.e.

$$n(\omega, I) = n_0(\omega) + n_2(\omega) I(t) \quad (2.12)$$

$$I(t) = \exp(-\Gamma t_2) \quad (2.13)$$

CHAPTER 2

Where, the $n_2(\omega)$ is the non linearity of the refractive index and it is positive for this cavity, i.e. In Gaussian distribution of TEM₀₀ mode intensity is higher in centre, resulting the higher refractive index at the central axis than the leading and trailing edge. The Ti-sapphire crystal itself converged the high power lasing in the gain medium, termed as “optical Kerr effect”. At high lasing power the additional focal length of kerr lens is placed after adjusting the sum of the focal length (f_1+f_2) of the cavity mirror. The kerr lens is responsible for the power dependent energy loss in the gain medium, by which the resonator of CW mode becomes unstable. The pulse can be generated by the slight disturbance of the cavity. This is termed as “Kerr lens mode (KLM)” locking because the mode lock is enforced by the self focussing of the kerr lens. Very short pulse (<10 fs) can be generated by this passive mode locking as the broad PL band ($\Delta t \sim \lambda^2/c\Delta\lambda$; where λ is peak wavelength) of Ti-sapphire crystal. The long PL life time ($\sim 3.2 \mu\text{s}$) of the Ti-sapphire crystal generates the 80-100 MHz pulse repetition rate (RR) in oscillator. The pulse repetition rate can be decided by the cavity length ($t=2L/c$, where L is the cavity length). The group velocity dispersion (GVD) of the fs pulse is raised when the pulse passes through the Ti-sapphire crystal in round trip of the cavity. The relative delay between the red and blue edge of the pulse is responsible for the GVD. The GVD can be compensated by using the prism compressor or chirped pulse mirror in the cavity resonator. The thickness of Ti-sapphire crystal and GVD are responsible for the pulse width of the laser. The “birefringent” properties of Ti:sapphire crystal is affected by the non linear kerr lens which change the polarisation and this is minimised by accurate alignment of the “Brewster’s angle surfaces”.

In the present thesis work the CDP (Russia) oscillator which generates 50 fs pulse width 500 mW power (4W DPSS pump power) and 88 MHz RR. The layout of this oscillator has been shown in figure 2.5. In this oscillator the two prisms with (high reflected) HR mirror

assembly is used for GVD minimisation. The 800 nm 50 fs pulse is selected by adjusting the location and slit width between the P2 and HR M5.

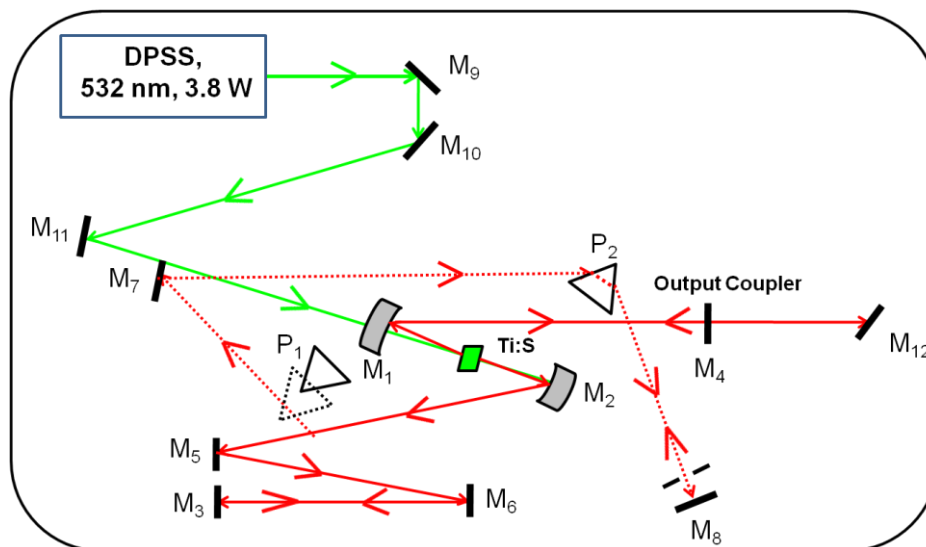


Figure 2.5. Schematic block diagram of Ti-Sapphire Oscillator.

The output power of this oscillator is not sufficient for pump probe experiment and can be used after amplification (>100 nJ) where the 50 fs pulse acts as seed pulse.

ii) Chirped Pulse Amplification of ultra short pulses

The power of the generated fs pulse from oscillator is too low for performing the experiment in the pump probe system, hence it is necessary to amplify the seed pulse several times.¹²¹ The energy (1 μ J) of the seed pulse is sufficiently high to optical damage of optics in amplification system. Therefore before amplification of the seed pulse, it is necessary to stretch the seed pulse. After the amplification (100 nJ/pulse energy) the pulse is regained at its own pulse width ~ 50 fs. The $> 10^5$ times amplification can be done in the chirped pulse amplification system by using low repetition rate (1 KHz) pump laser, such as Nd:YAG or Nd:YLF. The block diagram of the amplification process has been shown in figure 2.7.

iii) Pulse Stretcher

CHAPTER 2

The 10^4 times stretching of the seed pulse is necessary before amplification to keep away from the peak power damage ($<5 \text{ GW/cm}^2$) of the optics throughout the amplification

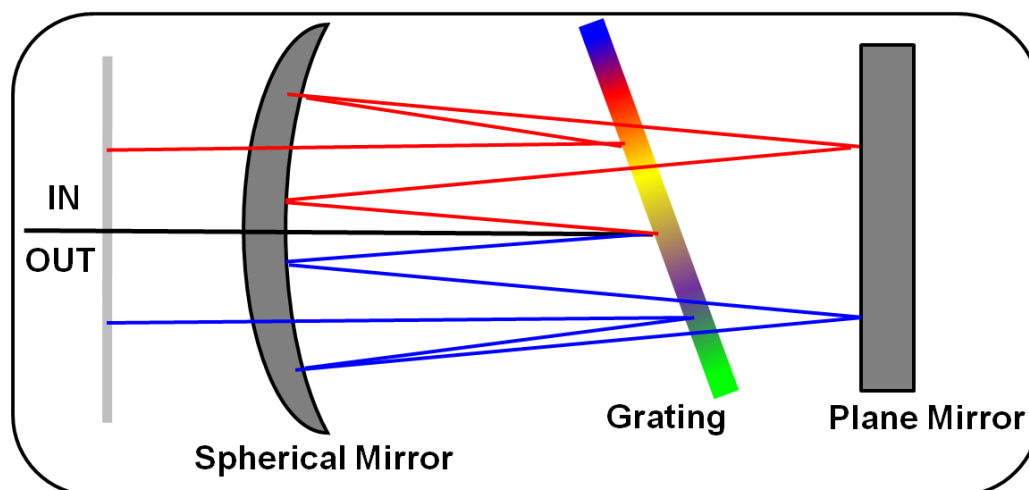


Figure 2.6. Optival layout of femtosecond pulse stretcher.

process. The stretching principle is figured out in figure 2.6. The pulse is stretched on the basis of wavelength dependent diffraction of the gratings. The FWHM of the 800 nm pulse is 40-50 nm, therefore the longer wavelength light diffracted more angle than the shorter wavelength. This makes path difference between red and blue light, which introduces the stretching of the pulse. All the wavelength components become in same direction after diffraction on the grating. The pulse width does not change after amplification and the GVD does not affect in the gain medium of the amplification like fs pulse. The stretcher lay out shows that it consists two curved mirror (one is concave and other one is convex) and a grating. The concave focal length is double than the convex mirror and these two mirrors are placed in such a way that they are separated by the focal length of concave mirror. This type of alignment of mirror and grating allows the stretched pulse to get back the reconstructed shape. The pulse is stretched up to 300 ps which has been feed for amplification.

iv) Femtosecond Confocal Multipass Amplification.

The stretched pulse is amplified after repetitive passes through Ti-sapphire crystal which acts as gain medium, is pumped by high power 5-25 W Nd:YAG or Nd:YLF laser.¹²²

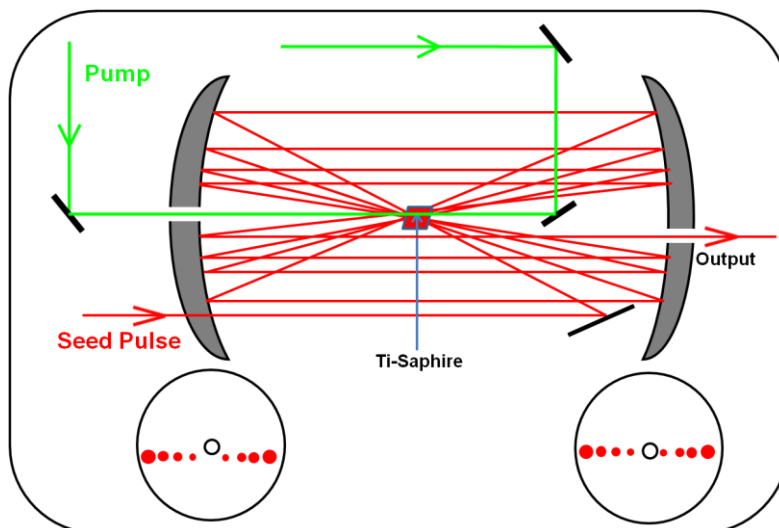


Figure 2.7. Schematic diagram of multipass amplification process in our used setup.

The seed pulse amplifies in each step of passing through gain medium with by depleting the inversion. Each round trip of seed pulse regenerates the gain by strong pump pulse through stimulated emission. After certain round trip the gain becomes saturated in the gain medium and extracted from cavity and feed for compression. The “confocal resonator” cavity is used for multipass amplification process. Before going to amplification, the seed pulse is passing through the pulse picker to select the pulse for amplification from a train of pulse. The pulse picker comprises the pockel cell and polariser. The horizontal polarised pulse falls by the pockel cell. The pulse exits from pockel cell when voltage is not applied. Here it acts as quarter wave plate. The pulse is allowed to enter for amplification. But when half voltage is applied across the pockel cell, the polarisation of the pulse is changed from horizontal to vertical and it is reflected by the polarizer adjacent to the Faraday isolator. The seed pulse is

trapped by the pockel cell during the amplification of the pulse which is in amplification medium. The pockel cell acts as pulse picker, where the other pulse is blocked during the amplification of the first pulse. Hence it is necessary to synchronize the applied voltage with seed pulse and pump pulse. Therefore the pulse repetition rate of the picked pulse has to be same as the pump pulse repetition rate. The confocal multipass amplification processes have been designed for amplification of the picked pulse by the pockel cell. The Ti-sapphire crystal is located at the focus of the two HR convex mirror, which have different focal length with central hole. The beam is passes through the Ti-sapphire crystal in multiple times and the number of passes depend on the alignment of the geometrical configuration of the mirror. Since the focal lengths of the two mirrors are different, the beam diameter is going to decrease with each pass and goes towards the centre of the mirror and is extracted. After passing through the crystal the energy of the pulse is increased gradually by the pumping of the high energy (5-15 W) Nd;YAG pump laser. The gain after amplification is in order of $\sim 10^5$.

In the present thesis work, the CDP (Russia) multipass amplification setup has been used for amplification, where the Nd;YLF pump laser with energy 5-15 W having 1 KHz pulse repetition rate has been used as pump source.

v) Pulse compressor:

After amplification the stretched amplified pulse is compressed to come back its previous pulse width. The pulse is compressed by using two grating configuration like stretching and shown in figure 2.8. Unlike stretching the afocal configuration between two parallel gratings are not configured in the compressor. The negative dispersion is occurred in compressor, i.e. the blue light travel more than the red amplified pulse through two parallel

grating configurations. It is necessary to compensate the various phases in compression distorted after the amplification. The spectral phase of stretcher (2nd order) can be compensated by the angle between two gratings. The distortion due to amplification (3rd order dispersion) can be recovered by the groove density, spatial separation of grating pair which are very difficult to adjust. To compress its initial pulse width (<50 fs), the groove density and the distance between two grating should be large. The pulse width of the exit pulse after compression is <100 fs with high energy >1mJ/pulse at 1 kHz repetition rate.

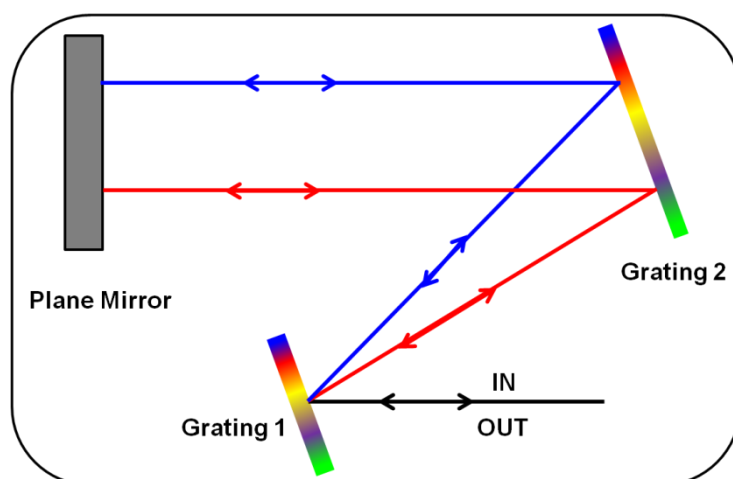


Figure 2.8. Schematic layout of two grating compressor.

vi) Second Harmonic Generation (SHG)

The doubling of 800 nm amplified pulse to 400 nm, which is adequate to excite various dye and material, can be occurred through non linear β -barium borate (BBO) crystal.^{123, 124} The BBO crystal has been chosen due to its very high damage threshold (5GWcm^{-2}) and suitable phase matching for 400 nm SHG. The second harmonic generation by this BBO crystal is possible when the non linear polarisation of the crystal is occurred by the pulse having high peak power. The induced dielectric polarization of a BBO crystal in presence of an electric field (E) of the pulse with high peak power is given by,

CHAPTER 2

$$P = E_0 (\chi^{(1)}E + \chi^{(2)}E^2 + \chi^{(3)}E^3 + \dots) \quad (2.14)$$

Where, $\chi(n)$ is the susceptibility of the nth order non-linearity. At high peak power the contribution of 2nd order susceptibility becomes significant. i.e.

$$P^{(2)} = E_0 \chi^{(2)} E^2 \quad (2.15)$$

$$P^{(2)} = 1/2 \chi^{(2)} E_0^2 (1 + \cos 2(\omega t - kr)) \quad (2.16)$$

Therefore the phase matching condition for second harmonic generation is $k(\omega) = k(2\omega)$ and second order non linearity emits the photons (2ω) with double energy than the initial photon. The birefringent BBO crystal satisfies the condition ($n_o(\omega) = n_e(2,\omega)$). In the present thesis, the 100 μ J 800 nm pulse is focussed on the 0.5 mm BBO crystal to generate 400 nm pulse with 10 μ J/pulse energy.

vii) White Light Generation (WLG).

To probe the transient species generated by the pump pulse, it is essential to generate white light as probe pulse. White Light is generated by the third order nonlinear light matter interaction, which governs by the 'self phase modulations (SPL)' phenomena.^{19, 122} The refractive index of the medium depends upon the intensity of the light. The intensity

distribution of a Gaussian pulse follow the eqn, $I = I_0 e^{(-\frac{t^2}{\tau^2})}$. 2.17

In our system, the white light is generated after focussing the 800 nm pulse with <100fs pulse width having 10 μ J energy on the 1.5 mm thick sapphire crystal. When the beam passes through the sapphire crystal the phase difference of the Gaussian shaped pulse is changed with refractive index of the crystal according to the eqn,

CHAPTER 2

$$\phi(\omega, t) = \frac{\omega\eta(\omega, t)}{c} L \quad 2.18$$

Hence the frequency is also changed with time dependent phase change according to the eqn

below,

$$\delta\omega = \frac{\partial\phi(t)}{\partial t} \quad 2.19$$

The gaussian shaped pulse changes the electric field of light photon due to frequency difference, which causes the frequency broadens and charging of the pulses. The frequencies are in same phase with well ordered due to third order nonlinearity.

vii) Pump-probe Transient Absorption Spectrometer:

The optical layout of the pump probe system has been shown in figure 2.9. The probe pulse after WLG is divided into two paths and both are passed through the sample. One probe beam is overlapped with the pump is referred as a signal and other one which is not overlapped with the pump referred as reference. The pump pulse passes through a polarizer with an angle 54.7° to minimise the anisotropy effect. A mechanical chopper with 500 Hz frequency is placed in pump path before the sample and it chopped the alternative pump

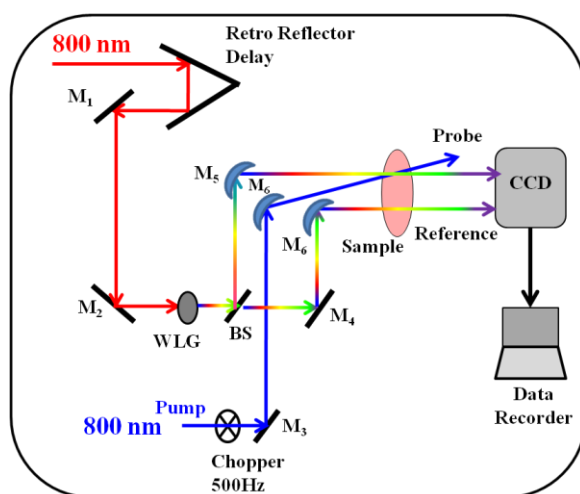


Figure 2.9. Optical layout of Excipro pump-probe setup.

pulse so that the ratio of transmitted intensities of consecutive probe pulses corresponds to the transient absorbance. The absorbance change can be calculated by the equation discussed earlier. In our thesis work we used the Excipro pump probe setup, where retroreflector for delay stage and CCD (charge coupled device) to detect the signal have been used. The excited state dynamics of the samples can be probed from 0.66 fs to 4 ns time delay using retroreflector after exciting the sample by the 400 nm pump. The instrument resolution of this pump-probe set up is measured by bleach signal of meso-tetrakis-(4-sulphanatophenyl) porphyrin dianion (TPPS) at 710 nm (λ_{pump} at 400 nm, aqueous solution at pH 1) and found to be ~100fs. The sample is taken in a 1 mm width rotating sample holder to minimise the photo bleaching caused by intense pump during the course of experiment. Finally the Lab-view programme is used to fitting and analysis of the experimental data. All the fitted parameters have 5-10% error.

2.8. Photovoltaic Measurement (IPCE and IV):

In this present thesis to measure the photovoltaic performance in terms of current density versus voltage curves (J-V curves), Peccell (model: PEC-L01) solar simulator with a 100 W/m² AM 1.0 G short-arc Xe lamp has been used. The intensity of illuminating source was calibrated using a standard Si-photodiode provided by Peccell, Keithley. To record the J-V characteristic of the QDSC 2400 source meter has been used. To measure the IPCE, Action Spectrum Measurement System (Peccell, model: PEC-S20) with a xenon lamp (150 W) as the light source and 400-800 nm measurement wavelength range has been appointed.

The solar cell efficiency (η) can be defined as the ratio of the electrical energy output to the incident energy from the sun. The efficiency term of the solar cell can be represented by the percentage of exposed solar energy converted into electrical energy. It can be

calculated by the ratio of power output (in watts) at its maximum power point (P_m) and the input power from sunlight (E , W/m²). i.e.

$$\eta = \frac{P_m}{EA_C} \quad (2.20)$$

Where, A_C represents the exposed area of the solar cell.

On the other hand, the efficiency of the solar cell can be defined in terms of fill factor (FF), open circuit voltage (V_{OC}) and short circuit current (I_{SC}). The FF defines the nonlinear electrical behaviour of the solar cell. The FF is the available power at the maximum power point (P_m) divided by the V_{OC} (when a cell is operated at open circuit, i.e. no current is in circuit) and I_{SC} (when a cell is in short circuit i.e. $V = 0$). The FF is shown by the equation below,

$$FF = \frac{P_m}{I_{SC}V_{OC}} \quad (2.21)$$

From Equation 2.20 and we can define the efficiency by eq below,

$$\eta = \frac{FF I_{SC}V_{OC}}{EA_C} \quad (2.22)$$

From experimental value, we can calculate the efficiency of the QDSC by using above equation.

2.9. Synthesis of Nanostructures and Solar Cell Fabrication:

a. Materials.

Cadmium oxide (CdO, 99.5%), zinc acetate ($ZnAc_2 \cdot 2H_2O$, 99.9%), selenium powder (Se, 99.99%), sulphur powder (S, 99.99%) and tellurium powder (Te, 99.99%), caesium carbonate, lead bromide ($PbBr_2$), gold chloride (98%, Aldrich), trisodium citrate,

dodecylamine (DDA, Aldrich), Sodium borohydride, Didodecylammonium bromide (DDAB, Aldrich), indium (III) acetate ($\text{In}(\text{OAc})_3$, 99.99%), silver nitrate (AgNO_3 , 99%), oleic acid (OA), Trioctylphosphine (TOP, 90%), Dodecanethiol (DDT, >98%), oylamine (OAm), technical grade oleic acid (90%), tri-octylphosphine (TOP, 90%), 1-octadecene (ODE) (90%), Cadmium nitrate tetrahydrate ($\text{Cd}(\text{NO}_3)_2 \cdot 4\text{H}_2\text{O}$), zinc nitrate hexahydrate ($\text{Zn}(\text{NO}_3)_2 \cdot 6\text{H}_2\text{O}$), copper sulphate, sodium sulfide (Na_2S), potassium hydroxide (KOH), potassium chloride (KCl), mercaptopropionic acid (MPA), sulphuric acid (H_2SO_4) were purchased from Aldrich and used without further purification. Coumarin C343, Coumarin D1421, bromopyrogallol red (Br-PGR) and 4',5'-dibromo fluorescein (DBF) dyes were purchased from Aldrich and were used without further purification. Analytical grade methanol and tertiary butanol solvents were used for precipitation.

b. Gold nanoparticles synthesis: Gold nanoparticle was synthesized after adopting modified Turkevich method^{125, 126}. In brief, 250 μM gold chloride and 250 μM trisodium citrate were dissolved in aqueous medium. Then this solution was stirred for 5 minutes for complete dissolution. 1.2 mL ice cooled sodium borohydride solution (0.01M) was added into the stirred solution. Then the resultant solution turns into light orange. At that time the reaction mixture was left for 30 minutes to complete the reaction. The colour of the solution changed from light orange to wine red, which attributed to the formation of gold nanoparticles. These nano particles were diluted for further experiments.

c. Synthesis of CdSe QDs. Oleic acid-capped CdSe QDs were synthesized in non-coordinating solvent octadecene (ODE) after following previously reported high-temperature reaction method.^{90, 127} Briefly, in the beginning cadmium oleate complex was formed by heating the mixture of 3.4 ml oleic acid (10.6 mmol), 0.51 g cadmium oxide (4.0 mmol) and

CHAPTER 2

11.6 ml octadecene in a three-neck round-bottom flask at 240 °C under Ar atmosphere until a clear solution was obtained. Once the solution becomes clear, the reaction temperature was increased up to 280 °C. To prepare the selenium precursor solution, 0.16 g selenium powder (2 mmol) was mixed with 1.1 ml TOP (2.5mmol) in 4.4 ml octadecene and sonicated for complete dissolution. After that the TOP Se solution was injected at a single shot through a syringe to the reaction mixture at 280°C. Rapid color change from yellow to orange to red was occurred in the first 10-20 s after injection. The reaction mixture was kept at 280 °C for different time to get desired size of CdSe. After getting the desired size CdSe (by measuring the Exciton position) the reaction was quickly quenched. The reaction mixture was left to cool. Finally the synthesized CdSe was precipitated by methanol in three times and then dissolved in chloroform for experimental purpose.

d. Synthesis of CdSe/CdS Quasi Type-II core-shell. The CdSe/CdS Quasi Type-II core-shell was synthesized after following the reported literature^{128, 129} with some modification. Synthesized 2 μmole CdSe QD solution was used as core to synthesize the CdSe/CdS core-shell. Cd-oleate and sulfur powder were used as cadmium and S precursor respectively to grow the CdS shell on CdSe core. Now, to prepare Cd-oleate, 0.62 mmol (0.084 g) of CdO and 1.75 ml OA (5.4 mmol) in 10 ml ODE were refluxed at 180°C into a three-neck flask in inert atmosphere. After cooling down to room temperature the Cd-oleate was added to degas CdSe core solution. The temperature of the mixture was kept at 120°C for 20 min. Then the mixture was heated to 200 °C and the 0.62 mmol S solution in 0.25 mL TOP and 10 mL ODE was added drop wise into the mixture. After complete addition of S the solution temperature was kept at 200 °C for 1 hr. Then it was cooled down to room temperature and resulting

CdSe@CdS core shell was purified by precipitation in methanol three times and later dissolved in toluene for further use.

The CdSe@CdS2ML, CdSe@CdS 4ML and CdSe@CdS 6ML core shell was synthesised in the same way by using required amount of Cd and S precursors. The rest of the procedure is same as CdSe@CdS core shell.

e. Synthesis of CsPbBr₃ QDs. The colloidal CPB QDs has been synthesised after following the method by Kovalenko and his co- worker.¹³⁰ To synthesise the CPB QDs, first we have made the Cs-oleate stock solution. In three neck RB flask, 1.25 mmol (~0.41 g) Cs₂CO₃ was taken along with 20 mL ODE and 4 mmol OA (~1 mL). To dry this precursor, it was heated at 130 °C for 1 hour then it was further heated to 150 °C for complete dissolution of the Cs₂CO₃. The resulting solution formed Cs-oleate and was used as Cs precursor. In another three neck RB flask 0.188 mmol PbBr₂ (~0.069 g) and 5 mL ODE were taken and heated to 120 °C in vacuum for one hour to complete dry. After complete dry, the mixture was heated to 180 °C and 0.4 mL Cs-oleate was injected at that temperature. Finally, the reaction was quenched in ice bath within one minute after injection of Cs precursor. The synthesised CPB was cleaned by precipitation in tertiary butanol and dissolved in toluene for further use.

f. Synthesis of AIS NCs in Different composition of Ag and In.

The AIS QDs have been synthesized by following the reported method in literature¹³¹. First sulphur stock solution was prepared after dissolving 0.3 mmol sulphur powder in 2 mL ODE. 0.1 mmol AgNO₃ and 0.1 mmol In(OAc)₃ were taken in 5 mL ODE in a three neck flask for the preparation AIS 3. After that 0.5 mL OAm and 2 mL DDT were added within the reaction mixture. The reaction mixture heated to 120° C in Ar atmosphere and keep it for 30 min to complete dissolution of the Ag and In precursor. At this temperature the S stock

CHAPTER 2

solution was injected and left the reaction mixture for 30 minutes to grow the NCs. Then the reaction mixture was allowed to cool in room temperature. The synthesized QDs were precipitated in methanol three times. Finally the NCs were dissolved in chloroform for characterisation and further use.

The AIS 1 and AIS 2 were synthesized after following the above method after keeping the Ag and In precursor ratio as 0.5:1 and 0.25:1.

g. Synthesis of CdSe{Au} Heterostructure: For synthesizing of Au-CdSe heterostructure freshly prepared CdSe QD was used. Growth of Au NP on CdSe QD surface was carried out after following the synthetic method reported earlier by Mokari et.al.¹³² with some modification. The gold precursor was prepared by the mixing of 15 mg AuCl₃ (0.05mmol), 50 mg DDAB (0.1 mmol) and 90 mg (0.46 mmol) DDA in 4 mL toluene. The color of the solution becomes dark orange to light yellow. Now 20 mg synthesized CdSe is dissolved in 4 mL toluene under Ar Atmosphere. The gold precursor was added dropwise to the CdSe solution for a time period of 4 minutes under Ar atmosphere at room temperature. Gradually the color of the solution becomes dark brown. The DDAB stabilize the QD and DDAB acts as surfactant of Au NP. Finally the nanohybrid materials were precipitated in methanol. Then the precipitated nanohybrid materials were dissolved in chloroform for characterization and further use.

h. Synthesis of CdSe@CdS{Au} Hetero-structures: To synthesise the CdSe@CdS{Au} Hetero-structures we have used the synthesized CdSe@CdS core shell. The CdSe@CdS core shell was used to synthesize the CdSe@CdS{Au} metal semiconductor nanohybrid materials. After following previously reported synthetic method by Mokari et.al.¹³³ Au NP was grown on the surface of CdSe@CdS core shell. 30 mg AuCl₃ (0.1mmol), 180 mg (0.92 mmol) DDA and 100 mg DDAB (0.2 mmol) were dissolved in Ar atmosphere in 8 mL toluene to prepare

the Au precursor for synthesizing the CdSe@CdS{Au}. The colour becomes light yellow from dark orange after complete dissolution of the Au precursor. 40 mg CdSe@CdS core shell was dissolved in 4 mL toluene in Ar atmosphere. Then Au precursor was added drop wise added to QDs solution at room temperature in Ar atmosphere. Then this solution was left for 30 minutes to complete the growth of Au NP on the surface of CdS shell. Finally the synthesized nano hybrid material was purified by precipitation in methanol three times and dispersed in toluene for further analysis.

i. Synthesis of Au@CdS Core Shell. The Au/CdS core shell was synthesised by following the Zhang's method after some modification.¹³⁴ All the methods was performed under inert Ar atmosphere and 6500 rpm centrifuge was used for precipitation. First Oleylamine capped Au NP was synthesised by following the method reported by Zamkov et. al.¹³⁵ 40 μ moles AuCl₃ was dissolved in 3 mL oleylamine by sonication. The colour becomes orange due to formation of Au-Oleylamine complex. Then the temperature of this complex was raised to 120° C and the colour is changed to pink. The reaction mixture was kept at this temperature for 30 minutes to complete growth of the gold NP. Then this solution was left for cooling and then precipitated with the ethanol and then centrifuge to collect the precipitate. Then it was dissolved in 5 ml toluene to synthesis of Au/Ag core shell.

The Au/Ag core shell was synthesised by following the method reported by Shore et. al. after some modification.¹³⁶ The Au NP solution was dissolved in 5 mL Oleylamine and heat to 120°C to evaporate the all toluene. By that time separately 11 mM AgNO₃ solution was prepared in nanopure water. After evaporation of all toluene the agNO₃ solution was added dropwise (0.1 mL per 5 minutes) to avoid the formation of Au/Ag alloy. The AgNO₃ was added to the action mixture on the basis of shell thickness. After addition of AgNO₃ the

temperature was decreased 10-15°C and again heated to 120°C. The shell thickness was monitored by the measurement of steady state optical absorption spectra. Then the solution was left to cool the Au/Ag core shell solution and precipitated by ethanol. The Au/Ag was collected by centrifugation. Finally it was dissolved in 4 mL toluene.

To convert Au/Ag core shell to Au/Ag₂S core shell, 7 mg S powder was dissolved in 2 mL oleylamine in inert atmosphere. 0.2 mL S solution was added in the Au/Ag core shell solution in room temperature with vigorous stirring. This solution was left for 10 minutes to complete formation of Au/Ag₂S from Au/Ag, and thickness of the shell was monitored by shifting of plasmonic band in steady state optical absorption. Then it was precipitated by ethanol and then dissolved in 5 mL toluene.

We synthesised the Au/CdS core shell from Au/Ag₂S core shell by cation exchange method. 50 mg Cd(NO₃)₂ and 100µL TBP were dissolved in 1 mL methanol by 15 minutes sonication. This solution was added to the Au/Ag core shell solution and the temperature was raised to 60°C. This reaction mixture was left for 1 hour to complete exchange of Ag by Cd. After cooling of this solution, precipitated by ethanol and collected by centrifugation. Finally it was dissolved in chloroform for characterisation and other experimental purpose.

2.10. Preparation of Solar Cell Assembly:

i) Phase transfer of QDs By MPA:

The OA capped CdSe and CdSe@CdS core shell in non aqueous medium transferred to aqueous medium by using MPA as phase transfer agent following the reported literature method.^{137, 138} The MPA solution was made in 3:1 methanol and water medium and maintaining the pH 12 by using 40% KOH. The QDs solution was made in minimum chloroform solution and MPA solution was added drop wise to this QDs solution. This

mixture was left for 15 mins in stirring condition to complete phase transfer. The transferred QDs was collected by precipitation in acetone. After centrifugation the precipitate was collected and dispersed in minimum amount of water.

ii) Preparation of TiO₂ Photoanodes:

The transparent layer of TiO₂ (dyesol, DSL 18NR-T, average particle size 20 nm) was made by doctor blade method on the cleaned FTO (F:SnO₂) coated glass plates . Then left these films open air for 2 hours to dry. The film was annealed at 450°C for 30 min followed by at 500°C for 15 min in a muffle furnace. On this transparent layer a scattering layer of TiO₂ (dysol,WER2-O, average particle size 150-200 nm) was put and sintered at 450°C for 30 min followed by heating at 500°C for 15 minutes. Two drops of MPA capped QDs solution in aqueous medium were drop casted on the TiO₂ film and left it for 2.5 hour in open air for dry. Then it was rinsed with double distilled water. A quasi shell of CdS shell was made on the QDs on the TiO₂ film by using SILAR techniques. Then a thin ZnS shell was deposited on the surface of CdS shell for passivation by using 0.1 M methanolic Zn(NO₃)₂. 6H₂O and 0.1 M methanol: water (1:1) solution of Na₂S for 1 min. At last the film was rinsed with water for clean and left it open air for dry.

iii) Counter Electrode:

Two aqueous baths namely 5 mM CuSO₄ with 5 mM H₂SO₄ and 5 mM CuSO₄ in 0.5 M H₃BO₃ were screened by cyclic voltammetry for the pulsed electrodeposition of copper on FTO electrodes.^{139, 140} FTO electrodes were annealed at 450 °C for 4 hours in inert atmosphere and were cleaned by acetone and water with ultrasonication before carrying out electrochemical studies. A pulsed potential deposition of copper was carried out using a solution of 5 mM CuSO₄ in 0.5 M H₃BO₃ with the deposit potential of -1.5 V (vs. SCE) for

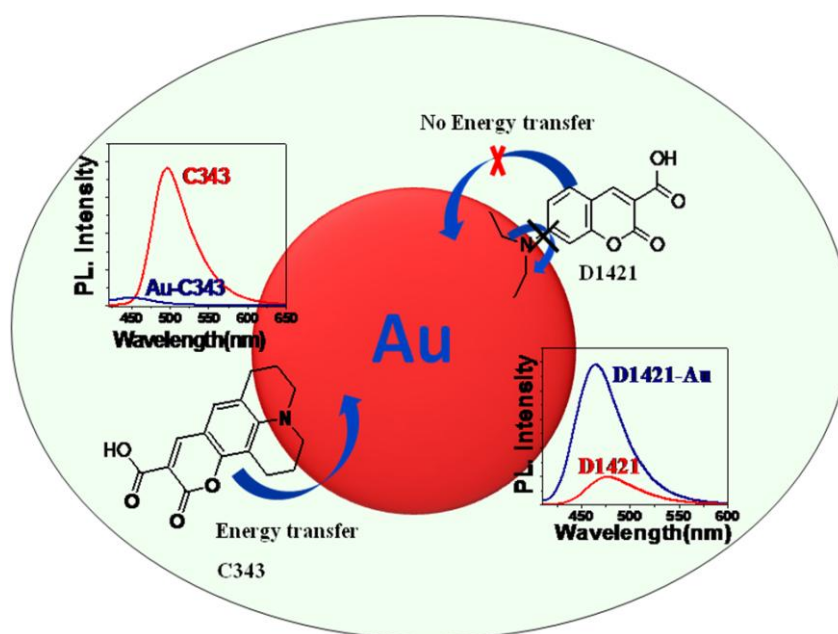
CHAPTER 2

0.2 s and holding potential of -0.1 V (vs. SCE) for 0.4 s for 5000 cycles. The cyclic voltammogram of FTO in sulfuric acid medium has shown a reversible behaviour with a reduction peak at -0.455 V and an oxidation peak at -0.376 V vs. SCE which correspond to deposition and oxidation of copper respectively. The corresponding peaks were seen at -0.284 V and 0.278 V in the boric acid medium. Here, there is no positive current in the entire region of reduction right upto 0 V, which would be beneficial in avoiding any oxidation of the copper on the surface in the pulsed deposition process. Also, a nucleation loop could be seen in the region of reduction in this medium. Thus, boric acid based deposition bath is found to be better suited for pulsed deposition of copper. The rise in negative current only with increased negative voltage in both media indicates the characteristics of over potential deposition.

CHAPTER 3

CHAPTER-3

PHOTOPHYSICAL BEHAVIOR OF TWO STRUCTURALLY SIMILAR COUMARIN DYES ON GOLD NANOPARTICLE SURFACE



J. Phys Chem C 119 (4), 2046-2052

CHAPTER 3

3.1. Introduction:

The interactions between molecular adsorbates and metal nanoparticles (NPs) have attracted tremendous attention due to their wide applications in optical material, biosensing, scanning probe microscopy etc¹⁴¹⁻¹⁴⁶ and plasmonic solar cell.^{147, 148} Coupling between molecular resonance and surface plasmon of metal NPs is an important parameter that is found to be strongly dependent on the spectral overlap between the molecular emission and absorption of the surface plasmon.¹⁴⁹⁻¹⁵² The fluorophore molecules optically interact with gold NPs due to their strong surface plasmon resonance. The cause of strong surface plasmon resonance is the collective oscillation of conduction band electron on metal NP surface.¹⁵³ To improve the efficiency of any device made out of these fluorophore-metal NP composite, it is important to know their interaction in both ground and excited states. It is reported in the literature that both enhancement and quenching of emission intensity of fluorophore strongly depend on size and shape of the quencher gold NPs, the orientation of fluorophore dipole moment, and overlap between emission spectrum of fluorophore and absorption spectrum of surface plasmon of gold NPs.¹⁵⁴⁻¹⁵⁶

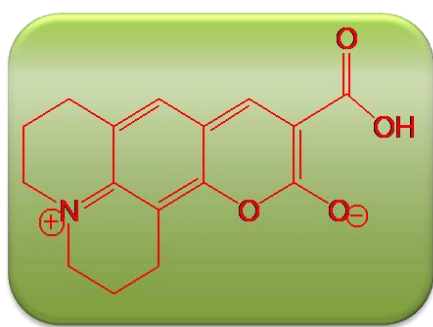
It is widely reported in the literature that in dye/Au NP composite systems emission quenching of fluorophores take place mainly due to Forster Resonance Energy Transfer (FRET)¹⁵⁷⁻¹⁶⁰ and nonradiative electron transfer from photoexcited dye molecules to Au NP.^{161, 162} In addition to that, recently Strouse and co-workers¹⁶³ have demonstrated surface energy transfer (SET) between Au NP and an emitting dipole (dye molecules). High molar extinction coefficient and broad bandwidth make Au NP a better fluorescence quencher. In FRET, energy goes from an excited dye molecule (donor) to metal NP (acceptor) surface through dipole–dipole interactions.^{164, 114} The energy transfer process strongly depends on the degree of overlap between absorption spectrum of quencher and emission spectrum of

CHAPTER 3

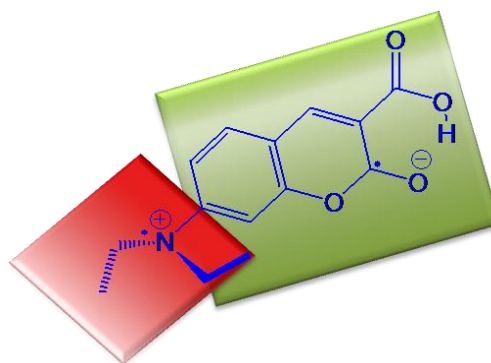
donor molecule. It has been observed that energy transfer efficiency changes with polarity, viscosity, and pH of the medium, which are responsible for the change in the excited state properties of the dye molecules.¹⁵⁹ However, there is no report in the literature on how molecular orientation in the excited state of dye molecules affects the energy transfer to the metal NP. Molecular structure and orientation of fluorophores on the NP surface are very important factors for both electron and energy transfer processes on semiconductor and metal NP surfaces. In our earlier investigation,¹⁶⁵⁻¹⁶⁸ we have demonstrated the effect of molecular structure of coumarin dyes on interfacial electron transfer reaction on both TiO₂ and ZrO₂ NPs. It has been observed that molecules which exist as twisted intramolecular charge transfer (TICT) state in the excited state in high polar solvent are better sensitizer for dye/TiO₂ composite materials.¹⁶⁵⁻¹⁶⁷ It has also been observed that TICT states facilitate interfacial charge separation and slow down back electron transfer reaction. Higher charge separation was observed due to different intramolecular charge delocalization in the excited state on the semiconductor NP surface, which completely depends on the molecular structure of the chromophore molecule. However, the effect of molecular structure and charge delocalization in the excited state of dye molecule on metal NP surface are never discussed in literature. Similarly effect of molecular structure on energy transfer from photoexcited dye molecule to metal NP is also not discussed in literature.

In the present chapter, to investigate the effect of molecular structure on energy transfer and charge delocalization of the photo excited dye molecules on Au NP surface C-343 and D-1421 are chosen. In C-343, the nitrogen atom lies in the ring and exists as intramolecular charge transfer (ICT) state; on the other hand, in D-1421, the nitrogen atom exists as a free rotating diethyl amino group that predominantly exists as a twisted intramolecular charge transfer (TICT) state in high polar solvents. Effect of molecular

structure on the interaction of molecular absorbance of dye molecules and plasmon band of Au NP has been discussed. Charge delocalization and excited state behaviour of both dye molecules on Au NP surface have been discussed. Finally, feasibility of energy transfer processes on molecular structure on NP surface has been demonstrated.



C343



D1421

3.2. Results and Discussion:

3.2.1. Solvatochromic Behaviour of C343 and D1421.

Before going to interaction of the structurally similar coumarin dyes with Au NP, we need to investigate the solvatochromic behaviour of these two dyes in different solvents. Figure 3.1 A (a, b) and (a', b') show the absorption and luminescence spectra of C343 in water and cyclohexane solvent medium, respectively. Similarly Figure 3.1 B (c) and (c') are the absorption and emission spectra of D1421 in water as solvent, while d and d' show the absorption and emission spectra of D1421 in cyclohexane. These figures attribute the Stoke's shift of C343 and D1421 in polar solvent is 80 nm and 75 nm respectively, whereas these Stoke's shift becomes shorter in non polar cyclohexane solvent and these values are 35 nm and 37 nm respectively. The change of stoke's shift with solvent polarity reveals that both dyes show different excited state in different solvent. The shorter stoke's shift in non polar solvent attributes that the both dyes show locally excited (LE) state in non polar solvent.

Stoke's shift of both the dyes in high polar solvent is higher compared to non-polar solvent. The larger Stokes shift of both the dyes in high polar solvent demonstrate that both dyes exist as charge transfer (CT) state in high polar solvent. The C343 shows the intra molecular charge transfer (ICT) state while the D1421 shows the ICT and TICT both but dominated by TICT due to free rotation of diethyl amino group.

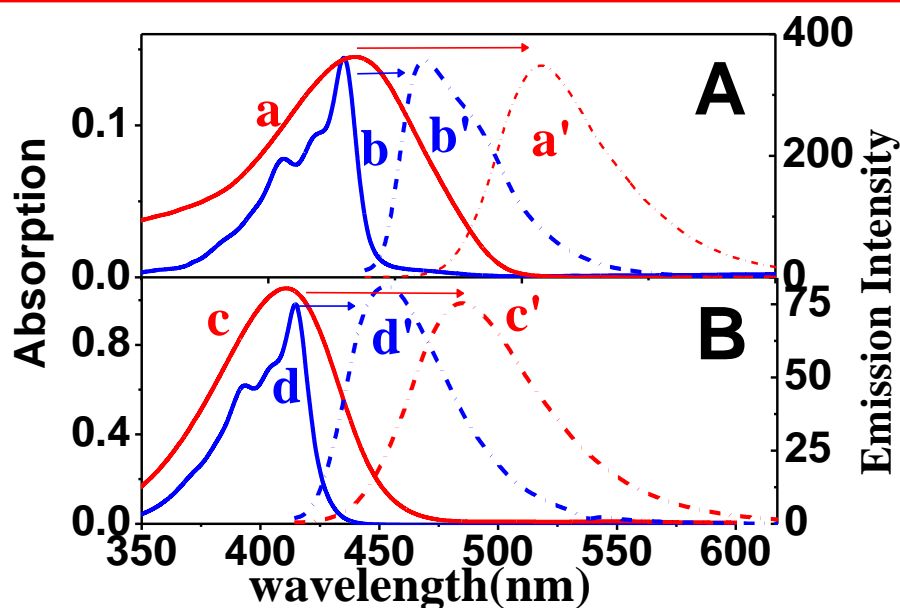


Figure 3.1: Panel-A: a and a' are the absorption and emission spectrum of C343 in water, b and b' are the absorption and emission spectrum of C343 in cyclohexane respectively. **Panel-B:** c and c' are the absorption and emission spectrum of D1421 in water, d and d' are the absorption and emission spectrum of D1421 cyclohexane respectively.

The solvatochromic behaviour can also be investigated by the luminescence life time of the C343 and D1421 in different solvent. Figure 3.2 (a) and (b) show the luminescence decay traces of C343 and D1421 in cyclohexane and the lifetimes are 3.2 ns and 2.9 ns, respectively. Therefore the luminescence life time of the LE state for both the dyes is almost same. But the luminescence lifetime of C343 and D1421 are different in aqueous medium.

Figure 3.2 (b) and (d) are the luminescence decay traces of the C343 and D1421 in water medium. The luminescence lifetime of C343 is 4.62 and interestingly this becomes extremely shorter 0.169 ns. The longer lifetime of the C343 is due to ICT state, whereas the shorter lifetime of D1421 represents the nonradiative recombination of TICT state.

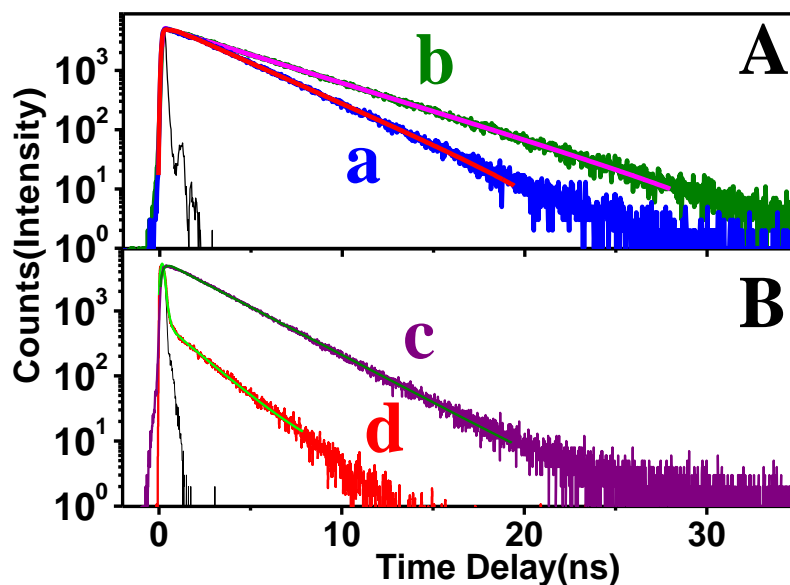


Figure 3.2: Panel-A: Time resolved emission decay traces of (a) C343 dye in water and (b) C343 dye in cyclohexane, probed at emission maxima after 406 nm excitation. **Panel-B:** Time resolved emission decay traces of (c) D1421 in cyclohexane and (d) D1421 in water probed at emission maxima after 406 nm excitation.

3.2.2. Characterisation of Au NP.

To characterize the Au NP, high resolution TEM measurement has been carried out. Figure 3.3 A shows the HR-TEM image of isolated well dispersed citrate capped Au NP. The average particle size of the Au NP is 7.3 ± 0.5 nm. The size distribution has been shown in inset of figure 3.3 A. Figure 3.3 B represents the extinction spectra of Au NP in water. The localized surface Plasmon band of Au NPs has been observed at 520 nm. Concentration of Au NP has been determined from extinction spectra and size of Au NP after following the

literature as reported by Haiss et al.¹⁶⁹

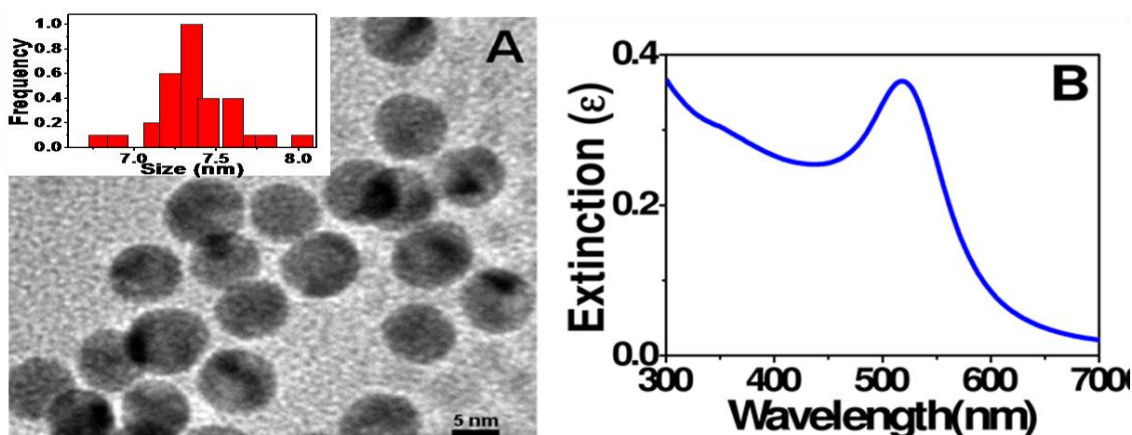


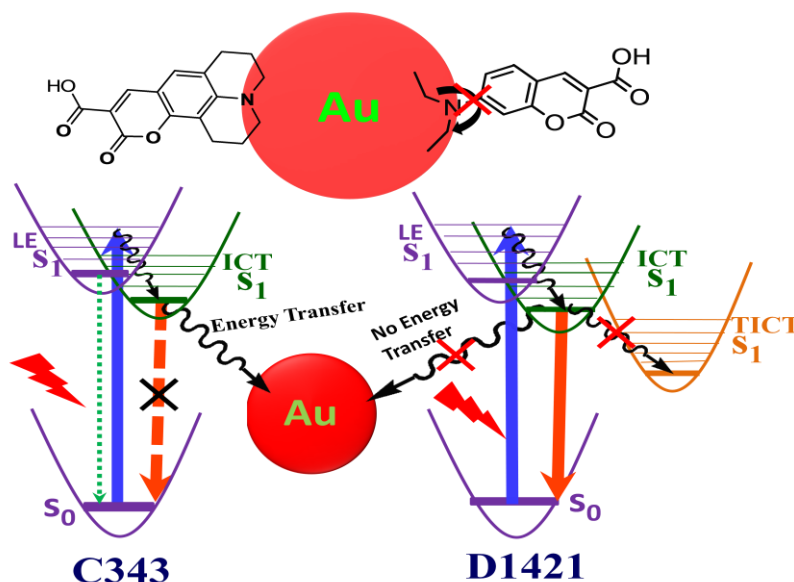
Figure 3.3 (A): High resolution TEM image of citrate stabilized Au NP. Inset: size distribution of citrate stabilized Au NP. **(B):** Extinction spectra of Au Nanoparticles in aqueous medium.

3.2.3. Interaction of C343 and D1421 with Au Nanoparticle.

a) Steady State Absorption Spectroscopy of C-343 and D-1421 on Au NP Surface:

Main aim of the investigation is to monitor the excited state photophysical behaviour of two structurally similar coumarin molecules (C343 and D1421) on the Au NP surface and also understand the effect of dye molecules on the Plasmon properties of Au NP. Before going to demonstrate the excited state behaviour, it is necessary to examine the ground state interaction between these two molecules and Au NP. However, it is important to know the surface properties of Au NP before carrying out ground state interaction studies. It has already been reported in the literature^{170, 171} that citrate-modified Au NP is negatively charged. So, the interaction between the coumarin dyes and Au NP will take place through an amino group instead of the negatively charged carboxylic moiety (Scheme 1). At This juncture it is very important to know the ionic charge of the coumarin dye molecules once they dissolved in water. pH of the of the aqueous solution of both C-343 and D-1421 were

Scheme 3.1: Schematic Diagram Showing Photoexcitation to LE States of Both C-343 and D-1421, Followed by De-Excitation to ICT States and Emission from Both LE and ICT States^a.



^aIn the case of C-343, energy transfer takes place from ICT states to Au NP, in addition to emission from the LE state (minor channel) due to restriction of charge delocalization. Population of TICT is completely blocked from ICT state in the case of D-1421 due to restriction of amino group rotation on the Au NP surface resulting drastic increments of ICT emission.

determined and found to be ~6. It is reported in the literature¹⁷² that pKa values of the coumarin dyes are ~4.6. It has also been reported that at acidic pH (pH < 4) C-343 exists as the neutral protonated form. However, above pH 5 and in basic solution it exists as the anionic form.¹⁷² As the pH of both coumarin dyes in water is ~6, both the coumarin dyes exist as anionic form. It has already been mentioned that the surface of the Au NP is negatively charged so both dye molecules will be attached with Au NP through an amino group.

In our earlier investigation^{165, 166} and earlier part of this chapter, we have reported the photophysical properties of both C-343 and D-1421. Figure 3.4 (a) shows the optical absorption spectra of citrate-stabilized Au NP, which has a plasmonic band at 520 nm. Figure 3.4 (b) shows an optical absorption spectrum of the C343 molecule in water, which has absorbance maxima at 435 nm. The composite mixture of C343/Au NP shows two absorption bands, one band at 448 nm and another broad red shifted band at 542 nm, as shown in Figure 3.4 (c). It is clearly seen that the optical absorption peak of C-343 on the Au NP surface

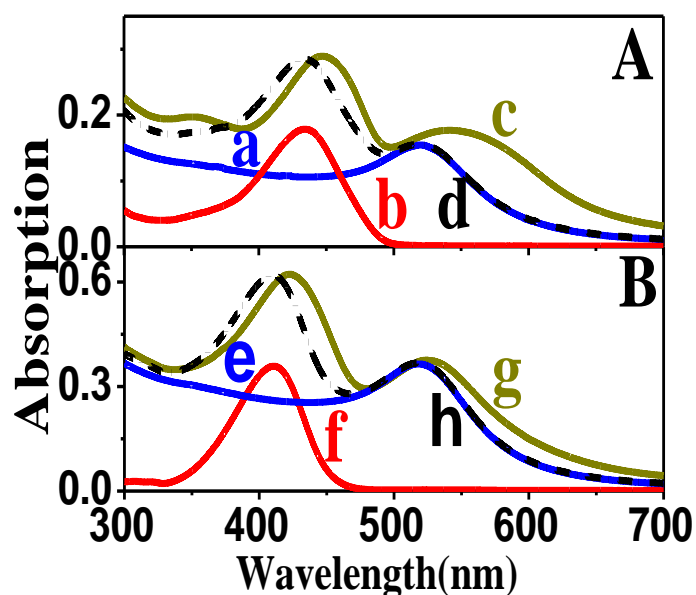


Figure 3.4: Panel-A: Steady state optical absorption spectra of (a) Au [40nM] (b) C343 [70 μ M] (c) C343 [70 μ M] and Au [40nM] in H₂O (d) addition of a and b. **Panel-B:** Steady state optical absorption spectra of (e) Au [100nM] (f) D1421 [100 μ M] (g) D1421 [100 μ M] and Au [100nm] in H₂O. (h) addition of e and f.

changes from 435 to 448 nm. On the other hand, the Plasmon band (peak) of Au NP changes from 520 to 544 nm and also become broad in the presence of C-343. Figure 3.4 B shows the optical absorption spectrum of D-1421 in the absence and in the presence of Au NP. Figure

3.4 f shows an optical absorption spectrum of the D-1421 molecule in water, which has absorption maxima at 411 nm. Figure 2g shows the optical absorption band of the D-1421/Au NP composite, which shows two absorption bands at 433 and 527 nm, respectively. It is interesting to see that the optical absorption band of D-1421 changes from 411 to 433 nm on the Au NP surface. Interestingly, the plasmon band of Au NP does not change much in the presence of D-1421, unlike in presence C-343. Wang and co-workers¹⁰¹⁷³ have reported plasmon band of Au nanorod becomes broad and red-shifted on adsorption of dye molecules due to their strong coupling with the surface plasmon of nanorod. Earlier Karam et al.¹⁷⁴ also have reported the change of extinction spectra of Au nanorod after adsorbing the organic fluorophore due to molecular and plasmonic resonance coupling. It is also reported in literature that the coupling strength is found to be strongly dependent on the spectral overlap between the molecular emission and absorption of the surface plasmon.¹⁵⁰⁻¹⁵² In the present investigation it is clearly seen that in both the dye/Au NP systems optical absorption band of the coumarin dyes are red shifted on the Au NP surface. However, it is seen that the spectral overlap between the plasmon band of Au NP and emission band of C-343 is better as compared to that of D-1421.

b) Steady State Emission Spectroscopy of C-343 and D-1421 on Au NP Surface:

To monitor the effect of molecular structure on molecular and plasmonic resonances in Au NP/dye interaction emission spectroscopy has been carried out for both C-343 and D-1421 in the presence of Au NP. Figure 3.5 shows the emission spectra of both C-343 in the absence and in the presence of Au NP of different concentrations. C-343 shows emission maxima at 495 nm in aqueous solution. However, it has been observed that emission intensity gradually decreases on addition of Au NP. It is clearly seen that the emission intensity of C-

343 at 495 nm is completely quenched in the presence of 5.5 nM Au-NP (Figure 3.5 e). The emission quenching of C-343 in the presence of Au NP can be attributed to energy transfer

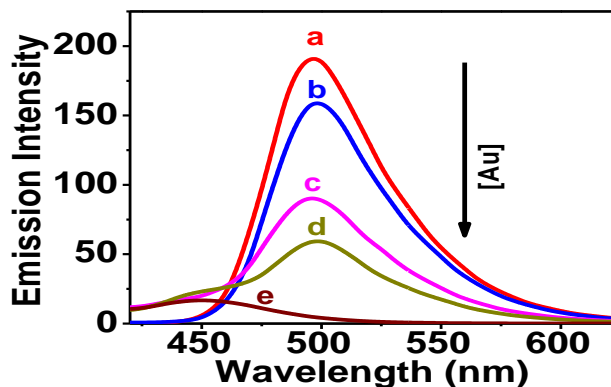


Figure 3.5: Steady state emission spectra of C-343 at different concentration (a) 0.0 nM (b) 10 nM (c) 20 nM (d) 30 nM (e) 40 nM of Au nanoparticles in water. [C-343] = 70 μ M.

from photo excited C-343 to Au NP. Energy transfer in Au-NP/C-343 system is a viable process as emission band of C-343 overlaps with the plasmon band of Au NP. It is interesting to see that, in the presence of 5.5 nM Au NP, the emission intensity at 495 nm is completely quenched; however, a low intensity emission band is appeared at 448 nm. Now it is very important to know thatn the nature of the emission band of C-343 at 448 nm on Au NP surface. Earlier of this chapter ,we have shown that C-343 has an emission band at 446 nm in cyclohexane, which is attributed to the locally excited state (LE).^{165, 166} The shape of the emission band of C343 on 5.5 nM Au NP surface matches quite well with emission band of C343 in cyclohexane, which arises due to the LE state emission. Thus, the emission band at 448 nm can be attributed to emission due to the LE state of C-343 on the Au NP surface. To confirm that the emission is not from Au NP, we have carried out emission spectroscopic studies of pure Au NP. No emission was observed from photoexcited Au NP. Earlier, Mattoussi and co-workers¹⁷⁵ have reported emission from Au nanoclusters appears to be at

~750 nm. In the present investigation, Au NP has a plasmon band at 520 nm, so the emission band at 448 nm can never be attributed to emission due to Au NP. The detailed explanation regarding the appearance of the LE state on the Au NP surface has been precisely described in the subsequent section.

Emission spectroscopy of D-1421 has also been carried out in the presence of different concentration of Au NP. Figure 3.6 (a) shows the emission spectrum of D-1421 in an aqueous solution, which has emission maxima at 475 nm. Interestingly, unlike the C-343/Au NP system, the emission intensity of D-1421 gradually increases with increasing Au NP concentration. Emission maximum of D-1421 also moves in the blue region of the spectrum with increasing Au NP concentration (Figure 3.6). Emission maxima of D-1421 also changes from 475 to 464 nm on Au NP surface at 12.5 nM Au NP concentration (Figure 3.6 e). In C343/Au NP system emission quenching was observed and attributed to energy transfer from photo excited C-343 to Au NP. As the molecular structure of D-1421 is very similar to C-343, so the energy transfer from the photoexcited state of D-1421 to Au NP is also expected. However, the emission intensity of D-1421 increases with Au NP concentration, suggesting no energy transfer process is active in D-1421/Au NP system. As the emission band of D 1421 does not overlap with the plasmon band of Au NP, it is expected that no energy transfer can take place in the D-1421/Au NP system. Earlier, Anger et al.¹⁷⁶ and Ming et al.¹⁷⁷ have reported that the enhancement of emission of fluorophore can take place in the presence of metal NP due to local electric field enhancement. The local field enhancement takes place when the surface plasmon band of metal nano particles lies in between the absorption band and emission band of the fluorophore. However, in D-1421/Au NP system emission band of D-1421 exists in the blue region as compared to Au NP Plasmon

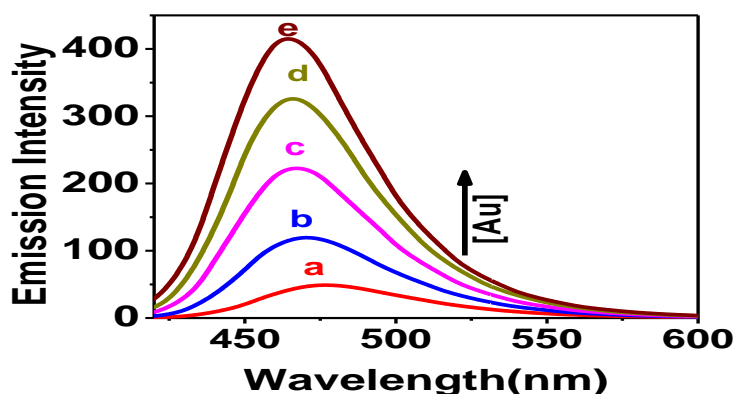


Figure 3.6: Steady state emission spectra of D1421 at different concentration (a) 0.0 nM (b) 40 nM (c) 60 nM (d) 80 nM (e) 100 nM of Au nanoparticles in water. [D-1421] = 100 μ M.

band. Ming et al.¹⁷⁷ reported that maximum local field enhancement occurred when the excitation wavelength is in the centre of surface plasmon band. If the excitation wavelength is in the red or blue region of the plasmon band then the local field enhancement decreases drastically. In the D-1421/Au NP system samples were excited at 400 nm so emission enhancement cannot be attributed to optical enhancement. However, it is important to know the reason behind the enhancement of emission intensity of D-1421 on Au NP surface. To understand the reason for formation of LE state for C-343 and increment of emission intensity of D-1421 on Au NP surface time-resolved emission studies have been carried out in both the systems and are described in the next section.

c) Time-Resolved Emission Spectroscopy of C-343 and D-1421 on Au NP Surface:

To reconfirm the above mentioned behaviour of both C-343 and D-1421 on the Au NP surface, time-resolved emission measurements have been carried out after exciting the samples at 406 nm. Figure 3.7 shows emission decay traces of C-343 in the absence and in the presence of Au NP of different concentrations at 500 nm in water. Figure 3.7a depicts the emission decay kinetics of C-343 in water which can be fitted single exponentially with time

constants of 4.63 ns. Interestingly in the presence of Au NP the emission kinetics decay faster and can be fitted bi-exponentially (Figure 3.7, Table 3.1). At 5.5 nM Au NP concentration, the emission kinetics of C-343 at 500 nm (Figure 3.7d) can be fitted bi-exponentially with time constants $\tau_1 = 0.68$ ns (6.5%) and $\tau_2 = 1.18$ ns (93.5%), with an average lifetime of 1.14 ns (Table 3.1). The decrement of emission lifetime on Au NP surface can be attributed to

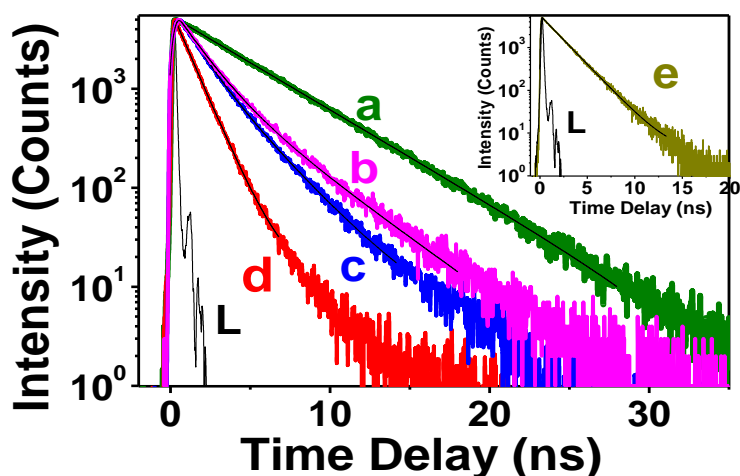


Figure 3.7: Time resolved emission decay traces of C-343 on Au NP surface at 500 nm at different concentration (a) 0.0 nM (b) 10 nM (c) 20 nM (d) 40 nM of Au nanoparticles in water. **Inset:** Emission of C-343 on 100 nM Au NP surface at 448 nm. Excitation wavelength was kept at 406 nm. **L** stands for Lamp profile of 406 nm laser excitation source.

energy transfer from photo excited C-343 to Au NP as we have mentioned earlier in steady state emission quenching studies. In steady state emission studies, we have observed C-343 shows weak intensity emission band peaking at 448 nm on Au NP at 5.5 nM concentration, which we have attributed to the LE state of C-343. The emission decay trace of C-343 at 448 nm on Au NP at 5.5 nM concentration (Figure 3.7e) can be fitted bi-exponentially with time constants $\tau_1 = 1.15$ ns (77%) and $\tau_2 = 2.56$ ns (23%), with an average lifetime of 1.74 ns. The longer component 2.56 ns can be attributed to the contribution from LE state of C-343. It has

CHAPTER 3

been observed that there is no overlap between LE state of C-343 and Plasmon band of Au NP. As a result no energy transfer can take place from LE state of C-343 to Au NP surface. Interestingly average emission lifetime of C-343 at 448 nm on Au NP at 5.5 nM concentration (1.74 ns) is much higher as compared to that at 500 nm (1.14 ns). This observation suggests that emission at 448 nm of C-343 on the Au NP surface can be attributed to the LE state.

Time-resolved emission studies have also been carried out for D-1421 in the absence and in the presence of different concentrations of Au NP in water and shown in Figure 3.8. It is very interesting to see that emission decay trace of D1421 in water (Figure 3.8a, Table 3.1) can be fitted bi-exponentially with time constants $\tau_1 < 0.1$ ns (95.6%) and $\tau_2 = 3.38$ ns (4.4%),

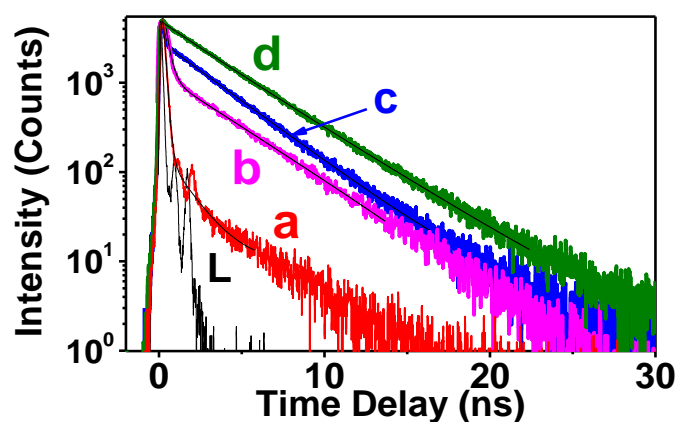


Figure 3.8: Time resolved emission decay traces of D-1421 on Au NP surface at 475 nm at different concentration (a) 0.0 nM (b) 20 nM (c) 60 nM (d) 100 nM of Au nanoparticles in water. Excitation wavelength was kept at 406 nm.

with an average lifetime of 0.17 ns. Major emission intensity (~96%) of D-1421 decays in water with pulse-width limited time constant (<0.1 ns). Earlier Rettig et al.¹⁷⁸ reported that the photo excited DMABEE (dimethyl amino benzoic acid ethyl ester) molecule exists as the

TICT state, and it decays non-exponentially with a very short lifetime in high polar solvents. They have suggested that, on photo excitation, such molecules are initially populated to LE or ICT state followed by very fast relaxation to the TICT state nonradiatively. The transition from LE/ICT state to TICT has been attributed to barrierless.¹⁷⁸ In our earlier

TABLE 3.1: Emission life times of C-343 and D-1421 in absence and in presence of Au NP of different concentrations after exciting the samples at 406 nm.

[Au NP] _{C343}	Emission life time of C343 at 500 nm	[Au NP] _{D1421}	Emission life time of D-1421 at 475 nm
0 nM	$\tau_1 = 4.63$ ns	0 nM	$\tau_1 = 0.02$ ns (96%), $\tau_2 = 3.38$ ns (4%) ($\tau_{av} = 0.17$ ns)
10 nM	$\tau_1 = 1.56$ ns (75%), $\tau_2 = 3.76$ ns (25%) ($\tau_{av} = 2.12$ ns)	20 nM	$\tau_1 = 0.19$ ns (89%), $\tau_2 = 3.16$ ns (11%) ($\tau_{av} = 0.42$ ns)
20 nM	$\tau_1 = 1.30$ ns (62%), $\tau_2 = 2.68$ ns (38%) ($\tau_{av} = 1.82$ ns)	60 nM	$\tau_1 = 0.14$ ns (64%), $\tau_2 = 3.4$ ns (36%) ($\tau_{av} = 1.3$ ns)
40 nM	$\tau_1 = 0.68$ ns (6.5%), $\tau_2 = 1.18$ ns (93.5%) ($\tau_{av} = 1.14$ ns)	100 nM	$\tau_1 = 3.52$ ns

investigations^{165, 166} we have already demonstrated that, in polar solvents, the D1421 molecule exists predominantly as the TICT state. In polar solvents on excitation of the D-1421 molecule goes to the LE or ICT state and then very quickly relaxes to the TICT state through nonradiative way. The transition from the LE/ICT state to TICT has been attributed to barrierless; as a result, we can observe the pulse width limited decay component (<0.1 ns). The longer component (3.38 ns) can be attributed to the lifetime of ICT state in water. However, interestingly, on the Au NP surface with increasing NP concentration, contribution of fast component decreases and contribution of long component increases (Figure 3.8, Table 3.1). It has also been observed that the emission quantum yield of D-1421 also increases with

Au NP concentration. In 100 nM Au NP concentration, emission decay trace (Figure 3.8 d) can be fitted single exponentially with a time constant of 3.52 ns. Therefore, at 12.5 nM Au NP concentration, the emission decay trace can be attributed to decay trace due to ICT emission. This observation clearly indicates that, on the Au NP surface, relaxation from ICT states to TICT is completely blocked.

d) Restriction of Molecular Rotation and Charge Distribution in the Excited States of Coumarin Dyes on Au NP Surface.

Main aim of the present investigation is to see the effect of molecular structure on the excited state dynamics and energy transfer processes on Au NP surface. Two structurally similar coumarin dyes, C-343 and D-1421, were chosen for that purpose. Steady state absorption studies suggest that the effect of molecular adsorption of C-343 on plasmon absorption of Au NP is more as compared to that of D-1421. In the presence of C-343, the plasmon absorption band of Au NP becomes broad and red-shifted (Figure 3.4), suggesting better interaction between C-343 and Au NP in the ground state. Steady state and time-resolved emission studies suggest that energy transfer takes place from photo excited C-343 to Au NP. This energy transfer process can be attributed to nonradiative energy transfer (NRET), where photo excited C-343 acts as energy donor and Au NP as energy acceptor. Nonradiative energy transfer (NRET) efficiency (η) and rate k_{ET} can be calculated by using the following equations:⁴⁸

$$\eta = 1 - \tau_{DA} / \tau_D \quad (1)$$

$$k_{ET} = 1 / \tau_{DA} - 1 / \tau_D \quad (2)$$

CHAPTER 3

“ η ” and “ k_{ET} ” define the energy transfer efficiency and rate of energy transfer, respectively. τ_D and τ_{DA} represent the corresponding decay time of the donor molecule (C-343) in the absence and in the presence of acceptor (Au NP; Figure 3.7, Table 3.1). In C-343/Au NP pair, energy transfer efficiency has been calculated to be 75% and energy transfer rate to be $6.5 \times 10^8 \text{ s}^{-1}$. The most interesting part of this observation is that, at 40 nM Au NP concentration, emission intensity of the ICT state of C-343 is completely quenched; however, a new band appears at 448 nm, which has been attributed to the LE state of C-343. We have mentioned that the emission lifetime of C-343 at 448 nm is $\sim 1.74 \text{ ns}$. This interesting behaviour of C-343 can be explained as follows. In aqueous solution, C-343 exists as the ICT state, where charge delocalization takes place between the coumarin moiety and an amino group. However, on Au NP surface majority of excited states exist as ICT states which go for energy transfer to Au NP (Scheme 3.1). In addition to that, on the Au NP surface, due to interference of charge delocalization, the excited state of C-343 also exists as LE state. Due to poor overlap between LE emission and Au NP plasmon band, no energy transfer can take place from LE state of C-343 to Au NP. To the best of our knowledge, this is the first example of restriction of charge delocalization of photo excited dye molecules on the Au NP surface. Now, let us discuss the excited state behaviour of D-1421 on the Au NP surface. From steady state and time-resolved emission studies it is confirmed that there is no energy transfer from photo excited D-1421 to Au NP. However, interestingly, the emission intensity increases drastically on the Au NP surface. We have already discussed earlier and in our earlier investigation^{165, 166} that photoexcited D-1421 predominantly exists both as ICT state and non emitting TICT state. Conversion of TICT state from ICT state takes place due to the rotation of a diethyl amino group in the photo excited state of D-1421. However, the emission

band appears at 475 nm can be attributed purely to the ICT state. Now, on the Au NP surface molecular rotation of the diethyl amino group of D-1421 is completely restricted, and consequently, relaxation from ICT state to TICT is completely blocked (Scheme 3.1). As a result, we can see the drastic increment of emission due to ICT emission of D-1421 on Au NP surface. In our earlier investigations,^{165, 166} we have demonstrated the effect of molecular structure on interfacial electron transfer dynamics for both C-343 and D-1421. We have shown clearly that the TICT state facilitates higher charge separation and slower back electron transfer in dye/TiO₂ composite materials. We would like to mention that both of the dyes coupled with TiO₂ nanoparticles through a carboxylic moiety result in the amino group of the coumarin dyes being free (not coupled with TiO₂ NP). So the excited state D-1421 can demonstrate its TICT behaviour on the TiO₂ NP surface. However, in the present investigation, both the dye molecules are coupled with Au NP through an amino group. As a result, the excited state of D-1421 cannot demonstrate TICT behaviour on the Au NP surface.

3.3. Conclusions:

Excited state dynamics and energy transfer behaviour of two structurally similar coumarin dye molecules (C-343 and D-1421) have been investigated on the Au NP surface by using steady state and time-resolved emission spectroscopy. Steady state absorption studies indicate that the C-343/Au NP system has higher coupling strength between the molecular and the plasmonic resonances due to higher spectral overlap as compared to the D-1421/Au NP system. In nonpolar solvent both the molecules exist in the LE state, while in polar solvent, C343 exists in the ICT state and D1421 exists both in ICT and TICT states. ICT emission of C-343 was found to be quenched drastically due to energy transfer from photoexcited C-343 to Au NP. In addition to that, the excited state of C-343 also exists as the

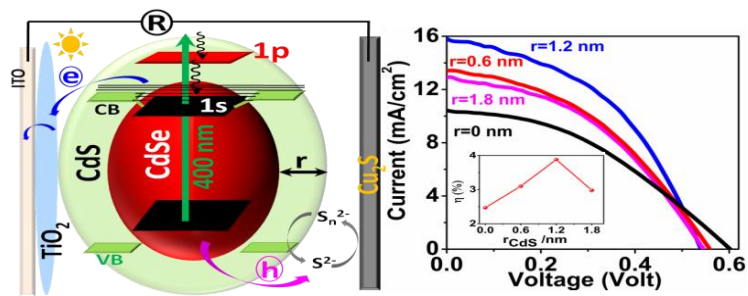
CHAPTER 3

LE state on the Au NP surface due to restriction of intramolecular charge delocalization of C-343. No energy transfer could take place from photoexcited D-1421 to Au NP due to poor overlap between D-1421 emission band and Au NP plasmon absorption band. Interestingly, emission intensity of ICT state of D-1421 drastically increases on Au NP surface due to restriction of amino group rotation on NP surface. Our observation on restriction of charge delocalization of photo excited dye molecules on NP surface opens up new phenomenon in dye-metal NP interaction. Still, further investigations in this field are necessary for in-depth understanding of the phenomenon.

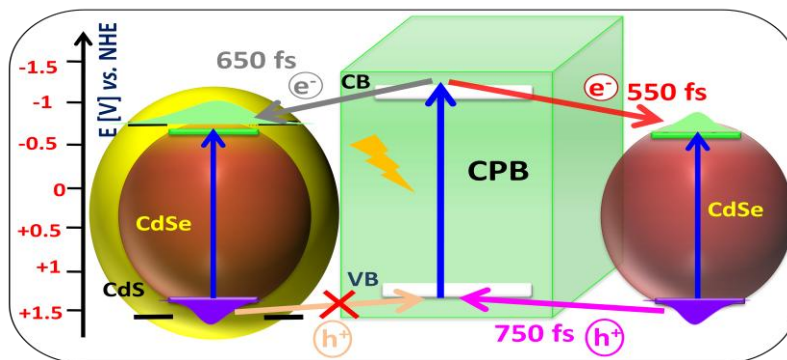
CHAPTER 4

CHAPTER-4

CHARGE (HOLE AND ELECTRON) CARRIER DYNAMICS OF SEMICONDUCTOR NANOCRYTALS AND ITS SOLAR CELL APPLICATION



Communicated...



Communicated.....

CHAPTER 4

4.1 Introduction.

Research on semiconductor quantum dot materials found a huge surge in last decade due to their sensational opto-electronic properties like size and composition dependent optical tuneability, large extinction coefficient, long excited state lifetime, slow carrier cooling, ability to generate multiple excitons, large intrinsic dipole moment and high stability.^{106, 108, 109, 179-182} Due to the above excellent properties QD materials in particular, such as II–VI^{105, 183, 184} and IV– VI¹⁸⁵⁻¹⁸⁷ semiconductor materials are widely used as light harvesters in quantum dot solar cells (QDSC) for their high absorption cross section in the visible to near IR region. In addition to that many narrow band gap ternary and quaternary semiconductor materials like CuInS_2 ,¹⁸⁸ CuInSe_2 ,^{35, 189} and ZnAgInSe_3 ¹⁹⁰ have been extensively used as sensitizer in the low-cost third generation solar cell. Furthermore, utilizing the concept of band gap engineering a series of core-shell hetero-structures, such as ZnTe/CdSe ,¹³⁸ CdS/CdSe ,¹⁹¹ CdTe/CdS ,¹⁰⁷ etc have been used as photo sensitizer. The $\text{CdSe}_x\text{Te}_{1-x}$,¹⁴⁰ $\text{PbS}_x\text{Se}_{1-x}$,¹⁹² and $\text{CdS}_x\text{Se}_{1-x}$ ¹³⁹ alloy QDs deposited photo anode are used as development of higher efficient QDSC. In spite of continuous efforts in last couple of years till date photo-conversion efficiency (PCE) of quantum dot solar cell (QDSC) is over shadowed by relatively moderate performance with a reported value of $\sim 12\%$ ¹⁹³ which is still lower as compared to both dye-sensitized solar cell (DSSC) and organic inorganic perovskite solar cell.^{194, 195}

The efficiency of the QDSC device depends on many factors, such as dissociation of exciton by injecting of electron to the metal oxide, back electron recombination between CB of TiO_2 and hole in QDS and regeneration of the redox couple.^{103, 137, 196} In addition to that other major cause of low efficiency of QDSC is charge carrier trapping in the surface states

of the QDs and in the interface of QDs and metal oxide surface due to low quality loading of the QDs.^{107, 191} To overcome the above shortfalls researchers are involved in modifying the photo-anode while depositing the QDs on the electrodes.¹⁹⁷ To cover the maximum area of QDs with transporter, the QDs are loaded on the different morphologies of wide band gap metal oxide.^{198, 199} To enhance the PCE of the QDSC the QDs are often passivated by wider band gap semiconductor to reduce the defect state.¹³⁸ The trap state at the interface of TiO₂ and QDs are extensively eliminated by post deposition of ZnS as passivating layer on the photoanode.²⁰⁰ This passivated layer (ZnS) developed a potential energy barrier to prevent the back electron transfer from metal oxide and slows down the carrier recombination.^{137, 201-203} In addition to that these passivating layers also prevent the cell from corrosion and provide the longer life time of the cell. We have already mentioned that through band-gap engineering efficiency can be increased significantly by changing the band alignment of QDs through type II core shell arrangement. Type II arrangement core shell semiconductor forms a long lived charge separated state after photo excitation, where the electrons and holes are localised in shell and core respectively, where photo excited electron can easily be transferred to the metal oxide.^{50, 204} At the same time shell in QDs also can play barrier for charge recombination.^{205, 206} Bisquert and co-workers have reported the PCE efficiency ~7.17% by type II ZnTe/CdSe core-shell which absorbs in NIR region of the solar spectrum.¹³⁸ In addition to type II band alignment there is another kind of hetero-structure reported in the literature, i.e. quasi type II where the electrons are delocalised in the conduction band of both core and shell and holes are localized in the shell. Due to the quasi type II structure electron and holes are de-coupled leading to higher electron cooling time and slower charge recombination which is desired for the design of higher efficient solar cell.^{51, 52, 139, 207} Changing the thickness of the shell QD often change the type II structure to quasi type II

CHAPTER 4

structure and vice versa. Lian and co-workers.⁵² demonstrated thickness dependent photo-reduction quantum efficiency of quasi-type II core/shell quantum dots. However in literature no report is available where thickness dependent PCE of quasi type II core-shell is demonstrated and directly correlated with electron cooling, e-h recombination and back electron transfer (BET) dynamics as monitored through ultrafast spectroscopy.

Although it has been realized that all-inorganic perovskites are much superior materials in terms of stability however power conversion efficiency of these provskites are way poorer as compared to organic-inorganic metal halide perovskite materials. Kulbak et al.²⁰⁸ reported ~6.6% solar efficiency inorganic-based cesium lead tri-halide perovskite material.⁴⁵ Recently Swarnkar et. al.²⁰⁹ reported power-conversion efficiency of maximum 10.77% for quantum dot-induced phase stabilization of α -CsPbI₃, which is the highest efficiency for all inorganic perovskite materials so far. It has been realised that to get higher photovoltaic performance the photo-generated hole has to be removed very fast before it corrodes the photo anode. It's always a challenging task to find suitable hole transporting materials to stop the carrier recombination. In addition to that another important factor for lower efficiency for the all inorganic perovskites are due to limited absorption of solar radiation (below 600 nm). Now to tackle the dual problem concept of co-sensitization can be incorporated where with the perovskite material another II-VI quantum dot material can be used. Due to suitable band energy level alignment better charge separation can take place through interfacial electron and hole transfer reaction. Synergistically both perovskite and II-VI QDs can behave as super sensitizer and absorbs more solar light as compared to individual material. Earlier we have demonstrated ultrafast charge transfer dynamics between CPB NCs and dibromo fluorescence (DBF) molecule where photo-excited hole from CPB was extracted by DBF and photo-excited DBF injects electron into the conduction band of CPB

CHAPTER 4

resulting grand charge separation.²¹⁰ Earlier we have also demonstrated ultrafast charge transfer dynamics of II-VI quantum dots after sensitisation with different molecular adsorbates.²¹¹⁻²¹³⁴⁸⁻⁵⁰ However, till date charge transfer dynamics between the perovskite NCs and II-VI QDs are never been discussed in literature.

Herein we are reporting the optimisation of PCE of quasi type II CdSe@CdS core-shell sensitized QDSC with changing the CdS shell thickness. To demonstrate the above phenomena CdSe QDs and CdSe@CdS core-shells with different shell (CdS) thickness have been synthesized following high temperature synthetic method and characterized by HR-TEM techniques and steady state optical absorption and luminescence spectroscopy. Solar cells have been fabricated after transferring the QDs to aqueous medium by using mercaptopropanoic acid as phase transfer reagent and deposited on the mesoporous TiO₂ film to make the photoanode of the QDSC. The Cu₂S deposited ITO film and polysulphide solution were used as photocathode and electrolyte, respectively. PCE of quasi type II CdSe@CdS core-shell with intermediate CdS shell (4 mono layer) found to give highest efficiency (3.88 %). Using Femtosecond transient absorption spectroscopy, we have monitored electron cooling, carrier trapping and carrier recombination dynamics of the QDs along with different core-shells on ITO film and after depositing on TiO₂ thin film. PCE of CdSe@CdS core-shell QDSC have directly correlated with ultrafast spectroscopic data and detailed mechanism has been discussed.

Additionally we are reporting the charge separation between photoexcited CsPbBr₃ (CPB) perovskite and CdSe QDs by ultrafast time resolved absorption and luminescence spectroscopy. The redox band alignment of CPB perovskite and CdSe QDs suggests that the electron transfer from CB of CPB to CB of CdSe QD and hole transfer from VB of CdSe QDs to VB of CPB NCs can concomitantly take place. Selective excitation through steady

state and time-resolved luminescence spectroscopic studies confirm the above processes. To determine the electron and hole transfer time in the above system, we have carried out femtosecond upconversion luminescence with femtosecond transient absorption studies and correlated the data. To reconfirm the above processes further we have carried out ultrafast spectroscopic studies between CPB NCs and CdSe@CdS core shell and results are discussed.

4.2. Results and Discussion.

4.2.1 Optimisation of Shell Thickness in Highest Efficiency CdSe@CdS Core Shell Quantum Dots Solar Cell

a. Characterisation of Materials.

The High resolution transmission electron microscopic (HRTEM) measurements and X-ray diffraction (XRD) have been carried out to analyse the crystal structure of the synthesised materials, have been shown in Figure 4.2.1. The 4.1 A (a), (b), (c) and (d) shows the HR-TEM image of CdSe, CdSe@CdS 2ML, CdSe@CdS 4ML and CdSe@CdS 6ML core shell NCs. The calculated average diameter of CdSe@CdS 2ML core shell is 3.45 nm (± 0.1 nm) (mono dispersed uniform size distribution). The thickness of two mono layer CdS is 0.6 nm. The Powder XRD patterns of the CdSe, CdSe/CdS 2ML, CdSe/CdS 4ML and CdSe/CdS 6ML have been shown in Figure 4.1 B (a), (b), (c) and (d) respectively. The peaks of CdSe for angle (111), (220) and (311) are 25.58° , 42.14° and 50.1° respectively. These angles are shifted towards longer angle with increasing the thickness of CdS shell, by which we can confirm the growth of CdS shell on CdSe core. To investigate the optical properties of CdSe@CdS core@shells, at first the steady state optical absorption (solid lines) and luminescence (dotted lines) measurements of these materials have been carried out as shown in figure 4.1(C). The 1st excitonic band due to the $1S_e-1S_{3/2}$ (1S bleach) transition is seen at

570 nm for CdSe which red shifts to 578 nm, 588 nm and 600 nm for CS 1, CS 2 and CS 3 respectively. In case of CdSe@CdS core shell, the band off set between valence band of

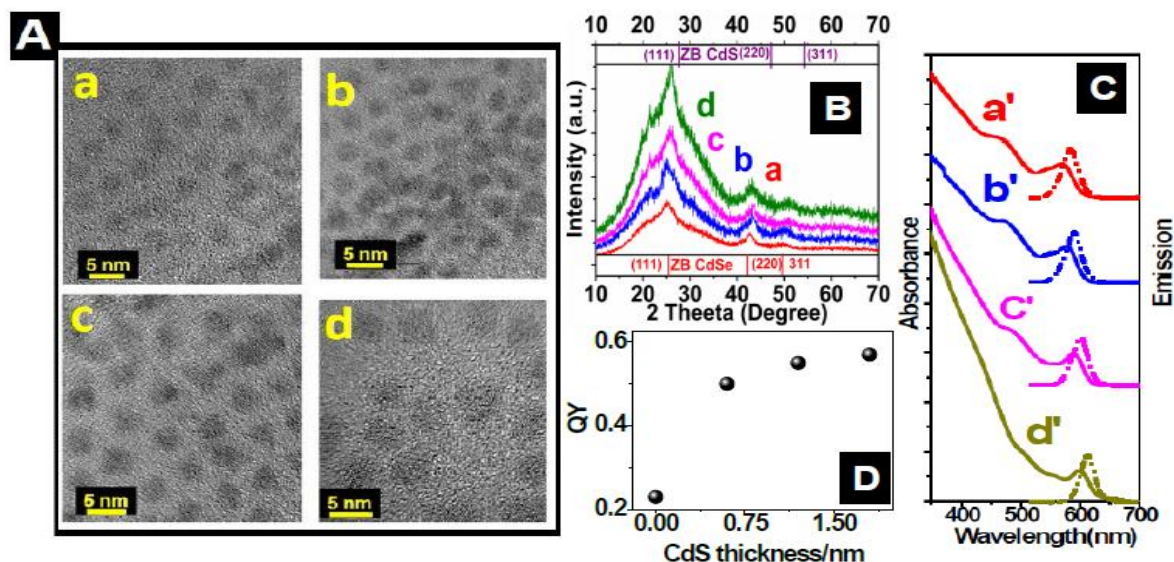


Figure 4.1: (A) HR-TEM images of CdSe (a), CdSe@CdS 2ML (b), CdSe@CdS 4ML (c) and CdSe@CdS 6ML (d). (B) Powder X-ray diffraction pattern of (a) CdSe QD, (b) CdS/CdSe 2ML, (c) CdS/CdSe 4ML and (d) CdS/CdSe 6ML core-shell respectively. (C) UV-Visible absorption and luminescence spectrum of CdSe (a'), CS 1 (b'), CS 2 (c') and CS 3 NCs (d'). (D) Graphical plots of Quantum Yields (QY) Vs CdS shell thickness.

CdSe and CdS is $\sim 0.2\text{eV}$ but the band offset for conduction band of CdSe and CdS is higher ($\sim 0.5\text{eV}$). Hence the photo excited electron does not localize in CB of CdSe, it delocalizes throughout the CB of CdSe and CdS. Therefore the binding energy of the charge carrier is decreased, results the red shift of the excitonic band. With increasing the thickness of the CdS shell the size of the overall QDs increases and the electron will be more delocalized throughout the CB of CdSe and CdS.^{51, 52} Therefore the more red shifting of exciton is observed when CdS shell is thicker. Three distinct bands are shown in the spectra for all the three different core@shell structure. The band at 530, 535, 545 and 560 nm are the

transition due to $2S(1Se-2S_{3/2})$ for CdSe, CS 1, CS 2 and CS 3 respectively. The absorption

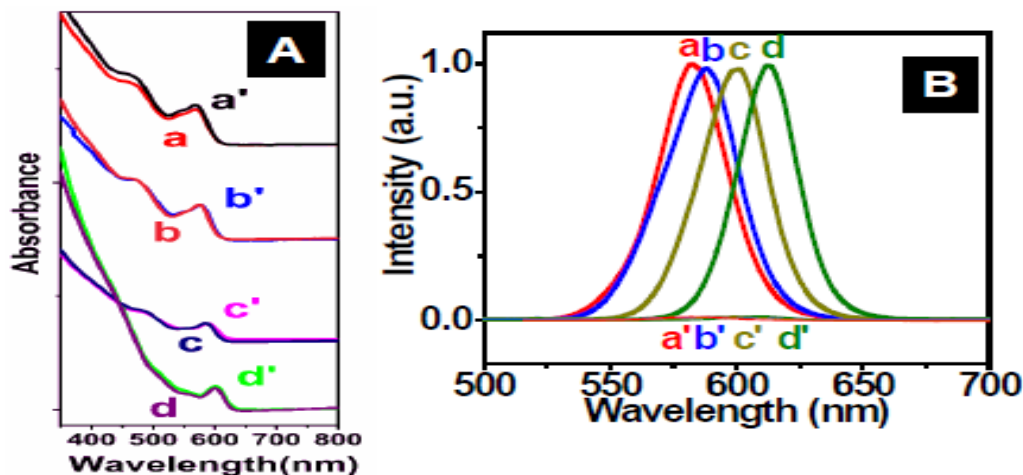


Figure 4.2. **A:** a, b, c, d and a', b', c', d' are the UV-Visible absorption spectra of CdSe, CS 1, CS 2 and CS 3 in Chloroform and Water respectively. **B:** a, b, c, d and a', b', c', d' are the UV-Visible luminescence spectra of CdSe, CS 1, CS 2 and CS 3 in Chloroform and Water respectively.

below 500 nm is gradually increases with CdS shell due to CdS shell absorption itself. From figure 4.1C, we have seen that the luminescence maxima red shifted with thickness of CdS shell. The calculated quantum yield (QY) of these CdSe, CS 1, CS 2 and CS 3 core@shells are 27%, 50%, 55% and 57% respectively as shown in figure 4.1D. Enhancement of the QY with thickness of CdS shell is due to elimination of the surface trap states. We have carried out the optical studies of all materials after phase transfer by MPA phase transfer catalyst into water, shown in Figure 4.2. There is no change of absorption spectra after phase transfer, which signifies that no change of confinement of exciton is occurred after phase transfer. The luminescence of the materials after phase transfer are quenched due to hole transfer, has been

shown in 4.2 B representing the change of surface passivation by the MPA.

b. IV and IPCE Measurement.

To optimise the shell thickness of CdS QDs to get higher efficient solar cell, we have measured the current density (mA/cm^2)-voltage (V) curves for MPA capped CdSe QDs, CS 1, CS 2 and CS 3 NCs loaded on mesoporous TiO_2 films upon illumination with 1 sun generated by PECCEL solar simulator. Cu_2S film on ITO plate has been deposited for counter electrode and discussed in chapter 2. Polysulphide was used as electrolyte in the photovoltaic performance measurements. Generally successive ion layer absorption and reaction (SILAR)²¹⁴⁻²¹⁶ and chemical bath deposition (CBD) techniques are used to deposit QDs directly on the metal oxide film.^{110, 217} In addition to that other techniques are like deposition of synthesised QDs on the metal oxide films through electrophoretic²¹⁸ and ligand exchange techniques.²¹⁹ Through direct growth techniques both size distribution and quantum confinement can not be controlled. Moreover a large number of defect states can be generated in direct growth techniques which can trap both the electrons and holes, as a result efficiency of the solar cell can be decreased drastically. However through post deposition techniques after synthesizing the QDs at high temperature both size distribution and quantum confinement can be controlled.^{138, 140, 220} Therefore we have deposited the QDs on the photoanode through post deposition technique. To stabilize the solar cell and enhance the efficiency we have deposited CdS quasi shell and ZnS passivation layer on top of CdSe QDs and core-shells.^{190 137} The larger band gap shell not only passivates the QDs and core shell also passivate the surface states of TiO_2 .

Figure 4.3 a, b, c and d show the current density (mA/Cm^2) Vs Voltage (J-V) curves of CdSe, CS 1, CS 2 and CS 3 NCs respectively. In Table 1 we have shown the measured

value of short circuit current density (J_{sc}), open circuit voltage (V_{oc}), fill factor (FF) and power conversion efficiency (η) for different systems. The overall efficiency for CdSe QDs,

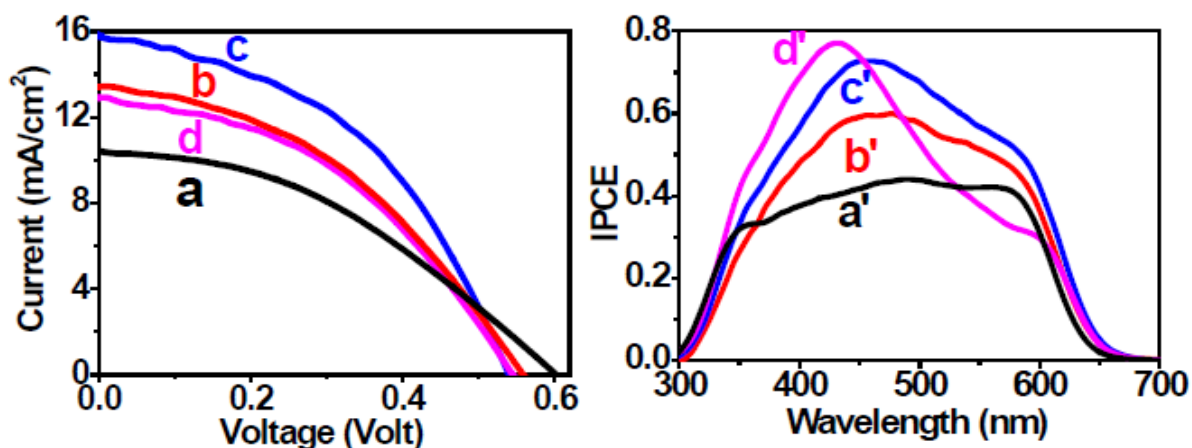


Figure 4.3. Left Panel. Current density (mA/Cm^2) Vs Voltage (Volts) plot of (a) CdSe, (b) CS 1 (c) CS 2 and (d) CS 3. **Right Panel:** Incident photon to current conversion efficiency Spectra of (a') CdSe, (b') CS 1 (c') CS 2 and (d') CS 3.

Table 4.1: The measured J_{sc} , V_{oc} , Fill factor and PCE of CdSe and all core shells.

QDs System	J_{sc} (mA/Cm^2)	V_{oc} (Volt)	Fill Factor (%)	PCE(%)
CdSe	10.67	0.59	39	2.47 (± 0.11)
CdSe@CdS2ML	13.76	0.55	41	3.1 (± 0.09)
CdSe@CdS4ML	16.2	0.54	44	3.88 (± 0.12)
CdSe@CdS6ML	13.32	0.54	42	2.98 (± 0.1)

CS 1, CS 2 and CS 3 NCs are found to be 2.47% (± 0.1), 2.98% (± 0.1), 3.88% (± 0.1) and 3.1% (± 0.1) respectively. Here in the J_{sc} (short circuit current) in CdSe QDs sensitized solar cell found to be $10.67 \text{ mA}/\text{Cm}^2$ which goes to a maximum value of $16.7 \text{ mA}/\text{Cm}^2$ for CS 2 (CdSe@CdS 4ML) and finally decreases to $13.32 \text{ mA}/\text{Cm}^2$ for CS 3 (CdSe@CdS 6ML).

Similarly overall power conversion efficiency for CdSe QDs increases from 2.47 % to 3.88% in CS 2 shell then decreases to 2.98 % for CS 3. Our investigation clearly suggests that there is ~57% increment in photo-conversion efficiency and ~56 % increment in current has been observed in CS 2 as compared to CdSe QDs.

Figure 4.3a', b', c' and d' show the incident photon to current conversion efficiency (IPCE) curve for CdSe QDs, CS 1, CS 2 and CS 3 NCs, respectively. It's interesting to see that the area under the curve of IPCE Vs wavelength found to increase from CdSe QDs to CS 2 and again decreases for CS 3 in range of 500 nm to 600 nm. However the area in the region 400-450 nm range gradually increases from CdSe to CS 3 due to contribution of CdS shell.

c. TA Measurement.

From I-V and IPCE measurements, we have observed a trend of efficiency change in the QDSC with CdS shell thickness, where the efficiency increases with shell thickness and beyond a certain thickness the efficiency again decreases. To understand the mechanism of change of PCE with shell thickness, we have carried out ultrafast transient absorption studies of CdSe QDs and core-shells before and after depositing the QDs on TiO₂ film and monitor both charge carrier cooling, charge transfer and recombination dynamics after exciting the samples at 400 nm and probing the transient in the visible region. Figure 4.4 (a), (b), (c) and (d) are the TA spectra of CdSe, CS1, CS2 and CS3 respectively at different time delay. Three negative absorption bands have been observed in the spectra of pure CdSe QDs which is in accordance to the steady state absorption spectrum. The negative absorption bands at 570, 540 and 478 nm in CdSe QDs spectra (Figure 4.4 a) can be attributed to the transient bleach due to the transitions of 1S (1Se-1S_{3/2}), 2S (1Se-2S_{3/2}), and 1P (1Pe-1P_{3/2}) respectively. It's interesting to see that the nature of the transient spectra of CdSe@CdS core-shells do not

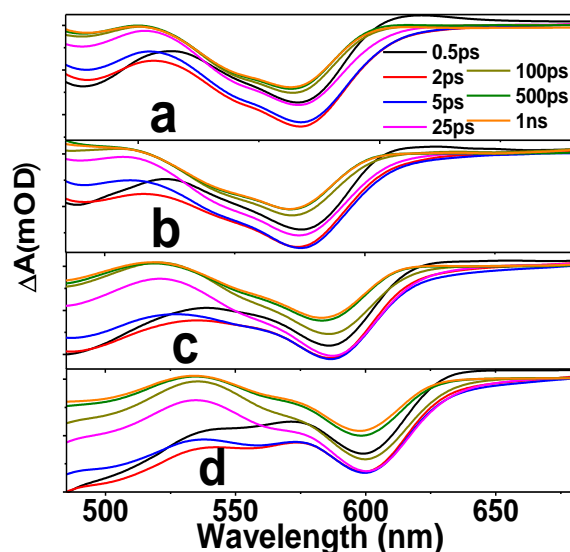


Figure 4.4. TA spectra of (a) CdSe, (b) CS 1, (c) CS 2 and (d) CS 3 core-shell NCs at different time delay. (All TA measurements have been carried out after 400 nm Laser excitation).

change much as compared to pure CdSe QDs after growing CdS shell on it. Only the transient bleach peaks shifted to the red region of the spectrum with increasing the thickness of CdS shell which actually matches well with optical absorption spectra (Figure 4.1B). No photo-induced absorption band was observed in the transient spectra of all the systems, suggesting very less defect states in the QDs or the core-shells. It's interesting to see that the bleach intensity in the blue region of the spectrum increases with increasing the shell thickness which can be attributed to absorption by thicker CdS shell in the core-shell.

To investigate the carrier dynamics of CdSe QDs and core shell materials we probed the kinetics at the excitonic wavelength. Figure 4.5a, b, c and d are the 1st excitonic bleach recovery kinetics of CdSe QDs at 572 nm, CS 1 at 580 nm, CS 2 at 588 nm and CS 3 at 600 nm respectively and the kinetic traces are fitted multi-exponentially as shown in Table 2. The

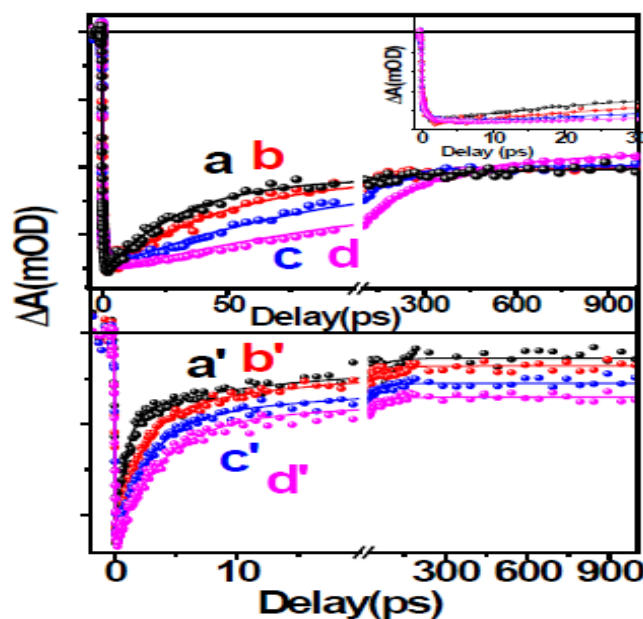


Figure 4.5: Upper Panel: Bleach recovery kinetics of (a) CdSe at 570 nm, (b) CS 1 at 578 nm (c) CS 2 at 588 nm and (d) CS 3 at 600 nm on ITO film. **Inset.** Early scale bleach kinetics of a, b, c and d. **Lower Panel:** Bleach recovery kinetics of (a') CdSe at 570 nm, (b') CS 1 at 578 nm (c') CS 2 at 588 nm and (d') CS 3 at 600 nm on TiO₂ film. (All TA measurements have been carried out after 400 nm Laser excitation)

bleach kinetics at 572 nm for CdSe QDs can be fitted with bi-exponential growth with time constants $\tau_1 = <100\text{fs}$ (75%) and $\tau_2 = 500\text{ fs}$ (25%). The 500 fs component can be due to electron cooling from higher excited state to band edge state.²²¹ On the other hand growth kinetics for CS1 can be fitted bi-exponentially with time constants $\tau_1 = <100\text{fs}$ (75%) and $\tau_2 = 1.5\text{ ps}$ (25%). Similarly with increasing CdS shell thickness in CS2 and CS3 growth kinetics of the excitonic bleach become slower with tri-exponential kinetics with longer components as shown in Table 4.2. It's interesting to see that with increasing shell thickness not only growth component changes from bi-exponential to tri-exponential but also the time-constants and contributions of the longer component increases. As CdSe@CdS form quasi-

type II core-shell structure where photo-excited electrons and holes are decoupled with the core-shell, as a result carrier cooling time increases with the formation of CdS shell. Interestingly we have observed that with increasing CdS shell thickness, the carrier cooling time increases as electrons and holes are more and more decoupled in higher thickness shell in core-shell like CS2 and CS3. It is exciting to see that the bleach recovery of CdSe after increasing the thickness of CdS shell. All of the excitonic bleach recovery is bi-exponential. From Table 4.2 we have seen that the faster component gradually increases from CdSe QD to CdSe@CdS 6ML, e.g. 30 ps (39%) for CdSe, 47 ps (-37%) for CdSe@CdS 2ML, 95 ps (-43%) for CdSe@CdS 4ML and 150 ps (-46%) for CdSe@CdS 6ML. The time constant gradually increases with CdS thickness, attributing the slow recombination due to electron hole decoupling in quasi type II core shell. In addition to decoupling of electrons and holes with the formation of core-shell, trap state in the surface of CdSe core QDs decreases, as a result trapping of charge carrier decreases which eventually increases the carrier cooling and recombination time. With the reduction of surface states life time of the charge carriers increases which in turn increases the PCE of the core-shell sensitized solar cell. Therefore ideally PCE of CS3 should be maximum, however efficiency measurements studies suggest that PCE of CS3 sensitized solar cell is 2.98% while it is 3.88% for CS2. This observation clearly suggests that only slow electron cooling and slower electron hole recombination in the CdSe@CdS core-shell QD necessarily will not give the highest efficiency in solar cell devices. It has been realized that in QD solar cell devices multiple processes are involved and to get maximum efficiency all the process has to be optimized. Next it is also important to investigate how efficiently the photo-excited QDs or core-shell QDs transfer its electron to the TiO₂ electrode. To understand the electron injection dynamic from the photo-excited

CHAPTER 4

QDs/core-shell to TiO₂ electrode bleach kinetics have been monitored at the excitonic wavelengths of different systems after depositing them on TiO₂

Table 4.2: The exponential fitted parameters at the first excitonic bleach kinetics of CdSe QD, CS1, CS2 and CS2 core shells in chloroform and on TiO₂ film after exciting at 400 nm.

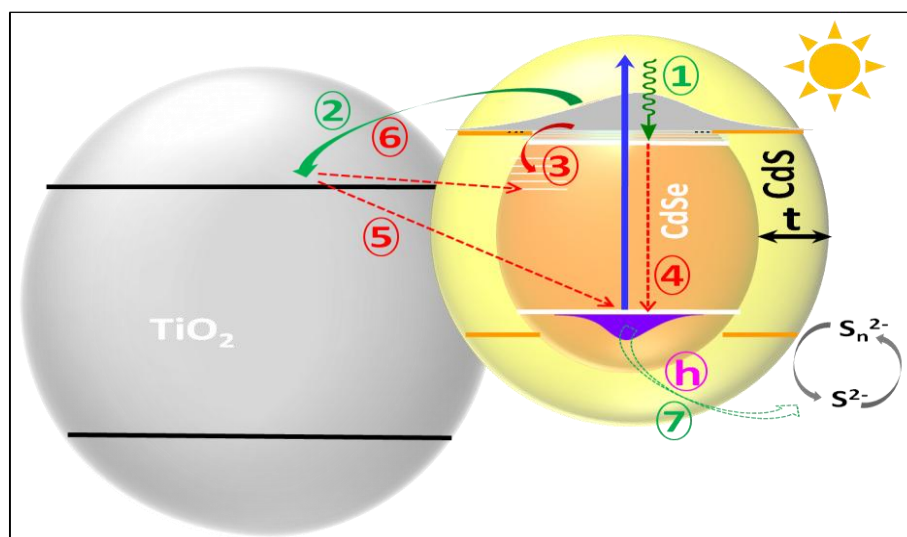
System @ λ nm	τ_{g1} (%)	τ_{g2} (%)	τ_{g3} (%)	τ_1 (%)	τ_2 (%)	τ_3 (%)
CdSe-570 nm	<100 fs (75%)	500 fs (25%)		30 ps (-39%)	>1 ns (-61%)	
CS 1-578 nm	<100 fs (75%)	500 fs (18%)	1ps (7%)	47 ps (-40%)	>1 ns (-60%)	
CS 2-588 nm	<100 fs (75%)	1ps (20%)	5ps (5%)	95 ps (-43%)	>1 ns (-57%)	
CS 3-600 nm	<100 fs (75%)	1ps (21%)	8 ps (4%)	150 ps (-45%)	>1 ns (-55%)	
CdSe/TiO₂-570nm	<100 fs (100%)			750 fs (-67%)	10 ps (-17%)	>1ns (-16%)
CS1/TiO₂-578 nm	<100 fs (100%)			1.75 ps (-69%)	10 ps (-12%)	>1ns (-18%)
CS 2/TiO₂-588 nm	<100 fs (100%)			2.5 ps (-65%)	15 ps (-10%)	>1ns (-25%)
CS 3/TiO₂-600 nm	<100 fs (100%)			3.5ps (-63%)	15ps (-7%)	>1ns (-30%)

film and shown in Figure 4.5B. Figure 4.5 a', b', c' and d' show the bleach recovery kinetics of CdSe QDs, CS 1, CS 2 and CS 3 after deposited the materials on TiO₂ film at their excitonic bleach wavelengths. It's interesting to see that bleach recovery kinetics look completely different on TiO₂ film and found to recover much faster with no bleach growth. The growth of the bleach kinetics in all the system found to pulse-width limited (< 100 fs) which clearly suggests that in all the above systems the photo-excited electrons are transferred to TiO₂ before cooling to the band edge. The bleach recovery kinetics can be fitted multi-exponentially and shown in Table 4.2. It's interesting to see that first components are 750 fs (-67%), 1.75 ps (-69%), 2.5 ps (-65%) and 3.5 ps (-63%) for CdSe/TiO₂, CS1/TiO₂, CS2/TiO₂ and CS3/TiO₂ systems, respectively (Table 4.2). However the longer components

are very similar only the contributions are different (Table 4.2). The faster bleach recovery component for all the systems are attributed to electron transfer from QDs/core-shell to TiO₂ film (Table 4.2) however the longer components are attributed to charge recombination between electron in TiO₂ and hole in the CdSe QDs/Core-shell. It is clearly seen that with increasing the shell thickness the electron transfer reaction from photo-excited QDs/core shell to TiO₂ film slows down due to presence of CdS shell which acts as a barrier. However more interesting part is that as we increase the thickness of CdS shell charge recombination (back electron transfer) reaction between electron in TiO₂ and hole in the CdSe core also slows down which again suggest slower charge recombination reaction takes place in CdSe@CdS/TiO₂ system with thicker CdS shell.

e. Discussions

The main aim of the present investigation is to optimize the PCE of CdSe@CdS core-shell QDSC with changing the shell thickness which can be directly correlated with ultrafast spectroscopic data to get an idea of different processes involved in working mechanism of QDSC. It has been observed that the overall efficiency of the CdSe@CdS core-shell QDSC increases with thickness of the CdS shell, and after certain thickness the efficiency again decreases (Table 4.1). This observation clearly suggests that CdS shell plays a vital role in PCE of QDSC. We have tried to correlate the change in efficiency of the QDSC with CdS shell by the help of TA spectroscopic data. The efficiency of the CdSe@CdS core shell sensitized solar cell depends on various processes as shown in Scheme 4.1. In this Scheme we have shown as many as seven processes (both constructive and destructive) which are responsible for efficiency of CdSe@CdS core-shell QDSC and each process is directly or indirectly controlled by the CdS shell. Process 1 is carrier (electron) cooling from upper excitonic states to the conduction band edge. In case of CdSe@CdS core shell it forms quasi



Scheme 4.1. Scheme representing multiple processes which take place in CdSe@CdS core-shell sensitized solar cell, Where 1-electron cooling, 2-electron transfer, 3-electron trapping, 4-exciton recombination, 5-Back electron transfer, 6-Carrier trapping, 7-hole neutralisation.

type II structure which retards the electron cooling as compared to bare CdSe QD. The carrier cooling time increases with increasing the thickness of CdS shell due to delocalisation of electron throughout the core and shell and is explained in TA studies. Therefore the carrier (electron) transfer time from above the band edge state of QD to TiO_2 for current generation increases with increasing the shell thickness. However after photo-excitation photo-excited electrons have to be transferred from core-shell to TiO_2 film which we have designated as Process 2. From Figure 4.5 and Table 4.2 we have observed that the electron transfer process from core-shell to TiO_2 film slows down with increasing thickness of CdS shell. Earlier Lian and co-workers⁵² have also demonstrated that the electron transfer is slowed down with increasing the shell thickness in CdSe@CdS core shell. They have observed that the CdS shell plays as a barrier by which electron transfer (charge separation) process is slowed down. As a result the efficiency should decrease with increasing the thickness of CdS shell. However in addition to charge separation (Process 2) process photo-excited electrons can get

CHAPTER 4

trapped in the trap sites of the QDs. The trapping process can be attributed as Process 3. However due to growth of CdS shell on CdSe core QDs trap states are passivated which is clear from our transient data that with increasing CdS shell thickness carrier trapping decreases. As a result with increasing the shell thickness PCE of a solar cell is expected to increase. The other important process prior to electron transfer, the photo-excited charge carriers (exciton) go for exciton recombination which has been attributed as Process 4. Exciton recombination can be determined from time-resolved absorption and emission studies. It has been observed that the exciton recombination slows down after growth of CdS shell and it becomes slower with increasing the thickness of CdS shell. Being a quasi-type II core-shell materials, photo-excited electrons are delocalised through the CB of both CdSe core and CdS shell in CdSe@CdS. Therefore the exciton recombination slows down after formation of CdS shell, as a result PCE can be enhanced with increasing the thickness of the shell. Another very important process is Process 5, which indicates the back electron transfer (BET) from TiO₂ to VB of CdSe QD after tunnelling through CdS shell. Herein the CdS shell prevents charge recombination by acting as a barrier. Therefore the BET reaction slows down with increasing CdS shell thickness, which in turn can increase the PCE of QDSC. In addition to that electron in CB of TiO₂ can be trapped by the surface states of CdSe core which can be designated as Process 6 and will be negligible in presence of CdS shell, as we have already mentioned that trap states of CdSe core drastically reduced in core-shell structure. Therefore the efficiency should be increased with CdS thickness. Finally one of the most important process is the hole neutralization reaction which we have designated as Process 7. Photo-excited hole located in the VB of CdSe core. In a working solar cell the hole has to be neutralized fast to achieve high efficiency, which means in CdSe@CdS core-shell it has to tunnel through the CdS shell. Therefore, with increasing shell thickness it is difficult

for the heavier hole to go for tunnelling.²⁰⁶ As a result efficiency of the solar cell can be decreased with increasing the shell thickness of CdSe@CdS core-shell. Now if we analyse all the seven processes, out of them processes 1, 3, 4, 5 and 6 play as constructive factors to achieve higher efficiency with increasing shell thickness. On the other hand processes 2 and 7 are the loss factors to achieve higher efficiency while increasing CdS shell thickness. Analysis of the above processes clearly suggests that there should be some optimum shell thickness for enhancement of PCE in CdSe@CdS core-shell sensitized solar cell. In the present investigation from photo-conversion efficiency (PCE) measurements, it has been observed CS2 (CdSe@CdS4ML) i.e. CdSe core QDs with 4 monolayers of CdS gives us the highest efficiency (3.88%). Herein in CS2 the constructive factors like slow carrier cooling, slow exciton recombination, slow back electron transfer, minimizing surface states of core CdSe QD dominates over the processes like charge separation and hole neutralization which are retarded with the thickness of CdS shell as compared to other systems like CS1 and CS3. In the present investigation we have demonstrated interplay of different thickness dependent processes (process 1-7, Scheme 1) involved in quasi type II core-shell sensitized solar cell for optimizing the photo-conversion efficiency (PCE) which never been demonstrated in the literature.

4.2.2 Charge transfer in QDs and CPB perovskite composite system..

a. Characterisation.

To analyse the morphology of the synthesized CsPbBr₃ nanocrystals we have carried out the HR-TEM and XRD studies. Figure 4.6 A shows the HR-TEM image of the synthesized CsPbBr₃ NCs. The size of the cubic shaped NCs is 12.5 (longer edge) nm 11 nm (shorter edge). XRD pattern has been shown in Figure 4.6 B. Three major peaks (2θ) at $\sim 15^\circ$, 21.69° and, 30.5° for [100], [110] and, [200] planes, respectively reveals the cubic phase of

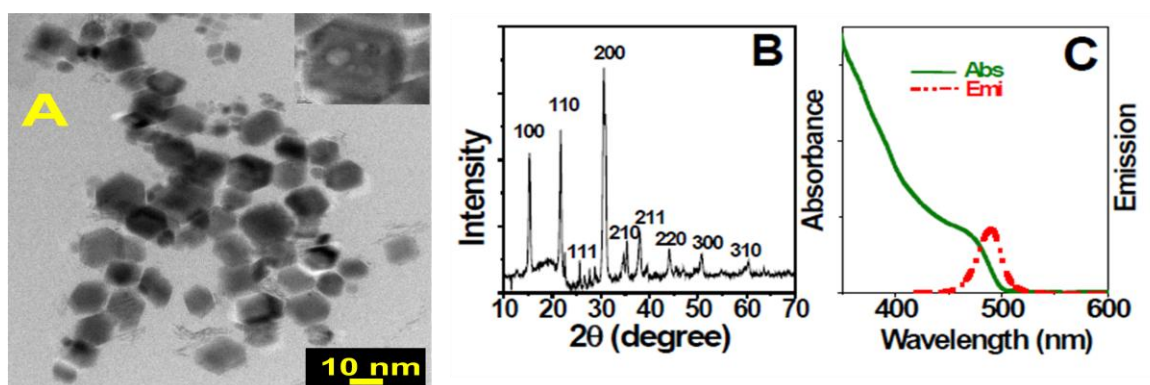


Figure 4.6. (A) HR-TEM image (B) XRD pattern and (C) UV-Visible absorption (olive solid line) and photoluminescence spectra (red dotted line) of CPB NCs. **In inset** of figure A shows the single particle of CPB.

CsPbBr₃ NCs. To characterise the CsPbBr₃ NCs optically we have performed the steady state absorption and luminescence spectroscopic measurements. The 1st excitonic absorption of CsPbBr₃ appears at 472 nm as seen in Figure 4.6 C and the corresponding band edge luminescence peak appears at 487 nm with very high emission quantum yield (QY = ~85%).

b. Interaction of CdSe QDs with CPB Perovskite.

The main endeavour of the present study is to investigate the interfacial electron and hole transfer dynamics of CPB NCs in presence of CdSe QDs and CdSe/CdS core-shell nanocrystals. Study of ground state interaction is one of the key measurements for such charge transfer reactions. To examine the interaction between the CPB NCs and CdSe QDs, we have carried out steady state optical absorption and photoluminescence studies. Figure 4.7 (a), (b) and, (c) show the steady state optical absorption spectra of CPB, CdSe and, colloidal mixture of CPB and CdSe QDs, respectively in toluene as solvent. It's interesting to see that the absorption peaks at 472 nm for CPB and at 555 nm for CdSe QDs are almost unchanged in the CPB/CdSe QDs mixture. The spectrum (d) shows the simple addition of (a) and (b), which is not very different from the spectrum (c) except in the blue region of the spectrum.

Higher absorption in the blue region of the spectrum suggests that there might be interaction in high energy states of both CdSe QD and CPB. Figure 4.7B (a) shows the steady state photoluminescence spectrum of CPB NCs with peak maxima at 487 nm having ~ 85% emission quantum yield in toluene. On the other hand the band edge emission peak maxima of the CdSe QDs appear at 570 nm (Figure 4.7 B trace b) with emission quantum yield ~23 % in toluene. It's interesting to see that on addition to CPB and CdSe QDs (Figure 4.7 B trace c) the emission intensity of at CPB position (487 nm) drastically reduced and it disappears at

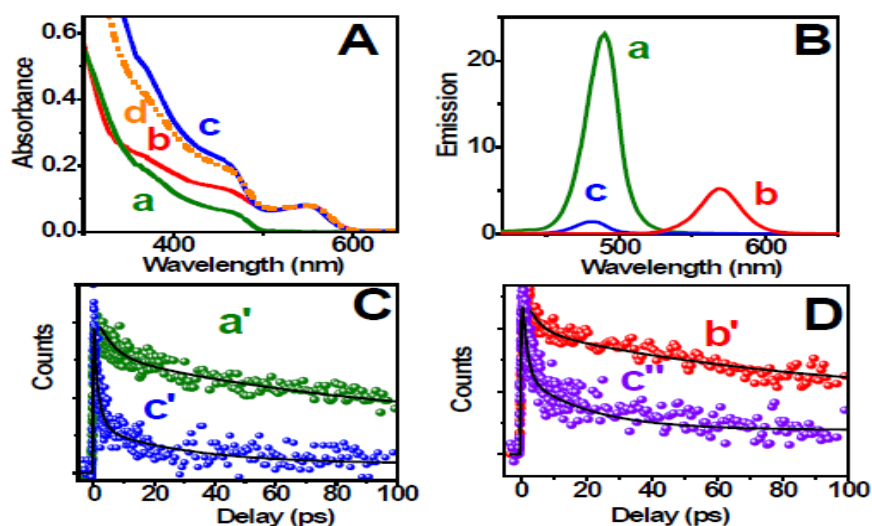


Figure 4.7: Steady state (A) UV-Vis absorption and (B) photoluminescence spectra of (a) CPB, (b) CdSe QDs, and (c) colloidal mixture of CPB and CdSe QDs. Spectrum (d) shows simple addition of spectra a and b. (C, D) Up-conversion luminescence decay traces of (a') CPB at 487 nm, (b') CdSe at 570 nm, (c' and c'') mixture of CPB and CdSe at 487 nm and 570 nm, respectively. For Up-conversion luminescence measurements the samples were excited at 400 nm.

CdSe QDs position (570 nm). The energetics of CPB and CdSe QDs are drawn in Scheme 4.3 which suggests that the conduction band (CB) and valence band (VB) maxima of the CPB

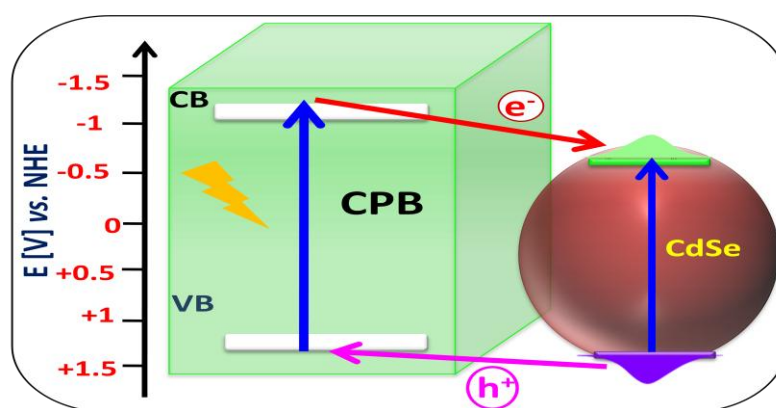
CHAPTER 4

NCs lies energetically higher and lower than the CB and VB of CdSe QDs, respectively. Therefore, upon photo excitation at 400 nm light both CdSe QDs and CPB can be excited, where photo-excited electron from CPB can be transferred to CdSe QDs and photo-excited hole from CdSe QDs can be transferred to CPB as both the processes are thermodynamically feasible. Now to determine the time scale of both electron and hole transfer processes

Table 4.3: Time resolved multi-exponential fitted parameters of CPB, CdSe QDs and mixture of these two at two different wavelengths (λ). Parentheses indicate the percentage of decay component.

System, λ (nm)	τ_1 (%)	τ_2 (%)	τ_3 (%)	τ_4 (%)
CPB, 487 nm	5ps (29%)	60 ps (21%)	>100 ps (50%)	
CPB/CdSe, 487 nm	0.55ps (55%)	3 ps (22%)	30 ps (13%)	>100ps (9%)
CdSe, 570 nm	4ps (24%)	60ps (23%)	>100ps (53%)	
CPB/CdSe, 570 nm	0.75 ps (43%)	3 ps (16%)	20 ps (23%)	>100ps (18%)

time-resolved up-conversion measurements have been carried for both CdSe QDs and CPB at their photoluminescence maxima position both in absence and in presence of each other after exciting them at 400 nm laser light and shown in Figure 4.7 C



Scheme 4.2: Schematic representation of electron from CB of CPB to CdSe and hole transfer from VB of CdSe to CPB QDs, respectively.

and D. Figure 4.7 C (a') shows the upconversion decay trace of CPB measured at wavelength

of 487 nm and can be fitted multi-exponentially with time components of $\tau_1 = 5$ ps (29%), $\tau_2 = 60$ ps (21%) and $\tau_3 = >100$ ps (50%) (Table 4.3). It is interesting to see that the decay components become faster in presence of CdSe QDs (Figure 4.7 C (c')) which can be fitted tri-exponentially with time components of $\tau_1 = 0.55$ ps (47%), $\tau_2 = 2$ ps (27%), $\tau_3 = 30$ ps (17%) and $\tau_4 = >100$ ps (9%) (Table 4.3). The extremely fast component (550 fs) in the decay trace can be attributed to the electron transfer from CPB to CdSe QDs as the process is energetically viable (Scheme 4.2). The luminescence decay trace of CdSe measured at 570 nm is shown in Figure 4.2D (b') and has been fitted multi-exponentially with time constants of $\tau_1 = 4$ ps (24%), $\tau_2 = 60$ ps (23%) and $\tau_3 = >100$ ps (53%) (Table 4.3). Interestingly this decay kinetics becomes faster when CdSe QDs interacts with CPB, has been illustrated in Figure 4.7D (c'') and can be fitted multi-exponentially with time constants of $\tau_1 = 0.6$ ps (29%), $\tau_2 = 1.5$ ps (30%), $\tau_3 = 20$ ps (23%) and $\tau_4 = >100$ ps (18%) (Table 4.3). Here in the faster decay component (600 fs) can be attributed to the hole transfer time from CdSe QDs to CPB.

c. Interaction of CdSe@CdS Core Shell with CPB Perovskite.

For better understanding of this charge transfer process in two different nanocrystals interface we impose band engineering concept. To do this we deliberately synthesized CdSe-CdS core-shell using same CdSe as core and have carried out the charge transfer interaction with CPB NCs. The steady state optical absorption spectra of CPB, CdSe@CdS core shell and the mixture of these two are shown in Figure 4.8 A (a), (b), and (c), respectively. The absorption spectrum of the mixture (c) is not changed from pure CPB or CdSe@CdS core shell, which signifies that there is no strong complexation between these NCs like CdSe QDs. Unlike CdSe, the steady state luminescence spectrum of the mixture of CPB and CdSe@CdS

core shell is different. Figure 4.8 B (a) and (b) depict the luminescence spectra of CPB and CdSe/CdS core shell, respectively after 400 nm excitation. Figure 4.8 B (c) shows the luminescence spectrum of colloidal mixture of CPB and CdSe@CdS core shell. Similar to CdSe QDs (Figure 4.8 B c'), the PL spectrum of the mixture of CPB-CdSe@CdS core shell shows the luminescence of CPB is drastically quenched. However, the luminescence of

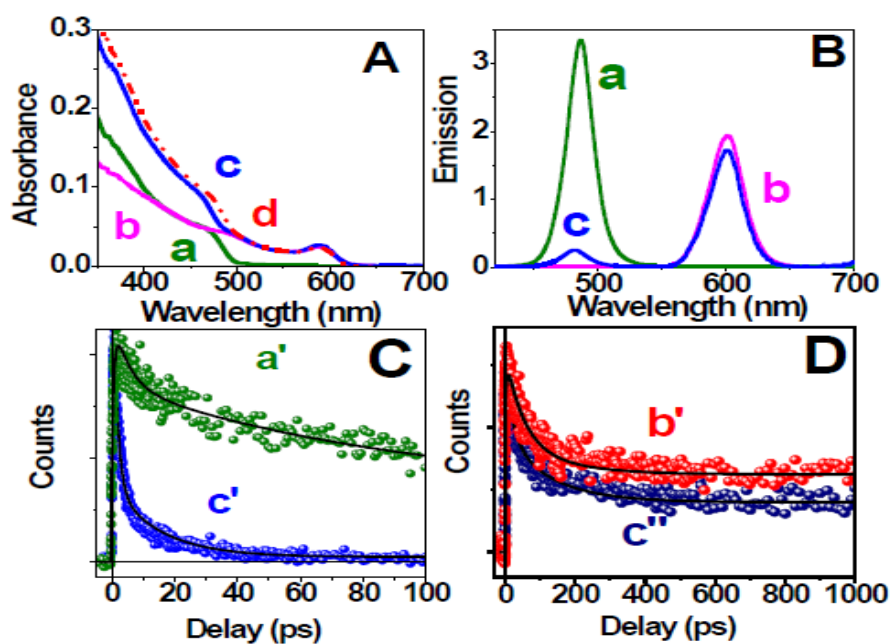


Figure 4.8: Steady state (A) UV-Vis absorption and (B) photoluminescence spectra of (a) CPB, (b) CdSe/CdS, and (c) colloidal mixture of CPB and CdSe/CdS. Spectrum (d) shows simple addition of spectra a and b. (C, D) Luminescence up-conversion decay traces of (a') CPB at 487 nm, (b') CdSe/CdS at 600 nm, (c' and c'') mixture of CPB and CdSe/CdS at 487 nm and 600 nm, respectively.

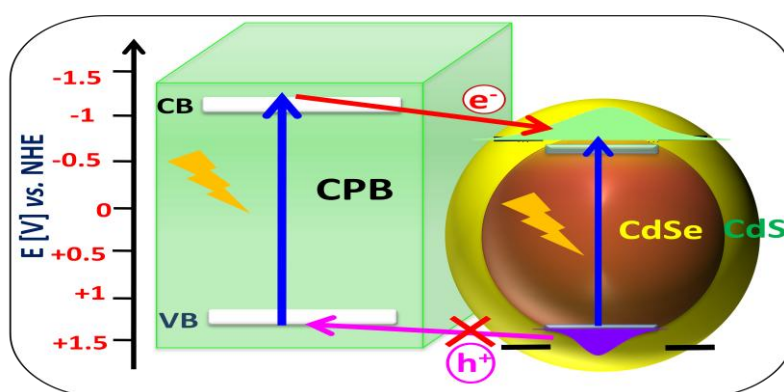
CdSe@CdS core shell is not quenched in presence of CPB which is different from CdSe QDs. To realize the distinct charge (electron and hole) transfer processes we have drawn the energetic of CPB and CdSe@CdS core-shell in Scheme 4.3. The band energy alignment of

the CdSe@CdS suggests quasi type-II structure where valence bands of CdSe and CdS have higher energy offset.^{51, 52} Again Scheme 4.3 suggests that the CB and VB of the CPB NCs lies energetically higher than the CB and VB of CdSe@CdS core-shell. Thus, upon photo-excitation the photo-excited electron from CPB to CdSe@CdS core-shell can take place as the process is energetically favourable. However, photo excited hole transfer from

Table 4.4: Up-conversion multi-exponential fitted parameter of CPB, CdSe@CdS and mixture of these two at two different wavelengths (λ). Parentheses indicate the percentage of decay component.

System, λ (nm)	τ_1 (%)	τ_2 (%)	τ_3 (%)	τ_4 (%)
CPB, 487 nm	5 ps (29%)	60 ps (21%)	>100 ps (50%)	
CPB-CdSe@CdS, 487 nm	0.65 ps (64%)	15 ps (33%)	>100ps (3%)	
CdSe@CdS, 600 nm	10 ps (21%)	50 ps (31%)	150 ps (3%)	>1ns (45%)
CPB-CdSe@CdS, 600 nm	7 ps (33%)	25 ps (25%)	130 ps (7%)	>1 ns (35%)

CdSe@CdS core shell to CPB is restricted due to presence of CdS shell which make the process energetically unfavourable. In case of CPB and CdSe QDs mixture, we have seen that the luminescence quenching of both CPB and CdSe QDs is due to electron transfer from CPB to CdSe QDs and hole transfer from CdSe QDs to CPB respectively. Herein the luminescence



Scheme 4.3: Allowed electron and restricted hole transfer processes from CPB to CdSe/CdS core shell and CdSe/CdS to CPB NCs, respectively..

quenching of CPB in presence of CdSe@CdS core shell can be attributed as electron transfer from CPB to core shell. However PL intensity of CdSe@CdS core-shell decrease marginally in presence of CPB which suggests that hole transfer is restricted from core shell to CPB NCs. The hole is confined in the core CdSe, due to large VB offset energy core CdSe QD and shell CdS QD (Scheme 4.3). Although the hole transfer process is not thermodynamically viable still we have observed marginal luminescence quenching of CdSe@CdS core shell which can be attributed to leaking of hole from CdSe core of the core-shell to CPB through CdS shell QD.

To reconfirm the electron transfer from CPB to CdSe@CdS core-shell and the restriction of hole transfer from core-shell to CPB and determine the time constants of charge transfer processes, we have carried out femtosecond up-conversion luminescence studies after the samples at 400 nm. Figure 4.8 C (a') is the luminescence decay trace of CPB at 487 nm which we have already mentioned earlier (Figure 4.7 C (a')) and has been fitted bi-exponentially (Table 4.4). Interestingly in presence of CdSe@CdS core-shell the CPB luminescence decay much faster as shown in Figure 4.8 C (c') and can be fitted bi-exponentially with time constants of $\tau_1 = 0.65$ ps (64%) and $\tau_2 = 15$ ps (33%) (Table 4.4). This faster component of the decay can be attributed to electron transfer from CPB to CdSe@CdS core shell. On the other hand luminescence decay kinetics of CdSe@CdS core-shell in absence and in presence of CPB at 600 nm have been shown in Figure 4.8D (b') and (c'') respectively. It is seen that emission decay kinetics CdSe@CdS core-shell are not changed significantly in absence and in presence of CPB. The luminescence decay trace of CdSe@CdS core-shell can be fitted multi-exponentially with time constants of $\tau_1 = 10$ ps (21%), $\tau_2 = 50$ ps (31%), $\tau_3 = 150$ ps (3%), and $\tau_4 = >1$ ns (45%) in absence of CPB (Table

4.4) and $\tau_1 = 7$ ps (33%), $\tau_2 = 25$ ps (25%), $\tau_3 = 130$ ps (7%) and $\tau_4 = >1$ ns (35%) in presence of CPB (Table 4.4). However, little change in decay dynamics might be due to leaking of hole from core CdSe QD to CPB through CdS shell. Therefore in the present investigation it has been observed simultaneous both electron and hole transfer take place in CPB and CdSe QDs system, however, in case of CPB and CdSe@CdS core-shell system electron transfer from photo-excited CPB to core-shell is facile, but hole transfer from photo-excited CdSe@CdS core-shell to CPB is restricted.

e. TA Spectroscopy Measurement of CdSe QDs and CPB Perovskite mixture.

From steady state and time resolved luminescence studies it is confirmed the electron transfer takes place from photo-excited CPB perovskite to CdSe QDs and the hole is transferred from photo-excited CdSe QDs to CPB perovskite. To reconfirm the electron and hole transfer dynamics between CPB perovskite and CdSe QDs more precisely, femtosecond transient absorption spectroscopic studies have been carried out and correlated the electron

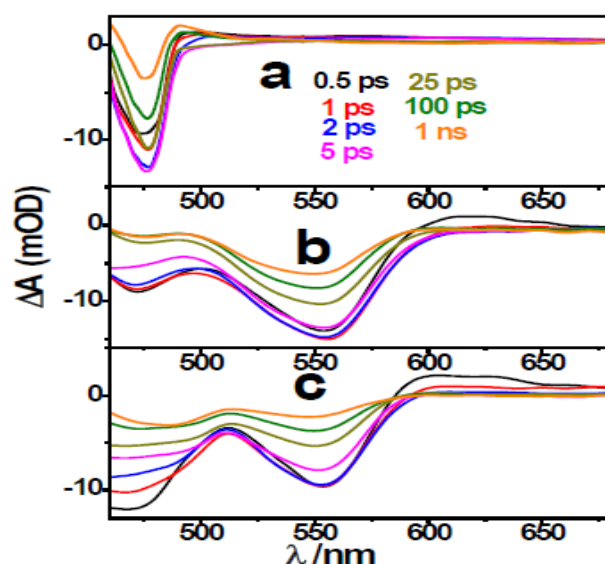


Figure 4.9: TA spectra of (a) CPB perovskite, (b) CdSe QDs, and (c) mixture of CPB and CdSe at different time delay after 400 nm pulse excitation in toluene.

and hole transfer dynamics with fluorescence up-conversion data. Figure 4.9 (a) shows the TA spectra of CPB after 400 nm laser excitation at different time delay. The spectra at all the time delay show sharp negative absorption change (bleach) peaking at 477 nm which can be attributed to the ground state excitonic absorption which nicely matches with steady state absorption spectrum (Figure 4.6 C). In addition to the bleach photo-induced absorption (PA) at 485–530 nm was observed which can be attributed to hot exciton induced absorption^{19, 222}. The TA spectra of CdSe QDs is shown in Figure 4.9 (b) which consists two negative absorption bands (bleach) at 555 and 480 nm due to 1S, and 1P electronic transition, respectively. Weak photo-induced absorption band in the red region of the spectra suggests presence of minimum defect states in CdSe QDs. Similar to the steady state optical absorption spectrum, the TA spectra of the CPB and CdSe mixture show individual spectral feature which has been illustrated in Figure 4.9 C. Herein one negative absorption band appears at 555 nm can be attributed to 1S excitonic bleach of CdSe QDs while the second one which is quite broad can be attributed to combination of excitonic bleach of CPB and 1P excitonic bleach of CdSe QDs where primarily the bleach is dominated by CPB NCs.

To monitor the electron and hole transfer dynamics between CPB NCs and CdSe QDs, we probed the bleach kinetics at the key wavelengths in different systems. Figure 4.10 A (a) represents the bleach kinetics of pure CPB NCs at 477 nm. The growth of the bleach kinetics can be fitted bi-exponentially with time constants of $\tau_1 = 150$ fs (70%) and $\tau_2 = 1$ ps (30%) (Table 4.5) which can be attributed to the carrier cooling time from upper excitonic states to the band edge states of CPB NCs. Now the bleach recovery kinetics can be fitted with time components of 5 ps (26%), 70 ps (35%) and >1 ns (37%) (Table 4.5) which can be attributed to charge recombination dynamics between photo-excited electron and hole in CPB

NCs. It's interesting to see that the bleach recovery kinetics matches nicely with the upconversion luminescence decay (Figure 4.11). This observation suggests that majority of the charge carriers recombine through radiative process, which makes it high QY material.⁵²⁵² Now it has been observed that bleach recovery kinetics at 477 nm drastically changes in CPB/CdSe QD system as shown in Figure 4.10 (b), where the bleach growth time found to be pulse-width limited (< 100 fs) (Table 4.5). Ultrafast bleach growth indicates electron transfer from photo-excited hot states of CPB NCs to CdSe QDs before cooling to the band edge

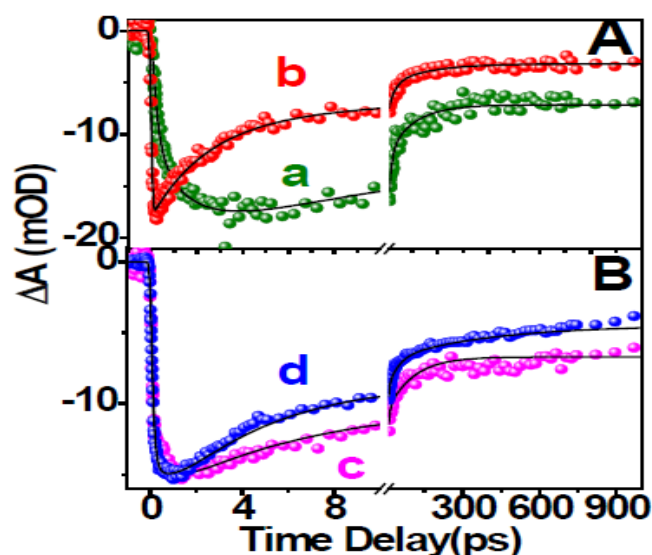


Figure 4.10: TA bleach dynamics of (a, b) CPB NCs and CPB/CdSe QD system at 477 nm, and (c,d) CdSe QDs and CPB/CdSe QD system at 555 nm after 400 nm excitation.

states. Now the bleach recovery kinetics can be fitted multi- exponentially with time constants $\tau_1 = 0.65$ ps (42%), $\tau_2 = 10$ ps (30 %), $\tau_3 = 150$ ps (10%) and $\tau_4 = >1$ ns (18%) (Table 4.5). Bleach recovery found to be much faster in CPB/CdSe QD system as compared to pure CPB NCs attributes the fast electron transfer from CPB to CdSe QDs. Here in the 0.65 ps component represents the electron transfer time from CPB

CHAPTER 4

SI Table 4.5: Fitted parameter of bleach dynamics of CPB, CdSe and mixture of CPB-CdSe at mentioned wavelength (λ).

System, λ (nm)	τ_1 (%)	τ_2 (%)	τ_1 (%)	τ_2 (%)	τ_3 (%)	τ_4 (%)
CPB, 477	150fs (70%)	1 ps (30%)	5 ps (30%)	70 ps (28%)	>1 ns (42%)	
CPB/CdSe, 477	<100fs (100%)		0.65 ps (42%)	10 ps (30%)	150ps (10%)	>1 ns (18%)
CdSe, 555	100 fs (75%)	0.5 ps (25%)	6 ps (35%)	100 ps (21%)	>1ns (44%)	
CPB/CdSe, 555	150 fs (75%)	0.4 ps (25%)	5 ps (23%)	22 ps (34%)	130 ps (12%)	>1 ns (31%)

NCs to CdSe QDs which closely matches with the electron transfer time constants determined from fluorescence up-conversion data. Now transient bleach recovery kinetics for CdSe QDs and CPB/CdSe QDs system was monitored at 555 nm which is the first excitonic

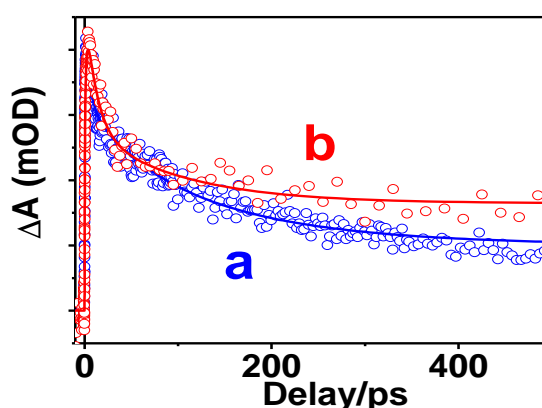


Figure 4.11: comparison of upconversion decay dynamics (a) and bleach decay dynamics (b) of CPB nanocrystals. These figures show the luminescence decay and bleach decay dynamics is almost matches.

bleach peak for CdSe QDs and are shown in Figure 4.10. Figure 4.10 B (c) indicates the first excitonic bleach recovery kinetics of CdSe QDs which can be fitted with bi-exponential growth constants of 100 fs (75%) and 0.5 ps (25%) (Table 4.5) where the longer growth component can be attributed to the electron cooling time from upper electronic states to the

band edge states. Now the 1S bleach recovery can be fitted multi-exponentially with time constants of $\tau_1 = 6$ ps (35%), $\tau_2 = 100$ ps (21%) and $\tau_3 = >1$ ns (44%) (Table 4.5). The faster (6 ps) and longer (100 ps and > 1 ns) time components represents the carrier recombination due to trapping and exciton recombination, respectively.⁵³⁻⁵⁴ Now Figure 4.10 B (d) indicates the first excitonic bleach recovery kinetics of CdSe QDs in presence of CPB NCs, which can be fitted with bi-exponential growth constants of 150 fs (75%) and 0.4 ps (25%) and multi-exponential recovery components with time constants of $\tau_1 = 5$ ps (23%), $\tau_2 = 22$ ps (34%), $\tau_2 = 130$ ps (12%) and $\tau_3 = >1$ ns (31%) (Table 4.5). It's interesting to see that the growth component of CdSe QDs at excitonic wavelength in presence of CPB NCs does not change (Figure 4.10 B d), which reveals that electron in CdSe QDs is not affected in presence of CPB NCs. However, the bleach recovery found to be little faster as compared to pure CdSe QDs which might be due to hole transfer from CdSe QDs to CPB NCs.

f. TA Spectroscopy Measurement of CdSe@CdS Core Shell and CPB Perovskite mixture.

To investigate the charge transfer dynamics in CdSe@CdS core-shell in presence of CPB NCs in ultrafast time scale femtosecond transient absorption studies have been carried out for pure CdSe@CdS core-shell and CdSe@CdS/CPB NCs systems and shown in figure 4.12. The spectral profile of core shell have not been change in presence of CPB according to steady state absorption studies.

To follow the charge transfer dynamics in CdSe@CdS/CPB NCs composite system we monitored the bleach recovery kinetics at different excitonic wavelengths (477 nm and 590 nm) and compared with the bleach recovery kinetics with pure CdSe@CdS QDs and CPB NCs respectively and shown in Figure 4.13. Figure 4.13 (a) and (b) show the bleach

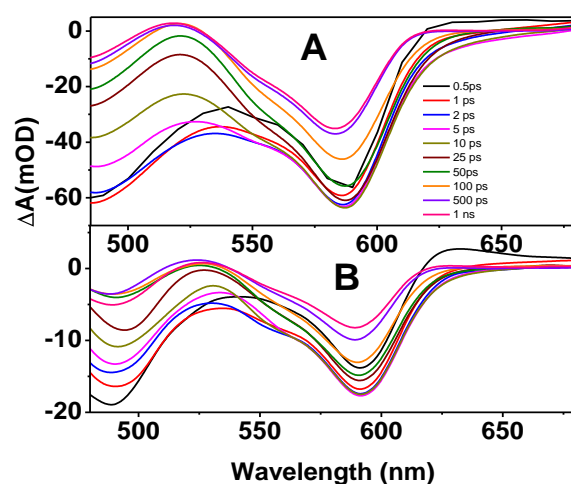


Figure 4.12: TA spectra of (A) CdSe QDs and (B) mixture of CdSe@CdS and CPB at different time delay after 400 nm pulse excitation in toluene.

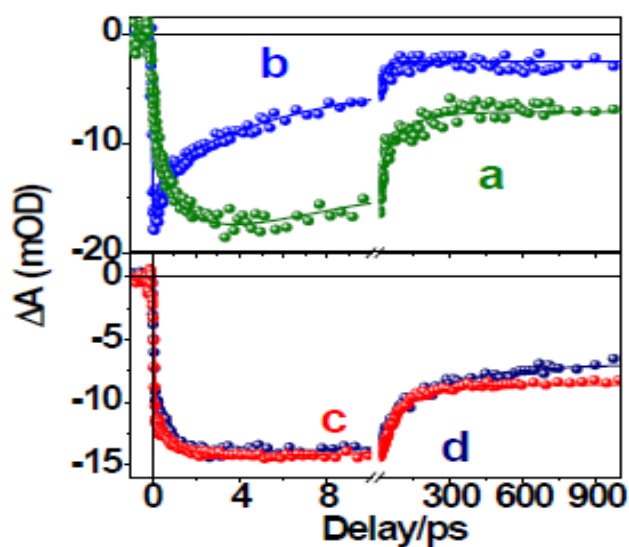


Figure 4.13: TA bleach dynamics of (a) CPB at 477 nm (b) CdSe@CdS/CPB at 477 nm (c) CdSe@CdS core shell at 590 nm and (d) CdSe@CdS/CPB at 590 nm after 400 nm excitation.

kinetics of CPB NCs at 477 nm in absence and presence of CdSe@CdS core shell. The bleach dynamics of pure CPB NCs has already been discussed in earlier part of this manuscript. It's interesting to see that the bleach kinetics of CPB NCs at 477 nm drastically

CHAPTER 4

changes in presence of CdSe@CdS core shell, which can be fitted with pulse-width limited growth (<100 fs) and multi-exponential recovery with time constants of $\tau_1 = 0.45$ ps (37%), $\tau_2 = 5$ ps (41%), $\tau_3 = 30$ ps (15%) and $\tau_4 = >1$ ns (7%) (Table 4.6). Pulse width limited bleach growth kinetics clearly suggests transfer of hot electrons from CPB NCs to the core-shell. However it's quite interesting to see that bleach recovery kinetics at 590 nm looks marginally different in case of pure CdSe@CdS core shell and CPB/ CdSe@CdS core shell system. This observation clearly indicates hole transfer from the core-shell to CPB NCs is restricted and the results quite matched with fluorescence up-conversion data.

Table 4.6. Fitted parameter of bleach dynamics of CPB, CdSe/CdS core shell and mixture of CPB-CdSe/CdS at mentioned wavelength (λ).

System, λ (nm)	τ_1 (%)	τ_2 (%)	τ_1 (%)	τ_2 (%)	τ_3 (%)	τ_4 (%)
CPB-CdSe/CdS, 477	<100fs (100%)		0.45 ps (37%)	5 ps (41%)	30 ps (15%)	>1 ns (7%)
CdSe/CdS,590	<100 fs (70%)	1.5 ps (25%)	35 ps (32%)	250 ps (10%)	>1ns (58%)	
CPB/CdSeCdS,590	<100 fs (70%)	1.5 ps (30%)	35 ps (32%)	250 ps (15%)	>1 ns (53%)	

4.3 Conclusion:

In conclusion, we have demonstrated thickness dependent power conversion efficiency of quasi type-II CdSe@CdS core-shell after directly correlating the ultrafast spectroscopic data. CdSe QDs and CdSe@CdS quasi type-II core-shell with different shell thickness have been synthesized following high temperature synthetic methods and characterized by optical spectroscopy and high resolution TEM technique. Quantum dot solar cells have been fabricated using QDs/core-shell deposited on TiO₂ film as photoanode, Cu₂S deposited on ITO film as photocathode and polysulphide solution as electrolyte. Power conversion efficiency (PCE) found to initially increase and then decrease with shell (CdS)

thickness. Here in CdSe@CdS core-shell with 4 monolayer of CdS found to give highest efficiency (3.88 %) which is ~ 57% higher as compared to pure CdSe QDs sensitized solar cell (2.47%) under similar condition. Charge carrier cooling, carrier trapping, charge separation and charge recombination dynamics in different QDSC systems have been monitored by using femto-second transient absorption spectroscopic studies directly correlated with PCE measurement data. With increasing shell thickness certain processes like electron cooling, trapping of charge carriers, exciton recombination, charge carrier recombination reaction show positive outcome and other process like charge separation and hole neutralization show negative outcome for PCE of QDSC. Optimization of shell thickness to achieve highest efficiency has been done after correlating PCE value of different core-shell samples with the corresponding ultrafast spectroscopic data. This is first report in literature where thickness dependent electron cooling, carrier trapping, charge separation and charge recombination processes have been directly correlated to the beneficial of PCE in quasi-type II core-shell QD sensitized solar cell.

In addition to that, interfacial charge (both electron and hole) separation between photo-excited CsPbBr₃ (CPB) NCs and CdSe QDs and CdSe@CdS core-shell has been demonstrated through steady state and ultrafast time-resolved luminescence and absorption techniques. Energy level diagram suggests electron transfer from photo-excited CPB NCs to CdSe QDs and hole transfer from CdSe QDs to CPB NCs is thermodynamically viable process. Both steady state and time resolved PL studies suggests the concurrent electron and hole transfer from CPB NCs to CdSe QDs and CdSe QDs to CPB NCs, respectively. On the other hand in case of CPB NCs and CdSe@CdS core-shell system photo-excited electron transfer from CPB NC to the core-shell found to be facile whereas the hole transfer from

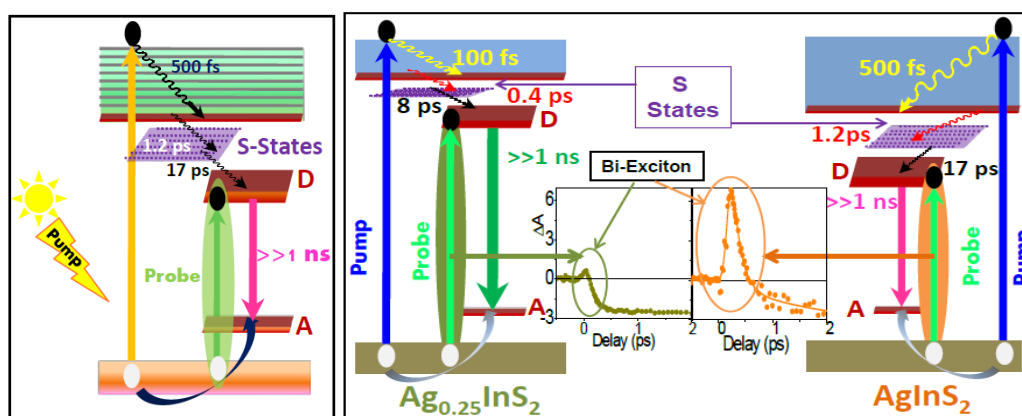
CHAPTER 4

core-shell to CPB NCs found to be restricted due to presence of CdS shell. To monitor the charge transfer dynamics in ultrafast time scale two complimentary techniques both Femto-second transient absorption and Fluorescence up-conversion techniques were employed. Photo-excited electron transfer time from CPB NCs to CdSe QDs and CdSe@CdS core-shell were measured to be 550 and 450 fs, respectively. On the other hand hole transfer time from photo-excited CdSe QDs to CPB NCs found to be 750 fs. Present investigation suggests in CPB NCs and CdSe QDs composite system on photo-excitation grand charge separation takes place where all the electrons are localized to CdSe QDs and holes are localized in CPB NCs. This charge separated composites can be used as efficient materials for photo catalysis and photovoltaic applications.

CHAPTER 5

CHAPTER-5

ULTRAFAST EXCITON AND BI-EXCITON DYNAMICS OF TERNARY AgInS_2 NANOCRYSTALS



J. Phys. Chem. Let. 7 (16), 3206-3214

CHAPTER 5

5.1. Introduction:

Silver indium sulfide (AgInS_2 , referred to as AIS), a ternary I–III–VI nanocrystal (NC), has been the subject of tremendous interest in research since last decade due to its enormous potential application in thin-film photovoltaic, light emitting diodes, and bioimaging.^{218, 223-226} Relatively lower band gap and large absorption cross section in the visible to near-infrared (NIR) region make AIS NCs a perfect material for harvesting the solar light. The tunable photoluminescence (PL), high quantum yield, and larger Stoke's shift make it attractive for environment friendly alternatives of more toxic II–VI quantum dots (QDs) in various optical devices.^{189, 227-229} Exciton (electron hole pair) generation after absorbing photon is the general property of the bulk semiconductor and the exceeding band gap energy released as heat energy when hot electron and hole are relaxed to its minimum energy of band-edge state. In quantum dots, more than one electron hole pair, that is, carrier multiplication (CM), can be realized by single photon when the band gap of the semiconductor is low and the photon energy is more than twice the band gap of the semiconductor.^{34, 36, 37, 218, 229-233} Therefore, the solar cell efficiency can be enhanced by extracting more than one charge carrier through multi- or bi-exciton generation using single photon. In this regard, the I–III–VI ternary NCs are efficient materials for CM processes.²²⁶ Previously, Stolle et al.²³³ reported the CM of ternary CuInS_2 (CIS) NCs, where they have shown longer Auger lifetime and lower threshold energy for CM of CIS as compared with that of PbSe NCs. Such bi-exciton can be generated during the CM in NCs, which increases the spatial overlap of charge carriers than the bulk semiconductor, thereby enhancing bi-exciton binding energy.^{26, 33, 234} Recently we have demonstrated probe-induced bi-exciton generation of CIS NCs, where antisite defect states (donor states) are found to be responsible for the process.²³⁵ The AIS NCs are low-band-gap-defect-induced ternary systems, which are

effective materials for multi exciton generation and can be promising materials for designing higher efficient solar cell. These inquisitive optical properties in I-III-VI ternary systems are originated due to recombination of charge carriers through intra-band gap defect states rather than due to recombination of exciton.²³⁶⁻²⁴⁰ The photoexcited electrons and holes are trapped at donor and acceptor sites, and the estimated binding energy of the donor and acceptor sites is 100 and 220 eV, respectively.²⁴¹ The antisite defect states are created due to the vacancy of Ag (V_{Ag}), S (V_S), silver interstitial, and sulfur interstitial.^{242, 243} Here the silver interstitial (and V_S) acts as donor site, whereas the sulfur interstitial (and V_{Ag}) acts as acceptors.²⁴¹ Because of interference of these internal defect states, carrier recombination time drastically increased in these systems, which makes them a unique material for solar energy harvesting.²⁴⁴ Previously Burda et al.²⁴⁴ and Torimoto et al.²⁴⁵ reported band-edge, trap state, and intrinsic donor state life times for AIS NCs. In our previous investigation²³⁵ we have reported that emission in CIS NCs is responsible from both external and internal defect states, and defect-induced carrier dynamics have also been revealed. However, to date, in literature no reports are available on ultrafast carrier cooling and bi-exciton dynamics involving sub-band gap states (S-states) and also the effect of Ag/In ratio in AIS NCs.

In this chapter we are describing the detailed spectroscopic investigation of AIS NCs in different stoichiometry of Ag and In by both steady-state and time-resolved spectroscopic techniques. The role of cationic ratio, i.e. the ratio of Ag and In, on PL quantum yield and lifetimes is related to different intra-bandgap states, which have been addressed in detail. Ultrafast carrier cooling dynamics involving multiple states like band-edge, S-states, and antisite states with different Ag/In ratio have been investigated using femtosecond transient absorption spectroscopy. The most interesting revelation of this report is the observation of

bi-exciton and its dynamics in the antisite state of AIS NCs with 3.1 eV pump at low pump fluence ($\langle N \rangle = \sim 0.2$), which have explained on the basis of a probe induced bi-exciton formation mechanism. Also, the bi-excitonic feature was found to depend strongly on the stoichiometric ratio of Ag and In.

5.2. Results and Discussions:

A. Characterisation of AIS NCs.

Ag_xInS_2 (AIS) ternary NCs (where Ag:In is x:1) with varying x (0.25 to 1) have been synthesized following the synthetic procedure developed by Peng and co-workers³⁴. Three AIS NCs e.g. $\text{Ag}_{0.25}\text{InS}_2$, $\text{Ag}_{0.5}\text{InS}_2$ and AgInS_2 indicates Ag:In ratio's are 0.25:1, 0.5:1 and 1:1 were synthesized (chapter 2) and named as AIS 1, AIS 2 and AIS 3 respectively.

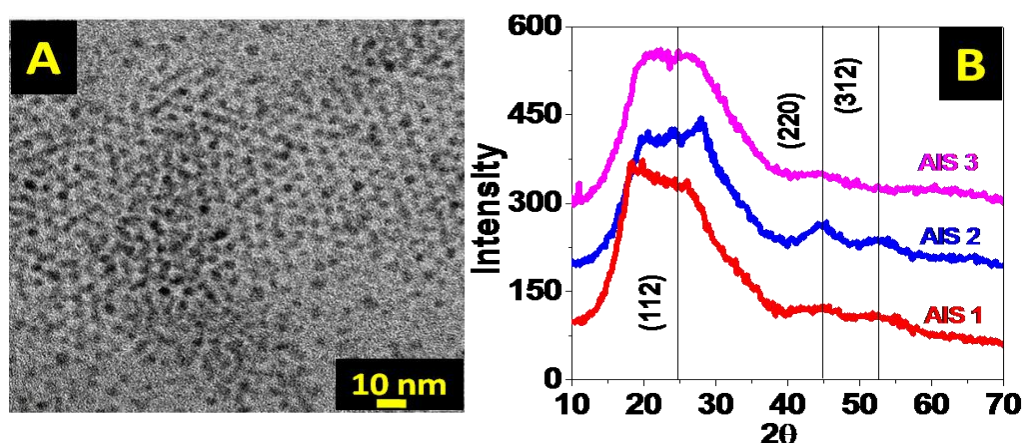


Figure 5.1.A: HR-TEM image of AIS 3 QDs. **B.** XRD pattern of AIS 1, AIS 2 and AIS 3 NCs.

The synthesized NCs were characterized by high-resolution TEM and XRD measurements. Figure 5.1 A shows the HR-TEM images of AIS 3. Average particle size of the AIS NCs was determined to be ~ 3 nm, which clearly suggests that particle sizes are in the range of strong confinement regime. These XRD spectrum has been show Fig-5.1 B and the major peaks for all AIS NCs are are at 26.2° , 44.5° and 53° for the plane of (112), (220) and (312),

respectively. These reveal that all NCs are tetragonal crystal lattice and there is no change of lattice in different stoichiometry of Ag and In ratio.

B. Steady State Optical Absorption and Emission Studies.

Steady state optical absorption and emission studies have been carried out to monitor the quantum confinement behaviour of AIS NCs in different composition of Ag:In ratio.

Figure 5.2 (a), (b) and (c) show the optical absorption spectra of AIS 1, AIS 2 and AIS 3

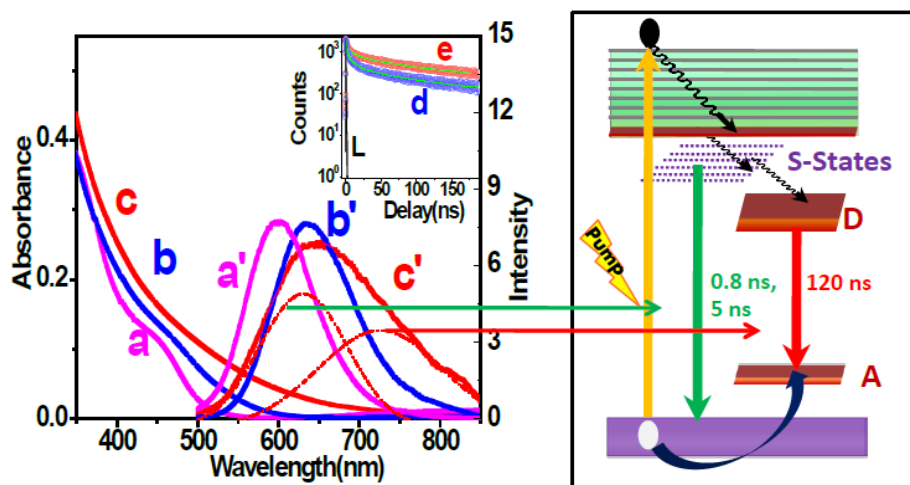


Figure 5.2. Left panel: Steady state optical absorption and luminescence spectra of (a, a') AIS 1 ($\text{Ag}_{0.25}\text{InS}_2$) (b, b'') AIS 2 ($\text{Ag}_{0.5}\text{InS}_2$) and (c, c') AIS 3 (AgInS_2) respectively. Spectra in dotted line are the de-convoluted emission spectra of AIS 3 (Figure 2 c'). Deconvolution of c' to two Gaussians (peaking at 630nm and 727nm) also have been shown. **Inset.** Time-resolved luminescence spectra of AIS 3 monitored at (d) 630 nm and (e) 727 nm after 445 nm laser excitation. **L** is the lamp profile of 445 nm laser. **Right panel:** Schematic diagram of photoinduced processes, which shows that the electron is trapped either in lower lying Ag related S-States or donor state (D) and the hole is trapped in internal defect (acceptor state, A). The straight arrows show radiative recombination.

respectively. Figure 5.2 (a) shows clear excitonic absorption peak for AIS 1 at 450 nm,

however with increasing concentration of Ag in the AIS NCs the excitonic absorption peak become broad and moves in the red region of the spectra. At higher concentration of Ag i.e. in AIS 3 the absorption band becomes extremely broad (no sharp excitonic feature) and the absorption tail continues up to 750 nm. In our earlier investigation we have also observed absence of sharp excitonic absorption in CuInS₂ (CIS) NC materials.^{235, 246} The lack of sharpness of excitonic peak of I-III-VI ternary system attributes the weak carrier confinement of the excited state of this system and delocalisation of electron is occurred through out the manifold of electronic states.^{235, 246}

Recently, Kamat and coworkers²⁴⁷ reported optical absorption spectra of CuInS₂ NCs with changing [Cu]/[In] ratio and have observed long absorption tail in the red region of the spectra with the absence of sharp excitonic feature at higher concentration of Cu, which has been attributed to Cu-related sub-band gap state absorption. Similarly, in the present studies the long absorption tail up to 750 nm in AIS 3 can be attributed to Ag-related S-states. Steady-state luminescence studies have also been carried out for the AIS NCs samples and are shown in Figure 5.2. Analogous to the absorption spectra, as the Ag concentration increases in the host AIS NC the luminescence spectra become broad and red-shifted. Previously Chen et al.²⁴⁸ also made a similar kind of observation in CIS NCs, where luminescence spectra shifted to the red region as the ratio of Cu/In increased. Here the luminescence quantum yield was found to decrease with increasing Ag concentration and was determined to be 23%, 17%, and 13% for AIS 1, AIS 2, and AIS 3, respectively. To understand the effect of Ag concentration in different optical properties, we have plotted the change of luminescence quantum yield, Stoke's shifts, and fwhm of luminescence spectra of AIS NCs with different composition of Ag/In, shown in the Figure 5.3. Both the fwhm of

emission spectra and Stoke's shift increases with Ag concentration. This observation suggests the reduction of confinement in AIS NCs with increasing Ag concentration. The red end of the broad emission spectra becomes asymmetric with increase in Ag concentration, which is clearly discernible in AIS 3. Previously, Burda and coworkers²⁴⁴ demonstrated broad and asymmetric PL spectra by deconvoluting into two Gaussian spectra, which they have attributed to luminescence due to mid band gap states and intrinsic defect states. Similarly, to characterize the emissive states of AIS samples, we have deconvoluted the PL spectra, shown in Figure 5.2 (for AIS 3) Fig. 5.3 (for AIS 1 and AIS 2). The deconvoluted emission spectra of AIS 3 show two emission maxima at 630 and 727 nm, respectively (Figure 5.2 c'). The emission spectra in the red region ($\lambda_{em}^{max} = 727$ nm) can be attributed to intrinsic trap states, which are generated due to interstitial atoms or vacancies and are responsible for donor-acceptor transitions²⁴⁹⁻²⁵² in I-III-VI semiconductors. On the contrary, the emission spectra in the blue region ($\lambda_{em}^{max} = 630$ nm) can be ascribed to the Ag-related mid-bandgap states, which are usually shallow and high in energy compared with intrinsic trap states.^{235, 246, 253} In AIS 3, the emission peak due to intrinsic trap states moves to the red region of the spectra, which clearly suggests that the energy gap between donor-acceptor states decreases with increasing Ag concentration (Figure 5.2).

Time-resolved emission studies have been carried out after exciting AIS 3 at 445 nm and monitoring at 630 and 727 nm to figure out the life times at both of the emitting states, shown in Figure 5.2 inset. The emission decay trace at 630 nm can be fitted multiexponentially with time constants of $\tau_1 = 0.8$ ns (25%), $\tau_2 = 5$ ns (37%), and $\tau_3 = 105$ ns (38%), while at 727 nm can be fitted multi-exponentially with time constants of $\tau_1 = 1.3$ ns (24%), $\tau_2 = 7$ ns (32%), and $\tau_3 = 120$ ns (44%) (Table 5.1). In our previous investigation,²³

we have accounted with similar kind of observation for CuInS₂ (CIS) NCs, where the fast two components were assigned to nonradiative decay to surface states, while

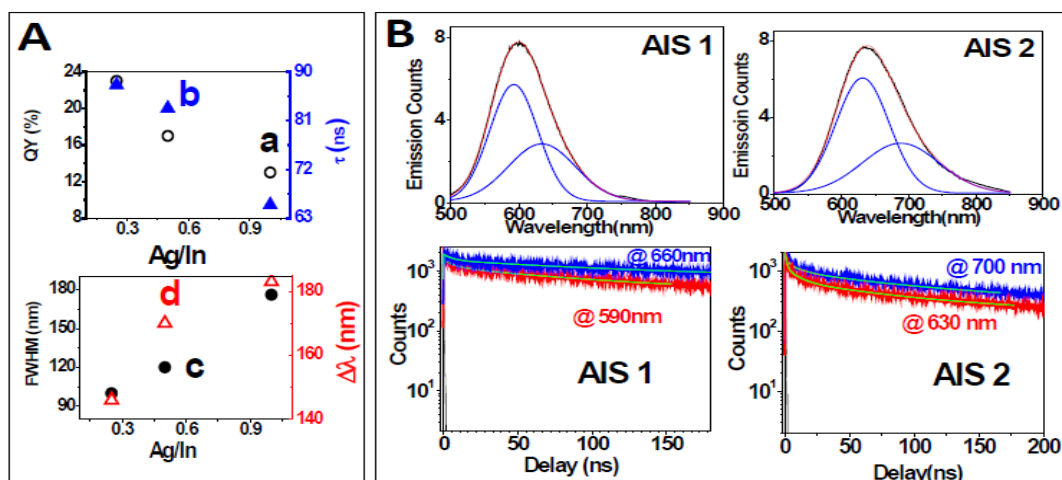


Figure 5.3.A: Graphical plot of (a) Emission QY Vs Ag/In (b) Emission life time at peak wavelength Vs Ag/In (c) FWHM of luminescence Vs Ag/In and (d) Stokes shift Vs Ag/In ratio. **B.** Deconvoluted PL spectra of AIS 1 and AIS 2 and the time resolved PL kinetics of AIS 1 and AIS 2 at the respective peak wavelength after exciting at 445 nm wavelength.

the slow component was attributed to the recombination of charge carriers. It has been reported in literature that majority of the charge carriers in CIS are trapped in the internal defects and depend on the Cu/In ratio, which has a strong effect on optical properties.^{254, 255}

The emission spectra for both AIS 1 and AIS 2 have also been deconvoluted into two emission spectra, shown in Fig 5.3 B. Time-resolved emission studies have also been carried out for both AIS 1 and AIS 2 at both blue emission band and red emission band positions, shown in Table 5.1. Now if we compare the longer lifetime component for all three AIS NCs at the red region of the deconvoluted spectra, it is interesting to see that with increasing Ag concentration the component for intrinsic defect states decreases from 156 ns

Table 5.1. Exponentially fitted parameter of time resolved luminescence decay traces of AIS

NCs at different wavelengths after exciting the samples at 445 nm.

System	τ_1	τ_2	τ_3
AIS 1-600 nm	2 ns (25%)	9.6 ns (30%)	145 ns (45%)
AIS1-640 nm		6.21ns (35%)	156 ns (65%)
AIS2-630 nm	1.1 ns (25%)	6 ns (30%)	115 ns (45%)
AIS2-700 nm	1.4 ns (23%)	8 ns (30%)	127 ns (47%)
AIS 3-630 nm	0.8 ns (25%)	5 ns (37%)	105 ns (38%)
AIS 3-727 nm	1.3 ns (24%)	7 ns (32%)	120 ns (44%)

for AIS 1 to 120 ns for AIS 3 (Table 5.1). On the contrary, time constants for the shorter components decrease from 2 ns for AIS 1 to 0.8 ns for AIS 3 at the blue region of the deconvoluted emission spectra (Table 5.1). The PL life time constant due to antisite state decreases with increasing Ag ratio (156 ns to 120 ns), which suggests the decrement of antisite states that involve the recombination reaction. At the same time, recombination through S-states increases, and thereby PL lifetime of the shorter component decreases (2 to 0.8 ns) as the Ag concentration increases. This observation suggests that with increasing Ag concentration in AIS NCs, antisite defect (internal defect state) decreases, however, high-energy S-states increase. Therefore, the overall excited-state carrier dynamics of AIS NCs are governed by both S-states and intrinsic defect states. The excited-state carrier cooling, trapping, and recombination take place on the ultrafast time scale; therefore, these carrier dynamics cannot be addressed by nanosecond PL dynamics.^{8, 256, 257}

C. Femto Second Transient Absorption Studies.

Previously Burda and coworkers²⁴⁴ carried out transient absorption (TA) studies in sub-100 ps and nanosecond time domain on AIS NCs to study the excited dynamics in

ternary AIS NCs. However, they have never discussed the ultrafast carrier cooling dynamics, where S-states and intrinsic defect states are involved. To monitor the above ultrafast

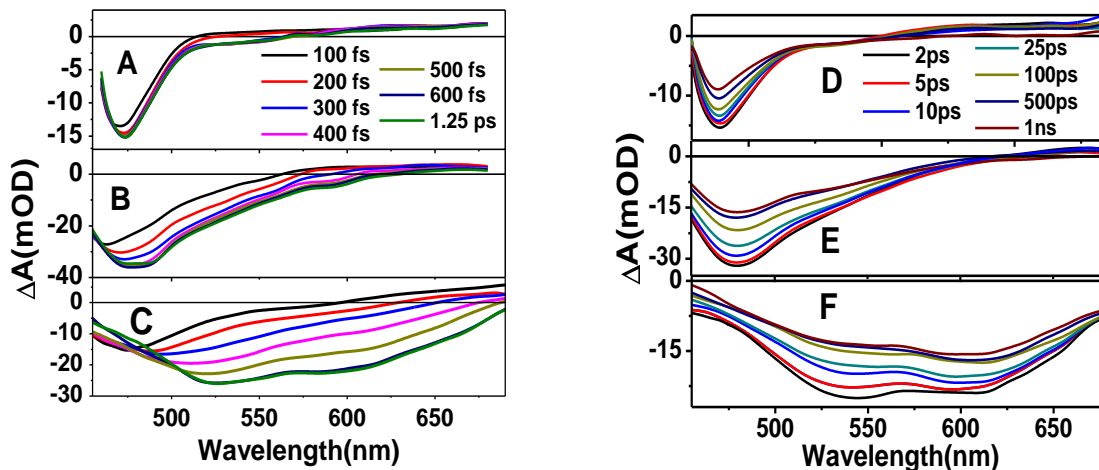


Figure 5.4. Left Panel. Early time scale (100fs to 1.5 ps) TA spectrum of (A) AIS 1 (B) AIS 2 and (C) AIS 3. Right panel. Longer time scale TA spectrum of (D) AIS 1 (E) AIS 2 and (F) AIS 3 after 400 nm laser excitation in the toluene solvent.

dynamic processes in different AIS NCs, we carried out femtosecond TA measurements. The TA spectrometer consists of a multi-pass Ti:sapphire laser system (CDP, Moscow, 800 nm, <100 fs, 1.2 mJ/pulse, and 1 kHz repetition rate) as femtosecond light source and Excipro pump-probe spectrometer (CDP, Moscow) as pump-probe measurement. The NCs dispersed in toluene solvents have been excited with 400 nm laser light, and the pump-induced population changes in excited state were measured in the visible region (450–800 nm). Figure 5.4 A, B and C illustrates the transient spectra at early time (100 fs to 1.25 ps) delay, and Figure 5.4 D,E and F shows the transient spectra at longer time (2 ps to 1 ns) delay for AIS 1, AIS 2, and AIS 3 NCs, respectively. Negative absorption band (bleach) has been observed for AIS 1 in 450–560 nm region peaking at ~475 nm, and a low-intensity positive absorption band appears in the red region (570–700 nm) of the spectra. The negative absorption band

can be attributed to the bleach due to the exciton, which exactly matches the ground-state excitonic absorption. Interestingly, TA spectra for AIS 2 (Figure 5.4 B,E) seems very different on both early and late time scales, which look further complicated for AIS 3 (Figure 5.4 C,F). In the case of AIS 2, initially at 100 fs the transient bleach appeared at ~460 nm, which finally red-shifted to 485 nm at 600 fs delay time (Figure 5.4 B). The spectral width of the bleach spectrum also increases with shifting the bleach maxima toward the red region up to 600 fs delay. It is clear from Figure 5.4 B and E that the bleach has a broad tail in the red region of the spectrum (520–600 nm). Again, in addition to the transient bleach, at early time the transient spectra (Figure 5.4 B) show small positive absorption in the 600–700 nm regions. The TA spectrum of AIS 3 has the bleach maxima in the blue region (475 nm) of the spectra with fwhm of ~62 nm at very early time delay (~100 fs). As the delay time of the probe pulse increases, the bleach maxima shifts toward the red region of the spectrum with the appearance of broad and dual bleach in 450–700 nm region. Shifting and broadening of bleach spectra saturates at ~2 ps time delay, where the bleach maxima appear at 535 nm with a hump at ~610 nm with fwhm ~160 nm. Previously Korgel and coworkers have observed shifting of excitonic bleach for CuInSe₂ NCs on early time scale, which they have attributed to cooling of hot carriers.²³³ Recently we have reported a notable spectral shift of 75 nm and considerable spectral broadening of 20 nm (from 110 nm in 50 fs to 130 nm in 1 ps) on an early time scale for CuInS₂ NCs, which we attributed to electron cooling processes through the manifolds of excited states. Thus, as the Ag concentration increases, excitonic bleach maxima move in the red region of the spectra, which is directly correlated with the degree of confinement; that is, as concentration of Ag increases in the NCs, the degree of confinement also reduces. Thus, unlike II–VI NCs, confinement is much weaker in AIS (similar to CIS);

as a result, electron can be populated in a wide range of manifold electronic states above the conduction band edge of AIS NCs. Again, the width of the transient bleach spectrum increases with Ag concentration from AIS 1 to AIS 3 (Figure 5.4). This observation clearly signifies that Ag plays a vital role in the confinement of the excited state. Now the appearance of red shifted transient bleach in addition to the ground-state bleach in AIS 3 NCs is really surprising (Figure 5.4), which becomes prominent in AIS 3 NCs (Figure 5.4). Unlike

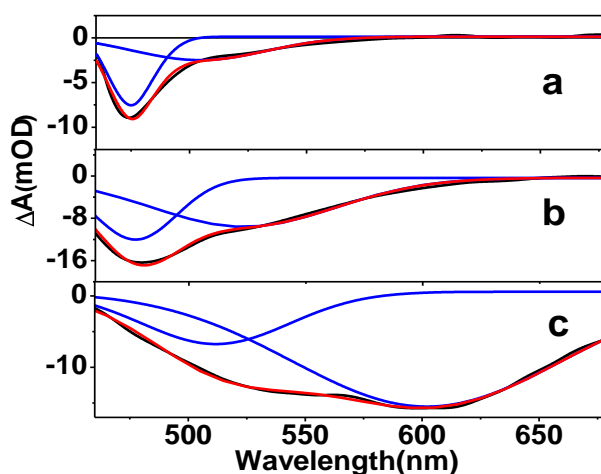


Figure 5.5: Deconvoluted TA spectrum of AIS 1, AIS 2, and AIS 3 NCs after 1 ns time delay.

CIS NCs dual bleaches have been observed in AIS NCs depending on the Ag concentrations. Now, to understand the nature of transition and dual nature of the bleach spectrum for all AIS NCs, the transient spectra at 2 ps time delay for AIS 1, AIS 2, and AIS 3 NCs samples have been deconvoluted and shown in Figure 5.5. It is interesting to see that with increasing Ag concentration the intensity of the red region band increases and has been summarized in Figure 5.5. Here, in all of the systems, bleach bands appearing in the blue region can be attributed to transient bleach due to excitonic absorption, while the bleach in the red region is due to mid S-states. Recently, Kamat and coworkers reported the generation of Cu state in CIS NCs at higher concentration Cu, which leads to the formation of separate bleach in the

spectrum of CIS NCs in addition to band-edge bleach.²⁴⁷ Similarly here also the bleach at the red region of the spectrum in AIS NCs is related to the S-states of Ag. Thus, in the present investigation, at higher Ag concentration the spectral and dynamical behaviour are completely different as compared with AIS with low Ag concentration, which has been revealed in subsequent sections.

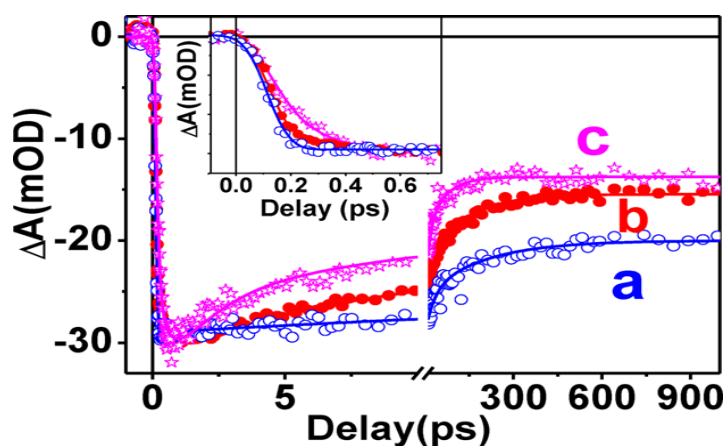


Figure 5.6: TA bleach recovery kinetics of (a) AIS 1 at 475 nm (b) AIS 2 at 485 nm and (c) AIS 3 at 535 nm after 400 nm laser excitation in toluene solvent. **Inset:** Bleach recovery kinetics at early time scale of a, b and c.

Excited-state charge carrier dynamics of AIS NCs with different Ag/In ratio were unravelled through monitoring the transient bleach kinetics at corresponding excitonic position for all AIS NCs, shown in Figure 5.6. Table 5.2 summarizes the multiexponential fitted time constants for all AIS NCs at their corresponding bleach maxima position. Here the growth kinetics at excitonic bleach position gives an idea of electron cooling dynamics through the manifold of electronic states above the CB edge of AIS NCs, while the bleach recovery kinetics suggests depopulation dynamics of charge carriers from the conduction band edge. The growth of the bleach was found to increase gradually from AIS 1 to AIS 3; that is, carrier cooling time from higher excited state to the conduction band edge increases

CHAPTER 5

from 100 fs for AIS 1 to 500 fs for AIS 3 (Table 5.2). Although the degree of confinement decreases for AIS 3, electron cooling time is still more compared to AIS 1. This might be due to 400 nm excitation in the case in which AIS 3 electrons are excited to upper excitonic state (as the excitonic bleach appears at 535 nm) as compared to AIS 1 (where the excitonic bleach appears at 475 nm). On the contrary, the bleach recovery kinetics becomes faster in AIS 3 as compared with AIS 1. We have already mentioned from steady-state

Table 5.2: Exponential fitted parameter for bleach recovery kinetics of AIS 1, AIS 2 and AIS 3 NCs at their bleach maxima.

System	$\tau_{1 \text{ growth}}$	τ_1	τ_2	τ_3	τ_4
AIS 1-475 nm	100 fs	9 ps (16%)	130 ps(14%)	>1 ns(70%)	
AIS 2-485 nm	240 fs	4 ps (23%)	70 ps(22%)	>1ns(55%)	
AIS 3-535 nm	500 fs	1.2 ps (26.8%)	15 ps (25.7%)	100 ps(8.5%)	>1ns (39%)

analysis that degree of confinement is much less in AIS 3 due to presence of higher concentration of Ag, where Ag-related S states are created in the NCs. Thus, the fast recovery components observed in AIS 3 (1.2 and 15 ps) can be assigned to the transition to Ag-related S-states and finally to antisite state (donor states), respectively (Table 5.2). These fast transition time constants are in good agreement with our previous report on CIS NCs²³ and also the report by Critchley and coworkers²⁵⁸ on the CIS/ZnS system. Interestingly with decreasing Ag concentration in AIS NCs, time constants related to S-states increase 4 ps for AIS 2 and 9 ps for AIS 1. The longer time constants in the bleach recovery kinetics in Table 5.2 can be attributed to the recombination dynamics of the charge carriers in the photoexcited AIS NCs. It is quite clear that just by monitoring the kinetic trace at excitonic wavelength for such defect-induced NCs the whole summary of charge carrier cooling dynamics and effects

of Ag concentration on different dynamical process cannot be extracted. To get better insight into the charge carrier cooling dynamics of such multinary NCs, we have compared the

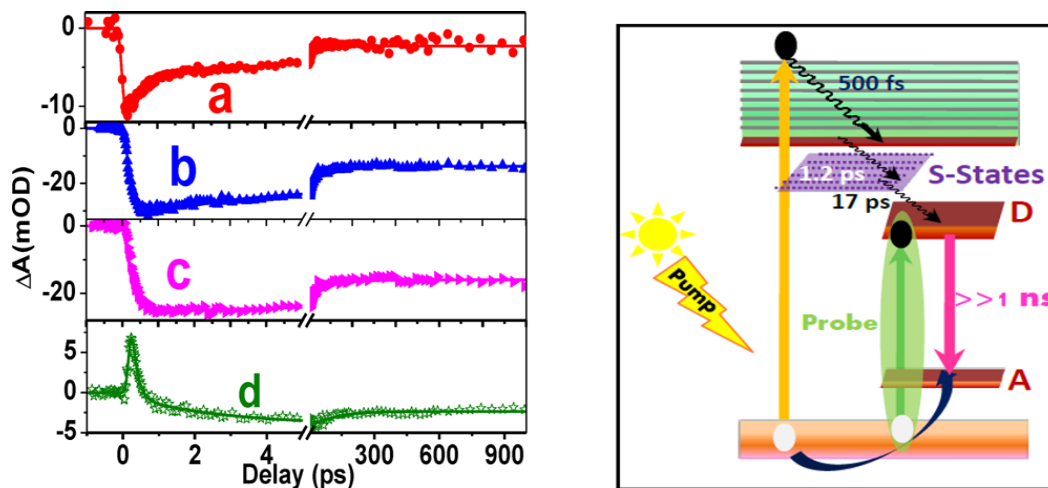


Figure 5.7. Left panel: TA bleach recovery kinetics of AIS 3 (a) at 455 nm (b) at 535 nm, (c) at 610 nm and (C) at 690 nm after 400 nm laser excitation in toluene solvent. **Right Panel:** Pictorial representation of electron transition from higher excited state to band edge, band edge to Ag related S-States followed by antisite state. Finally recombination takes place through donor acceptor pair.

transient bleach kinetics at above band edge, band edge, and below band edge (both S-states and antisite states) regions for AIS 3 NCs. Figure 5.7 compares the bleach recovery dynamics of AIS 3 at 455, 535, 610, and 690 nm. The bleach recovery kinetics of the above band-edge state at 455 nm can be fitted with pulse-width-limited growth ($\tau_g = <100$ fs), followed by a fast recovery of 500 fs (Table 5.3). Because in the present investigation the NCs are excited with 400 nm laser light, <100 fs growth component at 455 nm probe wavelength can be attributed to fast electron cooling to the probed state (above conduction band). On the contrary, the fast recovery component (500 fs) was due to depopulation of electron from the probed state. The bleach kinetics at 535 nm can be fitted with 500 fs growth component, followed by a fast recovery of $\tau_1 = 1.2$ ps (25%) and $\tau_2 = 15$ ps (28%) (Table 5.3). Here the

CHAPTER 5

slow growth component in the band-edge state (535 nm) is found to be 500 fs, which matches with the fast recovery component of the above band-edge state (i.e., at 455 nm) and has been

Table 5.3: Multiexponential Fitting Time Constants for the Bleach Kinetics of AIS 3 NCs at Different Wavelengths after Exciting the Sample at 400 nm.

λ_{probe}	Bi-exciton		Single exciton			
	$\tau_{1\text{growth}}$	$\tau_{2\text{ growth}}$	τ_1	τ_2	τ_3	τ_4
455 nm	<100 fs		500fs (52%)	10.5 ps (28%)	>1ns (20%)	
535 nm	500fs (100%)		1.2ps (25%)	15ps (28%)	100ps (5%)	>1ns (42%)
610 nm	500fs (92%)	1.2ps (8%)	15ps (25%)	120ps (14%)	>1ns (61%)	
690 nm	$\tau_{\text{growth}} < 100\text{fs}$, $\tau_{\text{decay}} \sim 150\text{ fs}$	1.2ps (85%)	17ps (15%)	70 ps (41%)	>1ns (59%)	

attributed to electron cooling to the band-edge state. At 535 nm (band-edge state) the fast recovery time constants like 1.2 and 15 ps can be assigned to transition from band-edge to S-states, followed by antisite donor state. Now, the third probing wavelength, that is, 610 nm, where transient bleach appears due to presence of S- states, can be fitted with bi-exponential growth with time constants of $\tau_{g1} = 500\text{ fs}$ (92%) and $\tau_{g2} = 1.2\text{ ps}$ (8%), followed by recovery with time constants of $\tau_1 = 15\text{ ps}$ (25%), $\tau_2 = 120\text{ ps}$ (14%), and $\tau_3 > 1\text{ ns}$ (61%) (Table 5.3). Here 500 fs can be attributed to population of electron from above conduction band-edge state to the band edge state and 1.2 ps component can be attributed to band edge state to the Ag-related S-states (right panel in Figure 5.7). Finally the transient kinetics at 690 nm can be fitted with additional positive growth (<100 fs), followed by a very fast decay (150 fs) and bi-exponential bleach growth (1.2 ps, 17 ps), which finally recovers bi-exponentially with time constants of 70 ps (41%) and >1 ns (59%) (Table 5.3). Such kinetics related to antisite state

carries two very significant information that are summarized as follows. First, the initial positive growth in <100 fs followed by very fast decay within 150 fs can be explained on the basis of probe induced bi-exciton mechanism. Previously, Kambhampati and co-workers have elucidated similar observation in CdSe NCs (at low pump fluence $\langle N \rangle < 0.5$) where state-specific laser pulse excitation pump-and probe pulse separately created two excitons that behave as bi-exciton and give the positive feature within the bleach signal.^{20, 33, 259} In the present investigation on 400 nm laser excitation, the pump places the electron in a much higher state than the antisite state, which results in an excited exciton; however, the probe created a ground-state exciton in the antisite state and together they behave like an excited bi-exciton and give the positive feature.³³ The excited exciton relaxes to antisite state by releasing excess energy (phonons) and forms a ground-state bi-exciton. Because the ground-state bi-exciton has lower binding energy as compared to the excited-state bi-exciton, the positive feature disappears as the excited electron relaxes to the lower state. Recently, Ruhman and co-workers²⁶⁰ made a similar observation in PbSe nanocrystals through three pulse femtosecond spectroscopy. Of late we have also demonstrated a clear picture of such probe-induced bi-exciton feature in CuInS₂ NCs at low pump fluence as well as varying pump fluence. Here, in AIS NCs in the early time delay, the positive absorption within the bleach signal observed in the red region of the spectrum, which is associated with the antisite state, can also be explained in similar fashion. In addition to that, the dependence of such bi-exciton feature on pump fluence as well as Ag-to In ratio has also been precisely analyzed, which has been depicted in the consequent sections.

In regards to the second feature, it is really surprising to observe the extremely slow bi-exponential growth components in the kinetics of the sub-band-edge state, that is, at the antisite state (at 690 nm for AIS 3 in Figure 5.7 d), which nicely matches with the decay

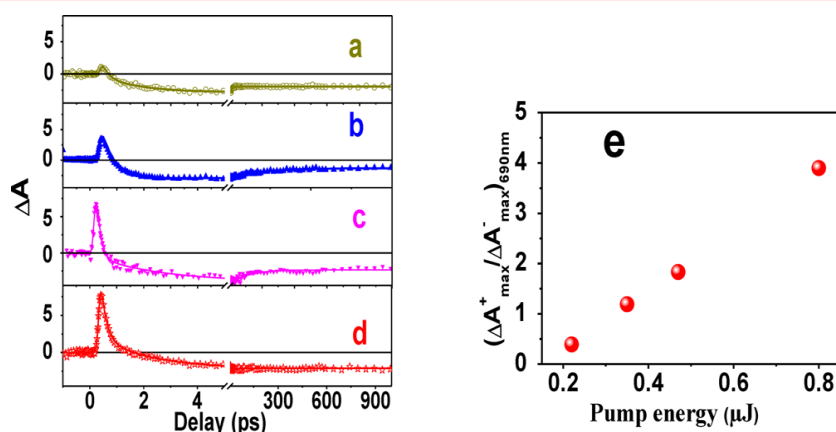


Figure 5.8: The bi-exciton dynamics of the of the AIS 3 at the 690 nm in pump energy of (a) 0.2 μJ (b) 0.35 μJ (c) 0.45 μJ and (d) 0.8 μJ . e. The graphical representation of change of $\Delta A_{\max}^+ / \Delta A_{\max}^-$ with changing the pump energy.

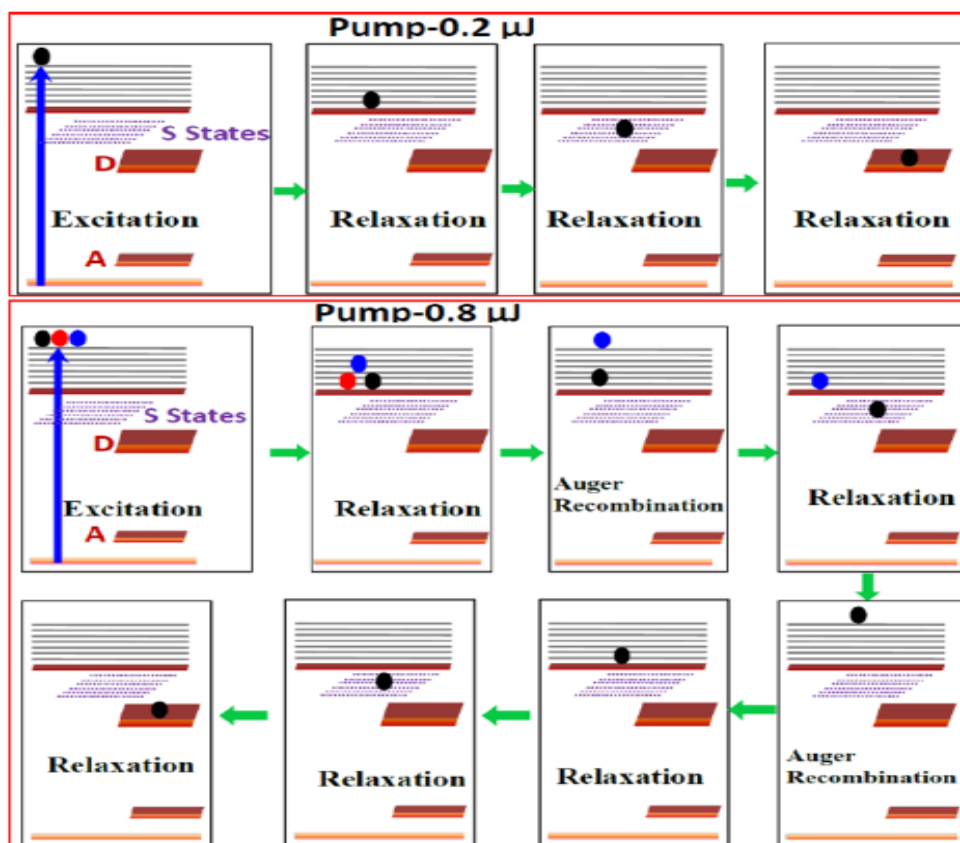
components of the band-edge bleach kinetics. Such observation validates our explanation of existence and active participation of S-states just below the band-edge state in bi-exciton dynamics (right panel in Figure 5.7), which also acts as an electron storage center. Initially the electron moves relatively fast to this state (in 1.5 ps) after 400 nm laser excitation where electron gets stored and finally the S-state releases the electron very slowly to antisite state (in 17 ps). The extremely slow recovery component (>1 ns) is due to recombination of electron in the antisite state and hole in the acceptor state (Figure 5.7d). Previous ultrafast study of such AIS system carried out by Burda and coworkers also reveals the existence of such surface-related states just below the band-edge state, which can store electrons. Thus, the existence of such shallow surface related states has an enormous implication in electron cooling dynamics to antisite state, which actually governs the bi-exciton dynamics of such NCs. To have a better idea of S-states as well as antisite state on electron cooling and trapping dynamics, we have carried out both pump fluency and Ag/In ratio-dependent kinetic analysis at the antisite state of AIS NCs.

Table 5.4. The exponential fitted parameter of single and bi-exciton dynamics of AIS 3 at 690 nm at different Laser fluency.

System	Bi-exciton	Single -exciton
AIS 3-690 nm-0.2 μJ	$\tau_{\text{growth}} < 100\text{fs}$ $\tau_{\text{decay}} = 150\text{fs}$	$\tau_{\text{growth}} = 0.5 \text{ ps}(85\%), 2\text{ps} (15\%)$ $\tau_{\text{decay}} = 12 \text{ ps}(34\%), >1\text{ns}(66\%)$
AIS 3-690 nm-0.35 μJ	$\tau_{\text{growth}} < 100\text{fs}$ $\tau_{\text{decay}} = 150\text{fs}$	$\tau_{\text{growth}} = 1 \text{ ps}(87\%), 10 \text{ ps}(13\%)$ $\tau_{\text{decay}} = 60 \text{ ps} (48\%), >1\text{ns}(52\%)$
AIS 3-690 nm-0.45 μJ	$\tau_{\text{growth}} < 100\text{fs}$ $\tau_{\text{decay}} = 150\text{fs}$	$\tau_{\text{growth}} = 1.2 \text{ ps} (85\%), 17 \text{ ps} (15\%)$ $\tau_{\text{decay}} = 80 \text{ ps} (41\%), >1\text{ns}(59\%)$
AIS 3-690 nm-0.8 μJ	$\tau_{\text{growth}} < 100\text{fs}$ $\tau_{\text{decay}} = 150\text{fs}$	$\tau_{\text{growth}} = 1.8 \text{ ps}(86\%), 100\text{ps}(14\%),$ $\tau_{\text{decay}} = \gg 1\text{ns}$

Figure 5.8 (left panel) depicts the kinetic traces of AIS 3 NCs at 690 nm with varying laser pump energy ~ 0.2 to $0.8 \mu\text{J}$. It can be clearly seen that as the pump energy increases the amplitude of the positive absorption in the early time delay increases, which indicates that bi-exciton binding energy also is enhanced. However, the ultrafast growth ($< 100 \text{ fs}$) and the fast decay ($\sim 150 \text{ fs}$) component do not change with pump intensity (Table 5.4). On the contrary, the value of bleach growth increases with pump energy. The multiexponential fitted time constants for all kinetics of AIS 3 NC at 690 nm for different laser intensities have been summarized in Table 5.4. Although the bleach growth can be fitted bi-exponentially with 0.5 (85%) and 2 ps (15%) for pump energy $0.2 \mu\text{J}$ and 1 ps (87%) and 10 ps (13%) time constants for pump energy $0.35 \mu\text{J}$, unusual slow bi-exponential growth of 1.8 ps (86%) and 100 ps (14%) has been observed for pump energy of $0.8 \mu\text{J}$. As the bleach growth reflects the electron cooling from higher excited state to lower excited state, the experimental result signifies that electron cooling time to antisite state is enhanced for AIS 3 NCs when laser

fluency increases. Previously Mohammed and co-workers²⁶¹ observed the phenomenon of increased carrier cooling time for higher $\langle N \rangle$ value in PbS NCs. To unravel the slow electron cooling with laser intensity in terms of bi-exciton binding energy, we plot the positive absorption maxima (ΔA^+_{\max}) to negative absorption maxima (ΔA^-_{\max}) as a function of pump



Scheme 5.1. Pictorial representation of carrier cooling in antisite state with different pump energy~ 0.2 and 0.8 μJ in AIS 3 NCs. The electron cooling slows down with increasing the pump energy.

energy for AIS 3 NC (Figure 5.8). Because the value of $\Delta A^+_{\max}/\Delta A^-_{\max}$ increases with pump energy, the bi-exciton binding energy also increases. In the present study, at higher pump fluency recombine through the Augur process by releasing the extra energy as phonons, which can further re-excite the carriers to higher energy state, which results in slow electron

cooling with progressive increase in binding energy. In Scheme 5.1 we have demonstrated the mechanism of carrier cooling with lower (pump energy = 0.2 μJ) and higher (pump energy = 0.8 μJ) laser intensity. At lower laser intensity, for example, a single exciton is generated, and it relaxes through multiple states like band-edge, S-states, and, finally, antisite (donor) state bi/multiexcitons are generated that have increased binding energy. (Scheme 5.1). However, on increasing laser intensity, multiexcitons are generated, followed by Auger recombination; as a result, the electron can be re-excited to higher states and finally go for cooling processes involving band-edge, S-states, and, finally, antisite state (Scheme 5.1). The most interesting observation in the present investigation is that S-states are acting like electron storage center that facilitate both slow electron cooling and efficient bi-exciton generation (Scheme 5.1).

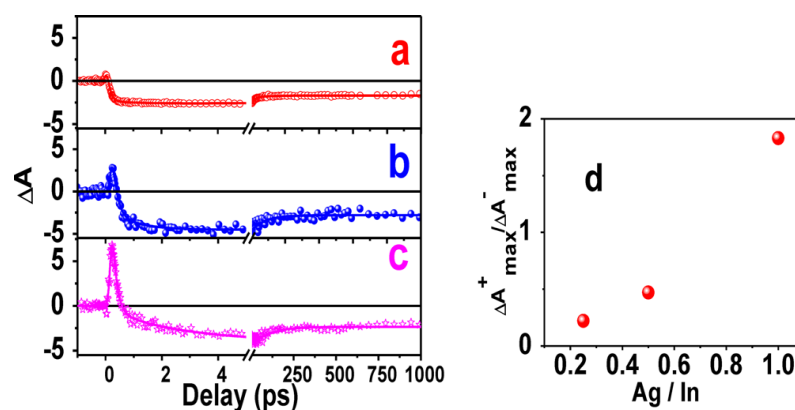


Figure 5.9: The bi-exciton dynamics of (a) AIS 1 at 520 nm (b) AIS 2 at 600 nm and (c) AIS 3 at 690 nm with pump energy 0.45 μJ . d) The graphical representation of change of $\Delta A_{\max}^+ / \Delta A_{\max}^-$ with changing the ratio of Ag and In.

The appearance of a biexcitonic feature in the AIS NC at low pump fluence in the red region of the spectrum is another major endeavour of the present investigation. The observation becomes more interesting when we analyze the bi-excitonic feature in terms of

CHAPTER 5

composition variation of Ag and In. Figure 5.9 illustrates the kinetic traces of AIS 1, AIS 2, and AIS 3 NCs at 520, 600, and 690 nm, respectively, with the same laser energy 0.45 μJ . The early time dynamics clearly show that the amplitude of positive absorption increases as the Ag/In ratio increases. The bi-exciton binding energy is also found to increase as the Ag/In ratio increases, as can be seen from the graphical representation of $(\Delta A^+_{\text{max}}/\Delta A^-_{\text{max}})$ with respect to Ag/In ratio for a fixed pump energy (Figure 5.9 d). Although in the early time delay growth and fast decay of all positive absorption can be fitted with <100 fs and ~ 150 fs time scale, the bleach growth component varies. The bleach growth can be bi-exponentially fitted and is enhanced from 0.4 ps (90%) and 8.1 ps (10%) in AIS 1 to 1.5 (85%) and 17 ps (15%) in AIS 3. (Fitted time constants of the kinetics are summarized in Table 5.5.) In the previous section we have discussed that the bleach growth of such kinetic traces reflects the

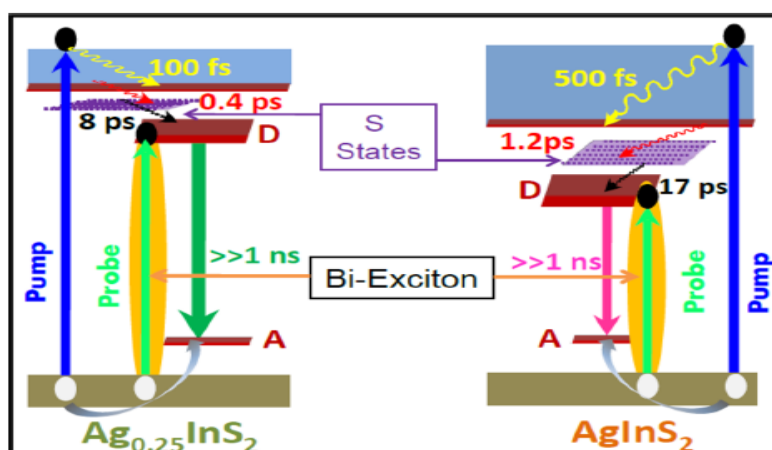
Table 5.5. The exponential fitted parameter of single and bi-exciton dynamics of AIS 1, AIS 2 and AIS 3 with laser energy ~ 0.45 μJ .

System	Bi-exciton	Single-exciton
AIS 1-520nm	$\tau_{\text{growth}} < 100\text{fs}$	$\tau_{\text{growth}} = 0.4$ ps(90%), 8.1 ps (10%)
	$\tau_{\text{decay}} = 150\text{fs}$	$\tau_{\text{decay}} = 20$ ps(35%), $>1\text{ns}$
AIS 2-600nm	$\tau_{\text{growth}} < 100\text{fs}$	$\tau_{\text{growth}} = 1$ ps(88%), 12 ps(12%)
	$\tau_{\text{decay}} = 150\text{fs}$	$\tau_{\text{decay}} = 80$ ps(38%), $>1\text{ns}$
AIS 3-690nm	$\tau_{\text{growth}} < 100\text{fs}$	$\tau_{\text{growth}} = 1.2$ ps, 17 ps
	$\tau_{\text{decay}} = 150\text{fs}$	$\tau_{\text{decay}} = 100$ ps, $>1\text{ns}$

electron cooling time to the antisite states. Thus, as the Ag/In ratio increases the electron cooling time to antisite state increases, which is one of the biggest findings of the present work. As conferred in the previous sections, S-states increase as the Ag/In ratio increases

CHAPTER 5

(i.e., AIS 1 to AIS 3). The relative energy difference between band-edge state and antisite state for different Ag/In ratio was calculated approximately by using the shift in bleach maxima and bi-excitonic bleach position in the red region of the spectrum. For example, in the case of AIS 1 the bleach maxima appears at 470 nm and the bi-excitonic feature appears at 520 nm. Therefore, the difference between band-edge and antisite state is ~ 0.26 eV. Similarly the difference between band-edge and antisite state was calculated for AIS 2 and AIS 3 to be ~ 0.5 and ~ 0.61 eV, respectively. Thus, it is clearly seen that the difference between band-edge state and donor state increases with Ag/In ratio. Now it can be easily understood that the reason for slowing down of electron cooling from 0.4 ps and 8.1 ps in



Scheme 5.2: Schematic representation of electron cooling and bi-excitonic feature of AIS 1 and AIS 3. Longer electron cooling time in antisite state and higher bi-excitonic feature are shown in AIS 3 than AIS 1.

AIS 1 to 1.5 and 17 ps in AIS 3 is due to the increase in energy gap between band-edge and antisite states in addition to the presence of S-states (Scheme 5.2), which act as electron storage centers. Slowing down of the second growth component in AIS 3 as compared with

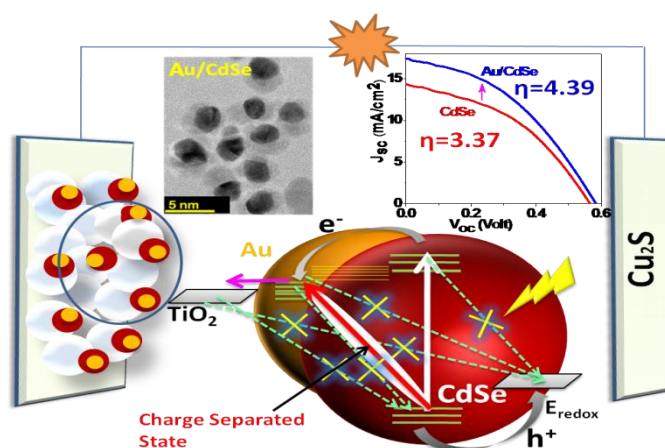
AIS 1 (i.e., 17 ps with respect to 8.1 ps) is further enhanced due to storing of electrons in S-states, where the number of such states is higher in AIS 3 (Scheme 5.2).

5.3. Conclusion:

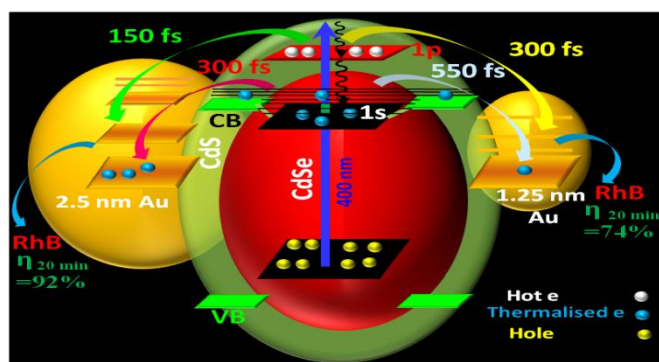
In conclusion, a series of AgInS₂ (AIS) with different stoichiometric ratio of Ag and In have been synthesized, and detailed spectroscopic investigations have been carried out by using both steady-state and time-resolved absorption and emission techniques. The excitonic absorption peak was found to become broad with increasing Ag/In ratio in AIS NCs. Steady-state PL spectra indicate that two types of emission are originated from AIS NCs, which are due to Ag-related sub-band gap defect states and antisite states (donor states), depending on the stoichiometric ratio of Ag and In in AIS NCs. PL intensity due to Ag-related sub-band gap defect states increases and antisite states decreases with increasing Ag concentration in AIS NCs. Femtosecond TA studies have been carried out to monitor charge carrier dynamics in AIS QDs, which involve multiple states like higher excited state, conduction band-edge, S-states, and antisite (donor) states. Transient absorption spectra were found to dominate by bleach (negative absorption) due to excitonic absorption, S-states, and antisite (donor) states. The probe-induced bi-excitonic feature originated from the antisite state has been observed in AIS NCs even at low pump energy of $\sim 0.2 \mu\text{J}$. Carrier cooling time constant was found to increase drastically with pump energy and concentration of Ag in AIS NCs and was found to facilitate drastically the efficiency of bi-exciton generation with higher Ag concentration. To the best of our knowledge, for the first time we are reporting ultrafast charge carrier dynamics of AIS NCs with different stoichiometry ratio of Ag and In, which involve different states like band-edge, S-states, and antisite states. Our experimental observation clearly suggests that higher concentration of Ag in AIS NCs can give better efficiency of bi-exciton generation, which, in turn, can help us to design nontoxic higher efficient solar cell.

CHAPTER-6

CORRELATION OF ENHANCED PHOTOVOLTAIC AND PHOTOCATALYTIC EFFICIENCY OF THE METAL-SEMICONDUCTOR NANOHYBRID MATERIALS WITH ULTRAFAST SPECTROSCOPY.



Communicated



Nanoscale, 2017, 9, 9723-9731

6.1. Introduction.

Hybrid nanostructured materials composed of metal and semiconductor, a promising material for catalysis and solar energy conversion due to excellent amalgamation of electronic and optical properties in a heterostructure.^{91, 95, 133, 137, 262-264} These hybrid materials can harvest the solar light and convert the photon energy to a long lived charge separated state in a single architecture.^{92, 265} Due to generation of charge separated state after photo excitation in metal semiconductor hetero-interface, these hybrid nanostructures are novel material for next generation solar cell, hydrogen generation, many electronic and optical devices etc.^{92, 266-270} Since last decade water splitting and dye degradation by Co-CdSe/CdS,²⁷¹ Au-CdSe,²⁷² Au-CdSe/CdS,⁹² and Pt-CdS²⁷³ hetero-structures have been extensively demonstrated in the literature. Among many hetero-structures, the nano-hybrid made out of CdSe and CdS QDs are most attractive materials due to their strong binding with Au NPs and also their photo-catalytic behaviour is driven by solar light radiation.⁸⁸ Surface Plasmon of metal nanoparticles can enhance the photo-catalytic and photo-voltaic efficiency of the semiconductor-metal hetero-structures by either making the charge separated states or enhancing the local field by increasing the optical response towards solar radiation.²⁷⁴⁻²⁷⁷ In the hetero-structure as the metal and semiconductor domains are spatially connected to each other, the optical properties changes completely with formation of unique material as compared to the individual materials.²⁷⁸⁻²⁸⁰ Due to spatial contact of the metal and semiconductor the magnetic and nonlinear optical properties also are found to be drastically modified.²⁸¹ Banin and his co-workers^{278, 282} extensively reported how the electronic configuration and optical properties have been changed in the hetero-structures made out of metal and semiconductor materials.

It has been reported in the literature that due to strong exciton-plasmon interaction in the hetero-structure confinement of semi-conductor materials are changed, where photo-excited electrons are transferred from semiconductor domain to metal domain in sub picoseconds time scale.^{87, 135} As a result Auger recombination and multi-exciton generation processes are minimised in the metal semiconductor nano-hybrid (MHM).²⁸³ Zamkov & co-workers^{87, 91} demonstrated the suppression of both exciton and plasmon bands in the hetero-structure due to strong Exciton-Plasmon coupling. They have also reported higher charge separation in ZnSe@CdS{Pt} hetero-structure as compared to ZnSe@CdS core shell through ultrafast transient absorption spectroscopy and demonstrated their superior photo-catalytic behaviour.²⁸⁴ Ultrafast electron transfer from the photo-excited semiconductor rod to the Au tip and furthermore plasmonic hot electron transfer from the Au tip to the CB of the semiconductor rod has been reported by Lian and co-workers.^{93, 94} Park and co-workers²⁶⁹ described hot carrier driven photo-catalytic reactions in Pt–CdSe–Pt nano-dumbbells and suggested electron transfer from photo excited CdSe to Pt metal in ultrafast time scale. Recently we have also demonstrated interfacial electron and hole transfer dynamics in CdSe{Au}-BrPGR tri composite system where photo-excited electron transfer from CdSe QD to Au NP and the hole transfer from CdSe to Br-PGR were found to be 270 and 500 fs, respectively.⁹⁰ It is reported that hot electrons in nanocrystals of semiconductors, metals, and their hetero-structures can induce energetically difficult chemical reactions.^{49, 285-290} Excess energy of hot electrons can lower the energy barriers of the electron transfer reaction which eventually facilitate charge separation reaction and often can be faster than electron relaxation time.²⁸⁷⁻²⁸⁹ Tang and co-workers²⁹¹ reported hot and thermalized electron transfer reaction in CdSe/Au and CdSe/Pt Nanorods through intensity dependence ultrafast transient absorption however, the time components of the electron transfer reactions were not

discussed. To make efficient practical application out of these hetero-structure materials, it's important to understand the mechanism and time scale of both hot and thermalized electron transfer reaction in these hetero-structures.

Exceeding 12 % efficiency of the QDSC have been reported by Zhong and his co-worker.¹⁹⁴ But some of the main limitations of the QDSC are the electron hole recombination within the QD and/or at the TiO₂/QD/electrolyte interface.^{107, 191} It has been realized that the power conversion efficiency (PCE) of the QDSC can be enhanced drastically by the reducing the exciton recombination. It is reported in literature that exciton recombination can be reduced by the spatial attachment of the metal NP on the QDs.^{95, 291} In literature it is well established that after photo excitation fast electron transfer is occurred from QDs to metal NP, hence the long lived charge separated state can be generated within the NHM, where the electron is localised in metal NP and hole is localised in the semiconductor.^{89, 90, 135} So we can expect that more charge carriers will be available for current generation in solar cell where NHM can be used as photo-sensitizer in QDSC. Ultrafast electron transfer from QDs to metal NP reduces the Auger recombination of the QDs²⁸³, can ideally improves photo-conversion efficiency of the solar cell. The low quality loading and trap state (surface) of the QDs also limit the power conversion efficiency.^{107, 191} Therefore it is essential to passivate the QDs by the large band gap material which reduces the trap state.^{201, 292} The passivated layer reduces the recombination between electron in TiO₂ and hole in QDs by making an energy barrier and enhances the PCE.^{197, 206, 293} Many reports are available in literature,^{92, 266, 269, 270} where the enhancement of photo catalytic efficiency of semiconductor-metal nano-hybrid material is found to be much higher as compared to pure semiconductor. However till date no report is available in literature, where photo-conversion efficiency of nano-hybrid material ever reported and role of metal particles are demonstrated by any spectroscopic technique.

CHAPTER 6

In this chapter, we are reporting the significant improvement in the power conversion efficiency of the CdSe QDs after formation of Au/CdSe NHM and enhancement of photocatalytic efficiency of CdSe@CdS{Au} nanohybrid material. We synthesised the Au/CdSe and CdSe@CdS{Au} nanohybrid material (NHM) and characterised the material by HR-TEM and optical studies. The device has been made in the assembly of FTO/TiO₂/AuCdSe/CdS/ZnS/Cu₂S and measured the PCE under one sun illumination by using polysulfide electrolyte. The measured PCE for the Au/CdSe is 4.39% which is ~30% higher compared to the mother CdSe. The tremendous enhancement of PCE in Au/CdSe NHM compared to CdSe QDs has been discussed in detail by the time resolved absorption, luminescence and EIS studies. From steady state, the broad absorption upto 800 nm after Au growth on CdSe QDs plays a significant role in the enhancement of efficiency. The steady state and time resolved luminescence studies reveal the fast electron transfer from CdSe to Au NP. Finally by TA study we have shown the ultrafast electron transfer followed by the charge separated state formation within the NHM correlated with the enhancement of the PCE of the solar cell. By EIS we have measured the higher recombination resistance of Au/CdSe NHM compared to CdSe QDs and correlated with the enhancement of PCE by the NHM. Additionally we investigated the inner mechanism of both hot and thermalized interfacial electron transfer dynamics in CdSe@CdS{Au} nanohybrid material and the effect of particle sizes of metal nanoparticles in the hetero-structure. We have synthesized CdSe@CdS quasi type II core-shell and impregnated two different sizes Au NPs on the core-shell with formation of CdSe@CdS{Au}-1 and CdSe@CdS{Au}-2 hetero-structures. Steady state optical absorption studies suggest Au NP form charge transfer complex with CdSe@CdS core-shell. CdSe@CdS core-shell form quasi type II structure where electrons are delocalized in the conduction band of both CdSe core and CdS shell QDs however, holes

are localized in the valence band of CdSe core. Both the time-resolved absorption and emission studies suggest that in CdSe@CdS{Au} HS the photo excited electrons are transferred from the semiconductor domain to the metal domain. Both hot and thermalized electron transfer from photo-excited CdSe@CdS core-shell to Au NP dynamics were monitored and effect of metal NP size has been discussed. Charge separation was found to be facilitated with bigger size Au NPs which was reconfirmed by photo-degradation of rhodamin B (RhB) in presence of the hetero-structures under illumination of visible light radiation. Effect of hot electron in the hetero-structure on photo-catalytic degradation was discussed in the present studies. Other than this, the electron hole decoupling in different thickness of shell in CdSe@CdS core shell has also been investigated in absence and presence of Au NP by TA spectroscopy. The shell thickness dependent charge separated state formation and life time of the CS have been investigated by the TA spectra.

6.2 Results and Discussions.

6.2.1 Enhancement of Power Conversion Efficiency (PCE) of CdSe{Au} QDSC.

A. Characterization and Optical Properties of CdSe{Au} HS:

The CdSe{Au} NHM were synthesised after following the reported method in literature^{127, 133} and discussed as in chapter 2. The synthesized CdSe{Au} NHMs were characterised by HR-TEM and steady state absorption spectroscopy as shown in figure 6.1. Clear growth of the Au NP on the surface of CdSe QDs has been shown in HRTEM images (Figure 6.1A). The dark patch in the CdSe{Au} NHM particle represents the Au NP on lighter shaded CdSe QD surface. The size of the Au NP on the 3.5 nm CdSe has been determined to be 2.65 nm. After determining the morphology of the particles the optical properties of the particles have also been monitored. Figure 6.1B (a) shows the steady state optical absorption spectra of the CdSe QDs, which has been changed after growth of the Au

NP as seen in Figure 6.1B (b). It's interesting to see that the first excitonic absorption peak at 563 nm for CdSe QD is blue shifted to 556 nm after growing Au NP on it due to little bit distortion of CdSe QDs after Au growth. Optical absorption spectrum of CdSe{Au} NHM

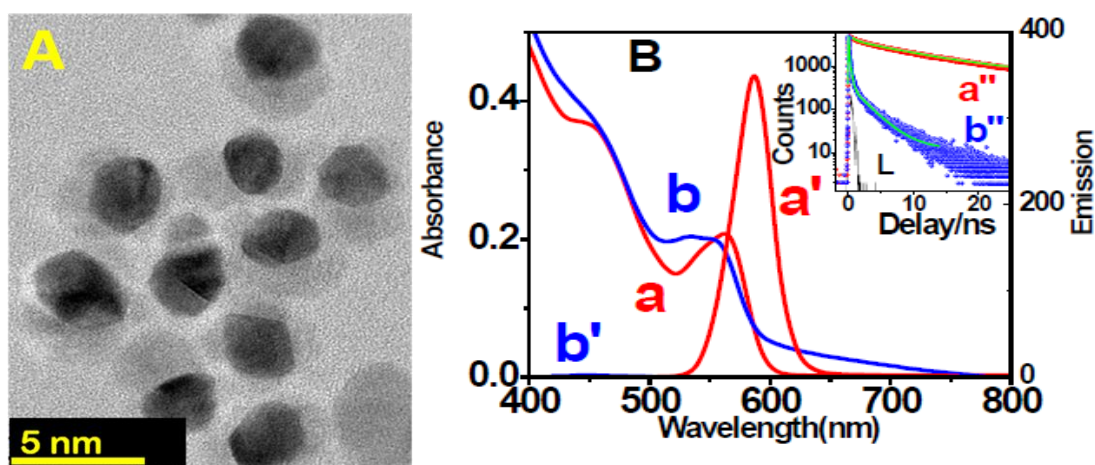


Figure 6.1-A: HR-TEM image of CdSe NH material. **B:** Steady state optical absorption and luminescence spectra of CdSe quantum dot (a and a') and CdSe²⁹⁴ HS (b and b') in chloroform. **In Inset.** The luminescence decay traces of (a'') CdSe and (b'') CdSe{Au} NH at 586 nm after 406 nm excitation. (**L is lamp profile**)

becomes broad as compared to the QDs due to mixing of excitonic states of CdSe QDs and plasmonic states of Au NPs.^{94, 95} Interestingly, broad absorption up to 760 nm is shown by the CdSe{Au} NHM, but there is no absorption at this red region in case of pure CdSe QDs. The broad absorption band can be attributed to the formation of charge transfer complex between VB of CdSe QD to Fermi level of Au NP.^{87, 90} Figure 6.1B (a') represents the photo-luminescence spectra of CdSe QDs which has very high quantum yield (23% QY). It's interesting to see that photo-luminescence of CdSe{Au} NHM drastically reduced due to growth of Au NP on CdSe QDs as shown in Fig 6.1B (b'). This photo-luminescence quenching can be attributed to excited electron transfer from CdSe QDs to Au NP in

CdSe{Au} NHM.^{87, 93, 283}

To investigate the charge transfer dynamics between CdSe QDs and Au NP in CdSe{Au} NHM time-resolved luminescence studies have been carried out after exciting the samples at 406 nm and monitoring at 586 nm and compared with pure CdSe QDs. Figure 6.1B(a'') shows the luminescence decay trace of the CdSe QDs, which can be fitted multi-exponentially with time constants $\tau_1 = 1.5 (\pm 0.05)$ ns (35%) and $\tau_2 = 17.5 (\pm 0.5)$ ns (65%)

Table 6.1: Multi exponential fitted parameter of luminescence decay traces of CdSe and CdSe/Au after exciting the samples at 406 nm and monitoring at 586 nm.

System	τ_1	τ_2	τ_{avg}
CdSe	1.5 ns (35%)	17.5 ns (65%)	11.37 ns
CdSe/Au	0.29 ns (86%)	3.65 ns (15%)	0.71 ns

with $\tau_{avg} = 11.37 (\pm 0.5)$ ns. However the luminescence trace (Fig 6.1B(b'')) found to decay much faster in CdSe{Au} NHM, which can be fitted multi-exponentially with time constants $\tau_1 = 0.29 (\pm 0.01)$ ns (86%) and $\tau_2 = 3.65 (\pm 0.16)$ ns (14%) with $\tau_{avg} = 0.71 (\pm 0.05)$ ns. Depleted luminescence intensity and fast emission decay kinetics in CdSe{Au} NHM suggest fast electron transfer from semiconductor domain (CdSe QD) to metal domain (Au NP),^{51, 90} where the hole is localized in CdSe QDs and electron is localized in metal NP forming a charge separated state.

B. Transient Absorption Study of CdSe{Au} HS:

To monitor the charge transfer processes in CdSe{Au} NHM femto-second transient absorption spectroscopic measurements have been carried out for both CdSe QDs and CdSe{Au} NHM after exciting the samples at 400 nm laser pulse. Figure 6.2 a and b show the TA spectra of CdSe QDs and CdSe{Au} NHM respectively at different time delay. The TA spectra shows a broad negative absorption band (480–600 nm region) peaking at 558 nm

which matches well with the optical absorption spectrum of CdSe QDs (Figure 6.1B, a) and can be attributed to bleach due to 1st exciton of CdSe QDs. In addition to that a short-lived

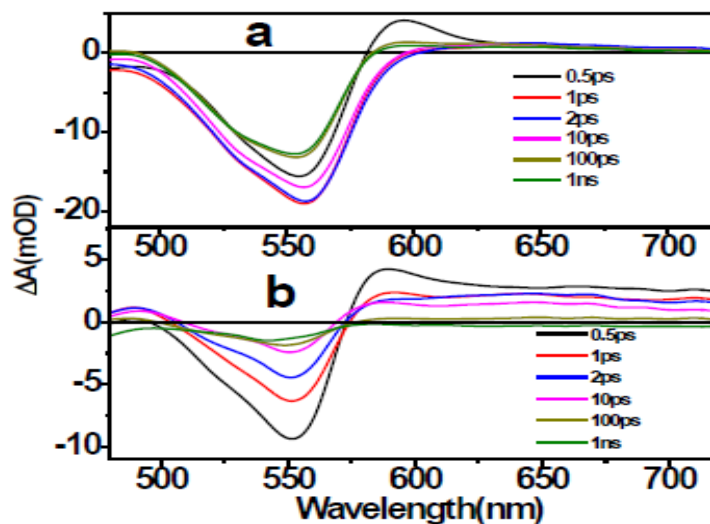


Figure 6.2: TA spectrum of (a) CdSe quantum dot and (b) CdSe{Au} HS at different time delay on the film after exciting the samples at 400 nm.

positive absorption band peaking at 580 nm can be attributed to bi-excitonic feature and low intensity broad positive absorption band beyond 600 nm signify the presence of minimum surface defect states in CdSe QDs. Figure 6.2 A (b) shows the TA spectra of CdSe{Au} NHM at different time delay. Interestingly, TA spectrum of the NHM looks very different as compared to CdSe QD (Figure 6.2A a). First excitonic peak for CdSe QD in CdSe{Au} NHM found to appear at 553 nm (blue shifted) which matches pretty well with ground state absorption. However no separate bleach was observed for Au NP in CdSe{Au} NHM spectrum due to small size of Au NP. Earlier Zamkov et al.^{87, 51} and we²⁹ have also reported suppression of surface plasmon of Au NP in CdS{Au} NHM and CdSe{Au} NHM respectively. Due to transfer of photo-excited electrons from semiconductor domain to metal domain electron density in the Fermi level of Au NP increases which causes the broad

absorption in the visible region of TA spectra of CdSe{Au} NHM.^{87, 90}

To explain the effect of Au growth on CdSe QD surface more elaborately, it is very important to investigate excited state dynamics of the CdSe{Au} NHM. To monitor the charge transfer and charge separation between Au and CdSe QDs, we have probed the kinetics at key wavelengths in the above systems. Figure 6.3 (a) shows the bleach kinetics of CdSe QDs at 560 nm, where the growth of bleach can be fitted bi-exponentially with time constants $\tau_1 < 100$ fs (85%) and $\tau_2 = 600$ fs (15%). Second growth component (600 fs) can be attributed to carrier cooling time from upper excitonic states to the band edge of first exciton

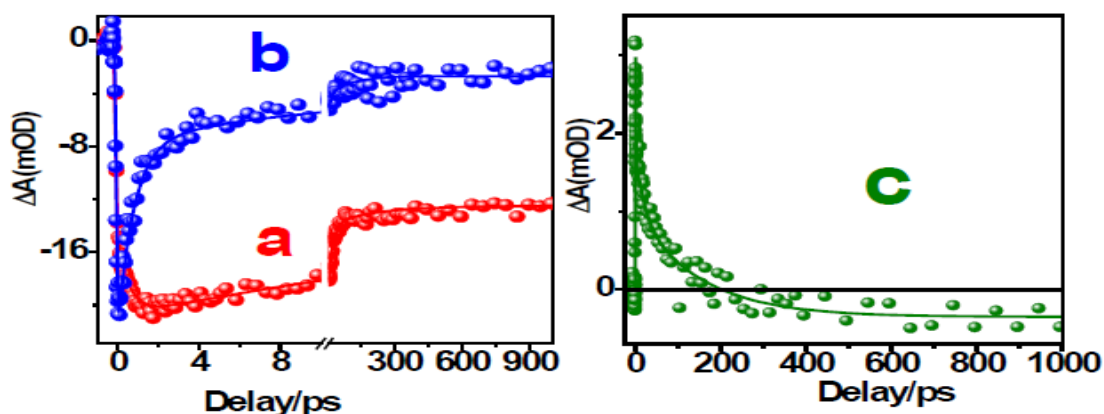


Figure 6.3: The decay kinetics of (a) CdSe quantum dot at 560 nm, (b) CdSe{Au} HS at 552 nm and (c) CdSe{Au} HS at 650 nm after exciting the samples at 400 nm.

state. While the bleach recovery kinetics can be fitted tri-exponentially with time components of $\tau_1 = 20$ ps (-35%), $\tau_2 = 200$ ps (-5%) and $\tau_3 = >1$ ns (-60%) where the fast component is attributed to trapping of carriers and longer components are due to slow exciton recombination.^{8, 257} On the other hand the bleach kinetics of CdSe{Au} NHM is dramatically changed as compared to CdSe QDs as shown in figure 6.3 (b). It's interesting to see that unlike Figure 6.3 (b) there is no slow growth component in the transient bleach and is pulse-

CHAPTER 6

width limited. This observation implies that transfer of hot electron from upper excitonic states of CdSe QD to the Fermi level of Au NP.⁹⁰ Now the bleach recovery kinetics can be fitted tri exponentially with time components $\tau_1 = 450$ fs (60%), $\tau_2 = 10$ ps (25%) and $\tau_3 = >1$ ns (15%) where the 450 fs component implies the electron transfer time constant from CdSe QD to Au NP in NHM.⁹⁰

In the transient absorption spectra CdSe{Au} NHM after photo-excitation of 400 nm laser pulse a broad positive absorption band was observed which attributed to transient absorption due to electron in the interface of semiconductor domain and metal domain. Figure 6.3 (c) represents the kinetics of photo induced absorption of CdSe{Au} NHM at 650

Table 6.2: The multi-exponential fitted parameters of bleach decay kinetics of CdSe and CdSe/Au hetero-structures.

System@ λ_{nm}	$\tau_{1(growth)}$	$\tau_{2(growth)}$	$\tau_1(\%)$	$\tau_2(\%)$	$\tau_3(\%)$
CdSe@560 nm	<100 fs (85%)	0.6ps (15%)	20 ps (- 35%)	200ps(5%)	>1 ns (60%)
CdSe/Au @550 nm	<100 fs (100%)		0.45 ps (60%)	10 ps (25%)	>1 ns (15%)

nm. The growth of the 650 nm kinetics is shown in inset in figure 2B (c) and fitted with 100 fs (80%) and 150 fs (20%) components, whereas the multi-exponential decay components are $\tau_1 = 0.8$ ps (-70%), $\tau_2 = 30$ ps (-30%) and $\tau_3 = >1$ ns (100%). The transient band in the red region of the spectra decays with the appearance of negative absorption at longer time scale, which is due to formation of long lived charge separated state between the Au and CdSe QDs.⁹⁰ No recombination reaction was observed in the hetero-structure within 1 ns suggesting a long live charge separated species. This red region bleach is the transition

between CdSe QD to Au NP, where after photo excitation the electron is localised at the Au NP and hole is localised at the VB of CdSe. This long lived charge separated states are expected to play an important role in PCE for the CdSe{Au} NHM sensitized solar cell.

C. Photovoltaic Measurement of CdSe/Au Nanohybrid materials.

Time-resolved luminescence and ultrafast transient absorption studies suggest that on photo-excitation ultrafast charge separation takes place in CdSe{Au} NHM where holes are localized in CdSe QD and electrons are localized in the Fermi-level of Au NP. Now to investigate the effect of charge separation within CdSe{Au} NHM on PCE, current density-voltage (J-V) and IPCE measurements were carried out in quantum dot solar cell by using for both CdSe QDs and CdSe{Au} NHM as sensitizers. The photo anodes have been prepared by loading CdSe QDs and CdSe{Au} NHM on the mesoporous TiO₂ film. To do so first of all the oleic acid capped QDs and nanohybrid materials were transferred from non-aqueous phase to aqueous phase by using MPA as phase transfer catalyst. The TiO₂ films were loaded with the aqueous QDs solution by drop casting method.¹³⁷ After this four layers of quasi CdS shell and two layers of ZnS shell were coated by the SILAR technique to reduce the trap state at the QDs and TiO₂ NP.^{139, 295} On the other hand Cu₂S and polysulphide were used as photocathode and electrolyte materials respectively.²⁹⁶ Deposition of Cu on ITO glass by electrophoresis has been discussed details in chapter 2. The device has been fabricated by assembling the photo cathode, electrolyte and Cu₂S counter electrode as described in details in Chapter 2. The photovoltaic performance of CdSe and Au/CdSe in terms of J-V have been measured after illuminating by one sun (AM 1.5G, 100mW/cm²) and is shown in Figure 6.4 A. The J-V curves of CdSe QDs and CdSe{Au} NHMs are represented in Figure 6.4 A (a) and (b), respectively. All the measured parameters, e.g. efficiency, fill factor(FF), short

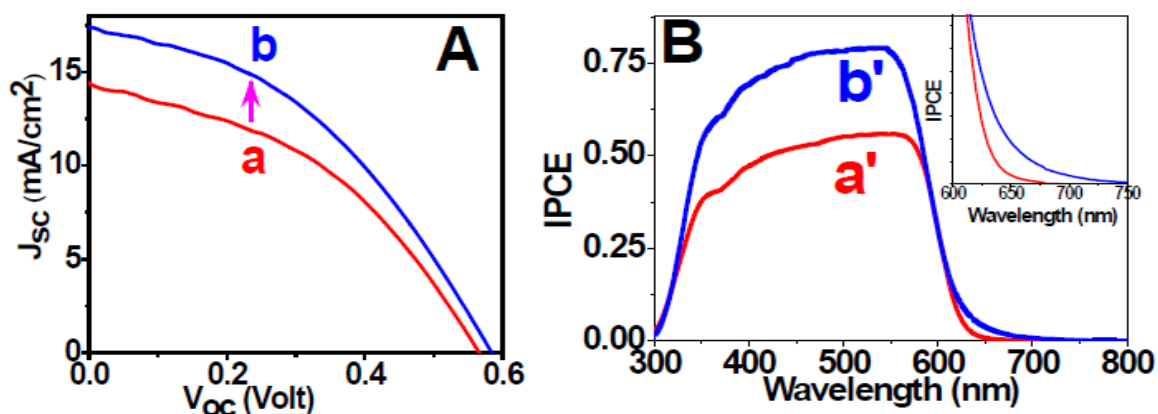


Figure 6.4. (A) J_{sc} - V curves of (a) CdSe QDs and (b) CdSe{Au} NHM material under 1 sun illumination. (B) IPCE spectra of (a') CdSe QDs and (b') CdSe{Au} NHM material. **Inset.** The magnified curves of a' and b' beyond 600 nm.

Table 6.3. The measured solar cell parameters in terms of short circuit current (J_{sc} , mA/cm^2), open circuit voltage (V_{oc} , V), fill factor (FF, %) and power conversion efficiency for CdSe QDs and CdSe{Au} NHM.

QD System	J_{sc} (mA/cm^2)	V_{oc} (V)	FF (%)	PCE (%)	Champion Cell PCE (%)
CdSe QDs	14.21	0.57	0.40	3.24(\pm 0.10)	3.37
CdSe{Au} NHM	17.39	0.59	0.41	4.2(\pm 0.22)	4.39

circuit current (J_{sc}) and open circuit voltage (V_{oc}) have been tabulated in Table 6.3. The measured power conversion efficiency for CdSe QDs was recorded to be 3.24% (\pm 0.10) with 14.21 mA/cm^2 J_{sc} . Open circuit voltage (V_{oc}) was determined to be 0.57 V with 40 % fill factor (FF). Interestingly J_{sc} improved significantly with a value of 17.39 mA/cm^2 with slight increase in V_{oc} (0.59 V) for CdSe{Au} NHMs. The PCE of CdSe{Au} QDSC was

CHAPTER 6

determined to be $4.2(\pm 0.22)\%$ with maximum 4.39% for the champion cell.

The induced photon to current conversion efficiency (IPCE) for CdSe QDs and CdSe{Au} NHMs have been shown in Figure 6.4B(a') and (b') respectively. It's clearly seen in Figure 6.4B that the IPCE spectra of CdSe{Au} NHMs at the range 350 nm to 600 nm increases quite reasonably as compared to pure CdSe QDs. It's more interesting to see in Figure 6.4B that IPCE spectra for CdSe{Au} NHMs appears beyond 700 nm where as in case of CdSe QDs it appears below 650 nm. Appearance of new broad band in case of CdSe{Au} NHMs can be attributed to the formation of new charge transfer state in the composite system, which is closely matched with steady state optical absorbance spectra.

Photo conversion efficiency (PCE) in a device depends on short circuit current (J_{SC}), open circuit voltage (V_{OC}) and fill factor (FF). Fill factors in both the systems found to be similar and V_{OC} is marginally higher in case of CdSe{Au} NHM system (Table 6.3). However J_{SC} found to be 22% higher in case of CdSe{Au} NHM system as compared to CdSe QD system. This might be due to higher mobility of photo-injected electron from CdSe{Au} NHM to TiO_2 electrode. Here in Au NP in the composite system play a vital role in CdSe{Au} NHM sensitized solar cell. After photo excitation of CdSe QDs in the NHMs electrons are transferred to Au NP in sub-picosecond time scale and finally it transferred to TiO_2 electrode while the holes are localized in the VBs of CdSe QDs which finally transferred to counter electrode through hole transporting electrolyte. As Au NP facilitates charge separation and slows down charge recombination as compared to pure CdSe QDs, J_{SC} in CdSe{Au} NHM sensitized solar cell increases. In addition to that CdSe{Au} NHM system absorbs solar radiation beyond 750 nm (upto 800 nm), as a result red region of solar light can create more charge carriers as compared to pure CdSe QDs resulting higher J_{SC} in

CHAPTER 6

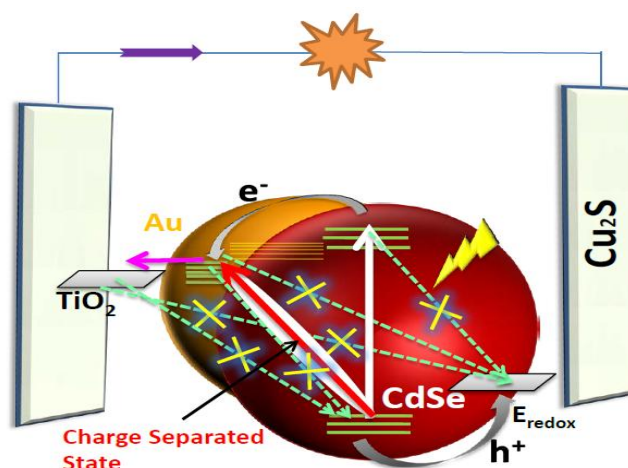
CdSe{Au} NHM sensitized solar cell.

In case of pure CdSe QDSC, the electrons are transferred from conduction band (CB) of photo excited CdSe QDs to CB of TiO₂. But there is competition between the charge collection efficiency (i.e. transfer of electron to TiO₂ film followed by to the photo-anode) with various other loss processes, like trapping of e⁻ on the CdSe QDs and TiO₂ surface, recombination electron in TiO₂ film and hole in CdSe QD and recombination between electron in TiO₂ and hole in electrolyte. Earlier it has been observed that the surface states in both CdSe QDs and TiO₂ film can be minimised by passivation of CdS and ZnS.^{137, 139, 293, 297} However in case of CdSe{Au} system trapping process can be reduced drastically due to ultrafast electron transfer from semiconductor domain to metal domain. As a result losses due to trapping process in device system reduced drastically, resulting increase of J_{SC}. The recombination processes such as e⁻(TiO₂)-h⁺(VB of CdSe), e⁻(Au)-h⁺(VB of CdSe), e⁻(CB of CdSe)-h⁺(electrolyte), e⁻(Au)-h⁺(electrolyte) and e⁻(TiO₂)-h⁺(electrolyte) (shown in scheme 6.1) are reduced in CdSe{Au} NHM sensitized solar cell. Au NPs restrict all these recombination processes (loss processes) by introducing a potential barrier. As a result the efficiency of the CdSe{Au} NHM sensitized solar cell is found to be higher as compared to CdSe QDSC.

J_{SC} depends on electron injection efficiency (ϵ_{INJ}), light harvesting efficiency (ϵ_{LHE}) and charge collection efficiency (ϵ_{CC})^{298, 299} which can be demonstrated in the equation below:

$$J_{SC} = \epsilon_{LHE} * \epsilon_{CC} * \epsilon_{INJ} \quad 6.1$$

Here in ϵ_{LHE} of NHM has been increased due to formation charge separated state between Au NP and CdSe QDs in CdSe{Au} NHM which absorbs more solar radiation upto 800 nm. We



Scheme. 6.1. Schematic diagram of the role of Au NP in CdSe{Au} NHM solar cell in enhancement of PCE. Various loss processes are found to be restricted by Au NP.

have already demonstrated the injection efficiency in NHM is much higher as compared to pure CdSe QDs due to formation of long lived charge separated states, which eventually improves both ϵ_{INJ} and ϵ_{CC} for NHM as compared to pure CdSe QDs. Au NP not only facilitates higher charge separation it also play as a barrier for charge recombination (CR) eventually slows down CR reaction. Therefore, all of the recombination processes (loss) mentioned above can be minimised by introducing Au NP on the CdSe QDs.

D. Electrochemical Impedance Spectroscopy Measurement.

So far in this chapter we have correlated the enhancement of PCE of CdSe{Au} NHM through TA spectroscopy compared with CdSe QDs. Further to explain the intrinsic mechanism of PCE enhancement by Au NP in CdSe{Au} NHM, we have also monitored the electrochemical impedance spectroscopy (EIS) of CdSe QDs and CdSe{Au} NHM in dark condition with -0.5 V forward bias having 10 mV ac perturbation in the frequency range 100 KHz to 0.1 Hz.^{214, 220, 300} Figure 6.5 (a) and 4 (b) are Nyquist plots for CdSe QDs and CdSe{Au} NHM, respectively. Two important components viz. chemical capacitance (C_{μ})

and recombination resistance (R_{rec}) for the chosen systems have been determined from the data fitting along with the series resistance (R_s) and presented in Table 6.4. Here C_μ stands for distribution of carrier density and density of states in the CB of TiO_2 and the trap state distribution at the TiO_2 surface.^{137, 188} It's interesting to compare the C_μ , R_s and R_{rec} values for both CdSe QDs and CdSe{Au} NHM. The values for the R_s and C_μ have shown practically no change for CdSe and CdSe{Au}, which implies that the CB position and density of states of TiO_2 are not affected by addition of Au NP in CdSe{Au} NHM.²¹⁴ However, R_{rec} , obtained from Nyquist fitting shows 2.8 times enhancement for CdSe{Au} NHM as compared to CdSe QDs. Here, R_{rec} represents the charge recombination resistance at the interface of TiO_2/QD sensitizers/electrolyte interface.¹³⁷ This quantity is inversely

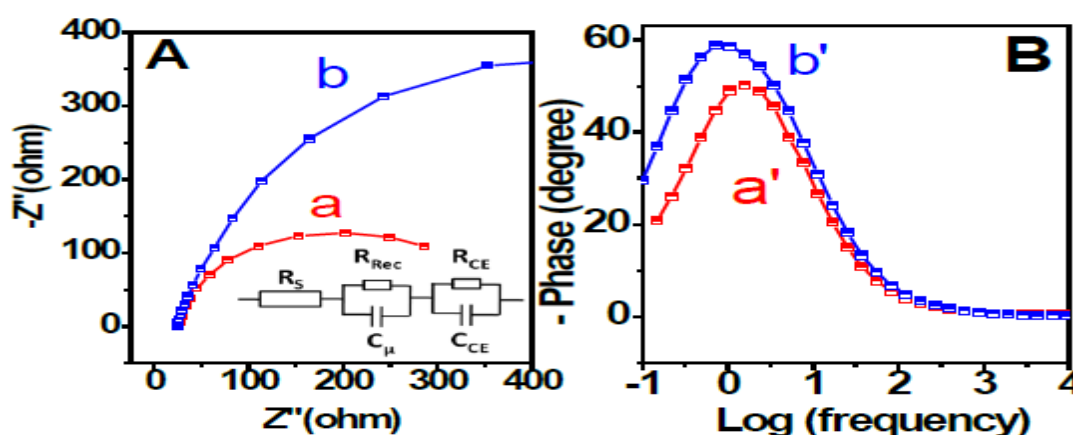


Figure 6.5.A. Nyquist plots for (a) CdSe NCs and (b) CdSe{Au} NHM at -0.5 V forward bias. The assumed equivalent circuit is shown in this figure. **B.** Bode phase diagram for (a') CdSe NCs and (b') CdSe{Au} NHM.

proportional to the recombination rate.^{188, 220} This finding is corroborated by recombination rate obtained from ultrafast spectroscopy. Femtosecond transient absorption studies suggest that on photo-excitation charge carriers are generated where the electron is localised in Au

NP and the hole is localised in VB of CdSe in CdSe{Au} NHM. Here in significant improvement of R_{rec} also suggests higher charge separation in CdSe{Au} NHM as compared to CdSe QDs, which is responsible for higher charge collection efficiency, improving the J_{SC} . The electron recombination lifetime (τ_{rec}) also can be determined from the Bode's plot for

Table 6.4. The Fitted Parameters for electrochemical impedance spectroscopy for CdSe NCs and CdSe{Au} NHM.

System	$R_s (\Omega)$	$R_{rec}(\Omega)$	$C_\mu (\text{mF cm}^{-2})$	$\tau_{rec} (\text{s})$
CdSe QDs	25.34	266.7	8.33	0.10
CdSe{Au} NHM	25.82	744.9	8.57	0.22

CdSe QDs and CdSe{Au} NHM as shown in figure 6.5 B.³⁰¹ The relation between frequency at the peak maxima of the Bode phase diagram and τ_{rec} is as follows,

$$\tau_{rec} = \frac{1}{2\pi f_{max}} \quad 6.2$$

Where, f_{max} represents the frequency maxima at the peak maxima of the Bode phase diagram.

From the Bode diagram it is clearly evident that electrons are longer lived for CdSe{Au} NHM as compared to CdSe QDs due to blockage of interfacial charge carrier recombination. It's interesting to see that Au NP in CdSe{Au} NHM enhances the light harvesting efficiency which is also indicated in IPCE measurements. The higher R_{rec} in the device improves the charge collection efficiency which increases the J_{SC} and enhances the PCE.

The above spectroscopic investigations clearly suggest that Au NP in CdSe{Au} NHM plays a major role for the increment of device efficiency from 3.37% for CdSe QD to

4.39% for CdSe{Au} NHM. To the best of our knowledge we are demonstrating for the first time, role of metal NP in NHM QDSC through monitoring the charge carrier life time with the help of femtosecond TA spectroscopy and EIS which is directly correlated with the device efficiency.

6.2.2 Size Dependent Hot Carrier Dynamics of CdSe@CdS{Au} Nanohybrid Materials.

A. Characterization and Optical Properties of CdSe@CdS{Au} HS:

To demonstrate ultrafast charge transfer dynamics in CdSe@CdS{Au} nano-hetero-structures with different Au NP sizes and their photo-catalytic behaviour, two composite systems (CdSe@CdS{Au}-1 and CdSe@CdS{Au}-2 hetero-structures) were synthesized where CdSe@CdS core shell material was kept same but two different sizes of Au NPs were appended on the core shell. The synthesised materials have been characterised by HR-TEM. The size of the CdSe@CdS core-shell has been determined to be ~3.5 nm. Figure 6.6A and B show the HR-TEM images of CdSe@CdS{Au}-1 (HS 1) and CdSe@CdS{Au}-2 (HS 2) where 1.25 and 2.5 nm Au NPs are grown on 3.5 nm CdSe@CdS core-shell, respectively. The HR-TEM images clearly show the different lattice of the Au NP on the surface of CdSe@CdS core-shell. The clear dark spot on the CdSe@CdS core-shell shows the growth of Au NP. The steady state optical absorption and luminescence spectroscopy have been carried out to characterise and investigate the charge transfer of the CdSe@CdS core-shell and CdSe@CdS {Au} hetero structure materials. Figure 6.6C (a) indicates the optical absorption spectra of CdSe@CdS core shell, which shows three distinct optical absorption bands at 578 nm, 530 nm and 480 nm and can be attributed due to 1S ($1S_{e-1S_{3/2}}$), 2S ($1S_{e-2S_{3/2}}$), and 1P($1P_{e-1P_{3/2}}$) transitions respectively. But on growing of Au NP on the surface of CdSe@CdS core-shell optical absorption spectra dramatically changed. Figure 6.6C (b) and (c) show the optical absorption spectra of HS 1 and HS 2 hetero nanostructures. Interestingly,

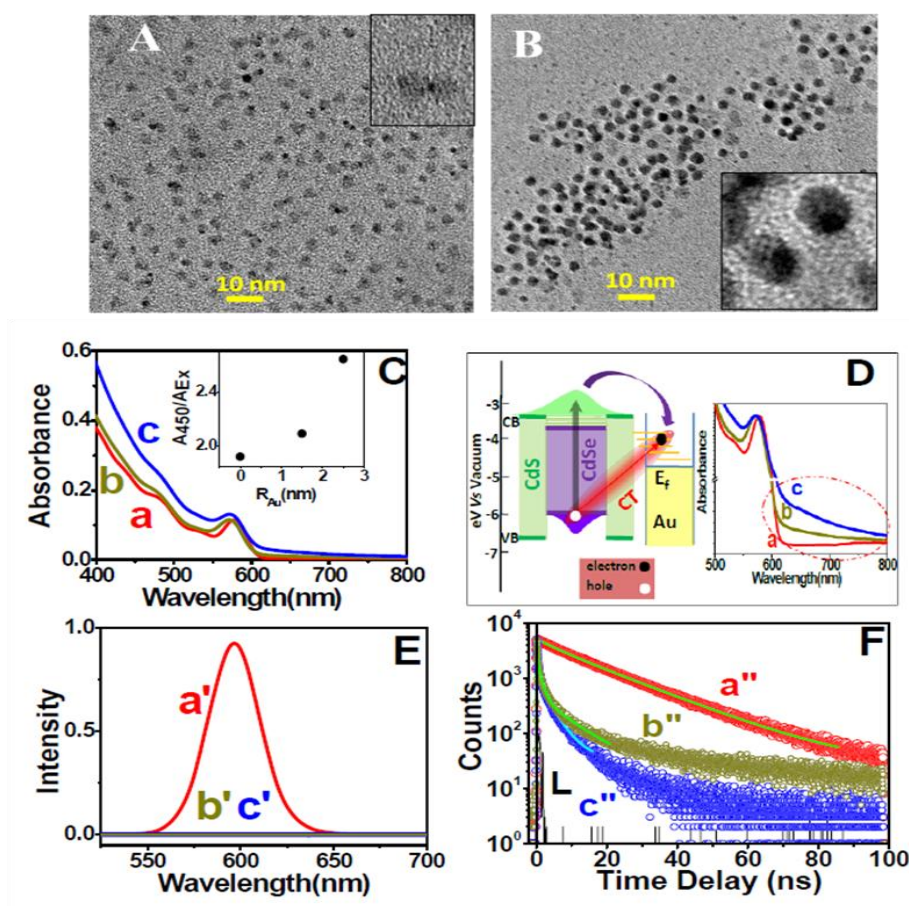


Figure 6.6: HR TEM image of (A) CdSe@CdS{Au}-1 and (B) CdSe@CdS{Au}-2. (C) UV-Visible steady state optical absorption spectra of (a) CdSe@CdS core shell (b) HS 1 and (c) HS 2 nano hybrid material in chloroform. **Inset:** Graphical plot of ratio of absorption at 450 nm and absorption at 1S excitonic wavelength versus radii of attached Au NPs. (D) Scheme of charge transfer transition within CdSe@CdS{Au} nano hybrid material. **Inset:** Optical absorption band of the CT transition. (E) Photoluminescence spectra of (a') CdSe@CdS core shell (b') HS 1 and (c') HS 2 hetero-structure after 400 nm excitation. (F) Time-resolved luminescence decay traces of (a'') CdSe@CdS core shell (b'') HS 1 hetero nanostructure and (c'') HS 2 hetero-structure monitoring at 596 nm after 445 nm laser excitation. L is the excitation lamp profile.

Table 6.5: Multi exponential fitted parameter of luminescence decay traces of CdSe@CdS, CdSe@CdS{Au}-1 and CdSe@CdS{Au}-2 after exciting the samples at 445 nm and monitoring at 596 nm.

System	τ_1	τ_2	τ_3	τ_{avg}
CdSe@CdS	3.61 ns (55%)	22.9 ns (45%)		12.28 ns
CdSe@CdS{Au}-1	0.045ns(93%)	1.23ns(5%)	9.31ns(2%)	0.29 ns
CdSe@CdS{Au}-2	0.04ns(88%)	0.6ns(9%)	3.83ns(3%)	0.2 ns

the 1S excitonic absorption band of the core-shell shifts in the blue region from 580 nm to 570 nm and become broad after growing Au NP on it.⁹⁴ Again the absorption spectrum of HS 2 is broader as compared to that of HS 1. This observation clearly suggests that the exciton-plasmon coupling increases with increasing the size of Au NPs on the surface of CdSe@CdS core-shell material. As the size of Au NP increases, number of interacting plasmon states of metal nanoparticles increases which interact with the excitonic states of core-shell.⁴⁵ The optical absorption spectra for both the hetero-structures do not show any absorption band due to surface plasmon of Au NP as the particle size of the metal nanoparticles are < 3 nm. The damping of plasmon band of small size Au NP was also observed by us⁹⁰ and Zamkov and co-workers⁸⁷ while it was attached with QDs. However absorption intensity at 450 nm which attributed to d to sp transition of Au NP, which is higher in HS 2 and HS 1 as compared to the CdSe@CdS core shell. It's clearly seen that there is no absorption beyond 620 nm for CdSe@CdS core shell however it goes beyond 750 nm for HS1 and 800 nm for HS 2 (Inset Figure 6.6D). This higher absorption in the red region of the spectra can be attributed to formation of semiconductor-to-metal charge-transfer transition in CdSe@CdS{Au} hetero-structure. It's interesting to see that as the size of Au NP increases CT interaction also increases in the hetero-structure which is clearly observed in HS 2. Earlier Lian and co-workers³⁵ demonstrated plasmon-induced metal-to-semiconductor charge-transfer transition

in CdSe-Au nanorod (NR) in visible to near IR region. They have attributed the broad near-IR absorption feature to a strongly damped Au plasmon caused by the strong mixing of Au and CdSe electronic levels. The charge transfer transition in the present studies can be demonstrated as shown in Figure 6.6D.

Now to understand the size dependent optical properties of the hetero-structures in the excited state, steady-state and time-resolved luminescence studies have been carried out for CdSe@CdS core-shell, HS 1 and HS 2 hetero nanostructures and shown in Figure 6.6 E. In our earlier investigation,^{89, 90} we have observed quenching of luminescence and reduction of luminescence life time of CdSe QDs in presence of Au NP in the metal semiconductor nanohybrid materials. Figure 6.6E (a') shows the luminescence spectra of CdSe@CdS core shell material with emission maxima at 596 nm with high emission quantum yield ($\phi_f = 0.7$) after exciting at 400 nm. Here, CdSe@CdS form quasi type II core-shell^{89, 207} structure due to low band gap off set (0.2 eV) in the conduction bands of CdSe and CdS QDs as it can be seen in Figure 6.6D. As a result, on photo-excitation electrons are delocalized in the conduction bands of both CdSe core and CdS shell while holes are localized in the CdSe core due to higher off-set in the valence bands of CdSe core and CdS shell (Figure 6.6D). Now it's interesting to see that high intensity luminescence of CdSe@CdS core-shell drastically reduced while Au NP was grown on the core-shell surface as it can be seen in Figure 6.6E (b') and (c'). Figure 6.6D suggest that the Fermi level of Au NP lies below the conduction band of CdS@CdS core-shell QD. The emission quenching of CdSe@CdS core-shell luminescence in CdSe@CdS{Au} HS materials can be attributed to the electron transfer from the CB of CdS@CdS core-shell to Au NP which is thermodynamically viable. To reconfirm the charge delocalisation in CdSe@CdS core shell and to follow photo-excited electron transfer to the Au NP time resolved luminescence measurements have also been carried out

and shown in Figure 6.6F. Figure 6.6F (a") shows the time resolved photo-luminescence (PL) decay trace of CdSe@CdS core shell at 596 nm after exciting the samples at 445 nm laser. The PL decay trace of CdSe@CdS quasi type-II core-shell can be fitted bi-exponentially with time components $\tau_1 = 3.61$ ns (55%) and $\tau_2 = 22.9$ ns (45%) with average life time 12.28 ns and are shown in table 6.5. This bi-exponential decay shows the trapping of the electron in the quasi type-II structure which is similar to our previous report.²⁰⁷ It is worth mentioned that the PL decay of CdSe QDs is tri exponential which convert to bi-exponential in core shell due to elimination of trap states. Figure 6.6F (b") and (c") show the PL decay traces of HS 1 and HS 2 hetero nanostructure, where both the decay traces can be fitted multi-exponentially with time constants of $\tau_1 = 0.45$ ns (93%), $\tau_2 = 1.23$ ns (5%) and $\tau_3 = 9.31$ ns (2%) with $\tau_{avg} = 0.29$ ns and $\tau_1 = 0.04$ ns (88%), $\tau_2 = 0.6$ ns (5%) and $\tau_3 = 3.83$ ns (3%) with $\tau_{avg} = 0.2$ ns, respectively (Table 6.5). The fast component in both the decay traces can be attributed to fast electron transfer from CdSe@CdS core-shell to the Au NPs. It's attractive to see that with increasing Au NP size, the faster time constant suggesting faster electron transfer from core-shell to Au NP. In larger size Au NP number of electron accepting states is much higher as compared to smaller size Au NP as a result electron accepting ability found to be much higher in larger Au NP.

B. TA Spectroscopy Measurement of CdSe@CdS{Au}

However, from our earlier report^{89, 90} it has been realized that to determine electron transfer time and find out the mechanism of charge transfer in nano-second time-resolved luminescence spectroscopy is not enough. So, to confirm the electron transfer at ultrafast time scale and to monitor the excited-state charge transfer and charge delocalization dynamics in the present investigation femto-second transient absorption (TA) measurements have been carried out in CdSe@CdS core-shell, HS 1 and HS 2 hetero nanostructures after exciting the

samples at 400 nm. All the experiments have been carried out at low pump fluence ($\langle N \rangle \sim 0.3$, $\langle N \rangle =$ average no. of exciton) to avoid the multi exciton generation. In our previous reports, we have demonstrated the charge carrier dynamics in CdSe{Au} heterostructures and 2-Dimension CdSe@CdS-Au hybrid platelets in ultrafast time scale.^{36,47} In both the cases electron transfer time were found to take place in ultrafast time scale. Zamkov and co-workers discussed the Exciton-Plasmon coupling in different sizes of Au NPs on the surface of CdS nanorod by TA studies.³¹ Figure 6.7A represents the TA spectrum of CdSe@CdS

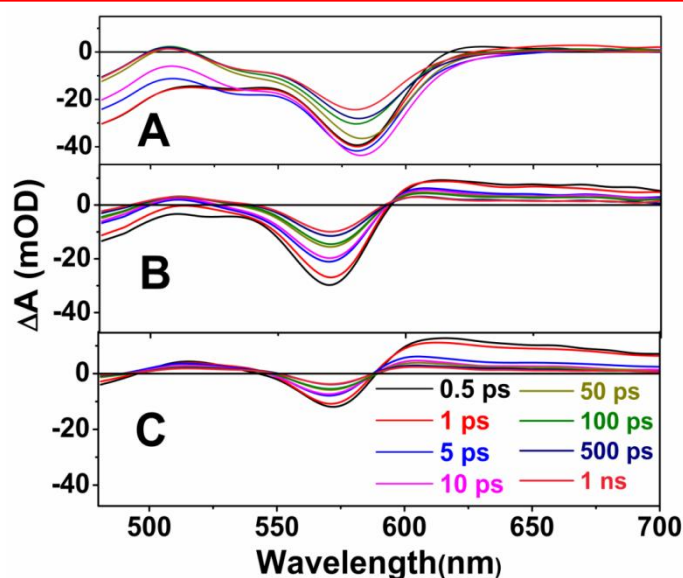


Figure 6.7: Transient Absorption spectra of (A) CdSe@CdS core shell nanoparticles (B) HS 1 and (C) HS 2 hetero-structure materials in chloroform at different time delay after 400 nm laser excitation.

core-shell material at different time delay after 400 nm excitation. In the transient spectra three negative absorption bands have been observed at 580 nm, 530 nm and 480 nm which can be attributed to the transient bleach due to 1S(1Se–1S_{3/2}), 2S (1Se–2S_{3/2}), and 1P (1Pe–1P_{3/2}) transitions, respectively. The negligible photo induced absorption in the transient spectra suggests minimum number of defect states in the core-shell materials. However, it is

CHAPTER 6

fascinating to see that transient spectra of HS 1 (Figure 6.7B) and HS 2 (Figure 6.7C) hetero-structure materials are completely different as compared to CdSe@CdS core-shell. The intensity of all the spectra have been shown after OD correction. It's clearly seen that the intensity of all the transient bleaches drastically reduced in both Figure 6.7B and Figure 6.7C and reduction is more for larger size Au NPs. In addition to that bleach due to 1S excitonic absorption moves towards the blue region of the spectra which matches well with steady state optical absorption spectra (Figure 6.6C). Again, the transient bleaches due to 2S and 1P excitonic states completely disappear with increasing size of Au NP. It's more interesting to see that with increasing the size of Au NP positive absorption band starts appearing in the red region of the spectra in both figure 6.7B and C. Similar positive absorption band was also observed by us in CdSe@Au hetero structure and was attributed to photo- excited electron transfer from CdSe QD to Au NP. So, in the present investigation PA band in both the hetero-structures can be attributed to the carrier density on Au NP which has transferred from photo-excited CdSe@CdS core-shell. This type of positive absorption was never observed neither in isolated core-shell or isolated Au NP. Au NP shows little bit positive absorption at the lower energy region. But this huge positive absorption compared to bleach intensity is due to generation of a new charge (electron) distribution at the semiconductor–metal interface after transfer from core shell.³¹ It's exciting to see that decreasing the bleach intensity and increasing the intensity of positive absorption band with increasing the size of Au NP in the hetero-structure implies the extraction of charge from CdSe@CdS core-shell to Au NP facilitates with size of Au NP in the heterostructure. In addition to that it's exciting to see that the spectra in 500-550 nm region of the CdSe@CdS{Au} heterostructure, a positive absorption band appears with maxima at ~515 nm whose intensity increases with the size of Au NP. This might be due to presence of higher density of states in the Fermi level in larger

Au NPs which facilitate more electron transfer from photo-excited CdSe@CdS core-shell within the hetero-structure. It has been observed in steady state absorption (Figure 6.6C) that the larger size Au form stronger CT complex with CdSe@CdS core-shell due to stronger coupling between exciton and plasmon which eventually facilitate electron transfer reaction within the nano hybrid materials. At this point we would like to mention that in the transient spectra of CdSe@CdS{Au} hetero-structures, no separate bleach due to surface plasmon of Au NPs was observed. This might be due to relatively smaller size of Au NP, which is analogous with our previous report.³⁶ The other important observation is the change of bleach intensity at 1P and 1S position of CdSe@CdS core-shell before and after the growth of different sizes Au NPs. It's interesting to see that 1P/1S bleach ratio CdSe@CdS core-shell is dramatically reduced in the hybrid structure with the size of Au NPs. This observation clearly suggests that the electron transfer from 1P level to Au NP is more efficient as compared to that of 1S level, i.e. the hot electron transfer is more efficient from CdSe@CdS to Au NPs as compared to thermalized electron.

Now to investigate the excited state charge carrier dynamics of the CdSe@CdS core-shell and CdSe@CdS{Au} nano-hybrid materials we have monitored the kinetics at key wavelengths in the above systems and are shown in Figure 6.8. We would like to mention that we have kept similar concentration in all the three systems to compare the change of bleach intensity at different excitonic wavelengths. Now, before monitoring the interfacial charge transfer dynamics within the hetero-structure we have followed the kinetics at 580 nm for CdSe@CdS core-shell and shown in Figure 6.8A (a). The bleach kinetics can be fitted with bi-exponential growth with time constants $\tau_1 = <100\text{fs}$ (86 %) and $\tau_2 = 3 \text{ ps}$ (14%) and multi-exponential recovery with time constants $\tau_1 = 50 \text{ ps}$ (-36 %) and $\tau_2 = 250 \text{ ps}$ (-6%), and $\tau_3 = >1\text{ns}$ (-58%) (Table 6.6). The second growth component can be attributed to electron

cooling, where holes are localized in the CdSe core and electrons are delocalized in the conduction bands of both CdSe core and CdS shell QDs, resulting the electron and hole are de-coupled in the quasi type II core-shell structure. Multi-exponential bleach recovery kinetics can be attributed to the recombination between electrons in the delocalized

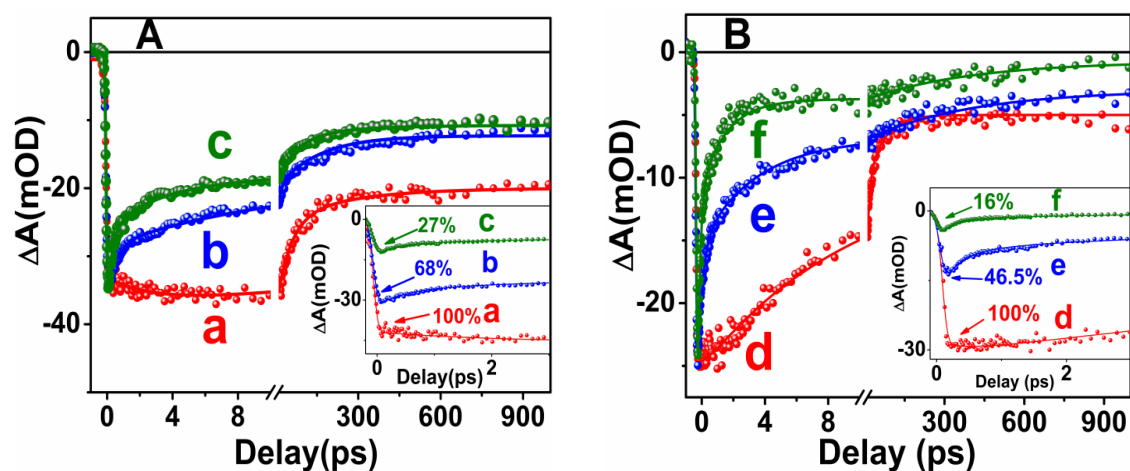


Figure 6.8: (A) Normalised bleach recovery kinetics at 1S excitonic wavelength (a) CdSe@CdS core shell at 580 nm (b) HS 1 at 570 nm and (c) HS 2 hetero-structure at 570 nm in chloroform after 400 nm laser excitation. **Inset:** Un-normalised bleach recovery kinetics at shorter time scale at same concentration to monitor the change of intensity after coupling with different sizes of Au NP. (B) Normalised bleach recovery kinetics at 1P excitonic wavelength of (d) CdSe@CdS core shell (e) HS 1 and (f) HS 2 hetero-structure at 480 nm in chloroform after 400 nm laser excitation. **Inset:** Un-normalised bleach recovery kinetics at shorter time scale at same concentration to monitor the change of intensity after coupling with different sizes of Au NP.

conduction band and holes in the CdSe valence band. Now it's interesting to see in the inset of Figure 6.8A, that the relative bleach intensity at 580 nm from 100% of CdSe@CdS core shell decreases to 68% and 27% for HS-1 and HS-2, respectively. In addition to that growth

CHAPTER 6

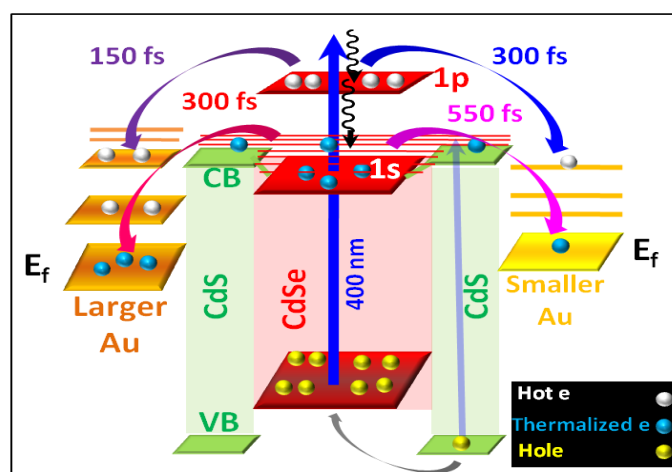
of bleach kinetics become single exponential in both the hetero-structures in presence of Au NP. However, the bleach recovery kinetics are fitted multi-exponentially with time constants $\tau_1 = 550$ fs (-22%), $\tau_2 = 10$ ps (-25%), $\tau_3 = 150$ ps (-12%), and $\tau_4 = >1$ ns (-41%) for HS-1 and $\tau_1 = 300$ fs (-24%), $\tau_2 = 3$ ps (-24%), $\tau_3 = 40$ ps (-16%), and $\tau_4 = >1$ ns (-36%) for HS 2 (Table 6.8). It's interesting to see that in presence of Au NP one extra faster component (550 fs and 300 fs) appears in the bleach recovery kinetics which becomes faster with increasing

Table 6.6: Multi-exponential fitted parameters of the decay kinetics at 1S and 1P excitonic bleaches of CdSe@CdS core shell, CdSe@CdS{Au}-1 and CdSe@CdS{Au}-2 hetero-structures.

System@ λ_{nm}	$\tau_{1(growth)}$	$\tau_{2(growth)}$	τ_1	τ_2	τ_3	τ_4
CdSe/CdS@ 580 nm	<100 fs (86%)	3 ps (14%)	50 ps (-36%)	250 ps (-6%)	>1 ns (-58%)	
AuCdSe/CdS-1 @570 nm	<100 fs		550 fs (-22%)	10 ps (-25%)	150 ps (-12%)	>1 ns (-41%)
AuCdSe/CdS-2 @570 nm	<100 fs		300 fs (-24%)	3 ps (-24%)	40 ps (-16%)	>1 ns (-36%)
CdSe/CdS @480 nm	<100fs (90%)	0.15ps (10%)	9ps (-67%)	60ps (-11%)	>1 ns (-22%)	
CdSe/CdS{Au}-1 @480 nm	<100fs		300 fs (-45%)	3.5ps (-27%)	160ps (-15%)	>1ns (-13%)
CdSe/CdS{Au}-2 @480 nm	<100fs		150 fs (-68%)	1.5 ps (-17%)	170ps (-12%)	>1 ns (-3%)

the size of Au NP in the hetero-structure. Decrement of 1S exciton bleach intensity and appearance of faster component can be attributed to transfer of photo-excited electron from

CdSe@CdS core-shell to the Au NPs. The faster bleach recovery components 550 fs (for HS-1) and 300 fs (for HS-2) can be attributed to electron transfer time from 1S state of CdSe@CdS core shell to Au NP (Scheme 6.2). In our earlier investigation similar faster bleach recovery at 1S excitonic position in CdSe{Au} hetero-structure was attributed to electron transfer to Au NP.³⁶ It's motivating to see that electron transfer is more efficient and faster with increasing the size of Au NPs as it can be seen in Figure 6.7 and 6.8. Interestingly the growth of the 1S exciton bleach CdSe@CdS core-shell disappears once Au NP is coupled with the QDs. This observation clearly indicates electrons from upper excitonic states (1P_e and above) get transferred to Au NP before it cools down to 1S excitonic state in the hetero-



Scheme 6.2: Photo-excited hot and thermalized electron transfer processes in the CdSe@CdS{Au}hetero-structure with different sizes of Au. It shows the photoexcitation of the hetero-structure electrons and holes are generated where the electrons are transferred to the Fermi level of Au NP and the holes are localized in the CdSe core.

structure. To monitor the electron transfer dynamics from upper excitonic states to the metal domain the bleach recovery kinetics has been monitor at 1P excitonic position (at 480 nm) and shown in Figure 6.8B. The bleach recovery kinetics for CdSe@CdS at 480 nm can be

fitted with bi-exponential growth with time constants $\tau_1 = <100\text{fs}$ (90 %) and $\tau_2 = 150\text{ fs}$ (10%) and multi-exponential recovery with time constants $\tau_1 = 9\text{ ps}$ (-67 %), $\tau_2 = 60\text{ ps}$ (-11%), and $\tau_3 = >1\text{ns}$ (-22 %) (Table 6.8). The second growth component (150 fs) can be attributed to the state filling of the charge carriers from higher excited state to 1P state. The decay of this bleach is not faster as that of CdSe. The slow decay of this higher excitonic bleach due to alloying at the interface of CdSe core and CdS shell at 200°C temperature. This type of slow decay of higher excitonic bleach is reported in previous literature.⁴⁸⁻⁵⁰ It has been observed in Figure 6.7 and in the inset of Figure 6.8B that the bleach intensity at 480 nm drastically reduces in the hetero-structure and reduction is more in larger Au NP. Relative bleach intensity at 480 nm found to decrease from 100% of CdSe@CdS core-shell to 47% and 16% for HS-1 and HS-2, respectively (Figure 6.8B). Interestingly, the growth of bleach kinetics becomes single exponential in both the hetero-structures suggesting hot electron transfer from core-shell to Au NPs. However, the bleach recovery kinetics be fitted multi-exponentially with time constants $\tau_1 = 300\text{ fs}$ (-45%), $\tau_2 = 3.5\text{ ps}$ (-27%), $\tau_3 = 160\text{ ps}$ (-15%), and $\tau_4 = >1\text{ns}$ (-13%) for HS-1 and $\tau_1 = 150\text{ fs}$ (-68%), $\tau_2 = 1.5\text{ps}$ (-17%), $\tau_3 = 170\text{ ps}$ (-12%), and $\tau_4 = >1\text{ns}$ (-3%) for HS-2 (Table 6.8). The faster bleach recovery components 300 fs and 150 fs for HS-1 and HS-2 can be attributed to hot electron transfer time from photo-excited CdSe@CdS core-shell to Au NPs (Scheme 6.2). It's exciting to see that with changing the size of Au NP from 1.25 nm to 2.5 nm the hot electron transfer time decreases from 300 fs (45%) to 150 fs (68%) which eventually facilitated charge separation reaction in the hetero-structure. The above experimental observations clearly suggest that electron transfer from 1P level (upper state) to Au NPs is more feasible than the 1S state when larger size of Au NP is attached on the surface of CdSe@CdS core-shell. Banin and co-workers have shown the rate

constant (k_{et}) for electron transfer from semiconductor to metal,³⁰² which follows the equation below:

$$k_{et} = (4/3\hbar) r^3 |t_e|^2 (2m_e^*/\hbar^2)^{3/2} [\epsilon_c + \Phi(r) + \epsilon_f(r)]^{1/2} \quad 6.3$$

Where, r is the radius of the metal nanoparticle, \hbar is the Planck constant divided by 2, m_e^* is the effective mass of the electron, t_e is the electron tunnelling matrix elements (independent of r), ϵ_c is conduction band energy of semiconductor, $\epsilon_f(r)$ is the Fermi energy level of metal and $\Phi(r)$ is the work function. The equation signifies the rate of electron transfer is strongly depend on the size of the Au NPs which exactly happening in our investigation where electron transfer rates are faster in HS-2 as compared to HS-1.

Now to follow the charge transfer dynamics we have also monitored transient kinetics of the positive absorption band at 620 nm for both HS-1 and HS-2 and at 510 for HS-2. Figure 6.9 (a) shows the transient kinetics at 620 nm for HS-1 which can be fitted with single exponential growth 150 fs and multi-exponential recovery with time constants $\tau_1 = 0.95$ ps (67%), $\tau_2 = 40$ ps (18%), and $\tau_3 = >1$ ns (15%) (Table 6.7). While Figure 6.9 (b) shows the transient kinetics at 620 nm for HS-2 which can be fitted with single exponential growth 140 fs and multi-exponential recovery with time constants $\tau_1 = 0.95$ ps (67%), $\tau_2 = 38$ ps (20%), and $\tau_3 = >1$ ns (13%) (Table 6.7). The growth component can be attributed to appearance time of electron from semiconductor domain to metal domain. However, the faster decay component of 0.95 ps component in both HS-1 and HS-2 can be attributed to the trapping of electron in the interface domain of metal and semiconductor.³⁶ The longer components can be attributed to recombination dynamics of electron in Au NP and hole in CdSe core of CdSe@CdS core-shell.

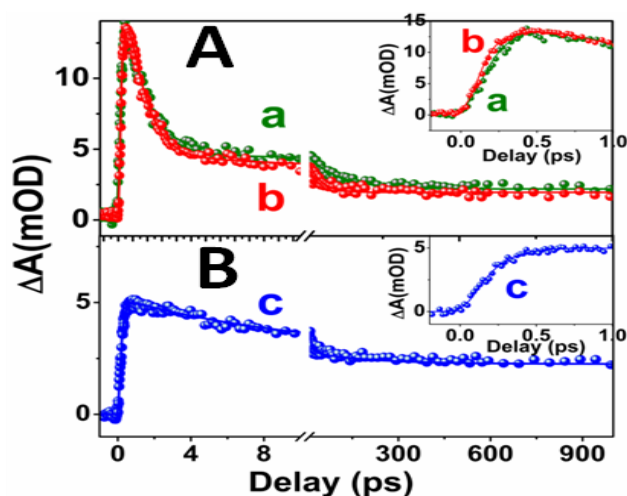


Figure 6.9: (A) Transient decay kinetics at 620 nm for (a) CdSe@CdS{Au}-1 (HS-1) and (b) CdSe@CdS{Au}-2 (HS-2) hetero-structure; (B) Transient decay kinetics at 510 nm for (c) CdSe@CdS{Au}-2 hetero-structure in chloroform after 400 nm laser excitation. **Inset:** Early time scale transient kinetics.

One of the most interesting observations in the present investigation is the appearance of the positive absorption band at ~ 515 nm in the transient spectra for HS-2 which can be attributed to charge separated state. Larger size of Au NP facilitates formation of CT complex (Figure 6.6D), and as a result charge separated band appears in the transient spectra of HS-2. Figure 6.9 (c) shows the transient kinetics at 510 nm which can be fitted with single exponential growth with time constant of 160 fs and multi-exponential decay with time constants of $\tau_1 = 10$ ps (41%), $\tau_2 = 200$ ps (8%), and $\tau_3 = >1$ ns (51%) (Table 6.7). The charge separated band appears due to transfer of photo-excited electron from different confined states of CdSe@CdS core-shell. From bleach recovery (at 480 nm) of HS-2 it can be concluded that major portion of the charge carriers are transferred to attached larger size Au NPs from hot

CHAPTER 6

states of quantum confined core-shell within 150 fs. So here in the 160-fs growth component can be attributed to hot electron transfer time from CdSe@CdS to Au

Table 6.7: The multi-exponential fitted parameters of decay kinetics of CdSe@CdS{Au}-1 and CdSe@CdS{Au}-2 hetero-structures.

System@ λ_{nm}	$\tau_{1(growth)}$	$\tau_1(\%)$	$\tau_2(\%)$	$\tau_3(\%)$
CdSe/CdS{Au}-1 @620 nm	150 fs	0.95ps (-67%)	40 ps (-18%)	>1 ns (-15%)
CdSe/CdS{Au}-2 @620 nm	140 fs	0.95ps (-67%)	38 ps (-20%)	>1 ns (-13%)
CdSe/CdS{Au}-2@ 510 nm	160 fs	10ps (-41%)	200 ps (-8%)	>1 ns (-51%)

in HS 2 is generated by hot electron transfer. The multi-exponential decay components can be attributed to charge recombination of electron in Au NPs and hole in the core-shell. Slow decay dynamics at 510 nm confirms slow charge recombination and higher charge separation.

C. Photocatalytic Study of CdSe@CdS{Au} NHM.

It's widely reported in the literature that Semiconductor-Metal hetero-structures are better materials for photo catalytic applications. From steady state and time-resolved absorption and luminescence studies, it's clearly confirmed that in the present investigation photo-excited electrons are efficiently transferred from semiconductor domain to metal domain in the hetero-structure. In our earlier investigation and also in the present studies we have observed that CdSe@CdS form quasi type II core-shell where electrons are delocalized in the conduction band of both CdSe core and CdS shell however, holes are selectively localized in CdSe core as a result electrons and holes are decoupled and give higher charge separation which is better materials for photo-catalysis and solar energy conversion. The photo-excited charges can further be separated if metal nanoparticles are couple with the

semiconductor, where electrons can be transferred to metal NPs. In our earlier studies, we have demonstrated higher charge separation vis a vis higher photo-catalytic activity in CdSe{Au} and CdSe@CdS{Au} hetero-structures. In the present investigation higher charge separated states are generated in CdSe@CdS{Au} depending on the size of the Au particles. So, to reconfirm higher charge separation in the above materials photo-degradation of Rh-B dye was carried out in presence of CdSe@CdS core-shell, HS 1 and HS 2 hetero-

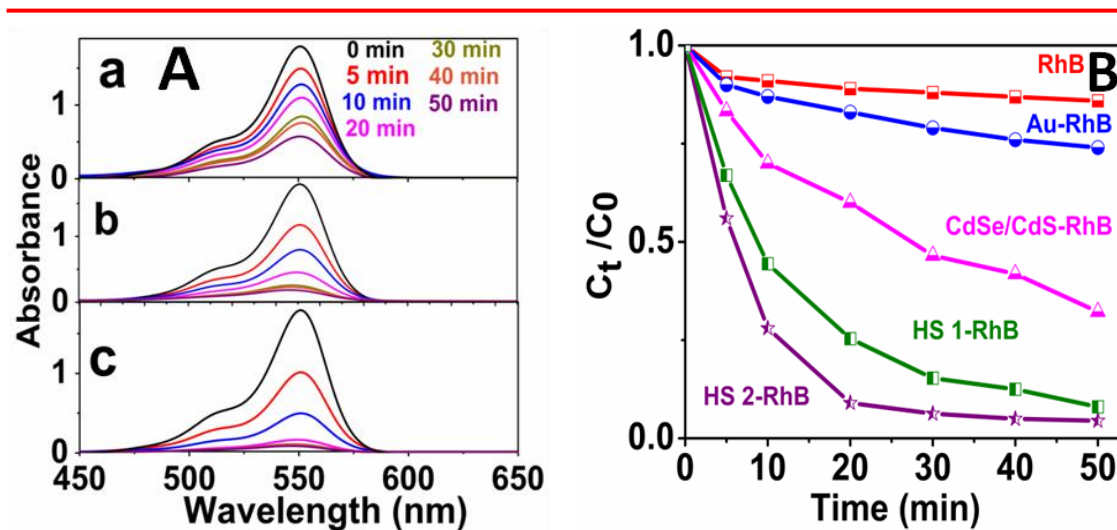


Figure 6.10: (A) Absorption spectra of rhodamin B (RhB) dye in presence of (a) CdSe/CdS core shell (b) HS 1 and (c) HS 2 at different time scale under 1 sun light illumination. (B) Plot of C_t/C_0 Vs time of RhB dye in presence of different materials under 1 sun light illumination.

structures. Figure 6.10 a, b and c show the absorbance spectra of RhB dye in presence of CdSe@CdS core-shell, HS 1 and HS 2 respectively at different time scale after illumination of 1 sun light. Before conducting photo-degradation of Rh-B dye in presence of the above nano-hetero structure materials we have also carried out optical absorption studies of Rh-B dye in presence of pure Au NP and in absence of any nano-structure materials. It has been observed that Rh-B dye is quite stable in presence of 1 sun light till 1 hour, and in presence of

Au NP minimum photo-degradation takes place under similar condition. However, in presence of the nano-structured materials photo-degradation of Rh-B dye is quite fast and found to be fastest in presence of HS 2. To investigate the rate of photo-degradation of RhB dye in presence of the above materials ratio of concentration at time t (C_t) and concentration at time zero (C_0) are plotted with time and shown in right panel of Figure 6.10 B. It has been observed that in presence of HS 2 more than 94% of RhB degraded within 20 minutes. On the other hand, only 75% of RhB degraded in presence of HS 1 within that time. Larger size of Au NP in the hetero-structure found to facilitate the photo-reduction of Rh-B dye. In our ultrafast transient absorption studies, we have observed that on photo-excitation HS 2 higher charge separation was observed due to hot electron transfer from CdSe@CdS core-shell to larger size Au NP. Exciton dissociation was facilitated due to strong coupling between QD exciton and Au plasmon band where hole was localized in the core of CdSe@CdS core-shell and electrons are quantitatively transferred to Au NP which eventually reduced the RhB molecules faster and effectively.

6.2.2 Shell Thickness Dependent Carrier Dynamics of CdSe@CdS{Au} Nanohybrid Materials.

A. Characterization and Optical Properties of CdSe@CdS{Au} NHM with Different Shell Thickness:

To characterise the CdSe@CdS{Au} NHM, we investigated the optical properties of CdSe@CdS core@shells before and after the growth of Au NP. At first the steady state optical absorption measurement of all the core shell and hybrid materials have been carried out. Figure 6.11 (a), (b), and (c) are the absorption spectra of CS 1, CS 2 and CS 3 NCs respectively. The 1st excitonic band (for 1Se–1S_{3/2} transition) at 578 nm for CS 1 gradually red shifted to 590 nm and 600 nm for CS 2 and CS 3 respectively. i.e. With increasing the shell thickness of CdS the red shifting of exciton reveals the decrease of binding energy due

to delocalisation of electron in the core and shell. From our earlier report we have seen that the CdSe@CdS core shell forms the quasi type II band alignment, because the band offset for conduction band of CdSe and CdS is higher ($\sim 0.2\text{eV}$), but the band off set between valence band of CdSe and CdS is $\sim 0.5\text{eV}$.^{45,46} The absorption at the blue region of the core shell is

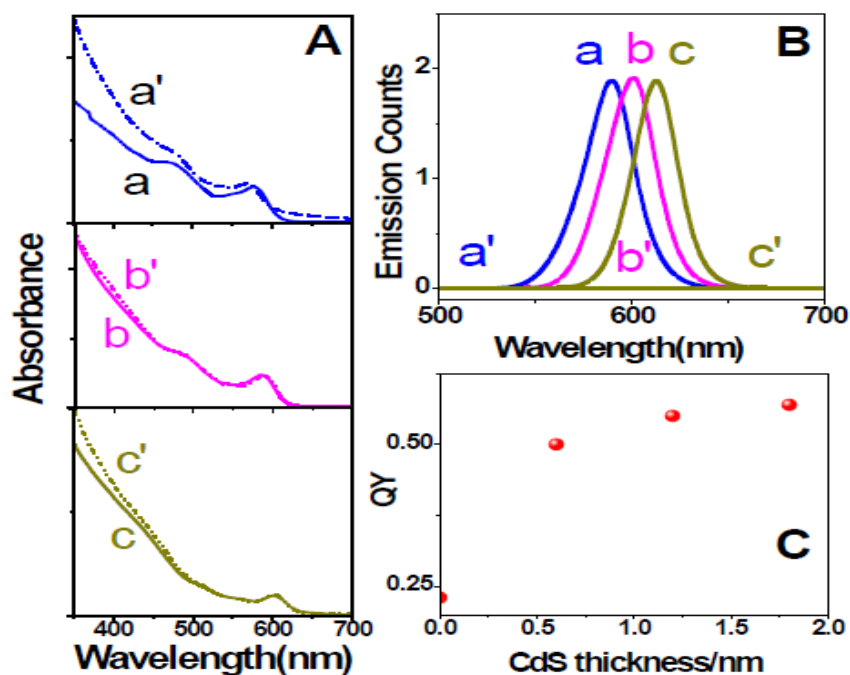


Figure 6.11: (A) UV-Visible absorption and of (a, a') CS 1 and HS 1(dotted line), (b, b') CS 2 and HS 2 (dotted line), (d) CS 3 NCs and HS 3. (B) Steady state luminescence spectra of (a, a') CS 1 and HS 1, (b, b') CS 2 and HS 2 (dotted line), (d) CS 3 NCs and HS 3. (C) Graphical diagram of QY Vs CdS Shell thickness.

increased with increasing the shell thickness corresponds to absorption due to CdS shell. All the absorption spectra of CdSe and core shell show the three distinct bands. The CS 1, CS 2 and CS 3 show the band for $1\text{Se}-2\text{S}_{3/2}$ transition at 545, 554 and 578 nm respectively. The absorption below 500 nm is contributed by 1P ($1\text{Pe}-1\text{P}_{3/2}$) transition and CdS absorption.

Figure 6.11 (a), (b), and (c) are the absorption spectra of HS 1, HS 2 and HS 3 NCs respectively. The changing the absorption profile of the core shell after growth of Au NP is more in case of thin layer of CdS and less change is observed in HS 3. The absorption profile of HS 3 is almost same as core shell. Only change is the absorption at the blue region of the spectra. This reveals that the exciton Plasmon coupling is going to reduce with increasing the thickness of the CdS shell. The shell acts as a barrier to couple the exciton with Plasmon. The figure 6.11 B (a), (b) and (c) show the luminescence spectra of CS 1, CS 2, and CS 3 respectively. The luminescence spectrum is red shifted with increasing the shell thickness of the CdS shell. The quantum yield of the CdSe core is 22% and enhanced tremendously in CS 1 (55%) than CdSe, but the QY does not change that much beyond the 2 ML shell thickness showing in figure 6.11 C. The enhancement of the luminescence is due to elimination of the trap state by the CdS shell. The luminescence of the all core shell is totally quenched after growth of Au NPs, are shown in figure 6.11. Figure 6.11 (a'), (b') and (c') are the luminescence spectra of HS 1, HS 2 and HS 3, respectively. The electron transfer from core shell to Au NP causes the quenching of luminescence of all the core shells.

B. TA Studies of CdSe@CdS{Au} NHM with Different Shell Thickness:

To investigate the charge carrier dynamics in ultrafast time scale we have measured the femtosecond transient absorption spectroscopy study of all the core shell and nano hybrid materials after 400 nm laser excitation. Figure 6.12 (a), (b) and (c) are the transient absorption spectrum of CS 1, CS 2 and CS 3 after 400 nm laser excitation. The bleach due to transition of $1S_e-1S_{3/2}$ are at 576 nm, 587 nm and 599 nm for CS 1, CS 2 and CS 3, respectively. The first exciton of the core shell is red shifted according to steady state absorption studies. The 2S bleach for CS 1, CS 2 and CS 3 are at 545 nm, 550 nm and 555 nm respectively. The bleach intensity below 500 nm gradually increases with increasing the

shell thickness of the core shell which reveals the CdS absorption is added up with 1p bleach intensity of the CdSe core. The minimum photo induced absorption at the red region of the spectrum introduces the negligible defect states in all the core shell materials.

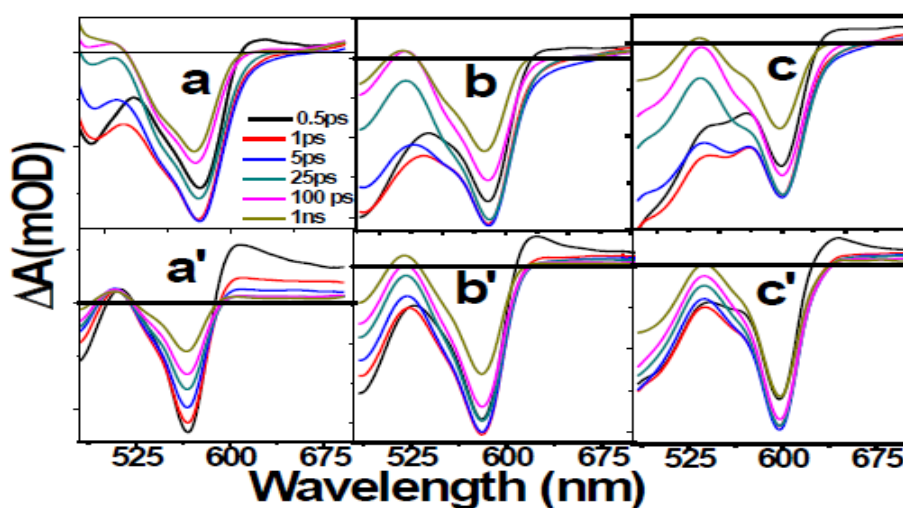


Figure 6.12. Transient absorption spectra of (a, a') CS 1 and HS 1, (b, b') CS 2 and HS 2, (c, c') CS 3 and HS 3 at different time delay after 400 nm laser excitation.

The spectral feature of all core shell is changed after growth of the Au NP. The figure 6.12 (a'), (b') and (c') are the TA spectra of HS 1, HS 2 and HS 3. The first exciton of the CS 1 is blue shifted to 565 nm from 576 nm. The first exciton of the CS 2 and CS 3 are at 581 nm and 597 nm. This blue shifting is lesser in HS 2 and HS 3 with compared to HS 1. The shell thickness of CdS decrease the interaction between gold NP and core. The interesting phenomenna of the hybrid structure is the positive absorption feature at the red region of the spectrum. The broad excited state photoinduced absorption introduces the charge separated state formation between the core shell and Au NP, which is discussed in earlier part of this chapter. The PA feature gradually decreases with increasing the shell thickness of the CdS shell. This reduction of PA reveals the electron transfer is restricted by the thicker CdS shell.

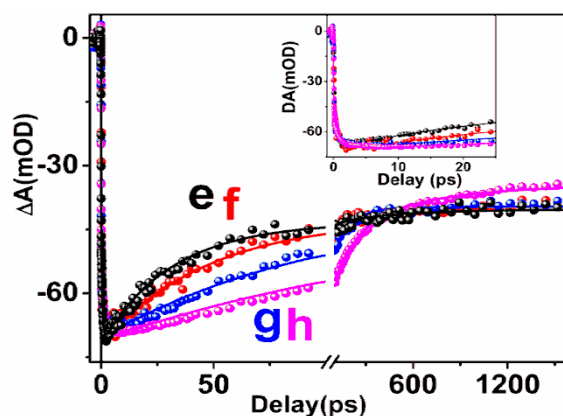


Figure 6.13. Exciton Bleach dynamics of (a) CdSe at 570 nm, (b) CS 1 at 578 nm (c) CS 2 at 587 nm and (d) CS 3 at 600 nm after 400 nm excitation. **In Inset.** Early time scale dynamics of a, b, c and d.

To investigate the shell thickness dependent charge transfer between core shell and gold NP, first we need to discuss the carrier cooling and recombination dynamics of CdSe@CdS core shell with different shell thickness. Figure 6.13 (a), (b), (c) and (d) are the first exciton dynamics of the CdSe, CS 1, CS 2 and CS 3 respectively. The growth component for CdSe are <100fs (75%) and 500 fs (25%), and the growth components dramatically changed with increasing the shell thickness of core shell. The growth components are <100fs (75%) and 1.5 ps (25%) for CS2, <100fs (75%), 1 ps (20%) and 7 ps (5%) for CS 2 and finally these components are <100fs (75%), 1ps (21%) and 9 ps (4%) for CS 3. These increments of the growth components reveal that the carrier cooling time increases with shell thickness. The enhancement of the carrier cooling introduces two factors, one is reduction of the trap state and other one is the quasi type II band alignment of the core shell. With increasing the shell thickness the surface trap state of the CdSe is going to eliminate, resulting slow down the carrier cooling. The other important factor for slow carrier cooling is the quasi type II band alignment of CdSe@CdS core shell. The electron wave

CHAPTER 6

function is delocalised through the CB of core and shell but the hole is confined in the core. Hence the electron and hole is more decoupled in thicker shell resulting the longer cooling. The recombination dynamics of the core shell is interestingly changed with changing the shell thickness. The CdSe bleach decays by a 30 ps faster component followed by a 400 ps longer component. The faster and longer components attribute the carrier trapping and exciton recombination. The faster component gradually increases with CdS shell thickness, are shown in table 6.8. The decay components are 47 ps (-37%) for CS 1, 95 ps (-43%) for CS2 and 150 ps (-46%) for CS 3. The decay is going to be extremely slow in higher shell thickness attributing the trap state is gradually eliminated with increasing the thickness of CdS shell. Therefore the recombination contributed by the trap state is eliminated by the shell thickness. The other important factor of the slow recombination is the electron hole decoupling in quasi type II band alignment due to delocalisation of the electron in the shell. With increasing the shell thickness the electron hole are more decoupled and slow down the recombination processes. To investigate the charge transfer processes we need to compare the carrier dynamics of the core shell absence and presence of Au NP. First we compare the bleach dynamics at the first exciton position. Figure 6.14 a',b',c' and d' are the bleach dynamics of the CdSe/Au@565 nm, HS 1@575nm, HS 2@588nm and HS 3@600nm respectively. The bleach dynamics of the HS is extremely faster than the CdSe. There is no growth component of this bleach and the decay components are 0.6 ps (-86%) and >1ns (-14%). But the scenario is going to change dramatically when CdS shell is present on the CdSe core. The bleach of the HS1 at 575 nm is faster compare to CS 1, but not that much faster like CdSe/Au nanohybrid and the decay components for HS 1 are 2 ps (28%), 85 ps (28%) and >1ns (44%). This reveals that the electron transfer is slowed down in presence of CdS shell. The bleach of HS 2 fitted by <100fs (85%) and 500 fs (15%) growth components

followed by the 5ps (10%), 40 ps (15%), 250 ps (9%) and >1 ns (66%) decay components. The 1st decay component is faster than the CS 2 but the longer components are slower than the CS 2.

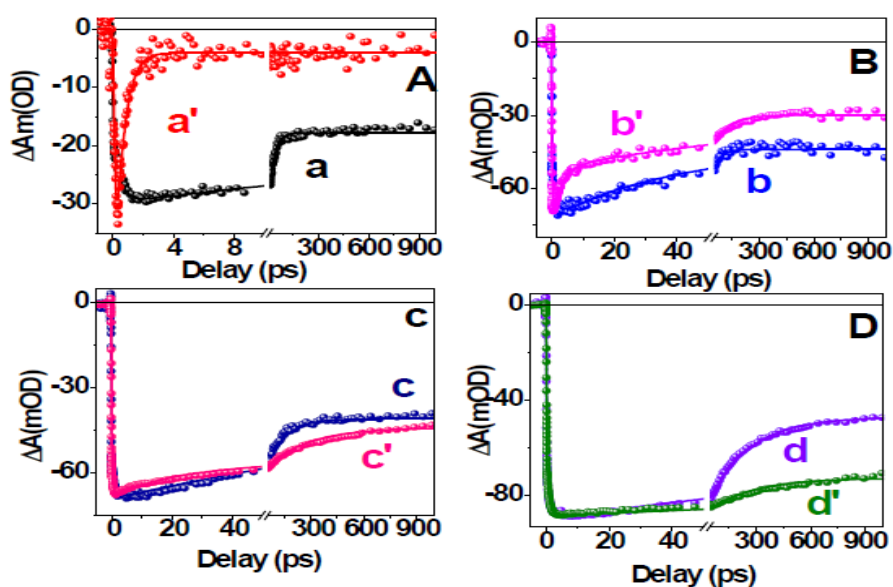


Figure 6.14. Bleach kinetics of (a,a') CdSe@570 nm and CdSe/Au@565 nm, (b,b') CS 1 and HS 1@575 nm, (c,c') CS 2 and HS 1@588 nm (d,d') CS 3 and HS 3 @600 nm.

The bleach of the HS 3 at 600 nm is more interesting. The growth components are 100 fs (75%), 1ps (20%) and 10 ps (5%) which is slower than the CS 3. The Decay components of this bleach are 250 ps (-18%) and >1ns (-82%), which are extremely slower than the CS 3. This represents that the electron transfer is slows down with increasing the shell thickness. In presence of Au NP on the surface of core shell, with increasing the shell thickness the decoupling of electron hole is also gradually increases, Therefore the back recombination becomes extremely slows down and the electron transfer also slows down with increasing the shell thickness. At HS 3 the extremely slow decay represents the slow recomobination. At highest shell thickness the slowest cooling hasbeen shown due to decoupling of electron and

CHAPTER 6

hole in this quasi type II core shell in presence of attached Au NP. The decoupling is more enhanced in presence of attached Au NP due to slow electron transfer from core shell to Au NP.

Table 6.8: Multi-exponential fitted parameters for bleach dynamics of all core shell and heterostructure at different wavelength.

System @wavelength	τ_{g1} (%)	τ_{g2} (%)	τ_{g3} (%)	τ_1 (%)	τ_2 (%)	τ_3 (%)
CdSe-570nm	<100fs (75%)	500fs (25%)		30 ps (- 37%)	400ps (- 4%)	>1 ns (- 59%)
CdSe@CdS2ML- 578 nm	<100fs (75%)	1.5ps (75%)		47 ps (- 37%)	600ps (- 5.5%)	>1 ns (- 57.5%)
CdSe@CdS4ML- 588 nm	<100fs (75%)	1ps (20%)	7 ps (5%)	95 ps (- 43%)	600 ps (- 2.5%)	>1 ns (- 54.5%)
CdSe@CdS6ML- 600 nm	<100fs (75%)	1ps (71%)	9 ps (4%)	150 ps (- -46%)	600 ps (- 2%)	>1 ns (- 52%)
CdSeAu-570nm	<100fs (100%)			0.6ps (- 86%)	>1ns(- 14%)	
CdSe@CdS2MLAu- 578 nm	<100fs (100%)			2ps(- 28%)	85ps(28%)	>1ns(- 44%)
CdSe@CdS4MLAu- 588 nm	<100fs (85%)	500fs (15%)		5ps(- 10%)	40ps(- 15%)	250ps(9%) >1ns(- 66%)
CdSe@CdS6MLAu- 600 nm	100fs (75%)	1ps (20%)	10ps (5%)	250ps(- 18%)	>1ns(- 82%)	

Figure 6.15 a, b and c represents the bleach dynamics of the CS1, CS2 and CS3 at 480 nm respectively. The bleach of CS 1 is grown in pulse width limited time and the decay components are 2.5 ps (-63%) and 11ps (-37%). Interestingly the growth components gradually increase with increasing shell thickness. The growth components for CS2 and CS 3 are <100fs (75%), 700 fs (25%) and <100 fs (25%), 0.5 ps, respectively. Similarly the decay also becomes slows down with increasing the thickness of the shell. The decay components for CS2 are 11 ps (-72%), 90 ps (-11%) and >1ns (-17%), whereas these components for CS 3 are 5.5 ps (51%), 70ps (-12%) and >1ns (-37%). The increasing lifetime at 480 nm

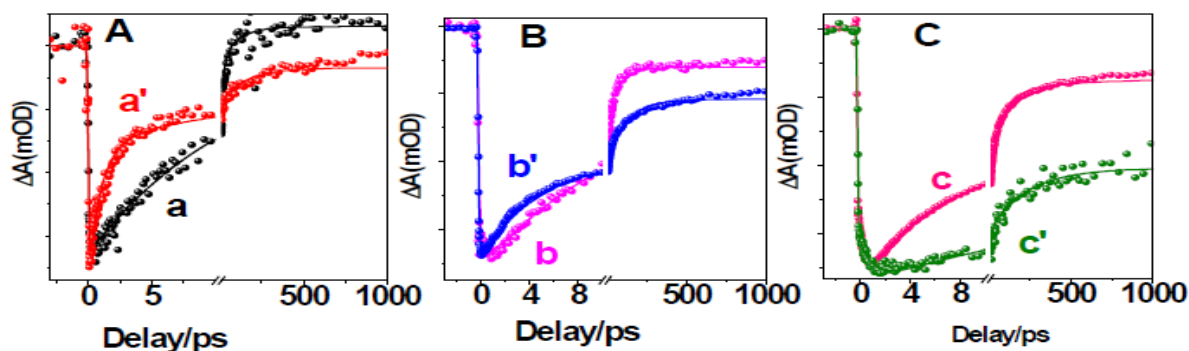


Figure 6.15. Bleach kinetics of (a,a') CS 1 and HS 1@480 nm, (b,b') CS 2 and HS 1@480 nm (c,c') CS 3 and HS 3 @480 nm.

reveals the mixing of state at the interface of the core shell. The bleach dynamics of all the core shell dramatically changes after growth of the Au NP. The figure 6.15 a', b' and c' show the bleach dynamics of the HS 1, HS2 and HS 3 at 480 nm respectively. The bleach of HS 1 is pulse width limited growth followed by very fast decay and the decay components are 1 ps (-22%), 10 ps (-17%), 150 ps (-9%) and >1 ns (-37%). The decay is very faster than the CS 1. This reveals the very fast electron transfer is occurred from core shell to Au. The decay of HS 2 bleach has decayed by a fast component followed by a longer component, i.e, 3 ps (41%), 70 ps (13%) and 1 ns (46%). These reveal that the fast electron transfer followed by the slow recombination. Most interesting is the bleach dynamics of HS 3. The longer cooling that CS 3 and slower recombination than core shell is observed after growth of the Au NP. The growth components are 100 fs (75%) and (25%), whereas the decay components are 10 ps (-22%), 200 ps (20%) and >1ns (58%). From the fitted parameter we have seen that the cooling of HS is increasing with increasing the CdS shell thickness and the recombination also slows down in presence of Au NP. This reveals that in thickest core shell the electron hole is already decoupled due to quasi type II core shell and it is enhanced in presence of Au NP. The electron-hole decoupling is more enhanced by slow electron transfer from core shell to Au

NP.

Table 6.9: Multi-exponential fitted parameters for bleache dynamics of all core shell and heterostructure at 480 nm wavelength.

System @wavelength	τ_{g1} (%)	τ_{g2} (%)	τ_1 (%)	τ_2 (%)	τ_3 (%)
CdSe@CdS2ML-480	<100fs (100%)		2.5 ps (- 63%)	11ps (- 37%)	
CdSe@CdS4ML-480 nm	<100fs (75%)	700fs (25%)	11 ps (- 72%)	90 ps (- 11%)	>1 ns (- 17%)
CdSe@CdS6ML-480 nm	<100fs (75%)	0.5ps (25%)	5.5 ps (- 51%)	70 ps (- 12%)	>1 ns (- 37%)
CdSe@CdS2MLAu-480 nm	<100fs (100%)		1ps(- 22%)	10ps(17%)	150ps(9%) >1ns(- 51%)
CdSe@CdS4MLAu-480 nm	<100fs (100%)		3ps(- 41%)	70ps(- 13%)	>1ns(- 46%)
CdSe@CdS6MLAu-480 nm	100fs (75%)	1.2ps (25%)	10ps(- 22%)	200 ps(- 20%)	>1ns(- 58%)

Earlier of this chapter we have discussed the photoinduced absorption at the red region of the spectra, representing the charge separated state between metal and semiconductor. We resolved these feature as electron density on the Au NP after transfer from photo excited core shell. The role of the shell thickness of CdS on the back recombination from Au NP can be discussed by the dynamics of the photoinduced absorption at the red region of the spectra. It is exciting to see that the dynamics of the HS 1, HS 2 and HS 3 at the wavelength of 680 nm and have been shown in figure 6.16 a, b and c. The growth component for HS 1 is 100 fs but this component gradually increases with increasing the shell thickness, shown in inset of figure 6.16. 150 fs (90%) and 400 fs (10%) (table 6.10) are the growth components for HS 2, whereas these components for HS 2 are 150 fs (90%) and 600 fs (10%) (Table 6.10). This growth component represents the electron transfer time, which slows down with increasing the shell thickness, which is already discussed in exciton bleach dynamics. The shell prevents

the electron transfer from core shell to Au NP by making a potential barrier. The tri-exponential decay components for HS 1 are 2 ps (-81%), 25 ps (-7%), 150 ps (-3%) and >1 ns (-9%). The decay is gradually slows down with increasing the shell thickness of CdS. The decay of HS 2 is bi-exponential and the components are 3

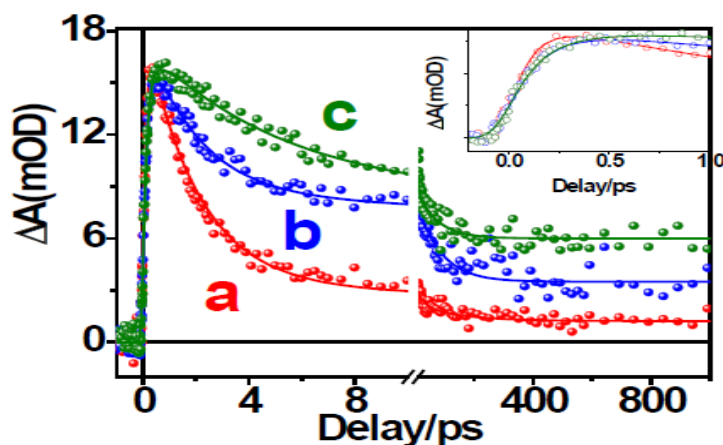


Figure 6.16. Photoinduced absorption dynamics of (a) HS 1 (b) HS 1 (c) HS 3 at 680 nm. **Inset.** Early time scale dynamics of a,b and c.

ps (-51%), 80 ps (-26%) and >1ns (-23%). The decay of HS 2 is slower than HS 1 and the components are 5 ps (-48%), 100 ps (-14%) and >1 ns (-38%). The decay represents the back

Table 6.10: The multi-exponential fitted parameters for decay kinetics of HS 1, HS 2 and HS 3 hetero-structures.

System @wavelength	τ_{g1} (%)	τ_{g2} (%)	τ_1 (%)	τ_2 (%)	τ_3 (%)	τ_4 (%)
CdSe@CdS2MLAu-680 nm	100fs (100%)		2ps(-81%)	25ps(7%)	150ps(3%)	>1ns(-9%)
CdSe@CdS4MLAu-680 nm	150fs (90%)	400fs(10%)	3ps(-51%)	80ps(-26%)	>1ns(-23%)	
CdSe@CdS6MLAu-680 nm	150fs (90%)	600ps (10%)	5ps(-48%)	100 ps(-14%)	>1ns(-38%)	

electron transfer from Au NP to core shell. But the slower decay of this positive absorption

reveals the back electron transfer becomes slow down with increasing the shell thickness of CdS. The CdS shell prevents to come back electron and recombine by making a potential barrier. Therefore the charge separation between core shell and Au NP is enhanced with increasing the shell thickness of CdS, despite the slower electron transfer. The thickest CdS shell makes a longer lived charge separated state between core shell and gold NP.

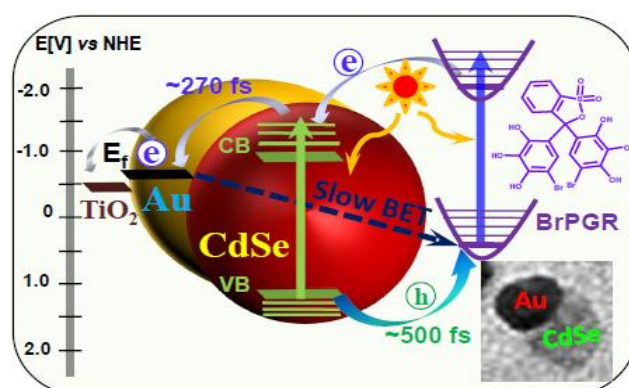
6.3 Conclusions.

In conclusion, the enhancement of PCE by the Au NP in Au/CdSe NHM has been discussed in this manuscript by detail spectroscopy study. The measured PCE of CdSe is found to be ~3.37% which is 30% enhanced to 4.39% in Au/CdSe NHM. The steady state study reveals the broadening the absorption spectra up to 800 nm by the Au NP in Au/CdSe NHM due to increase of carrier density on the Au NP surface after transfer from CdSe to Au NP, which is responsible for the enhancement of PCE efficiency. The steady state and time resolved luminescence studies represented the fast electron transfer from QDs to Au NP, which enhances the availability of carrier density to generate the more current. Finally the TA spectroscopy implies the formation of long lived charge separated state at the red region between Au and CdSe which enhances the PCE of the solar cell by improving the charge injection efficiency. The Au NP slows down the back electron-hole recombination process and enhances the PCE by increasing the charge collection efficiency of Au/CdSe. By EIS we have measured the three times higher recombination resistance of Au/CdSe NHM compared to CdSe QDs and correlated with the enhancement of PCE by the NHM. Additionally, the size dependent hot and thermalised electron transfer dynamics between CdSe@CdS core-shell and Au NPs have been discussed by femto second transient absorption studies. Hot and thermalized electron transfer times were determined to be 150 and 300 fs from 1P and 1S excitonic states of CdSe@CdS core-shell to Au NP in the hetero-structure, respectively.

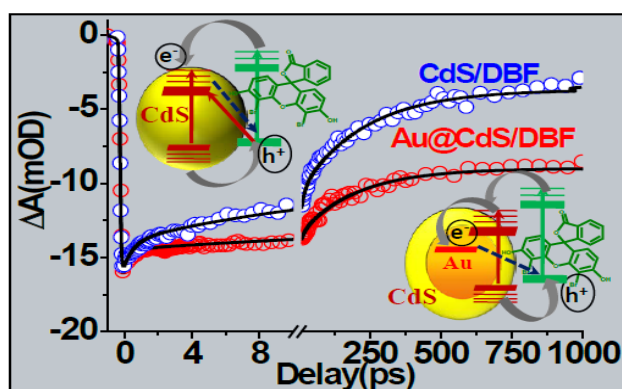
Formation of charge separated states found to be facilitated with larger size Au NP where both hot and thermalized electrons are captured by Au NP and holes are localized in CdSe core. Efficient charge separation in CdSe@CdS{Au} hetero-structure was reconfirmed by employing photo-catalytic degradation of RhB under visible radiation which suggests that hot electron in the hetero-structure play a major role in efficient photo-catalytic reactions. Again we extend this work by measuring shell thickness dependent carrier dynamics in CdSe@CdS{Au} hetero-structure. The CdS shell plays a vital role in charge transfer and separation processes. With increasing the shell thickness the electron transfer becomes slow down, but the life time of the charge separated state gradually increases with increasing the shell thickness. By making a potential barrier by CdS shell, restrict the back electron transfer from Au to core shell, resulting enhancement of charge separation.

CHAPTER-7

ENHANCEMENT OF CHARGE SEPARATION IN METAL-SEMICONDUCTOR NANOHYBRID MATERIAL BY SENSITISATION WITH DYE MOLECULE



J. Phys. Chem. C 119 (38), 22181-22189



To be Communicated.....

7.1 Introduction:

Research has been focused on the design and development of higher-efficiency quantum-dot sensitized solar cells (QDSCs) in the last decade due to the excellent optoelectronic properties of quantum dot sensitizers.^{104, 106, 109, 303, 304} Due to the strong confinement of charge carriers in QD materials there is significant enhancement of the electron-hole Coulomb interaction. This enhancement leads to efficient multiple exciton generation (MEG),³⁰⁵ a process where a single photon can generate more than one exciton (electron-hole pair). However, due to the strong confinement effect, Auger recombination takes place, which reduces the lifetime of the QD excitons on the order of tens of picoseconds.³⁴ So it is utmost important to extract the multiple excitons (charge carriers) before they go for efficient Auger recombination to design and develop higher efficient QD solar cell.

The nanohybrid material composed of metal and semiconductor is the subject of great current interest due to their potential applications in solar energy conversion, biosensing and photocatalysis.^{91, 95, 262-267, 274, 306} In nanohybrid material ultrafast electron transfer takes place from semiconductor/QD to metal as a result of Auger recombination is minimized. In semiconductor-metal nanohybrid material, metal NPs are directly grown on the semiconductor surface without any spacer, hence the electronic mixing between the electronic states of metal and semiconductor takes place very effectively.²⁷⁸ As a result, the inter domain charge transfer can take place very efficiently from the semiconductor domain to the metal domain.^{268, 279, 291} In most of the nanohybrid systems the Fermi level of the metal lies below the CB of the semiconductor. As a result, electron transfer from photoexcited QD to metal NP is thermodynamically viable. Park and co-workers²⁶⁹ demonstrated ultrafast electron transfer from photoexcited CdSe to Pt metal in Pt-CdSe-Pt nanodumbbells. Lian

and co-workers⁹⁴ demonstrated ultrafast electron transfer from the photoexcited CdS rod to the Au tip and also plasmonic hot electron transfer from the Au tip to the CB of the CdS rod. Again, ultrafast charge separation and a long-lived charge-separated state were observed by Lian and co-workers⁹⁵ in CdS–Pt nanorod heterostructures due to ultrafast electron transfer from CdS QD to Pt metal. Earlier, Mongin et al.²⁶⁵ demonstrated sub-20-fs electron transfer from the band-edge state ($1\sigma_e$ state) of CdS NRs. In addition to that, electron transfer was also demonstrated in a different kind of semiconductor-metal heterostructure such as metal-tipped CdS and CdSe nanorods (NRs),³⁰⁷ Au-appended CdSe and PbS quantum dots (QDs),^{308, 309} and a Au@PbS core@shell nanohybrid material.²⁸⁰ In all of the above systems charge-transfer dynamics were monitored by using different spectroscopic techniques such as single-molecule spectroscopy, time-resolved emission, and TA studies.

Ultrafast dissociation of excitons through electron and hole transfer processes in different QD/molecule systems and molecular adsorbate/semiconductor (TiO₂) systems have been extensively reported in the literature.^{107, 211-213, 310-317} Recently we have reported the dissociation of excitons through the extraction of both hot holes and thermalized holes by xanthenes, triphenyl methane, and catechol derivatives. Hot hole and thermalized hole extraction times were found to be 250 fs and 500 fs-1 ps,^{211-213, 316} respectively. So far all the reports available in the literature are for the dissociation of excitons either by electron transfer or by hole extraction. However, no report is available in the literature where both electrons and holes are extracted from the photoexcited QD materials at the same time.

To demonstrate exciton dissociation simultaneously by both electron and hole extraction, in this current investigation we have synthesized CdSe{Au} heterostructure (HS) and Au@CdS core shell materials and consequently sensitize CdSe{Au} HS and Au@CdS

core shell by the bromo-pyrogallol red (Br-PGR) and dibromo-fluorescein dye (DBF) molecule, respectively. Subsequently, the charge-transfer reaction was monitored by the time-resolved luminescence and ultrafast TA techniques. Both the time-resolved absorption and emission techniques suggest that in CdSe{Au} HS photoexcited electrons are transferred from the semiconductor domain to the metal domain. As the Fermi level of Au NP lies below the CB of CdSe QD, so electron transfer is thermodynamically viable. A steady-state optical absorption study suggests that Br-PGR molecules form a strong charge transfer (CT) complex. As the LUMO and HOMO of the Br-PGR molecule lie above the conduction band and valence band of CdSe QD,²¹² so electron injection from the photoexcited state to the CB of CdSe QD and hole transfer from the VB of photoexcited CdSe QD are thermodynamically viable. Both electron and hole transfer and charge recombination dynamic in the CdSe{Au}/Br-PGR tri-composite system have been unraveled by using both time-resolved luminescence and ultrafast TA spectroscopy techniques. Similarly, the steady state optical absorption measurement study confirms the charge transfer complex (CT) formation between Au@CdS core shell nanohybrid with the DBF molecule. The CB of the CdS is lies below the HOMO of the DBF molecule and the LUMO of the DBF molecule is lies above the VB of CdS.²¹¹ The steady state and time resolved luminescence studies reveal the charge transfer between core shell and DBF molecule. The electron transfer from HOMO of the DBF molecule to the CB of the CdS and hole transfer from VB of the CdS to the LUMO of the DBF after photo excitation is thermodynamically favorable. Finally the TA spectroscopy has been appointed to measure the electron and hole transfer dynamics in this triad system where the electron and hole transfer time from DBF molecule to the CB of the CdS and CdS to the DBF were <100 fs (pulse width limited) and 400 fs, respectively.

7.2. Results and Discussion:

7.2.1 Charge Separation in CdSe{Au} HS and BrPGR Triad System.

A. Characterization and Optical Properties of CdSe{Au} HS:

To characterize the Au-CdSe nanohybrid structure, HR-TEM measurements have been performed and are shown in Figure 7.1 A. It is clearly seen from the HRTEM image that Au NP is nicely coupled on the surface of CdSe QD, where the size of Au NP can be determined to be 3–3.5 nm and the size of CdSe QD is found to be 4–4.5 nm. The HR-TEM image clearly shows the homogeneous deposition of Au on the surface of CdSe QD. Separate lattice images of CdSe QD and Au NP are clearly seen in the TEM image. The optical

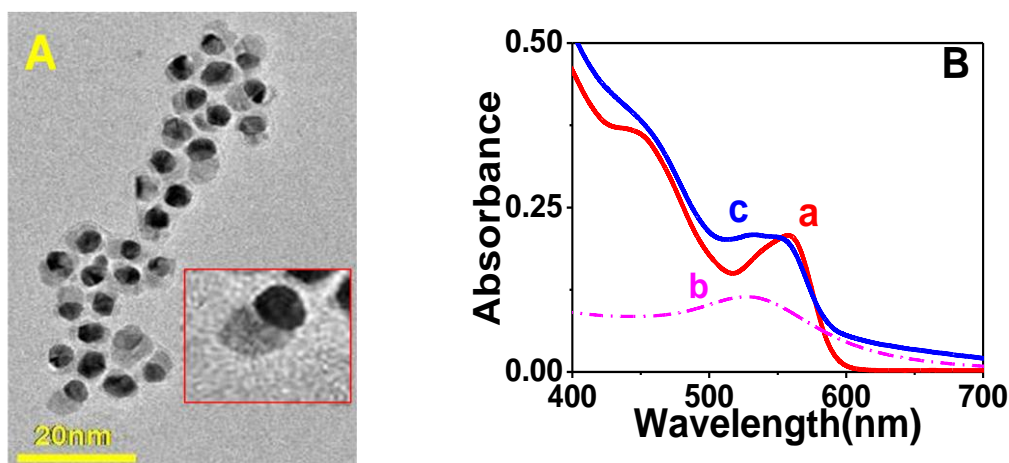


Figure 7.1 A: HR-TEM picture of CdSe{Au} HS material. (In Inset magnified image of Au/CdSe). **B**: Steady state optical absorption spectra of (a) CdSe quantum dot, (b) Au NP and (c) CdSe{Au} HS in chloroform.

absorption measurements have also been carried out to characterize the CdSe QD and CdSe{Au} heterostructures (HSs) in chloroform solution, which are shown in Figure 7.1.B. At this point, we have also synthesized Au NPs with size of 3 to 4 nm and have compared the optical properties with those of CdSe{Au} HS, as also shown in Figure 7.1.B. Figure 7.1a

shows that the steady-state optical absorption spectra of CdSe QD consists of two excitonic absorption bands at 560 and 450 nm which can be ascribed to $1S(e)-1S_{3/2}(h)$ and $1P(e)-1P_{3/2}(h)$ transitions, respectively. Figure 7.1B(b) shows the optical absorption spectra of Au NPs with a particle size of 3 to 4 nm, which has optical absorption due to the plasmon band at 527 nm. Figure 7.1c shows optical absorption spectra of CdSe{Au} HS where Au NP is grown on the surface of CdSe QD. It can be seen clearly that the optical absorption band becomes broad as compared to both CdSe QD and Au NP. From the optical absorption studies it is clear that the electronic interaction between the plasmonic band of Au NP and the excitonic band of CdSe QD is quite strong.

In an earlier investigation, Lian and co-workers⁹⁴ demonstrated the broadening of an optical absorption band for the CdS-Au composite materials where Au NP is located in the tip of the CdS nanorod. Due to direct coupling between the electronic states of the plasmon band of Au NP and the excitonic band of the QD, there is a change in the optical absorption spectra of the heterostructure materials. Due to mixing, the refractive index of the interdomain area changed, resulting the excited-state properties and the charge carrier dynamics of both Au NP and CdSe QD are expected to be changed.

To monitor the excited-state behaviour of the heterostructure, steady-state and time-resolved luminescence studies have been carried out for both CdSe QD and CdSe{Au} HS. Figure 7.2a shows the photoluminescence spectra of CdSe QD with an excitonic emission peak at 580 nm (emission quantum yield (QY) $\phi_f = 0.34$). The emission intensity of high QY CdSe is completely quenched (Figure 7.2b) in the case of CdSe{Au} HS. Scheme 7.1 suggests that the Fermi level of Au NP lies below the conduction band of CdSe QD. The emission quenching of CdSe luminescence in CdSe{Au} HS materials can be attributed to

the electron transfer from the CB of CdSe QD to Au NP which is thermodynamically viable.

The electron transfer reaction can be explained by the equations given below:

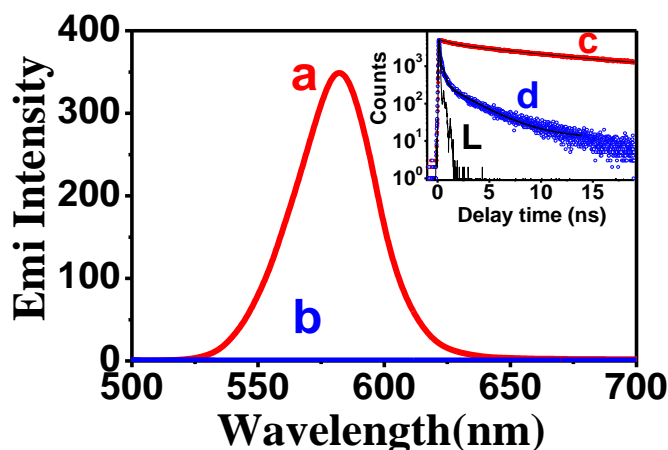
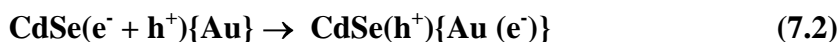
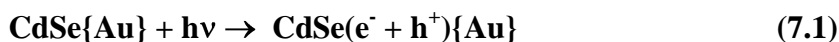
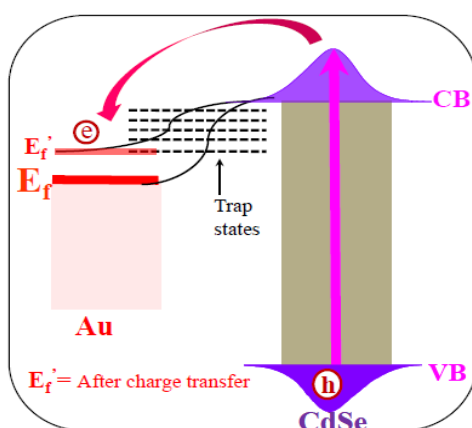


Figure 7.2: Steady state photoluminescence spectra of (a) CdSe quantum dot (b) CdSe{Au} HS. **Inset:** Time resolved luminescence decay trace of (c) CdSe quantum dot and (d) CdSe{Au} HS at 580 nm after exciting the samples at 406nm. (L is the lamp profile of 406nm laser)

To reconfirm the electron-transfer process, time-resolved luminescence measurements have also been carried out. Figure 7.2 (c) and (d) show the luminescence decay trace at 580 nm after exciting the sample at 406 nm for CdSe QD and CdSe{Au} HS, respectively. The emission decay trace of CdSe QD can be fitted bi-exponentially with time constants of $\tau_1 = 1.03 (\pm 0.05)$ ns (30%) and $\tau_2 = 16.13 (\pm 0.5)$ ns (70%) with $\tau_{\text{avg}} = 11.66 (\pm 0.5)$ ns. Interestingly, the emission kinetics for CdSe{Au} HS are found to decay much faster and can be fitted bi-exponentially with time constants of $\tau_1 = 0.31 (\pm 0.01)$ ns (86%) and $\tau_2 = 3.72 (\pm 0.15)$ ns (14%) with $\tau_{\text{avg}} = 0.72 (\pm 0.05)$ ns. In our earlier report²²¹ we have demonstrated

CHAPTER 7

(and also described by others)³¹⁸ that the shorter component of QD emission can be attributed to e/h trapping in sub-bandgap localized states of the QDs. On the other hand, the longer component can be assigned to the radiative recombination (orbital forbidden) of trapped



Scheme 7.1: Schematic diagram showing electron transfer from semiconductor domain to the metal domain in CdSe{Au} nano hybrid material.

charge carriers. In Au-CdSe the emission lifetime can be fitted bi-exponentially with time constants of $\tau_1 = 0.31$ ns (86%) and $\tau_2 = 3.72$ ns (14%). The faster decay components can be attributed to the nonradiative transfer of electrons from photo excited CdSe to Au NP. The average lifetime of the CdSe{Au} HS system is more than 16 times shorter as compared to that of CdSe QD, which confirms the electron transfer process in the composite materials as shown in eq 7.3. In all probability the observed reduction in lifetime arises due to electron transfer (ET) from CdSe QD to Au NP, and then the ET rate constant can be calculated from the following expression:

$$K_{ET} = 1/\tau_{CdSe\{Au\}} - 1/\tau_{CdSe} \quad (7.3)$$

From the average lifetime values, 11.66 (± 0.5) ns (CdSe) and 0.72 (± 0.05) ns (CdSe{Au}), the electron-transfer rate constant was determined to be 1.39×10^9 s⁻¹.

B. Transient Absorption Study of CdSe{Au} HS:

To confirm the electron transfer on the early time scale and to monitor the excited state properties specifically for CdSe{Au} HS, we have carried out femtosecond TA spectroscopic measurements by exciting CdSe QD and CdSe{Au} HS with a 400 nm laser pulse. Figure 7.3A shows the TA spectra of CdSe QD at different time delays. The TA spectra show a broad negative absorption band (500–600 nm region) which follows the

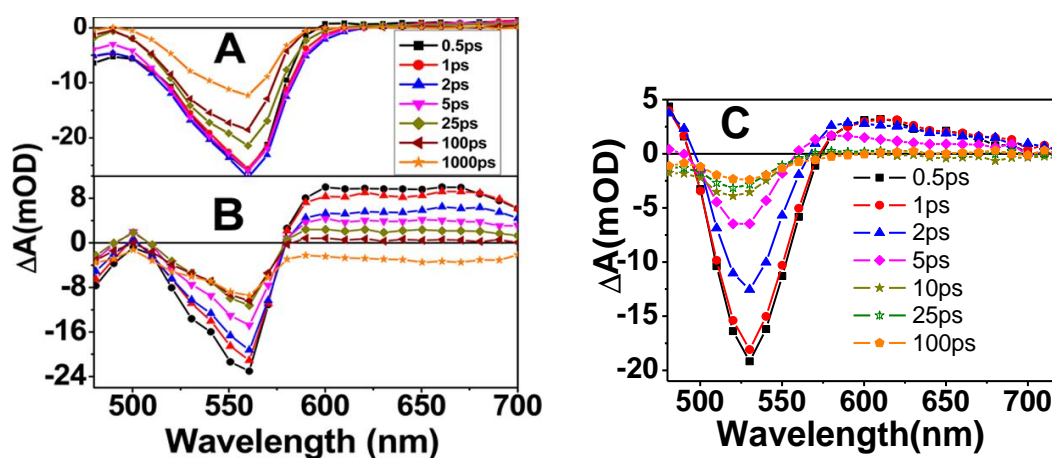


Figure 7.3: Transient absorption spectrum of (A) CdSe quantum dot and (B) CdSe{Au} HS (C) isolated Au NPs in chloroform solvent after exciting the samples at 400 nm.

steady state optical absorption spectrum of CdSe QD (Figure 7.1a) and can be attributed to an excitonic bleach. In addition to that, negligible photo induced absorption was observed beyond 600 nm, which signifies the presence of minimum surface defect states in CdSe QDs. At this point we would like to mention that before discussing the excited-state properties of CdSe{Au} HS material we have also performed TA studies of isolated Au NP after excitation with 400 nm laser light. The transient absorption spectra shows a negative absorption band in the 490–570 nm region peaking at 530 nm, which can be attributed to ground state bleach due to the plasmon band of Au NP, as shown in the Figure 7.3.C. Figure 7.3B depicts the transient

spectra of CdSe{Au} HS at different time delay. Remarkably, the transient spectra are very different as compared to both CdSe QD (Figure 7.3A) and Au NP (Figure 7.3C). The transient spectra consist of a negative absorption band in the 500-580 nm region peaking at 560 nm and another below the 500 nm region and a broad, positive absorption band in 580–700 nm region. The transient bleach spectrum looks quite similar to that of pure CdSe QD, but the signature of the plasmon bleach due to Au NP is completely absent. Earlier Zamkov et al.⁸⁷ reported the suppression of the surface plasmon of Au NP by the exciton of the CdS nanorod in the Au/CdS nanohybrid system. In the present investigation on photo excitation, photo excited electrons from the conduction band of CdSe QD are transferred to the Fermi level of Au NP (Scheme 7.1). As a result, electron density in the Fermi level increases, which facilitates exciton-plasmon coupling in CdSe{Au} HS. Interestingly, the broad positive absorption band in the 580-700 nm region in the CdSe{Au} HS system is totally different from those of isolated photoexcited CdSe QD (Figure 7.3A) and Au NP (Figure 7.3C). This positive absorption band can be assigned to the appearance of the electron in the Au NP^{135, 221, 319} (in the Fermi level) from the CB of CdSe QD which is a thermodynamically viable process (Scheme 7.1). Earlier, Zamkov et al.⁸⁷ also reported the appearance of a positive absorption band due to the transfer of electrons from the semiconductor domain (S) to the metal domain (M).

To monitor the charge carrier and transfer dynamics, transient kinetics at different wavelengths for both CdSe QD and CdSe{Au} HS have been monitored and are shown in Figure 7.4. The transient data have also been fitted multiexponentially and are shown in Table 7.1. The bleach recovery kinetics at 560 nm for CdSe{Au} HS is much faster as compared to that for pure CdSe QD. The faster recovery kinetics in the excitonic bleach position of CdSe{Au} HS can be attributed to photo induced electron transfer from the CB of CdSe QD

to the Fermi level of Au. The bleach at 560 for CdSe QD can be fitted with bi-exponential growth with time constants of $\tau_g^1 = < 100 (\pm 15)$ fs (67%) and $\tau_g^2 = 750 (\pm 50)$ fs (33%) and multiexponential recovery with time constants of $\tau_1 = 8.5 (\pm 0.35)$ ps (28%), $\tau_2 = 45$ ps (± 2) (12%), $\tau_3 = 350 (\pm 15)$ ps (15%), and $\tau_4 = >1 (\pm 0.05)$ ns (45%) (Table 7.1). The second

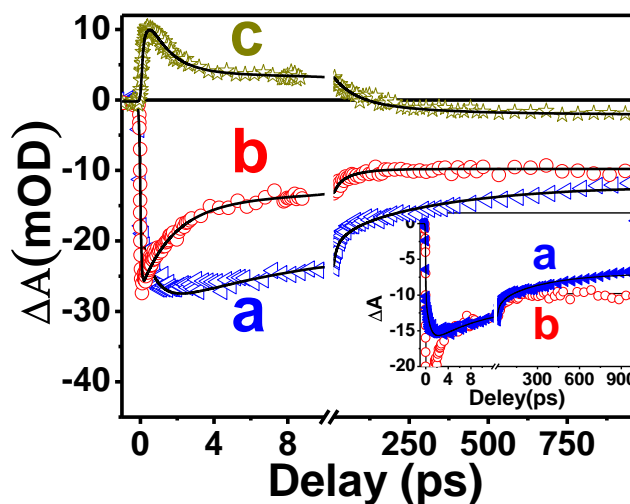


Figure 7.4: Bleach recovery kinetics at 560 nm for (a) CdSe quantum dot and (b) CdSe{Au} HS; and (c) transient absorption kinetics at 650 nm for CdSe{Au} HS in chloroform after 400 nm laser excitation. Inset: Bleach recovery kinetics for trace a and trace b after normalizing at 5 ps.

growth time constant can be attributed to cooling dynamics of the photoexcited electron in CdSe QD.²²¹ The multiexponential recovery with different time constants can be attributed to carrier recombination dynamics of the electron and hole at different trapped depths. However, the bleach at 560 nm for CdSe{Au} HS can be fitted with a single-exponential pulse width limited growth ($<100 (\pm 15)$ fs) and multiexponential recovery with time constants of $\tau_1 = 1.8 (\pm 0.1)$ ps (49%), $\tau_2 = 15 (\pm 0.5)$ ps (13%), $\tau_3 = 60 (\pm 2.5)$ ps (4%), and $\tau_4 = >1 (\pm 0.05)$ ns (34%) (Table 7.1). The bi-exponential growth at 560 nm bleach becomes single-exponential in

CHAPTER 7

CdSe{Au} HS, clearly suggest the photo excited electron in CdSe QD transfer to Au NP before cooling down to the lower excitonic states. It is also interesting that the majority of the

Table 7.1: Multi exponential fitted parameter of TA kinetics of CdSe and CdSe{Au} HS at different wavelengths after exciting the samples at 400 nm.

System@ Wavelength	$\tau_{1(\text{growth})}$	$\tau_{2(\text{growth})}$	τ_1	τ_2	τ_3	τ_4
CdSe@ 560nm	<100 (± 15) fs (67%)	750(± 50)fs (33%)	8.5 (± 0.35) ps (28%)	45 (± 2) ps (12%)	350 (± 15) ps (15%)	> 1(± 0.05) ns (45%)
CdSe{Au} @560nm	<100 (± 15) fs (100%)		1.8 (± 0.1) ps (49%)	15(± 0.5)ps (13%)	60 (± 2.5) ps (4%)	>1(± 0.05) ns (34%)
CdSe{Au} @650nm	<100 (± 15) fs (37%)	270 (± 25)fs (63%)	1.2 (± 0.05) ps (67%)	60 (± 2.5) ps (15%)	300 (± 20) ps (18%)	

bleach signal at 560 nm recovers very fast, which suggests the transfer of an electron from the semiconductor domain to the metal domain. The kinetics at 650 nm has also been monitored and fitted with biexponential growth with time constants of $\tau_g^1 = <100 (\pm 15) \text{ fs}$ (37%) and $\tau_g^2 = 270 (\pm 25) \text{ fs}$ (63%) and multiexponential decay with time constants of $\tau_1 = 1.2 (\pm 0.05) \text{ ps}$ (67%), $\tau_2 = 60 (\pm 2.5) \text{ ps}$ (15%), and $\tau_3 = 300 (\pm 20) \text{ ps}$ (18%) (Table 7.1). In the Au/CdSe composite system with 400 nm excitation, the majority of the light is absorbed by CdSe QD; however, a minor fraction of light can also be absorbed by Au NPs. So in the transient kinetics the pulse-width limited growth (<100 fs) can be attributed to plasmon excitation of Au NP and the 270 fs time constant can be attributed to the electron-transfer time from photo excited CdSe QD to Au NP. In an earlier investigation Zamkov and co-workers⁸⁷ also

reported an electron-transfer time of ~ 350 fs from the semiconductor domain to the metal domain. Now let us discuss the decay dynamics of the transient signal at 650 nm. It is interesting to see that the majority of the electron signal decay with a time constant of 1.2 ps can be attributed to the trapping of electrons in the interfacial zone of the metal and semiconductor. Due to the mismatch of the crystal structure of Au NP and CdSe QD, there might be some defect states in the interface zone.

The main goal of the present investigation is to determine the charge recombination dynamics between electrons in Au NP and the hole in the CdSe QD in CdSe{Au} HS material. Charge recombination dynamics in photoexcited QD are monitored from the bleach recovery of the excitonic bleach. Bleach kinetics at 560 nm for both CdSe QD and CdSe{Au} HS are normalized at 5 ps and are shown in the inset of Figure 7.4. The kinetics are normalized at 5 ps because until that time fast recovery in CdSe{Au} HS material is due to the transfer of electrons from CdSe QD to Au NP. It is clearly seen that charge recombination is much slower in CdSe{Au} HS material than in pure CdSe QD.

C. Sensitization of CdSe{Au} HS by BrPGR Molecule:

i) Charge Transfer Complexation Between CdSe{Au} HS and BrPGR Molecule:

The main theme of the present investigation is to investigate the charge-transfer process in CdSe{Au} HS sensitized with a molecular adsorbate. In an earlier section we have shown clearly that upon photo excitation of CdSe{Au} HS, photo excited electrons are localized in Au NP and holes are localized in the valence band of CdSe QD. To facilitate a further charge-separation process and slow down the charge recombination dynamics we have sensitized CdSe{Au} HS with bromo-pyrogallol red (Br-PGR). Before monitoring excited-state charge-transfer dynamics between CdSe{Au} HS and the Br-PGR molecule we have investigated the ground-state interaction between them through steady-state optical

absorption studies. Figure 7.5a and b shows the steady-state optical absorption spectra of Br-PGR dye and CdSe{Au} HS, respectively, in chloroform solvent. The optical absorption band maxima of Br-PGR is observed at 480 nm. Figure 7.5c shows the optical absorption spectra of CdSe{Au} HS sensitized with Br-PGR. It is exciting to observe that optical absorption spectra of CdSe{Au}/Br-PGR is entirely different as compared to that of both

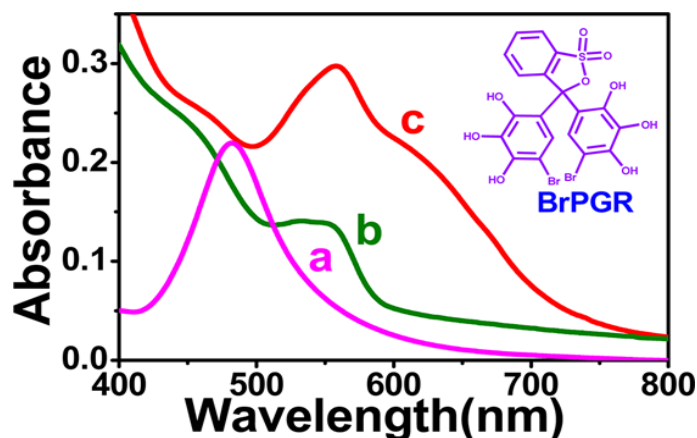


Figure 7.5: Steady state optical absorption spectra of (a) Br-PGR dye (10µM) (b) CdSe{Au} HS and (c) Br-PGR sensitize CdSe{Au} HS in chloroform. **Inset:** Molecular structure of Br-PGR.

Br-PGR and CdSe{Au} HS. The composite system shows an optical absorption band at 560 nm with a hump at 620 nm. The band at 560 nm can be attributed to the excitonic absorption band of CdSe QD in CdSe{Au} HS. However, the hump at 620 nm can be attributed to the formation of a CT complex between CdSe{Au} HS and the BrPGR molecule.

ii) Electron and Hole Transfer Dynamics in CdSe{Au}/BrPGR Tricomposite System:

To monitor the charge-transfer dynamics on an ultrafast time scale in the CdSe{Au}/Br-PGR tricomposite system, 400 nm laser light was used for excitation and is shown in Figure 7.6 A. Before discussing the TA of the tricomposite material we have also performed TA studies of isolated Br-PGR in chloroform, as shown in the Figure 7.6.B. TA

spectra of Br-PGR shows a negative absorption band below 600 nm and a photo induced absorption band in the 600–700 nm region with a peak at ~650 nm. The TA spectra of CdSe{Au}/Br-PGR tricomposite materials is completely different as compared to those of both CdSe{Au} HS and Br-PGR. The transient spectra consist of a positive absorption band below 515 nm and a broad bleach in the 515–715 nm region with a peak at ~560 nm and a hump at 630 nm which matches very closely with the steady state optical absorption spectrum

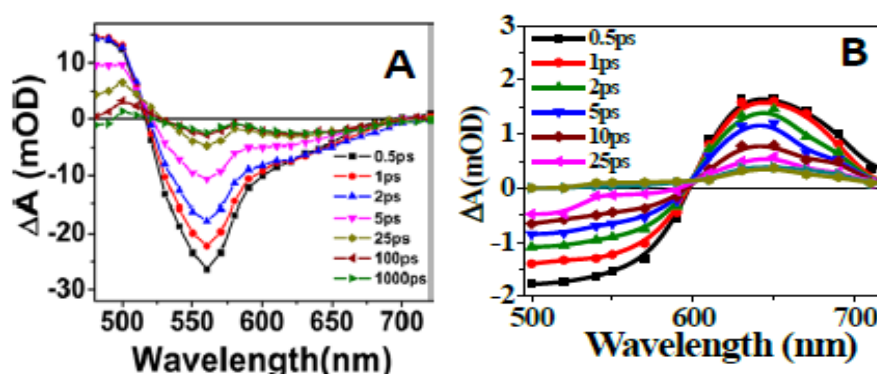
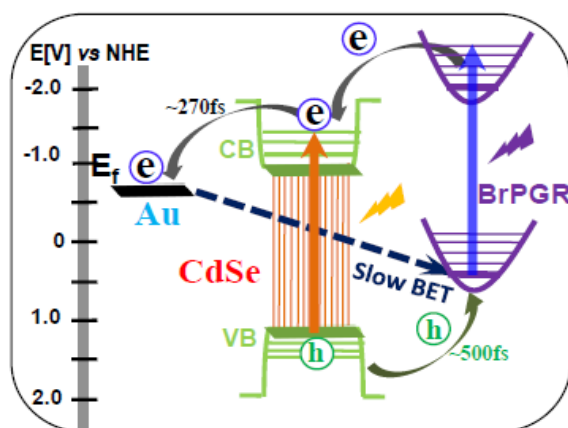


Figure 7.6: The transient absorption spectra of (A) CdSe{Au}/Br-PGR tri-composite system and (B) Br-PGR molecule at different time delay after exciting the samples at 400 nm in chloroform.

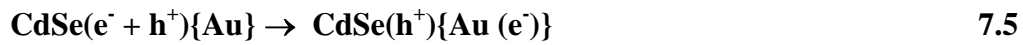
(Figure 7.5c). The negative absorption band at 560 nm is bleached due to the excitonic absorption of CdSe QD, and the hump at 630 nm can be attributed to the bleach due to the CT complex. It is exciting to see that at a longer time scale two clear bleach peaks appear at 555 and 630 nm in the transient spectra. The bleach due to the CT complex becomes more prominent on a longer time scale. However, unlike the CdSe{Au} HS system no photoinduced absorption band was observed in the wavelength region beyond 600 nm (Figure 7.3B). The photoinduced absorption might be completely suppressed due to the transient

bleach of strong CT complex CdSe{Au}/Br-PGR tricomposite materials. Again, due to the huge bleach signal of the CdSe{Au}/Br-PGR tricomposite system, a positive absorption band



Scheme 7.2: Schematic diagram illustrating the electron and hole transfer processes in CdSe{Au}/Br-PGR tri-composite system. It shows photo-excitation of QD electron and hole are generated where electron is transferred to the Fermi level of Au NP and hole is captured by Br-PGR molecules. On the other hand photo-excited Br-PGR injects electron into the CB of CdSe QD and finally transferred to Au NP. The dashed line indicates the charge recombination reaction between electron in Au NP and hole in Br-PGR.

due to the Br-PGR cation was also not observed. On photo excitation by 400 nm light, the charge-transfer reaction in the CdSe{Au}/Br- PGR tricomposite system can be demonstrated as shown in Scheme 7.2. Upon photo excitation of CdSe QD, electrons will be excited to the conduction band and holes will be localized in the valence band. Here the electrons will be transferred to Au NP, and holes will be scavenged by Br-PGR. Scheme 7.2 also suggests that photo excited Br-PGR also can inject electrons into the CB of CdSe QD, which eventually transferred to Au NP. Both electron and hole transfer reactions in the CdSe{Au}/Br-PGR tricomposite system can be demonstrated in the following equations:



To investigate the charge-transfer dynamics in the CdSe{Au}/ Br-PGR tricomposite system, transient kinetics at different wavelengths have been monitored. At this point, we mention that at 400 nm excitation in the CdSe{Au}/Br-PGR system the majority of the light will be absorbed by CdSe QD as compared to Au NP and Br-PGR. Therefore, the photo excitation process will be dominated by photo excited electron and hole transfer dynamics in the tricomposite materials. Figure 7.7A shows the bleach recovery kinetics at the first excitonic wavelength (555 nm) for CdSe{Au} HS (Figure 7.7a) and the CdSe{Au}/Br-PGR composite system (Figure 7.7b). Bleach recovery kinetics for pure CdSe{Au} HS have already been discussed (Table 7.2). The bleach at 555 nm for the CdSe{Au}/Br-PGR tricomposite system can be fitted with single-exponential pulse width limited growth (<100 fs) and multiexponential recovery with time constants of $\tau_1 = 1.1 (\pm 0.05)$ ps (53%), $\tau_2 = 9 (\pm 0.5)$ ps (31%), $\tau_3 = 50 (\pm 2)$ ps (10%), and $\tau_4 = >1 (\pm 0.05)$ ns (6%) (Table 7.2). The bleach recovery kinetics for CdSe{Au}/Br-PGR is much faster as compared to those of the CdSe{Au} system. We have already mentioned in an earlier section that bleach recovery in the CdSe{Au} system is faster as compared to that of pure CdSe QD due to the transfer of photo excited electron from CdSe QD to Au NP. However, in the CdSe{Au}/Br-PGR system, upon photo excitation, in addition to the transfer of photo excited electron to Au NP, the

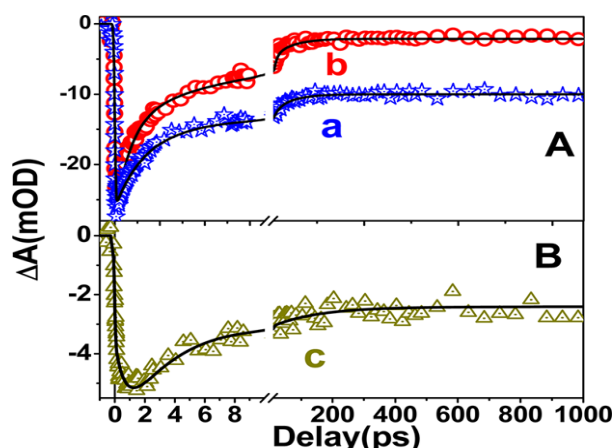


Figure 7.7-Panel A: Bleach recovery kinetics of (a) CdSe{Au} HS and (b) CdSe{Au}/Br-PGR tri-composite system at 555nm. **Panel B:** Bleach recovery kinetics of CdSe{Au}/Br-PGR tri-composite system at 655nm.

Table 7.2: Multi-exponential fitted parameters for the TA bleach recovery dynamics of CdSe{Au}/Br-PGR tri-composite system at 555nm and 655nm.

Wavelength (nm)	$\tau_{1(\text{growth})}$	$\tau_{2(\text{growth})}$	τ_1	τ_2	τ_3	τ_4
555nm	>100(±15) fs (100%)		1.1(±0.05) ps (53%)	9(±0.5) ps (31%)	50(± 2) ps (10%)	>1(±0.05) ns(6%)
655nm	100(±15) fs (49%)	500 (±50) fs (51%)	3(±0.2) ps (37%)	20(± 1) ps (5%)	>1(± 0.05) ns (58%)	

photo excited hole from CdSe QD is also transferred to Br- PGR molecules because both processes are thermodynamically feasible (Scheme 7.2). In addition to that, Scheme 7.2 also suggests that photo excited Br-PGR can inject electrons into the CB of CdSe QD, which eventually can be transferred to the Fermi level of Au NP. As a result, a total separation of charge is expected in the CdSe{Au}/Br-PGR tricomposite material. It has been observed in Figure 7.6 that the bleach peak due to the CT complex appeared at 630 nm; to monitor charge recombination dynamics in the composite system, bleach dynamics were followed at 655 nm

to avoid the contribution from the excitonic bleach recovery of CdSe QD. The recovery kinetics can be fitted with bi-exponential growth with time constants of $\tau_g^1 = <100 (\pm 15)$ fs (49%) and $\tau_g^2 = 500 (\pm 50)$ fs (51%) and multiexponential decay with time constants of $\tau_1 = 3 (\pm 0.2)$ ps (37%), $\tau_2 = 20 (\pm 1)$ ps (5%), $\tau_3 = >1 (\pm 0.05)$ ns (58%) (Table 7.2). To determine the hole-transfer time from photoexcited CdSe QD to Br-PGR in this present investigation, we have monitored the bleach at a wavelength of 655 nm. The second growth component (500 fs) in the 655 nm bleach growth kinetics can be attributed to the hole-transfer time from photo excited CdSe QD to Br-PGR. The charge recombination reaction was found to be very slow due to the localization of an electron in Au NP and the localization of a hole in Br-PGR (Scheme 7.2), which are spatially separated.

7.2.2 Charge Separation in Au@CdS core shell and DBF Triad System.

A. Characterization and Optical Properties of Au@CdS core shell:

First, we synthesised Au and Au@CdS core-shell (Chapter 2) and characterised by HR-TEM and steady state optical absorption measurements. Figure 7.8 (a) shows the HR TEM image of Au NP. The average size of this Au NP is around 6.3 nm with well size distribution have been clearly shown in this figure. The growth of the CdS layer on Au NP is clearly seen in figure 7.8 (b). Average 2 nm thickness CdS layer has been grown on the surface of Au NP which is shown in the figure 7.8 (b). There is clear lattice interference also shown in this figure.

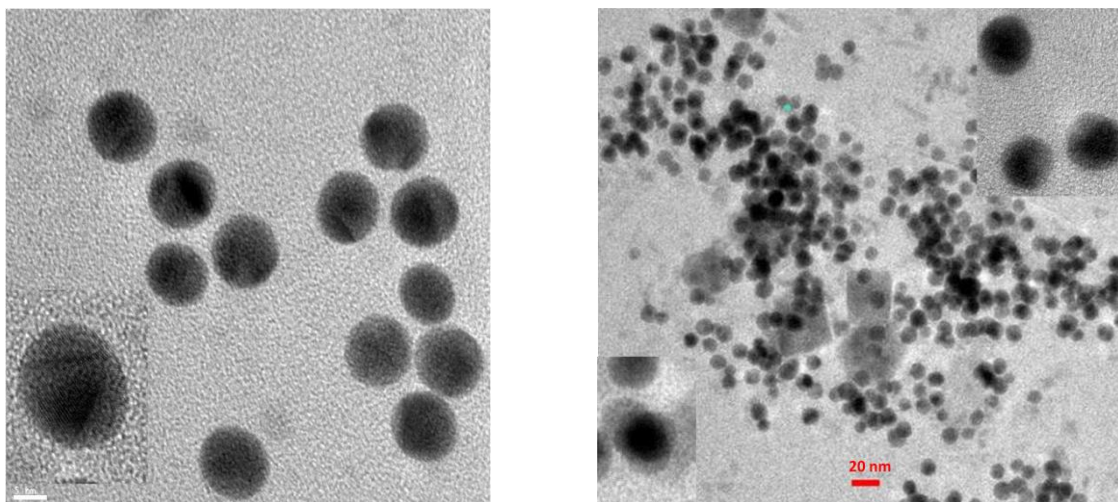


Figure 7.8: HR TEM image of **Left Panel:** Au NP and **Right Panel:** Au@CdS core shell nano hybrid structures.

The Steady state optical absorption study follows the result of HR-TEM. Figure 7.9 (a) shows the surface Plasmon band of Au nanoparticles and the peak of this band is at

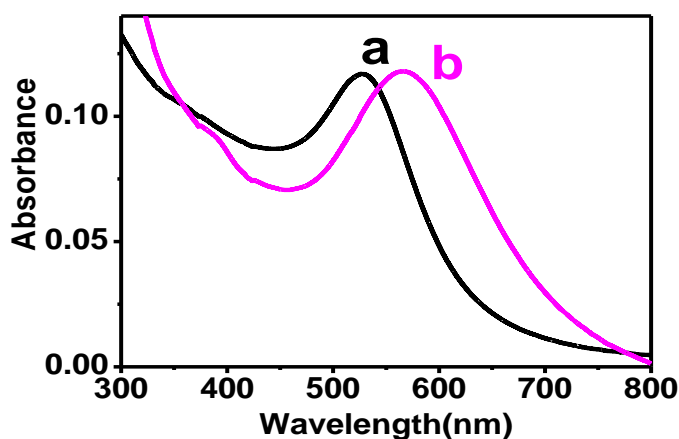


Figure-7.9: Steady state UV-Vis absorption spectra of (a) Au nano particles and (b) Au@CdS core shell nano particles in Chloroform.

around 527 nm. This surface Plasmon band in red shifted to 570 nm (Figure 7.9 (a)), depicts the formation of CdS shell on Au NP. According to Mie theory this red shifting of the surface

Plasmon band is due to change of refractive index and dielectric constant of the shell. No separate exciton band for CdS shell has not been observed in this Au@CdS spectrum as the shell thickness of the CdS is very thin and absorption of Au core is dominated over shell.

B. Carrier Dynamics of Au@CdS Core Shell.

To investigate the excited state dynamics of the hybrid material the transient absorption measurement has been carried out after 400 nm laser excitation. Figure 7.10 A represents the TA spectra of Au NP showing ground state bleach at 525 nm sandwiched by two excited state absorption band. This 525 nm bleach is due to ground state bleach of surface Plasmon. Totally different spectrum has been observed when CdS shell is formed on Au core as shown in figure 7.10 B. According to steady state spectra the ground state bleach of surface plasmon is red shifted from 525 nm to 570 nm with broadening after formation of CdS shell on Au core. This shifting of Plasmon is due to change of refractive index and dipole moment by CdS shell. Addition to surface Plasmon band one more bleach at 460 nm is also observed in Au@CdS spectra. This bleach corresponds to the lowest energy exciton transition ($1S_e - 1S_h$) of CdS shell. The bleach intensity of CdSe shell is very low compared to Au core due to very higher extinction coefficient of Au core than the thin CdS shell.

To monitor the excited state dynamics of the Au and Au/CdS hybrid material we have probed the bleach recovery dynamics of the Au and Au/CdS hybrid material excited by 400 nm laser. Figure 7.11 (a) shows the bleach dynamics of the Au NP. The hot Plasmon relaxes through three ways.⁷⁹ First, electron-electron scattering which is occurred within sub-10 femtosecond time scale which can't be shown in this fitting value due to low instrument resolution. Then it relaxes through electron phonon coupling within the sub ~10 ps time scale. Finally it relaxes through heat exchange with environment. The bleach of surface

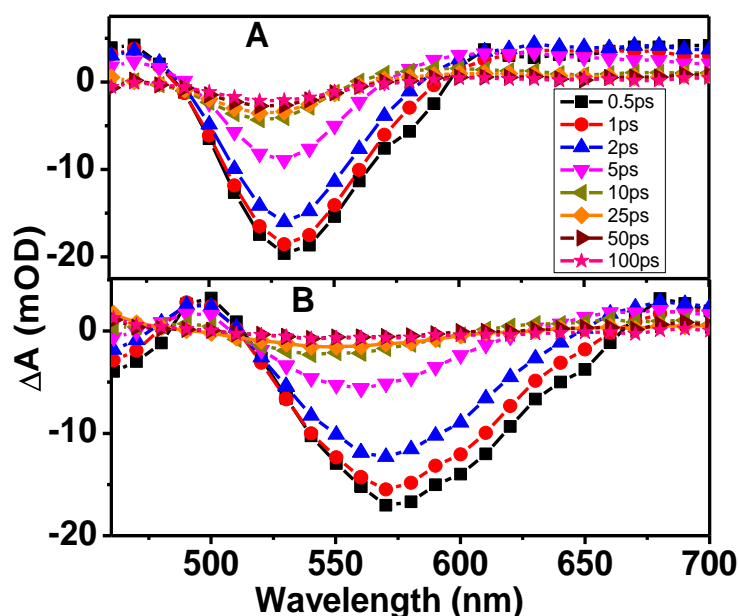


Figure 7.10. (A) TA spectrum of Au NP after 400 nm laser excitation and (B) TA spectrum of Au/CdS core shell nanohybrid after 400 nm laser excitation in chloroform solvent.

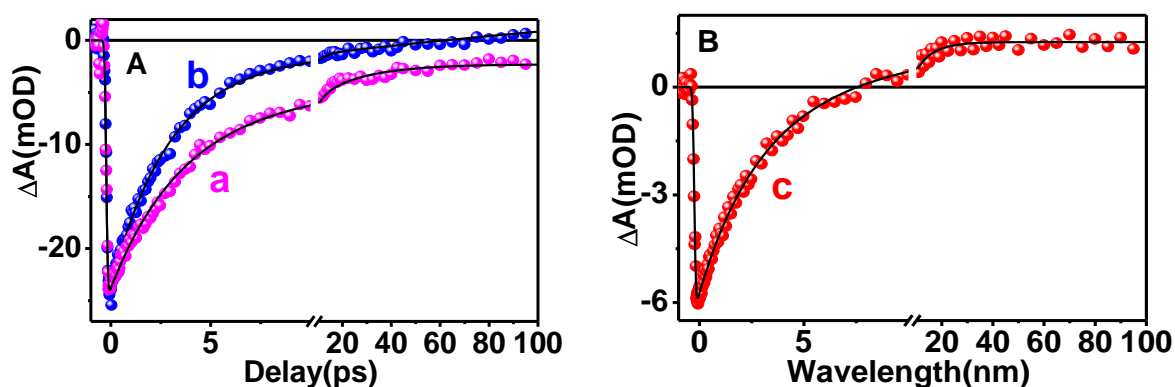


Figure 7.11: Bleach recovery dynamics of (a) Au NP at the wavelength of 525 nm (b) Au/CdS core shell nanohybrid at the wavelength of 570 nm and (c) Au/CdS at 465 nm in chloroform solution after 400 nm laser excitation.

plasmon has been grown within <100 fs followed by bi-exponential decay and the decay components are $\tau_1= 3.5$ ps, $\tau_2=13$ ps and >100 ps (11%) (Table 7.3 a). At 400 nm laser excitation Au core and CdS shell both will be excited simultaneously. But due to thin layer of

CHAPTER 7

CdS the major portion of the light will be absorbed by the Au core. This surface Plasmon bleach dynamics is changed in Au@CdS core shell and is shown in Fig 7.11 (b). The growth components is same as pure Au NP <100 fs, but the decay becomes faster as compared to pure Au and the components (Table 7.3) are 2.5 ps (95%) and 50ps (5%). This faster recovery of the plasmonic bleach is not due to electron transfer from Au NP to the CB of CdS because there is not possible to direct electron transfer from Au NP to the CB of CdS shell

Table 7.3: Multi exponential fitted value for bleach recovery of Au NP and Au@CdS core shell after 400 nm laser excitation.

System@wavelength	τ (growth)	τ_1	τ_2	τ_3
AuCdS@470nm	<100fs	1.5 ps(-100%)	7 ps (+95%)	50 ps (+5%)
Au@525nm	<100fs(100%)	3.5ps(76%)	13ps(13%)	>100ps(11%)
AuCdS@570nm	<100fs(100%)	2.5ps(-95%)	50ps(-5%)	

which is thermodynamically non favorable processes.¹³⁵ The faster recombination of Plasmon in presence of CdS shell represents the coupling of excited Plasmon with the phonon of the CdS lattice.¹³⁵ Due to this type of coupling the hot Plasmon transfer the energy to the lattice of the CdS leading to heating of the CdS lattice. This type of plasmonic energy transfer does not affect on the excited state dynamics of the CdS shell. The figure 7.11 (c) shows the exciton bleach dynamics at 470 nm of thin CdS shell in Au@CdS core shell with <100 fs growth component. The bleach recovery is extremely faster as compared to isolated CdS QDs and the component is 1.5 ps (-100 %) (Table 7.3). The faster bleach recovery compare to isolated CdS attributes the fast electron transfer from CdS shell to Au Core.¹³⁵ Therefore after photo excitation the charge separation between Au core and CdS shell is occurred due to

localisation of electron and hole in Au core and CdS shell, respectively.

C. Electron and Hole Transfer Dynamics in Au/CdS Core Shell Nanohybrid After Sensitization with DBF Molecule:

i) CT Complex Formation Between Au@CdS Core Shell and DBF Molecules.

To extent the charge transfer processes, we have investigated the photophysical interaction between Au@CdS core shell with DBF molecules. To explore the ground state interaction between Au/CdS core shell nanohybrid with DBF molecule, the steady state measurements have been carried out. Figure 7.12 (a) shows the absorption spectra of DBF molecule with 480 nm absorption maxima. Figure 7.12 (b) shows the absorption spectra of Au/CdS core shell nanohybrid. The absorption spectra become totally changed from isolated

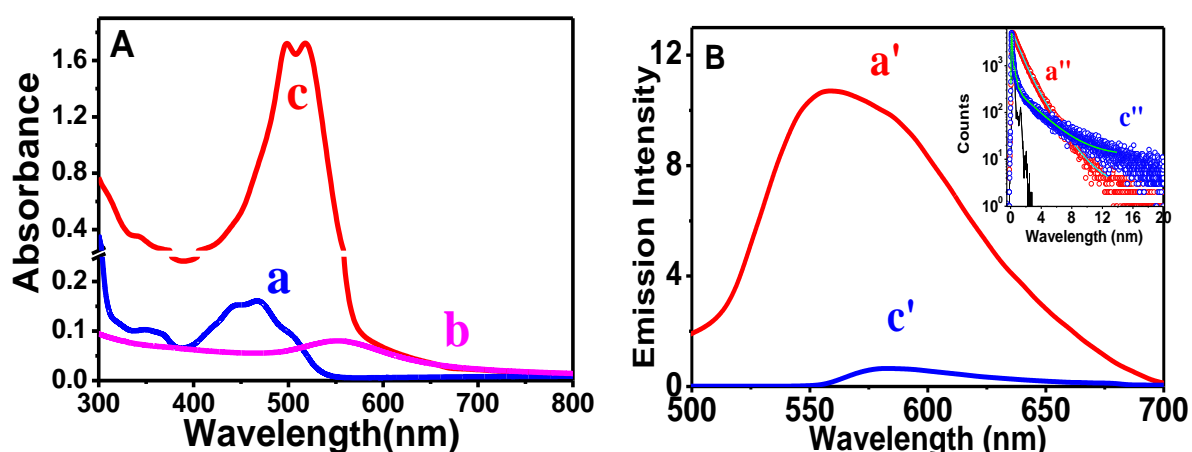
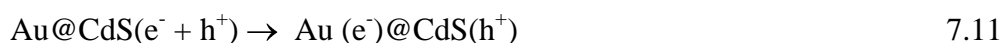
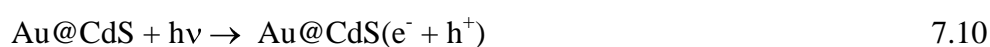


Figure 7.12. A: Steady state optical absorption spectra of (a) DBF dye molecule (b) Au@CdS core shell nanohybrid material and (c) After sensitization of Au@CdS core shell with DBF dye molecule. **B.** Steady state UV-Vis luminescence spectra of (a') DBF molecules and (c') Au/CdS-DBF triad system in chloroform after 480 nm excitation. **In Inset:** Time resolved luminescence spectra of (a'') DBF molecule and (c'') Au@CdS/DBF triad system at 570 nm after excitation of 445 nm laser. C is the lamp profile of the 445 nm laser. All of these spectrum are at the same concentration in chloroform solvent.

CHAPTER 7

DBF molecule and Au/CdS core shell nanohybrid when Au/CdS is sensitized by the DBF molecule which has been shown in the figure 7.12 (c). The tremendous enhancement of absorbance with change of absorption maxima is occurred, which attributes the formation of charge transfer (CT) complex between Au/CdS nanohybrid and DBF molecule.

In this investigation the CT complex is formed within the Au/CdS and DBF molecule and shown equationn below,



To study the electron transfer from the HOMO of DBF to the CB of DBF after photoexcitation, we have measured the steady state luminescence spectroscopy. Figure 7.12 (a') shows the luminescence spectra of DBF molecule and this emission is quenched in presence of Au@CdS core shell after photo excitation, which is shown in figure 7.12 (b'). This quenching of luminescence attributes the electron transfer from HOMO of DBF to the CB of CdS after photoexcitation which is thermodynamically favorable.

To confirm the electron transfer from HOMO of DBF to the CB of CdS shell after photo excitation, we have employed the time resolved luminescence measurement. Figure 7.12 B (a'') shows the time resolved luminescence spectra of DBF molecule. $\tau_1=0.924$ ns (76%) and $\tau_2=1.9$ ns (24%) are the time constant of this bi-exponential spectra with average time constant 1.15 ns. The luminescence decay of DBF becomes extremely fast in presence

of Au@CdS core shell and has been shown in 7.12 B (c’). The bi-exponential decay components are 0.28 ns (86%) and 3.35 ns (14%) with average life time 0.7 ns. The rate constant for electron transfer from HOMO of DBF to CB of CdS can be evaluated from eqn 7.16 and the determined the electron transfer rate constant was found to be $5.55 \times 10^8 \text{ Sec}^{-1}$.

$$K_{ET} = 1/\tau_{\text{Au@CdS/DBF}} - 1/\tau_{\text{DBF}} \dots\dots\dots 7.16$$

ii) TA Studies of Au@CdS Core Shell and DBF Tricomposite System.

To investigate the excited state charge carrier dynamics in Au@CdS/DBF triad system the femtosecond transient absorption spectroscopy measurement has been carried out. Figure 7.13 shows the transient absorption spectra of Au@CdS/DBF triad system after 400 nm laser excitation. The Spectrum of this triad material is totally different from the spectrum

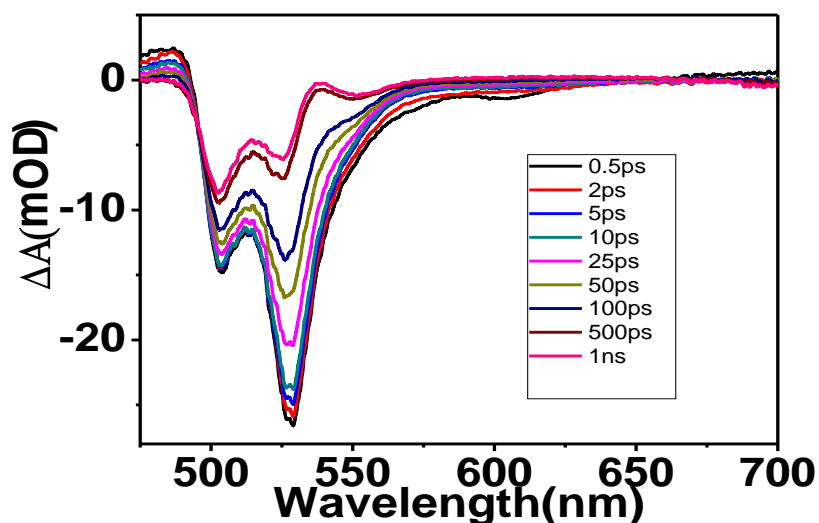
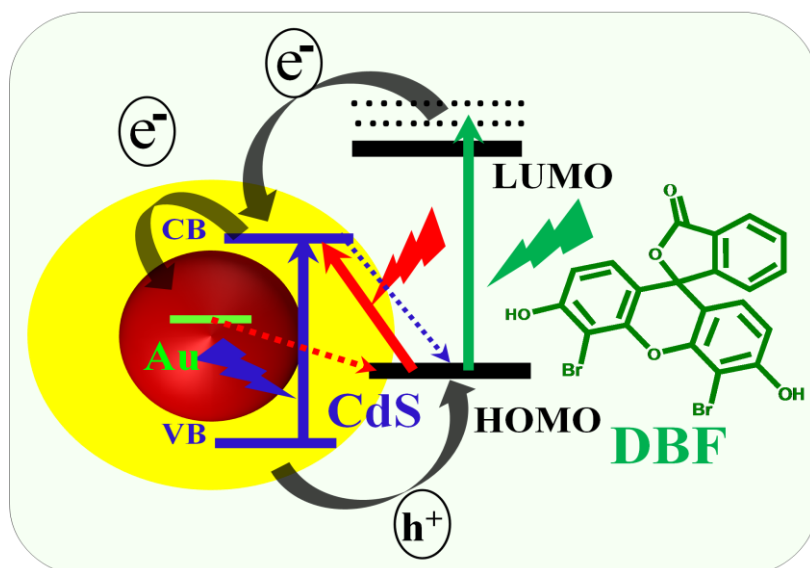


Figure 7.13: TA spectrum of Au/CdS-DBF triad system in chloroform solvent after 400 nm laser excitation.

of the isolated Au@CdS core-shell as earlier we have demonstrated the TA spectrum of the Au@CdS core shell nano hybrid material. Two ground state bleaches belong to this spectrum, one is 500 nm and other one is 530 nm, which are matches with the steady state absorption

spectra of this triad system. There is no separate cationic band for DBF in the spectrum of triad system due to overlap between the ground state bleach of Au@CdS and the cationic band for DBF.

To monitor the electron and hole transfer dynamics we have probed the bleach at 500 nm and 530 nm, shown in Fig 7.14 a and c, respectively. The 500 nm bleach is due to charge transfer complex between Au/CdS core shell and DBF molecule. The growth component of the bleach is <100fs which is electron transfer time from the DBF molecule to the CB of



Scheme 7.3: This Schematic diagram shows after photoexcitation the electron is transferred from LUMO of DBF to fermi level of Au NP via the the CB of CdS shell and simultaneously the hole is transferred to the HOMO of DBF from VB of CdS shell.

CdS. This bleach recovery is fitted tri-exponentially and components are $\tau_1= 400\text{fs}$ (10%), $\tau_2= 15\text{ ps}$ (12%), $\tau_3= 200\text{ ps}$ (20%), $\tau_4= >1\text{ ns}$ (58%) (Table 7.4). The faster 400 fs component of the bleach recovery attributes the hole transfer time from VB of CdS to the LUMO of DBF molecule. The bleach recovery is very slow, attributing the slow charge recombination in this

triad system. After photo excitation the electron transfer is happening from HOMO of DBF to the CB of CdSe shell and rapidly it transfers to the Fermi level of the Au NP core while the hole of the CdS has transferred to the HOMO of the DBF molecule. As a result the electron will be localised at Au core and the hole is localised at the HOMO of DBF. As a result the charge recombination of this triad system is extremely slow.

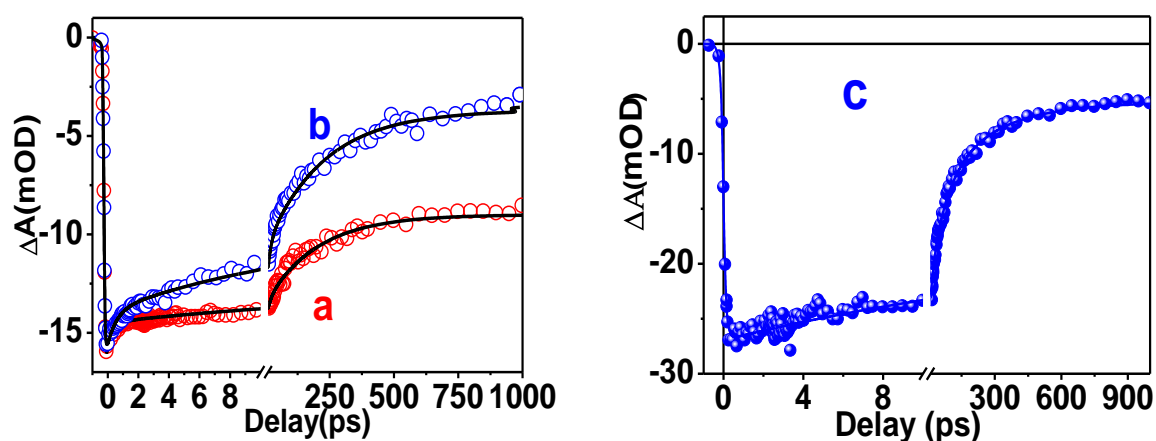


Figure 7.14: Bleach recovery dynamics of (a) CdS-DBF and Au@CdS-DBF triad system at (b) 500 nm and (c) 530 nm after 400 nm laser excitation.

Table 7.4: Multi exponential fitted value for bleach recovery of Au@CdS core shell and DBF tricomposite at different key wavelength.

System	$\tau_1(\text{growth})$	τ_1	τ_2	τ_3	τ_{avg}
@ wavelength					
Au/CdS-DBF@500nm	100fs(100%)	400fs (10%)	15ps (12%)	200ps (20%)	>1ns (58%)
Au/CdS-DBF@530nm	100fs(100%)	14ps (43%)	70ps (30%)	250ps (6%)	>1ns (21%)
CdS-DBF@500nm	100fs(100%)	600fs(15%)	12ps(28%)	225ps(34%)	>1 ns(23%)

Therefore the bleach recovery of this triad system is slower than the bleach recovery of the CdS-DBF system (Fig 7.14 b and Table 7.4) where the electron and hole are localised at CdS and DBF, respectively. After photo excitation all of the triad material being excited as a result the excited electron of DBF molecule is transferred from LUMO of DBF to the CB of CdS and the electron from CB of CdS transferred to the Fermi level of Au core. The bleach recovery at 530 nm is fitted tri-exponentially, e.g. $\tau_1=14$ ps (43%), $\tau_2=70$ ps (30%), $\tau_3=250$ ps (6%) and $\tau_4 \Rightarrow 1$ ns (21%). This bleach recovery is also slow but less slower than expectation due to contribution of the surface plasmon relaxation.

7.3. Conclusions:

In conclusion CdSe{Au} hetero-structure (HS) and Au@CdS core shell have been successfully synthesized and characterized by HR-TEM, steady state absorption and emission spectroscopy measurements. Surface plasmon of Au NP found to be suppressed in presence of CdSe QD due to strong exciton-Plasmon coupling between Au NP and CdSe QD. Photo-excited electron in CdSe QD is found to be transferred to the Au NP as monitored by both time-resolved emission and ultrafast transient absorption studies. Spectroscopic measurements have been carried out to study charge transfer dynamics after sensitizing CdSe{Au} HS with bromo-pyrogallol red (Br-PGR). Steady state optical absorption studies have confirmed formation charge transfer complex between CdSe{Au} HS and Br-PGR. Charge separation in CdSe{Au}/Br-PGR tri-composite system found to take place in different pathways, like electron transfer from the CB of CdSe QD to Au NP, hole transfer from VB of CdSe QD to Br-PGR, electron injection from photo-excited Br-PGR to the CB of CdSe QD. Spectroscopic investigations suggest that on photo-excitation CdSe{Au}/Br-PGR tri-composite system cascading electron transfer and hole transfer take place where all the electrons are localized in Au NP and all the holes are localized in Br-PGR. Electron and hole

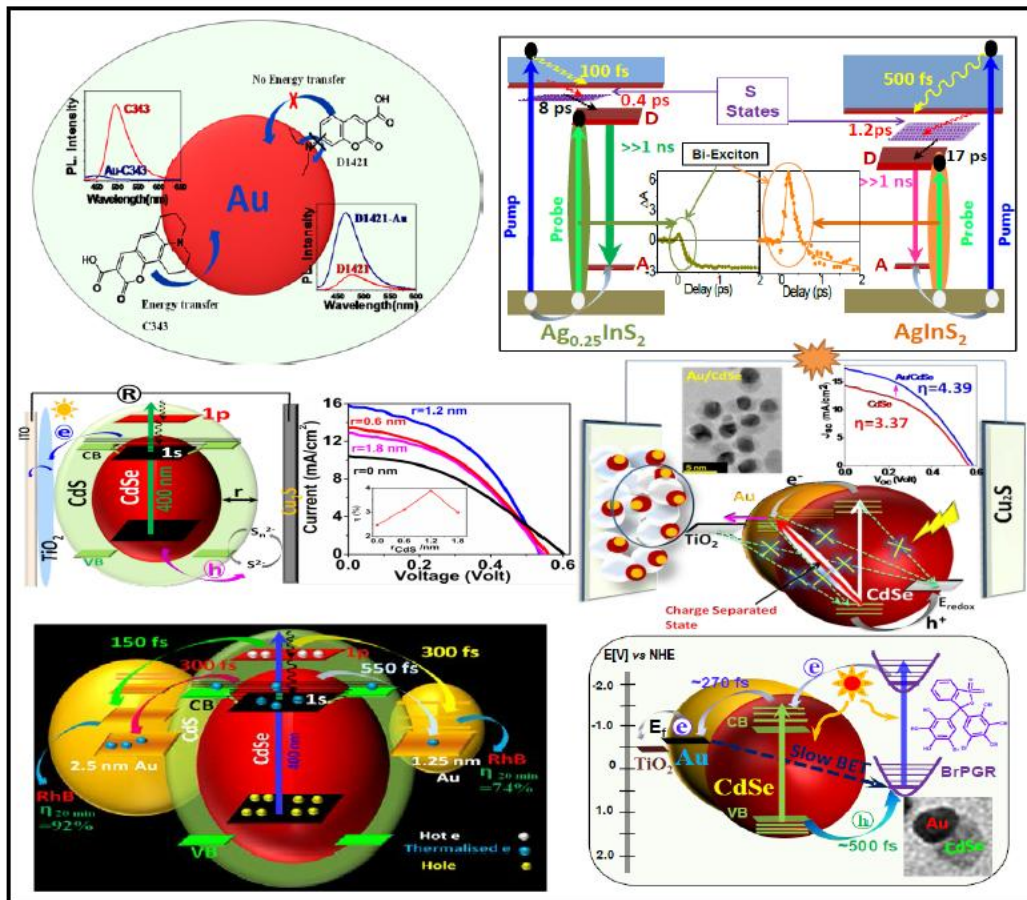
CHAPTER 7

transfer time from photo-excited CdSe QD to Au NP and Br-PGR were found to be ~ 270 fs and ~ 500 fs respectively. Charge recombination reaction between electron in Au NP and hole in Br-PGR was found to be very slow due to spatial separation of charges in CdSe{Au}/Br-PGR tri-composite system. Similarly, The transient absorption study shows that the charge transfer from CdS shell to Au NP, leading to a charge separated state between Au core and CdS shell in Au@CdS core shell itself. The TA measurement shows that the hot Plasmon of Au@CdS core shell relaxes faster compared to pure gold through electron-phonon interaction with CdS shell. To extent the charge separation, the Au@CdS core shell is sensitised by DBF dye molecule and form a CT complex between Au@CdS and DBF molecule, is confirmed by steady state optical absorption study. From steady state and time resolved luminescence study it is confirmed that the electron transfer from photo excitation LUMO of DBF molecule to the CB of CdS shell. The TA study has shown that the electron transfer is occurred from LUMO of DBF to the Au nano core through the CB of CdS shell and hole transfers from VB of CdS to the HOMO of DBF molecule. The measured electron transfer time was found to be <100 fs (pulse width limited) and hole transfer time from VB of CdS to the HOMO of DBF is 400 fs. Therefore after photo excitation all electron will be localised at the Au nano core and all hole will be localised at the LUMO of DBF in this triad system. As a result the charge separation in this triad system (Au@CdS/DBF) is higher than the charge separation in CdS/DBF system. Our experimental investigations clearly suggest that metal/semiconductor/molecular adsorbate tri-composite system can be the reality of multiple exciton dissociation and finally higher photo conversion efficiency in QDSCs.

CHAPTER 8

CHAPTER-8

SUMMARY and OUTLOOK



CHAPTER 8

8.1. Summary.

The main endeavour of this thesis is the demonstration of the charge carrier dynamics of metal-semiconductor NHM and metal-semiconductor-dye tricomposite system by ultrafast spectroscopy followed by investigation of their photocatalytic and photovoltaic applications. The ultrafast charge transfer dynamics of semiconductor QDs, metal-semiconductor NHM and dye sensitised NHM have been monitored in details. Hence we synthesised the Au NP, different QDs and core shell like CdSe, CdS, CdSe@CdS and metal semiconductor nanohybrid (CdSe/Au and CdSe@CdS/Au) by using different synthesis protocol. The morphology of the all synthesised materials have been characterised by the HR-TEM and X-Ray diffraction techniques. The optical characterizations have been carried out by steady state and time resolved absorption and luminescence spectroscopy studies. To investigate the charge carrier dynamics of the semiconductor QDs, metal-semiconductor NHM and dye sensitised NHM, the time resolved absorption and luminescence have been appointed. Finally we measured the photocatalytic and photovoltaic performances of the semiconductor QDs and metal-semiconductor NHM.

Excited state dynamics and energy transfer behaviour of two structurally similar coumarin dye molecules (C-343 and D-1421) have been investigated on the Au NP surface by using steady state and time-resolved emission spectroscopy. Steady state absorption studies indicate that the C-343/Au NP system has higher coupling strength between the molecular and the plasmonic resonances due to higher spectral overlap as compared to the D-1421/Au NP system. In nonpolar solvent both the molecules exist in the LE state, while in polar solvent, C343 exists in the ICT state and D1421 exists both in ICT and TICT states. ICT emission of C-343 was found to be quenched drastically due to energy transfer from photoexcited C-343 to Au NP. In addition to that, the excited state of C-343 also exists as the

CHAPTER 8

LE state on the Au NP surface due to restriction of intramolecular charge delocalization of C-343. Rather than luminescence quenching, interestingly the emission intensity of ICT state of D-1421 drastically increases on Au NP surface due to restriction of amino group rotation on NP surface. Our observation on restriction of charge delocalization of photo excited dye molecules on NP surface opens up new phenomenon in dye-metal NP interaction.

In chapter 4, we correlated shell thickness dependent carrier cooling and recombination dynamics of different CdSe@CdS core shell with power conversion efficiency. The CdS shell thickness increase the carrier cooling time, slow down the recombination due to elimination of trapping and retarding the back recombination from TiO₂. Therefore the PCE gradually increases with increasing the CdS thickness. At a certain thickness the efficiency is maxima and beyond this thickness again starts to decrease due to retardation of hole neutralisation by thicker CdS shell. The 4 ML CdS shell is optimised shell thickness where measured highest efficiency is 3.88 % which is 57% higher than the bare CdSe QDs. In addition to that, interfacial charge (both electron and hole) separation between photo-excited CsPbBr₃ (CPB) NCs and CdSe QDs and CdSe@CdS core-shell has been demonstrated through steady state and ultrafast time-resolved luminescence and absorption techniques. Both steady state and time resolved PL studies suggest the concurrent electron and hole transfer from CPB NCs to CdSe QDs and CdSe QDs to CPB NCs, respectively. On the other hand in case of CPB NCs and CdSe@CdS core-shell system photo-excited electron transfer from CPB NC to the core-shell found to be facile whereas the hole transfer from core-shell to CPB NCs found to be restricted due to presence of CdS shell. Photo-excited electron transfer time from CPB NCs to CdSe QDs and CdSe@CdS core-shell were found to be 550 and 450 fs respectively. On the other hand hole transfer time from photo-excited CdSe

CHAPTER 8

QDs to CPB NCs found to be 750 fs. Present investigation suggests in CPB NCs and CdSe QDs composite system on photo-excitation grand charge separation takes place

In chapter 5, we discussed the carrier dynamics of AgInS₂ (AIS) with different stoichiometric ratio of Ag and In. The excitonic absorption peak was found to become broad with increasing Ag/In ratio in AIS NCs. Steady-state PL spectra indicate that two types of emission are originated from AIS NCs, which are due to Ag-related sub-band gap defect states and antisite states (donor states) depending on the stoichiometric ratio of Ag and In in AIS NCs. PL intensity due to Ag-related sub-band gap defect states increases and antisite states decreases with increasing the Ag concentration in AIS NCs. Femtosecond TA studies have been carried out to monitor the charge carrier dynamics in AIS QDs, which involve multiple states like higher excited state, conduction band-edge, S-states, and antisite (donor) states. Transient absorption spectra were found to dominate by bleach (negative absorption) due to excitonic absorption, S-states, and antisite (donor) states. The probe-induced bi-excitonic feature originated from the antisite state has been observed in AIS NCs even at low pump energy of $\sim 0.2 \mu\text{J}$. Carrier cooling time constant was found to increase drastically with pump energy and concentration of Ag in AIS NCs and was found to facilitate drastically the efficiency of bi-exciton generation with higher Ag concentration.

The enhancement of PCE by the Au NP in Au/CdSe NHM has been discussed in chapter 6 by detailed spectroscopy study. The measured PCE of CdSe is found to be $\sim 3.37\%$ which is 30% enhanced to 4.39% in Au/CdSe NHM. The steady state study reveals the broadening the absorption spectra up to 800 nm by the Au NP in Au/CdSe NHM due to increase of carrier density on the Au NP surface after transfer from CdSe to Au NP, which is responsible for the enhancement of PCE efficiency. The steady state and time resolved

luminescence studies represented the fast electron transfer from QDs to Au NP, which enhances the availability of carrier density to generate the more current. Finally the TA spectroscopy implies the formation of long lived charge separated state at the red region between Au and CdSe which enhances the PCE of the solar cell by improving the charge injection efficiency. The Au NP slows down the back electron-hole recombination process and enhances the PCE by increasing the charge collection efficiency of Au/CdSe. By EIS we have measured the three times higher recombination resistance of Au/CdSe NHM compared to CdSe QDs and correlated with the enhancement of PCE for the NHM. Additionally, the size dependent hot and thermalised electron transfer dynamics between CdSe@CdS core-shell and Au NPs have been discussed by femto second transient absorption studies. Hot and thermalized electron transfer times were determined to be 150 and 300 fs from 1P and 1S excitonic states of CdSe@CdS core-shell to Au NP in the hetero-structure, respectively. Formation of charge separated states found to be facilitated with larger size Au NP where both hot and thermalized electrons are captured by Au NP and holes are localized in CdSe core. Efficient charge separation in CdSe@CdS{Au} hetero-structure was reconfirmed by employing photo-catalytic degradation of RhB under visible radiation, suggesting that hot electron in the hetero-structure play a major role in efficient photo-catalytic reactions. Again we extent this work by measuring shell thickness dependent carrier dynamics in CdSe@CdS{Au} hetero-structure. The CdS shell plays a vital role in charge transfer and separation processes. With increasing the shell thickness the electron transfer becomes slow down, but the life time of the charge separated state gradually increases with increasing the shell thickness. By making a potential barrier by CdS shell, restrict the back electron transfer from Au NP to core shell, resulting enhancement of charge separation.

CHAPTER 8

In last chapter we measured the charge transfer dynamics of metal-semiconductor NHM sensitised with dye molecules. Therefore first we sensitized CdSe{Au} HS with bromo-pyrogallol red (Br-PGR). Steady state optical absorption studies have confirmed formation of charge transfer complex between CdSe{Au} HS and Br-PGR. Charge separation in CdSe{Au}/Br-PGR tri-composite system found to take place in different pathways, like electron transfer from the CB of CdSe QD to Au NP, hole transfer from VB of CdSe QD to Br-PGR, electron injection from photo-excited Br-PGR to the CB of CdSe QD. Spectroscopic investigations suggest that on photo-excitation CdSe{Au}/Br-PGR tri-composite system cascading electron transfer and hole transfer take place where all the electrons are localized in Au NP and all the holes are localized in Br-PGR. Electron and hole transfer time from photo-excited CdSe QD to Au NP and Br-PGR were found to be ~ 270 fs and ~500 fs, respectively. Charge recombination reaction between electron in Au NP and hole in Br-PGR was found to be very slow due to spatial separation of charges in CdSe{Au}/Br-PGR tri-composite system. To extent the charge separation, the Au@CdS core shell is sensitised by DBF dye molecule and form a CT complex between Au@CdS and DBF molecule. From steady state and time resolved luminescence study it is confirmed that the electron transfer from photo excited DBF molecule to the CB of CdS shell. The TA study has shown that the electron transfer is occurred from LUMO of DBF to the Au nanocore through the CB of CdS shell and hole transfers from VB of CdS to the HOMO of DBF molecule. The measured electron transfer time was found to be <100 fs (pulse width limited) and hole transfer time from VB of CdS to the HOMO of DBF is 400 fs. Therefore after photo excitation all electron will be localised at the Au nano core and all hole will be localised at the LUMO of DBF in this triad system.

8.2 Outlook.

Charge carrier dynamics of metal-semiconductor NHM and metal-semiconductor-dye tricomposite system by ultrafast spectroscopy followed by their photocatalytic and photovoltaic applications have been discussed in this thesis. We investigated the different photophysical behavior of the two structurally similar coumarin dyes namely coumarin 343 (C-343) and 7-diethyl amino coumarin 3-carboxylic acid (D-1421) on the Au metal NP surface. Therefore Plasmon and molecular resonance coupling affects the excited state photophysical behavior of the the molecule.

The ultrafast charge transfer dynamics has been demonstrated in CdSe quantum dot (QD) and CdSe@CdS core shell with CsPbBr (CPB) perovskite NCs. The charge separated state formation between perovskite and QDs can acts as better solar energy material as compared to the individual. Additionally we measured the carrier dynamics of CdSe@CdS core shell with different CdS shell thickness and correlated with the measured power conversion efficiency (PCE). We optimised the CdS shell thickness in core shell by observing the carrier dynamics to have maximum PCE by CdSe@CdS core shell QDSCs. The maximum 3.88 % PCE has been measured by the CdSe@CdS 4ML where the CdSe shell thickness is 4 monolayer (ML).

The stoichiometry dependent exciton and bi-exciton Dynamics of defect oriented ternary AgInS₂ (AIS) nanocrystals have been discussed. The probe induced bi-exciton featured was observed in AIS NCs even at low pump fluency. The bi-exciton feature and carrier cooling at bi-exciton wavelength increased with increasing the Ag ratio and pump fluency as well, which make it better photovoltaic material.

CHAPTER 8

The enhancement of photovoltaic and photocatalytic efficiency of metal-semiconductor nanohybrid materials compared to semiconductor has been discussed by femtosecond transient absorption spectroscopy study. The measured PCE of CdSe{Au} was found to be 4.39 % which is enhanced from the CdSe QDs 3.37 % efficiency. The electron transfer is occurred from photoexcited CdSe QDs to Au NPs, results a long lived charge separated state is generated which enhanced the PCE. The induced photon to current conversion efficiency (IPCE) by CdSe{Au} NHM also enhanced tremendously than the CdSe QDs. Then we investigated the hot and thermalised electron transfer dynamics from CdSe@CdS core shell to different size of Au NPs followed by its photo catalytic activity. This faster hot electron transfer in larger Au NP enhances the photo degradation of rhodamin dye. i.e. the photo catalytic activity of CdSe@CdS{Au} nanohybrid material was more efficient in attached larger Au compared to smaller one.

We explored the enhancement of charge separation in metal semiconductor NHM by appended with the dye molecule. Therefore after photo excitation the electron has transferred from Br-PGR to CdSe followed by Au NP and hole has transferred from CdSe to Br-PGR. However the long lived charge separated state was generated between CdSe{Au} NHM and Br-PGR where all the electrons are localised in Au and all the holes are in Br-PGR. Additionally we investigated the charge separation between Au@CdS core shell and dibromo-fluorscene (DBF) dye molecule. A strong charge transfer (CT) complex was formed between Au@CdS core shell and DBF molecule. The electron has transferred from LUMO of DBF to the Au nano core through the CB of CdS shell and hole has transfers from VB of CdS to the HOMO of DBF molecule. As a result the charge separation in this triad system (Au@CdS/DBF) is higher than the charge separation in CdS/DBF system. The tri-composite

CHAPTER 8

system should be superior material as compared to NHM for solar energy conversion. However throughout this dissertation I tried to find out better solar energy material by investigating the charge transfer and charge recombination processes by ultrafast transient absorption spectroscopic technique.

References

References

References.

1. Lewis, N. S., Toward Cost-Effective Solar Energy Use. *Science* **2007**, *315*, 798-801.
2. Bartlett, A. A., Sustained availability: A management program for nonrenewable resources. *American Journal of Physics* **1986**, *54*, 398-402.
3. Brus, L. E., Electron–electron and electron-hole interactions in small semiconductor crystallites: The size dependence of the lowest excited electronic state. *The Journal of Chemical Physics* **1984**, *80*, 4403-4409.
4. Kamat, P. V., Meeting the Clean Energy Demand: Nanostructure Architectures for Solar Energy Conversion. *The Journal of Physical Chemistry C* **2007**, *111*, 2834-2860.
5. Alivisatos, A. P., Semiconductor Clusters, Nanocrystals, and Quantum Dots. *Science* **1996**, *271*, 933-937.
6. Nozik, A. J.; Beard, M. C.; Luther, J. M.; Law, M.; Ellingson, R. J.; Johnson, J. C., Semiconductor Quantum Dots and Quantum Dot Arrays and Applications of Multiple Exciton Generation to Third-Generation Photovoltaic Solar Cells. *Chem. Rev.* **2010**, *110*, 6873-6890.
7. Colvin, V. L.; Schlamp, M. C.; Alivisatos, A. P., Light-emitting diodes made from cadmium selenide nanocrystals and a semiconducting polymer. *Nature* **1994**, *370*, 354-357.
8. Klimov, V. I.; McBranch, D. W.; Leatherdale, C. A.; Bawendi, M. G., Electron and hole relaxation pathways in semiconductor quantum dots. *Phys. Rev. B* **1999**, *60*, 13740-13749.
9. El-Sayed, M. A., Small Is Different: Shape-, Size-, and Composition-Dependent Properties of Some Colloidal Semiconductor Nanocrystals. *Acc. Chem. Res.* **2004**, *37*, 326-333.

References

10. Klimov, V. I., Optical Nonlinearities and Ultrafast Carrier Dynamics in Semiconductor Nanocrystals. *J. Phys. Chem. B* **2000**, *104*, 6112-6123.
11. Norris, D. J.; Bawendi, M. G., Measurement and assignment of the size-dependent optical spectrum in CdSe quantum dots. *Phys. Rev. B* **1996**, *53*, 16338-16346.
12. Jr., J. R. A., Interaction of Ga and As₂ Molecular Beams with GaAs Surfaces. *J. Appl. Phys.* **1968**, *39*, 4032-4034.
13. Murray, C. B.; Norris, D. J.; Bawendi, M. G., Synthesis and characterization of nearly monodisperse CdE (E = sulfur, selenium, tellurium) semiconductor nanocrystallites. *J. Am. Chem. Soc.* **1993**, *115*, 8706-8715.
14. Norris, D. J. Measurement and assignment of the size-dependent optical spectrum in cadmium selenide (CdSe) quantum dots. Massachusetts Institute of Technology. , USA, 1995.
15. Guzelian, A. A.; Banin, U.; Kadavanich, A. V.; Peng, X.; Alivisatos, A. P., Colloidal chemical synthesis and characterization of InAs nanocrystal quantum dots. *Appl. Phys. Lett.* **1996**, *69*, 1432-1434.
16. Brus, L. E., A simple model for the ionization potential, electron affinity, and aqueous redox potentials of small semiconductor crystallites. *The Journal of Chemical Physics* **1983**, *79*, 5566-5571.
17. Efros, A. L., Luminescence polarization of CdSe microcrystals. *Phys. Rev. B* **1992**, *46*, 7448-7458.
18. Gfroerer, T. H.; Sturge, M. D.; Kash, K.; Yater, J. A.; Plaut, A. S.; Lin, P. S. D.; Florez, L. T.; Harbison, J. P.; Das, S. R.; Lebrun, L., Slow relaxation of excited states in strain-induced quantum dots. *Phys. Rev. B* **1996**, *53*, 16474-16480.

References

19. Aneesh, J.; Swarnkar, A.; Kumar Ravi, V.; Sharma, R.; Nag, A.; Adarsh, K. V., Ultrafast Exciton Dynamics in Colloidal CsPbBr₃ Perovskite Nanocrystals: Biexciton Effect and Auger Recombination. *J. Phys. Chem. C* **2017**, *121*, 4734-4739.
20. Kambhampati, P., Unraveling the Structure and Dynamics of Excitons in Semiconductor Quantum Dots. *Acc. Chem. Res.* **2011**, *44*, 1-13.
21. Nirmal, M.; Norris, D. J.; Kuno, M.; Bawendi, M. G.; Efros, A. L.; Rosen, M., Observation of the "Dark Exciton" in CdSe Quantum Dots. *Phys. Rev. Lett.* **1995**, *75*, 3728-3731.
22. Klimov, V., Nanocrystal Quantum Dots. **2010**, *2nd Edition*.
23. Henry, C. H.; Nassau, K., Lifetimes of Bound Excitons in CdS. *Phys. Rev. B* **1970**, *1*, 1628-1634.
24. Brennan, F. K., The Physics of Semiconductors,. **1997**.
25. Klimov, V.; Haring Bolivar, P.; Kurz, H., Hot-phonon effects in femtosecond luminescence spectra of electron-hole plasmas in CdS. *Phys. Rev. B* **1995**, *52*, 4728-4731.
26. Sewall, S. L.; Cooney, R. R.; Anderson, K. E. H.; Dias, E. A.; Sagar, D. M.; Kambhampati, P., State-resolved studies of biexcitons and surface trapping dynamics in semiconductor quantum dots. *The Journal of Chemical Physics* **2008**, *129*, 084701.
27. Benisty, H.; Sotomayor-Torrès, C. M.; Weisbuch, C., Intrinsic mechanism for the poor luminescence properties of quantum-box systems. *Phys. Rev. B* **1991**, *44*, 10945-10948.
28. Bockelmann, U.; Bastard, G., Phonon scattering and energy relaxation in two-, one-, and zero-dimensional electron gases. *Phys. Rev. B* **1990**, *42*, 8947-8951.
29. Klimov, V. I.; Schwarz, C. J.; McBranch, D. W.; Leatherdale, C. A.; Bawendi, M. G., Ultrafast dynamics of inter- and intraband transitions in semiconductor nanocrystals: Implications for quantum-dot lasers. *Phys. Rev. B* **1999**, *60*, R2177-R2180.

References

30. Klimov, V. I.; McBranch, D. W., Femtosecond P -to- S Electron Relaxation in Strongly Confined Semiconductor Nanocrystals. *Phys. Rev. Lett.* **1998**, *80*, 4028-4031.
31. Guyot-Sionnest, P.; Shim, M.; Matranga, C.; Hines, M., Intraband relaxation in CdSe quantum dots. *Phys. Rev. B* **1999**, *60*, R2181-R2184.
32. Klimov, V. I.; Mikhailovsky, A. A.; McBranch, D. W.; Leatherdale, C. A.; Bawendi, M. G., Mechanisms for intraband energy relaxation in semiconductor quantum dots: The role of electron-hole interactions. *Phys. Rev. B* **2000**, *61*, R13349-R13352.
33. Kambhampati, P., Hot Exciton Relaxation Dynamics in Semiconductor Quantum Dots: Radiationless Transitions on the Nanoscale. *J. Phys. Chem. C* **2011**, *115*, 22089-22109.
34. Klimov, V. I.; Mikhailovsky, A. A.; McBranch, D. W.; Leatherdale, C. A.; Bawendi, M. G., Quantization of Multiparticle Auger Rates in Semiconductor Quantum Dots. *Science* **2000**, *287*, 1011.
35. Semonin, O. E.; Luther, J. M.; Choi, S.; Chen, H.-Y.; Gao, J.; Nozik, A. J.; Beard, M. C., Peak External Photocurrent Quantum Efficiency Exceeding 100% via MEG in a Quantum Dot Solar Cell. *Science* **2011**, *334*, 1530-1533.
36. Beard, M. C.; Luther, J. M.; Semonin, O. E.; Nozik, A. J., Third Generation Photovoltaics based on Multiple Exciton Generation in Quantum Confined Semiconductors. *Acc. Chem. Res.* **2013**, *46*, 1252-1260.
37. Ellingson, R. J.; Beard, M. C.; Johnson, J. C.; Yu, P.; Micic, O. I.; Nozik, A. J.; Shabaev, A.; Efros, A. L., Highly Efficient Multiple Exciton Generation in Colloidal PbSe and PbS Quantum Dots. *Nano Lett.* **2005**, *5*, 865-871.
38. Pandey, A.; Guyot-Sionnest, P., Slow Electron Cooling in Colloidal Quantum Dots. *Science* **2008**, *322*, 929-932.

References

39. Guyot-Sionnest, P.; Wehrenberg, B.; Yu, D., Intraband relaxation in CdSe nanocrystals and the strong influence of the surface ligands. *The Journal of Chemical Physics* **2005**, *123*, 074709.
40. Cooney, R. R.; Sewall, S. L.; Dias, E. A.; Sagar, D. M.; Anderson, K. E. H.; Kambhampati, P., Unified picture of electron and hole relaxation pathways in semiconductor quantum dots. *Phys. Rev. B* **2007**, *75*, 245311.
41. Underwood, D. F.; Kippeny, T.; Rosenthal, S. J., Ultrafast Carrier Dynamics in CdSe Nanocrystals Determined by Femtosecond Fluorescence Upconversion Spectroscopy. *J. Phys. Chem. B* **2001**, *105*, 436-443.
42. Mooney, J.; Krause, M. M.; Saari, J. I.; Kambhampati, P., Challenge to the deep-trap model of the surface in semiconductor nanocrystals. *Phys. Rev. B* **2013**, *87*, 081201.
43. Garrett, M. D.; Bowers, M. J.; McBride, J. R.; Orndorff, R. L.; Pennycook, S. J.; Rosenthal, S. J., Band Edge Dynamics in CdSe Nanocrystals Observed by Ultrafast Fluorescence Upconversion. *J. Phys. Chem. C* **2008**, *112*, 436-442.
44. Saari, J. I.; Dias, E. A.; Reifsnnyder, D.; Krause, M. M.; Walsh, B. R.; Murray, C. B.; Kambhampati, P., Ultrafast Electron Trapping at the Surface of Semiconductor Nanocrystals: Excitonic and Biexcitonic Processes. *J. Phys. Chem. B* **2013**, *117*, 4412-4421.
45. Talapin, D. V.; Mekis, I.; Götzinger, S.; Kornowski, A.; Benson, O.; Weller, H., CdSe/CdS/ZnS and CdSe/ZnSe/ZnS Core-Shell-Shell Nanocrystals. *J. Phys. Chem. B* **2004**, *108*, 18826-18831.
46. Manna, L.; Scher, E. C.; Li, L.-S.; Alivisatos, A. P., Epitaxial Growth and Photochemical Annealing of Graded CdS/ZnS Shells on Colloidal CdSe Nanorods. *J. Am. Chem. Soc.* **2002**, *124*, 7136-7145.

References

47. Talapin, D. V.; Nelson, J. H.; Shevchenko, E. V.; Aloni, S.; Sadtler, B.; Alivisatos, A. P., Seeded Growth of Highly Luminescent CdSe/CdS Nanoheterostructures with Rod and Tetrapod Morphologies. *Nano Lett.* **2007**, *7*, 2951-2959.
48. Talapin, D. V.; Rogach, A. L.; Kornowski, A.; Haase, M.; Weller, H., Highly Luminescent Monodisperse CdSe and CdSe/ZnS Nanocrystals Synthesized in a Hexadecylamine–Trioctylphosphine Oxide–Trioctylphosphine Mixture. *Nano Lett.* **2001**, *1*, 207-211.
49. Furube, A.; Du, L.; Hara, K.; Katoh, R.; Tachiya, M., Ultrafast Plasmon-Induced Electron Transfer from Gold Nanodots into TiO₂ Nanoparticles. *J. Am. Chem. Soc.* **2007**, *129*, 14852-14853.
50. Kim, S.; Fisher, B.; Eisler, H.-J.; Bawendi, M., Type-II Quantum Dots: CdTe/CdSe(Core/Shell) and CdSe/ZnTe(Core/Shell) Heterostructures. *J. Am. Chem. Soc.* **2003**, *125*, 11466-11467.
51. Ghosh, H. N.; Dana, J.; Maity, P., Hot-Electron Transfer from Semiconductor Domain to Metal Domain in CdSe@CdS{Au} Nano-Heterostructure. *Nanoscale* **2017**.
52. Jia, Y.; Chen, J.; Wu, K.; Kaledin, A.; Musaev, D. G.; Xie, Z.; Lian, T., Enhancing photo-reduction quantum efficiency using quasi-type II core/shell quantum dots. *Chem. Sci* **2016**, *7*, 4125-4133.
53. Nan, W.; Niu, Y.; Qin, H.; Cui, F.; Yang, Y.; Lai, R.; Lin, W.; Peng, X., Crystal Structure Control of Zinc-Blende CdSe/CdS Core/Shell Nanocrystals: Synthesis and Structure-Dependent Optical Properties. *J. Am. Chem. Soc.* **2012**, *134*, 19685-19693.

References

54. Kobayashi, Y.; Chuang, C.-H.; Burda, C.; Scholes, G. D., Exploring Ultrafast Electronic Processes of Quasi-Type II Nanocrystals by Two-Dimensional Electronic Spectroscopy. *J. Phys. Chem. C* **2014**, *118*, 16255-16263.
55. Chuang, C.-H.; Lo, S. S.; Scholes, G. D.; Burda, C., Charge Separation and Recombination in CdTe/CdSe Core/Shell Nanocrystals as a Function of Shell Coverage: Probing the Onset of the Quasi Type-II Regime. *J. Phys. Chem. Lett.* **2010**, *1*, 2530-2535.
56. Wu, K.; Hill, L. J.; Chen, J.; McBride, J. R.; Pavlopolous, N. G.; Richey, N. E.; Pyun, J.; Lian, T., Universal Length Dependence of Rod-to-Seed Exciton Localization Efficiency in Type I and Quasi-Type II CdSe@CdS Nanorods. *ACS Nano* **2015**, *9*, 4591-4599.
57. Englebienne, P.; Hoonacker, A. V.; Verhas, M., Surface plasmon resonance: principles, methods and applications in biomedical sciences. *Spectroscopy* **2003**, *17*, 255-273.
58. Willets, K. A.; Duyn, R. P. V., Localized Surface Plasmon Resonance Spectroscopy and Sensing. *Annual Review of Physical Chemistry* **2007**, *58*, 267-297.
59. Kelly, K. L.; Coronado, E.; Zhao, L. L.; Schatz, G. C., The Optical Properties of Metal Nanoparticles: The Influence of Size, Shape, and Dielectric Environment. *J. Phys. Chem. B* **2003**, *107*, 668-677.
60. Wiley, B. J.; Im, S. H.; Li, Z.-Y.; McLellan, J.; Siekkinen, A.; Xia, Y., Maneuvering the Surface Plasmon Resonance of Silver Nanostructures through Shape-Controlled Synthesis. *J. Phys. Chem. B* **2006**, *110*, 15666-15675.
61. Lee, K.-S.; El-Sayed, M. A., Gold and Silver Nanoparticles in Sensing and Imaging: Sensitivity of Plasmon Response to Size, Shape, and Metal Composition. *J. Phys. Chem. B* **2006**, *110*, 19220-19225.
62. Grand, J.; Adam, P.-M.; Grimault, A.-S.; Vial, A.; Lamy de la Chapelle, M.; Bijeon, J.-L.; Kostcheev, S.; Royer, P., Optical Extinction Spectroscopy of Oblate, Prolate and

References

- Ellipsoid Shaped Gold Nanoparticles: Experiments and Theory. *Plasmonics* **2006**, *1*, 135-140.
63. Sosa, I. O.; Noguez, C.; Barrera, R. G., Optical Properties of Metal Nanoparticles with Arbitrary Shapes. *J. Phys. Chem. B* **2003**, *107*, 6269-6275.
64. Hao, E.; Schatz, G. C.; Hupp, J. T., Synthesis and Optical Properties of Anisotropic Metal Nanoparticles. *Journal of Fluorescence* **2004**, *14*, 331-341.
65. Eustis, S.; El-Sayed, M. A., Why gold nanoparticles are more precious than pretty gold: Noble metal surface plasmon resonance and its enhancement of the radiative and nonradiative properties of nanocrystals of different shapes. *Chemical Society Reviews* **2006**, *35*, 209-217.
66. Alsawafta, M.; Wahbeh, M.; Truong, V.-V., Simulated Optical Properties of Gold Nanocubes and Nanobars by Discrete Dipole Approximation. *Journal of Nanomaterials* **2012**, *2012*, 9.
67. Prescott, S. W.; Mulvaney, P., Erratum: "Gold nanorod extinction spectra" [J. Appl. Phys. 99, 123504 (2006)]. *J. Appl. Phys.* **2008**, *103*, 119901.
68. Burda, C.; Chen, X.; Narayanan, R.; El-Sayed, M. A., Chemistry and Properties of Nanocrystals of Different Shapes. *Chem. Rev.* **2005**, *105*, 1025-1102.
69. Stefan Kooij, E.; Poelsema, B., Shape and size effects in the optical properties of metallic nanorods. *Phys. Chem. Chem. Phys.* **2006**, *8*, 3349-3357.
70. Hutter, E.; Fendler, J. H., Exploitation of Localized Surface Plasmon Resonance. *Advanced Materials* **2004**, *16*, 1685-1706.
71. Collinge, M. J.; Draine, B. T., Discrete-dipole approximation with polarizabilities that account for both finite wavelength and target geometry. *Journal of the Optical Society of America A* **2004**, *21*, 2023-2028.

References

72. Kamat, P. V., Photophysical, Photochemical and Photocatalytic Aspects of Metal Nanoparticles. *J. Phys. Chem. B* **2002**, *106*, 7729-7744.
73. Kreibig, U. V., M., Optical Properties of Metal Clusters. Springer: Berlin. **1995**.
74. Link, S.; El-Sayed, M. A., Simulation of the Optical Absorption Spectra of Gold Nanorods as a Function of Their Aspect Ratio and the Effect of the Medium Dielectric Constant. *J. Phys. Chem. B* **2005**, *109*, 10531-10532.
75. Sau, T. K.; Murphy, C. J., Room Temperature, High-Yield Synthesis of Multiple Shapes of Gold Nanoparticles in Aqueous Solution. *J. Am. Chem. Soc.* **2004**, *126*, 8648-8649.
76. Link, S.; Mohamed, M. B.; El-Sayed, M. A., Simulation of the Optical Absorption Spectra of Gold Nanorods as a Function of Their Aspect Ratio and the Effect of the Medium Dielectric Constant. *J. Phys. Chem. B* **1999**, *103*, 3073-3077.
77. Atwater, H. A.; Polman, A., Plasmonics for improved photovoltaic devices. *Nat Mater* **2010**, *9*, 205-213.
78. Kim, S.; Jung, Y.; Gu, G. H.; Suh, J. S.; Park, S. M.; Ryu, S., Discrete Dipole Approximation Calculations of Optical Properties of Silver Nanorod Arrays in Porous Anodic Alumina. *J. Phys. Chem. C* **2009**, *113*, 16321-16328.
79. Jain, P. K.; Qian, W.; El-Sayed, M. A., Ultrafast Cooling of Photoexcited Electrons in Gold Nanoparticle–Thiolated DNA Conjugates Involves the Dissociation of the Gold–Thiol Bond. *J. Am. Chem. Soc.* **2006**, *128*, 2426-2433.
80. Ahmadi, T. S.; Logunov, S. L.; El-Sayed, M. A., Picosecond Dynamics of Colloidal Gold Nanoparticles. *The Journal of Physical Chemistry* **1996**, *100*, 8053-8056.
81. Link, S.; Burda, C.; Nikoobakht, B.; El-Sayed, M. A., How long does it take to melt a gold nanorod?: A femtosecond pump–probe absorption spectroscopic study. *Chemical Physics Letters* **1999**, *315*, 12-18.

References

82. Link, S.; Burda, C.; Wang, Z. L.; El-Sayed, M. A., Electron dynamics in gold and gold–silver alloy nanoparticles: The influence of a nonequilibrium electron distribution and the size dependence of the electron–phonon relaxation. *The Journal of Chemical Physics* **1999**, *111*, 1255-1264.
83. Link, S.; El-Sayed, M. A., Spectral Properties and Relaxation Dynamics of Surface Plasmon Electronic Oscillations in Gold and Silver Nanodots and Nanorods. *J. Phys. Chem. B* **1999**, *103*, 8410-8426.
84. Hartland, G. V., Optical Studies of Dynamics in Noble Metal Nanostructures. *Chem. Rev.* **2011**, *111*, 3858-3887.
85. Mulvaney, P., Surface Plasmon Spectroscopy of Nanosized Metal Particles. *Langmuir* **1996**, *12*, 788-800.
86. Huang, X.; Neretina, S.; El-Sayed, M. A., *Adv. Mater.* **2009**, *21*, 4880.
87. Khon, E.; Mereshchenko, A.; Tarnovsky, A. N.; Acharya, K.; Klinkova, A.; Hewa-Kasakarage, N. N.; Nemitz, I.; Zamkov, M., Suppression of the Plasmon Resonance in Au/CdS Colloidal Nanocomposites. *Nano Lett.* **2011**, *11*, 1792-1799.
88. Banin, U.; Ben-Shahar, Y.; Vinokurov, K., Hybrid Semiconductor–Metal Nanoparticles: From Architecture to Function. *Chem. Mater.* **2014**, *26*, 97-110.
89. Chauhan, H.; Kumar, Y.; Dana, J.; Satpati, B.; Ghosh, H. N.; Deka, S., Photoinduced ultrafast charge separation in colloidal 2-dimensional CdSe/CdS-Au hybrid nanoplatelets and corresponding application in photocatalysis. *Nanoscale* **2016**, *8*, 15802-15812.
90. Dana, J.; Debnath, T.; Maity, P.; Ghosh, H. N., Enhanced Charge Separation in an Epitaxial Metal–Semiconductor Nanohybrid Material Anchored with an Organic Molecule. *J. Phys. Chem. C* **2015**, *119*, 22181-22189.

References

91. Acharya, K. P.; Khnayzer, R. S.; O'Connor, T.; Diederich, G.; Kirsanova, M.; Klinkova, A.; Roth, D.; Kinder, E.; Imboden, M.; Zamkov, M., The Role of Hole Localization in Sacrificial Hydrogen Production by Semiconductor–Metal Heterostructured Nanocrystals. *Nano Lett.* **2011**, *11*, 2919-2926.
92. Wu, K.; Chen, Z.; Lv, H.; Zhu, H.; Hill, C. L.; Lian, T., Hole Removal Rate Limits Photodriven H₂ Generation Efficiency in CdS-Pt and CdSe/CdS-Pt Semiconductor Nanorod–Metal Tip Heterostructures. *J. Am. Chem. Soc.* **2014**, *136*, 7708-7716.
93. Wu, K.; Chen, J.; McBride, J. R.; Lian, T., Efficient hot-electron transfer by a plasmon-induced interfacial charge-transfer transition. *Science* **2015**, *349*, 632.
94. Wu, K.; Rodríguez-Córdoba, W. E.; Yang, Y.; Lian, T., Plasmon-Induced Hot Electron Transfer from the Au Tip to CdS Rod in CdS-Au Nanoheterostructures. *Nano Lett.* **2013**, *13*, 5255-5263.
95. Wu, K.; Zhu, H.; Liu, Z.; Rodríguez-Córdoba, W.; Lian, T., Ultrafast Charge Separation and Long-Lived Charge Separated State in Photocatalytic CdS–Pt Nanorod Heterostructures. *J. Am. Chem. Soc.* **2012**, *134*, 10337-10340.
96. Ancona, M. G.; Kooi, S. E.; Kruppa, W.; Snow, A. W.; Foos, E. E.; Whitman, L. J.; Park, D.; Shirey, L., Patterning of Narrow Au Nanocluster Lines Using V₂O₅ Nanowire Masks and Ion-Beam Milling. *Nano Lett.* **2003**, *3*, 135-138.
97. Lam, C.; Zhang, Y. F.; Tang, Y. H.; Lee, C. S.; Bello, I.; Lee, S. T., Large-scale synthesis of ultrafine Si nanoparticles by ball milling. *Journal of Crystal Growth* **2000**, *220*, 466-470.
98. Thessing, J.; Qian, J.; Chen, H.; Pradhan, N.; Peng, X., Interparticle Influence on Size/Size Distribution Evolution of Nanocrystals. *J. Am. Chem. Soc.* **2007**, *129*, 2736-2737.

References

99. and, C. B. M.; Kagan, C. R.; Bawendi, M. G., Synthesis and Characterization of Monodisperse Nanocrystals and Close-Packed Nanocrystal Assemblies. *Annual Review of Materials Science* **2000**, *30*, 545-610.
100. LaMer, V. K.; Dinegar, R. H., Theory, Production and Mechanism of Formation of Monodispersed Hydrosols. *J. Am. Chem. Soc.* **1950**, *72*, 4847-4854.
101. Marcus, R. A., Chemical and Electrochemical Electron-Transfer Theory. *Annual Review of Physical Chemistry* **1964**, *15*, 155-196.
102. Marcus, R. A., On the Theory of Oxidation-Reduction Reactions Involving Electron Transfer. I. *The Journal of Chemical Physics* **1956**, *24*, 966-978.
103. Barea, E. M.; Shalom, M.; Giménez, S.; Hod, I.; Mora-Seró, I.; Zaban, A.; Bisquert, J., Design of Injection and Recombination in Quantum Dot Sensitized Solar Cells. *J. Am. Chem. Soc.* **2010**, *132*, 6834-6839.
104. Hetsch, F.; Xu, X.; Wang, H.; Kershaw, S. V.; Rogach, A. L., Semiconductor Nanocrystal Quantum Dots as Solar Cell Components and Photosensitizers: Material, Charge Transfer, and Separation Aspects of Some Device Topologies. *J. Phys. Chem. Lett.* **2011**, *2*, 1879-1887.
105. Kamat, P. V.; Tvrđy, K.; Baker, D. R.; Radich, J. G., Beyond Photovoltaics: Semiconductor Nanoarchitectures for Liquid-Junction Solar Cells. *Chem. Rev.* **2010**, *110*, 6664-6688.
106. Mora-Seró, I.; Bisquert, J., Breakthroughs in the Development of Semiconductor-Sensitized Solar Cells. *J. Phys. Chem. Lett.* **2010**, *1*, 3046-3052.
107. Mora-Seró, I.; Giménez, S.; Fabregat-Santiago, F.; Gómez, R.; Shen, Q.; Toyoda, T.; Bisquert, J., Recombination in Quantum Dot Sensitized Solar Cells. *Acc. Chem. Res.* **2009**, *42*, 1848-1857.

References

108. Kamat, P. V., Quantum Dot Solar Cells. Semiconductor Nanocrystals as Light Harvesters. *J. Phys. Chem. C* **2008**, *112*, 18737-18753.
109. Kamat, P. V., Quantum Dot Solar Cells. The Next Big Thing in Photovoltaics. *J. Phys. Chem. Lett.* **2013**, *4*, 908-918.
110. Yu, X.-Y.; Lei, B.-X.; Kuang, D.-B.; Su, C.-Y., Highly efficient CdTe/CdS quantum dot sensitized solar cells fabricated by a one-step linker assisted chemical bath deposition. *Chemical Science* **2011**, *2*, 1396-1400.
111. Lee, Y.-L.; Lo, Y.-S., Highly Efficient Quantum-Dot-Sensitized Solar Cell Based on Co-Sensitization of CdS/CdSe. *Advanced Functional Materials* **2009**, *19*, 604-609.
112. Lakowicz, J. R., Principles of Fluorescence Spectroscopy, 3rd ed., Springer. **2006**.
113. Albani, J. R., Principles and applications of Fluorescence Spectroscopy, Blackwell Publishing,. **2007**.
114. Lakowicz, J. R., Principles of Fluorescence Spectroscopy, 3rd ed.; Springer: New York. **2006**.
115. Becker, W., Advanced Time-Correlated Single Photon Counting Techniques, Springer. **2005**.
116. O'Connor, D. V., Phillips, D., Time-Correlated Single-Photon Counting, Academic Press: London,. **1984**.
117. Shah, J., Ultrafast spectroscopy of semiconductors and semiconductor nanostructures, 2nd Ed., Springer,. **1999**.
118. Demtröder, W., Laser Spectroscopy: Basic concept and instrumentation, 3rd edition, Springer (India) Private Limited,. **2004**.
119. Abramczyk, H., Introduction to Laser Spectroscopy, Elsevier. **2005**.

References

120. Moulton, P. F., Spectroscopic and laser characteristics of Ti:Al₂O₃. *Journal of the Optical Society of America B* **1986**, *3*, 125-133.
121. Martin, M. M., Hynes, J. T., Femtochemistry and Femtobiology: Ultrafast Events in Molecular Science, Elsevier, 1st edition,. **2004**.
122. Rullière, C., 2005. **Femtosecond Laser Pulses: Principles and Experiments**, Springer Science + Business Media.
123. Diels, J.-C., Rudolph, W., Ultrashort Laser Pulse Phenomena: Fundamentals, Techniques, and Applications on a Femtosecond Time Scale, 2nd edition, Academic Press, Elsevier,. **2006**.
124. Georges, P.; Estable, F.; Salin, F.; Poizat, J. P.; Grangier, P.; Brun, A., High-efficiency multipass Ti:sapphire amplifiers for a continuous-wave single-mode laser. *Optics Letters* **1991**, *16*, 144-146.
125. Enustun, B. V.; Turkevich, J., Coagulation of Colloidal Gold. *J. Am. Chem. Soc.* **1963**, *85*, 3317-3328.
126. Kimling, J.; Maier, M.; Okenve, B.; Kotaidis, V.; Ballot, H.; Plech, A., Turkevich Method for Gold Nanoparticle Synthesis Revisited. *J. Phys. Chem. B* **2006**, *110*, 15700-15707.
127. Qu, L.; Peng, X., Control of Photoluminescence Properties of CdSe Nanocrystals in Growth. *J. Am. Chem. Soc.* **2002**, *124*, 2049-2055.
128. Li, J. J.; Wang, Y. A.; Guo, W.; Keay, J. C.; Mishima, T. D.; Johnson, M. B.; Peng, X., Large-Scale Synthesis of Nearly Monodisperse CdSe/CdS Core/Shell Nanocrystals Using Air-Stable Reagents via Successive Ion Layer Adsorption and Reaction. *J. Am. Chem. Soc.* **2003**, *125*, 12567-12575.

References

129. Dana, J.; Maity, P.; Ghosh, H. N., Hot-electron transfer from the semiconductor domain to the metal domain in CdSe@CdS{Au} nano-heterostructures. *Nanoscale* **2017**, *9*, 9723-9731.
130. Protesescu, L.; Yakunin, S.; Bodnarchuk, M. I.; Krieg, F.; Caputo, R.; Hendon, C. H.; Yang, R. X.; Walsh, A.; Kovalenko, M. V., Nanocrystals of Cesium Lead Halide Perovskites (CsPbX₃, X = Cl, Br, and I): Novel Optoelectronic Materials Showing Bright Emission with Wide Color Gamut. *Nano Lett.* **2015**, *15*, 3692-3696.
131. Xie, R.; Rutherford, M.; Peng, X., Formation of High-Quality I-III-VI Semiconductor Nanocrystals by Tuning Relative Reactivity of Cationic Precursors. *J. Am. Chem. Soc.* **2009**, *131*, 5691-5697.
132. Mokari, T.; Rothenberg, E.; Popov, I.; Costi, R.; Banin, U., Selective Growth of Metal Tips onto Semiconductor Quantum Rods and Tetrapods. *Science* **2004**, *304*, 1787-1790.
133. Mokari, T.; Rothenberg, E.; Popov, I.; Costi, R.; Banin, U., Selective Growth of Metal Tips onto Semiconductor Quantum Rods and Tetrapods. *Science* **2004**, *304*, 1787.
134. Zhang, J.; Tang, Y.; Lee, K.; Ouyang, M., Nonepitaxial Growth of Hybrid Core-Shell Nanostructures with Large Lattice Mismatches. *Science* **2010**, *327*, 1634-1638.
135. Lambright, S.; Butaeva, E.; Razgoniaeva, N.; Hopkins, T.; Smith, B.; Perera, D.; Corbin, J.; Khon, E.; Thomas, R.; Moroz, P.; Mereshchenko, A.; Tarnovsky, A.; Zamkov, M., Enhanced Lifetime of Excitons in Nonepitaxial Au/CdS Core/Shell Nanocrystals. *ACS Nano* **2014**, *8*, 352-361.
136. Shore, M. S.; Wang, J.; Johnston-Peck, A. C.; Oldenburg, A. L.; Tracy, J. B., Synthesis of Au(Core)/Ag(Shell) Nanoparticles and their Conversion to AuAg Alloy Nanoparticles. *Small* **2011**, *7*, 230-234.

References

137. Zhao, K.; Pan, Z.; Mora-Seró, I.; Cánovas, E.; Wang, H.; Song, Y.; Gong, X.; Wang, J.; Bonn, M.; Bisquert, J.; Zhong, X., Boosting Power Conversion Efficiencies of Quantum-Dot-Sensitized Solar Cells Beyond 8% by Recombination Control. *J. Am. Chem. Soc.* **2015**, *137*, 5602-5609.
138. Jiao, S.; Shen, Q.; Mora-Seró, I.; Wang, J.; Pan, Z.; Zhao, K.; Kuga, Y.; Zhong, X.; Bisquert, J., Band Engineering in Core/Shell ZnTe/CdSe for Photovoltage and Efficiency Enhancement in Exciplex Quantum Dot Sensitized Solar Cells. *ACS Nano* **2015**, *9*, 908-915.
139. Maity, P.; Maiti, S.; Debnath, T.; Dana, J.; Guin, S. K.; Ghosh, H. N., Intraband Electron Cooling Mediated Unprecedented Photocurrent Conversion Efficiency of CdS_xSe_{1-x} Alloy QDs: Direct Correlation between Electron Cooling and Efficiency. *J. Phys. Chem. C* **2016**, *120*, 21309-21316.
140. Pan, Z.; Zhao, K.; Wang, J.; Zhang, H.; Feng, Y.; Zhong, X., Near Infrared Absorption of CdS_xTe_{1-x} Alloyed Quantum Dot Sensitized Solar Cells with More than 6% Efficiency and High Stability. *ACS Nano* **2013**, *7*, 5215-5222.
141. Sapsford, K. E.; Berti, L.; Medintz, I. L., Materials for Fluorescence Resonance Energy Transfer Analysis: Beyond Traditional Donor–Acceptor Combinations. *Angewandte Chemie International Edition* **2006**, *45*, 4562-4589.
142. Ray, P. C.; Darbha, G. K.; Ray, A.; Walker, J.; Hardy, W., Gold Nanoparticle Based FRET for DNA Detection. *Plasmonics* **2007**, *2*, 173-183.
143. Daniel, M.-C.; Astruc, D., Gold Nanoparticles: Assembly, Supramolecular Chemistry, Quantum-Size-Related Properties, and Applications toward Biology, Catalysis, and Nanotechnology. *Chem. Rev.* **2004**, *104*, 293-346.
144. De, M.; Ghosh, P. S.; Rotello, V. M., Applications of Nanoparticles in Biology. *Advanced Materials* **2008**, *20*, 4225-4241.

References

145. Anker, J. N.; Hall, W. P.; Lyandres, O.; Shah, N. C.; Zhao, J.; Van Duyne, R. P., Biosensing with plasmonic nanosensors. *Nat Mater* **2008**, *7*, 442-453.
146. Fang, N.; Lee, H.; Sun, C.; Zhang, X., Sub-Diffraction-Limited Optical Imaging with a Silver Superlens. *Science* **2005**, *308*, 534-537.
147. Ferry, V. E.; Sweatlock, L. A.; Pacifici, D.; Atwater, H. A., Plasmonic Nanostructure Design for Efficient Light Coupling into Solar Cells. *Nano Lett.* **2008**, *8*, 4391-4397.
148. Kulkarni, A. P.; Noone, K. M.; Munechika, K.; Guyer, S. R.; Ginger, D. S., Plasmon-Enhanced Charge Carrier Generation in Organic Photovoltaic Films Using Silver Nanoprisms. *Nano Lett.* **2010**, *10*, 1501-1505.
149. Ni, W.; Yang, Z.; Chen, H.; Li, L.; Wang, J., Coupling between Molecular and Plasmonic Resonances in Freestanding Dye-Gold Nanorod Hybrid Nanostructures. *J. Am. Chem. Soc.* **2008**, *130*, 6692-6693.
150. Haes, A. J.; Zou, S.; Zhao, J.; Schatz, G. C.; Van Duyne, R. P., Localized Surface Plasmon Resonance Spectroscopy near Molecular Resonances. *J. Am. Chem. Soc.* **2006**, *128*, 10905-10914.
151. Zhao, J.; Jensen, L.; Sung, J.; Zou, S.; Schatz, G. C.; Van Duyne, R. P., Interaction of Plasmon and Molecular Resonances for Rhodamine 6G Adsorbed on Silver Nanoparticles. *J. Am. Chem. Soc.* **2007**, *129*, 7647-7656.
152. Wurtz, G. A.; Evans, P. R.; Hendren, W.; Atkinson, R.; Dickson, W.; Pollard, R. J.; Zayats, A. V.; Harrison, W.; Bower, C., Molecular Plasmonics with Tunable Exciton-Plasmon Coupling Strength in J-Aggregate Hybridized Au Nanorod Assemblies. *Nano Lett.* **2007**, *7*, 1297-1303.
153. El-Sayed, M. A., Some Interesting Properties of Metals Confined in Time and Nanometer Space of Different Shapes. *Acc. Chem. Res.* **2001**, *34*, 257-264.

References

154. Toshihiro, N.; Shinji, H., Enhancement of Dye Fluorescence by Gold Nanoparticles: Analysis of Particle Size Dependence. *Japanese Journal of Applied Physics* **2005**, *44*, 6833.
155. Dong, L.; Ye, F.; Hu, J.; Popov, S.; Friberg, A. T.; Muhammed, M., *Fluorescence quenching and photobleaching in Au/Rh6G nanoassemblies: impact of competition between radiative and non-radiative decay*. 2011; Vol. 6.
156. Thomas, K. G.; Kamat, P. V., Making Gold Nanoparticles Glow: Enhanced Emission from a Surface-Bound Fluoroprobe. *J. Am. Chem. Soc.* **2000**, *122*, 2655-2656.
157. Dulkeith, E.; Morteani, A. C.; Niedereichholz, T.; Klar, T. A.; Feldmann, J.; Levi, S. A.; van Veggel, F. C. J. M.; Reinhoudt, D. N.; Möller, M.; Gittins, D. I., Fluorescence Quenching of Dye Molecules near Gold Nanoparticles: Radiative and Nonradiative Effects. *Phys. Rev. Lett.* **2002**, *89*, 203002.
158. Dulkeith, E.; Ringler, M.; Klar, T. A.; Feldmann, J.; Muñoz Javier, A.; Parak, W. J., Gold Nanoparticles Quench Fluorescence by Phase Induced Radiative Rate Suppression. *Nano Lett.* **2005**, *5*, 585-589.
159. Sen, T.; Patra, A., Recent Advances in Energy Transfer Processes in Gold-Nanoparticle-Based Assemblies. *J. Phys. Chem. C* **2012**, *116*, 17307-17317.
160. Sen, T.; Sadhu, S.; Patra, A., Surface energy transfer from rhodamine 6G to gold nanoparticles: A spectroscopic ruler. *Appl. Phys. Lett.* **2007**, *91*, 043104.
161. Fan, C.; Wang, S.; Hong, J. W.; Bazan, G. C.; Plaxco, K. W.; Heeger, A. J., Beyond superquenching: Hyper-efficient energy transfer from conjugated polymers to gold nanoparticles. *Proceedings of the National Academy of Sciences* **2003**, *100*, 6297-6301.
162. Kamat, P. V.; Barazzouk, S.; Hotchandani, S., Electrochemical Modulation of Fluorophore Emission on a Nanostructured Gold Film. *Angewandte Chemie International Edition* **2002**, *41*, 2764-2767.

References

163. Breshike, C. J.; Riskowski, R. A.; Strouse, G. F., Leaving Förster Resonance Energy Transfer Behind: Nanometal Surface Energy Transfer Predicts the Size-Enhanced Energy Coupling between a Metal Nanoparticle and an Emitting Dipole. *J. Phys. Chem. C* **2013**, *117*, 23942-23949.
164. Huang, T.; Murray, R. W., Quenching of [Ru(bpy)₃]²⁺ Fluorescence by Binding to Au Nanoparticles. *Langmuir* **2002**, *18*, 7077-7081.
165. Ramakrishna, G.; Ghosh, H. N., Efficient Electron Injection from Twisted Intramolecular Charge Transfer (TICT) State of 7-Diethyl amino coumarin 3-carboxylic Acid (D-1421) Dye to TiO₂ Nanoparticle. *J. Phys. Chem. A* **2002**, *106*, 2545-2553.
166. Verma, S.; Ghosh, H. N., Tuning Interfacial Charge Separation by Molecular Twist: A New Insight into Coumarin-Sensitized TiO₂ Films. *J. Phys. Chem. C* **2014**, *118*, 10661-10669.
167. Debnath, T.; Maity, P.; Lobo, H.; Singh, B.; Shankarling, G. S.; Ghosh, H. N., Extensive Reduction in Back Electron Transfer in Twisted Intramolecular Charge-Transfer (TICT) Coumarin-Dye-Sensitized TiO₂ Nanoparticles/Film: A Femtosecond Transient Absorption Study. *Chem. Eur. J.* **2014**, *20*, 3510-3519.
168. Ramakrishna, G.; Singh, A. K.; Palit, D. K.; Ghosh, H. N., Effect of Molecular Structure on Interfacial Electron Transfer Dynamics of 7-N,N-Dimethyl Coumarin 4-Acetic Acid (DMACA) and 7-Hydroxy Coumarin 4-Acetic Acid (HCA) Sensitized TiO₂ and ZrO₂ Nanoparticles. *J. Phys. Chem. B* **2004**, *108*, 12489-12496.
169. Haiss, W.; Thanh, N. T. K.; Aveyard, J.; Fernig, D. G., Determination of Size and Concentration of Gold Nanoparticles from UV-Vis Spectra. *Analytical Chemistry* **2007**, *79*, 4215-4221.

References

170. Brewer, S. H.; Glomm, W. R.; Johnson, M. C.; Knag, M. K.; Franzen, S., Probing BSA Binding to Citrate-Coated Gold Nanoparticles and Surfaces. *Langmuir* **2005**, *21*, 9303-9307.
171. Chithrani, B. D.; Ghazani, A. A.; Chan, W. C. W., Determining the Size and Shape Dependence of Gold Nanoparticle Uptake into Mammalian Cells. *Nano Lett.* **2006**, *6*, 662-668.
172. Riter, R. E.; Undiks, E. P.; Levinger, N. E., Impact of Counterion on Water Motion in Aerosol OT Reverse Micelles. *J. Am. Chem. Soc.* **1998**, *120*, 6062-6067.
173. Wang, C.; Daimon, H.; Onodera, T.; Koda, T.; Sun, S. H., *Angew. Chem., Int. Ed.* **2008**, *47*, 3588.
174. Karam, T. E.; Haber, L. H., Molecular Adsorption and Resonance Coupling at the Colloidal Gold Nanoparticle Interface. *J. Phys. Chem. C* **2014**, *118*, 642-649.
175. Aldeek, F.; Ji, X.; Mattoussi, H., Quenching of Quantum Dot Emission by Fluorescent Gold Clusters: What It Does and Does Not Share with the Förster Formalism. *J. Phys. Chem. C* **2013**, *117*, 15429-15437.
176. Anger, P.; Bharadwaj, P.; Novotny, L., Enhancement and Quenching of Single-Molecule Fluorescence. *Phys. Rev. Lett.* **2006**, *96*, 113002.
177. Ming, T.; Chen, H.; Jiang, R.; Li, Q.; Wang, J., Plasmon-Controlled Fluorescence: Beyond the Intensity Enhancement. *J. Phys. Chem. Lett.* **2012**, *3*, 191-202.
178. Rettig, W.; Wermuth, G., The kinetics of formation of twisted intramolecular charge transfer (TICT) states in p-substituted dialkylanilines: consequences of conical intersections along the reaction coordinate. *Journal of Photochemistry* **1985**, *28*, 351-366.
179. Lan, X.; Masala, S.; Sargent, E. H., Charge-extraction strategies for colloidal quantum dot photovoltaics. *Nat Mater* **2014**, *13*, 233-240.

References

180. Kramer, I. J.; Sargent, E. H., Colloidal Quantum Dot Photovoltaics: A Path Forward. *ACS Nano* **2011**, *5*, 8506-8514.
181. Talapin, D. V.; Lee, J.-S.; Kovalenko, M. V.; Shevchenko, E. V., Prospects of Colloidal Nanocrystals for Electronic and Optoelectronic Applications. *Chem. Rev.* **2010**, *110*, 389-458.
182. Santra, P. K.; Kamat, P. V., Mn-Doped Quantum Dot Sensitized Solar Cells: A Strategy to Boost Efficiency over 5%. *J. Am. Chem. Soc.* **2012**, *134*, 2508-2511.
183. Bang, J. H.; Kamat, P. V., Solar Cells by Design: Photoelectrochemistry of TiO₂ Nanorod Arrays Decorated with CdSe. *Advanced Functional Materials* **2010**, *20*, 1970-1976.
184. Selopal, G. S.; Zhao, H.; Tong, X.; Benetti, D.; Navarro-Pardo, F.; Zhou, Y.; Barba, D.; Vidal, F.; Wang, Z. M.; Rosei, F., Highly Stable Colloidal “Giant” Quantum Dots Sensitized Solar Cells. *Advanced Functional Materials*, 1701468-n/a.
185. Choi, J.; Kim, Y.; Jo, J. W.; Kim, J.; Sun, B.; Walters, G.; García de Arquer, F. P.; Quintero-Bermudez, R.; Li, Y.; Tan, C. S.; Quan, L. N.; Kam, A. P. T.; Hoogland, S.; Lu, Z.; Voznyy, O.; Sargent, E. H., Chloride Passivation of ZnO Electrodes Improves Charge Extraction in Colloidal Quantum Dot Photovoltaics. *Advanced Materials*, 1702350-n/a.
186. Kim, G.-H.; García de Arquer, F. P.; Yoon, Y. J.; Lan, X.; Liu, M.; Voznyy, O.; Yang, Z.; Fan, F.; Ip, A. H.; Kanjanaboos, P.; Hoogland, S.; Kim, J. Y.; Sargent, E. H., High-Efficiency Colloidal Quantum Dot Photovoltaics via Robust Self-Assembled Monolayers. *Nano Lett.* **2015**, *15*, 7691-7696.
187. Jiao, S.; Wang, J.; Shen, Q.; Li, Y.; Zhong, X., Surface engineering of PbS quantum dot sensitized solar cells with a conversion efficiency exceeding 7%. *J. Mater. Chem. A* **2016**, *4*, 7214-7221.

References

188. Pan, Z.; Mora-Seró, I.; Shen, Q.; Zhang, H.; Li, Y.; Zhao, K.; Wang, J.; Zhong, X.; Bisquert, J., High-Efficiency “Green” Quantum Dot Solar Cells. *J. Am. Chem. Soc.* **2014**, *136*, 9203-9210.
189. Li, W.; Pan, Z.; Zhong, X., CuInSe₂ and CuInSe₂-ZnS based high efficiency "green" quantum dot sensitized solar cells. *J. Mater. Chem. A* **2015**, *3*, 1649-1655.
190. Halder, G.; Bhattacharyya, S., Zinc-diffused silver indium selenide quantum dot sensitized solar cells with enhanced photoconversion efficiency. *J. Mater. Chem. A* **2017**, *5*, 11746-11755.
191. Shalom, M.; Dor, S.; Rühle, S.; Grinis, L.; Zaban, A., Core/CdS Quantum Dot/Shell Mesoporous Solar Cells with Improved Stability and Efficiency Using an Amorphous TiO₂ Coating. *J. Phys. Chem. C* **2009**, *113*, 3895-3898.
192. Nam, M.; Kim, S.; Kim, S.; Kim, S.-W.; Lee, K., Efficient hybrid solar cells using PbS_xSe_{1-x} quantum dots and nanorods for broad-range photon absorption and well-assembled charge transfer networks. *Nanoscale* **2013**, *5*, 8202-8209.
193. Du, J.; Du, Z.; Hu, J.-S.; Pan, Z.; Shen, Q.; Sun, J.; Long, D.; Dong, H.; Sun, L.; Zhong, X.; Wan, L.-J., Zn–Cu–In–Se Quantum Dot Solar Cells with a Certified Power Conversion Efficiency of 11.6%. *J. Am. Chem. Soc.* **2016**, *138*, 4201-4209.
194. Jiao, S.; Du, J.; Du, Z.; Long, D.; Jiang, W.; Pan, Z.; Li, Y.; Zhong, X., Nitrogen-Doped Mesoporous Carbons as Counter Electrodes in Quantum Dot Sensitized Solar Cells with a Conversion Efficiency Exceeding 12%. *J. Phys. Chem. Lett.* **2017**, *8*, 559-564.
195. Bi, D.; Yi, C.; Luo, J.; Décoppet, J.-D.; Zhang, F.; Zakeeruddin, Shaik M.; Li, X.; Hagfeldt, A.; Grätzel, M., Polymer-templated nucleation and crystal growth of perovskite films for solar cells with efficiency greater than 21%. **2016**, *1*, 16142.

References

196. Kamat, P. V.; Christians, J. A.; Radich, J. G., Quantum Dot Solar Cells: Hole Transfer as a Limiting Factor in Boosting the Photoconversion Efficiency. *Langmuir* **2014**, *30*, 5716-5725.
197. Yang, S.-m.; Huang, C.-h.; Zhai, J.; Wang, Z.-s.; Jiang, L., High photostability and quantum yield of nanoporous TiO₂ thin film electrodes co-sensitized with capped sulfides. *J. Mat. Chem.* **2002**, *12*, 1459-1464.
198. Toyoda, T.; Shen, Q., Quantum-Dot-Sensitized Solar Cells: Effect of Nanostructured TiO₂ Morphologies on Photovoltaic Properties. *J. Phys. Chem. Lett.* **2012**, *3*, 1885-1893.
199. Du, Z.; Zhang, H.; Bao, H.; Zhong, X., Optimization of TiO₂ photoanode films for highly efficient quantum dot-sensitized solar cells. *J. Mater. Chem. A* **2014**, *2*, 13033-13040.
200. Guijarro, N.; Campina, J. M.; Shen, Q.; Toyoda, T.; Lana-Villarreal, T.; Gomez, R., Uncovering the role of the ZnS treatment in the performance of quantum dot sensitized solar cells. *Phys. Chem. Chem. Phys.* **2011**, *13*, 12024-12032.
201. Prasittichai, C.; Avila, J. R.; Farha, O. K.; Hupp, J. T., Systematic Modulation of Quantum (Electron) Tunneling Behavior by Atomic Layer Deposition on Nanoparticulate SnO₂ and TiO₂ Photoanodes. *J. Am. Chem. Soc.* **2013**, *135*, 16328-16331.
202. Palomares, E.; Clifford, J. N.; Haque, S. A.; Lutz, T.; Durrant, J. R., Control of Charge Recombination Dynamics in Dye Sensitized Solar Cells by the Use of Conformally Deposited Metal Oxide Blocking Layers. *J. Am. Chem. Soc.* **2003**, *125*, 475-482.
203. Chandiran, A. K.; Nazeeruddin, M. K.; Grätzel, M., The Role of Insulating Oxides in Blocking the Charge Carrier Recombination in Dye-Sensitized Solar Cells. *Advanced Functional Materials* **2014**, *24*, 1615-1623.
204. Ivanov, S. A.; Piryatinski, A.; Nanda, J.; Tretiak, S.; Zavadil, K. R.; Wallace, W. O.; Werder, D.; Klimov, V. I., Type-II Core/Shell CdS/ZnSe Nanocrystals: Synthesis,

References

Electronic Structures, and Spectroscopic Properties. *J. Am. Chem. Soc.* **2007**, *129*, 11708-11719.

205. Zhu, H.; Song, N.; Lian, T., Wave Function Engineering for Ultrafast Charge Separation and Slow Charge Recombination in Type II Core/Shell Quantum Dots. *J. Am. Chem. Soc.* **2011**, *133*, 8762-8771.

206. Abdellah, M.; Marschan, R.; Žídek, K.; Messing, M. E.; Abdelwahab, A.; Chábera, P.; Zheng, K.; Pullerits, T., Hole Trapping: The Critical Factor for Quantum Dot Sensitized Solar Cell Performance. *J. Phys. Chem. C* **2014**, *118*, 25802-25808.

207. Maity, P.; Debnath, T.; Ghosh, H. N., Ultrafast Charge Carrier Delocalization in CdSe/CdS Quasi-Type II and CdS/CdSe Inverted Type I Core–Shell: A Structural Analysis through Carrier-Quenching Study. *J. Phys. Chem. C* **2015**, *119*, 26202-26211.

208. Kulbak, M.; Gupta, S.; Kedem, N.; Levine, I.; Bendikov, T.; Hodes, G.; Cahen, D., Cesium Enhances Long-Term Stability of Lead Bromide Perovskite-Based Solar Cells. *J. Phys. Chem. Lett.* **2016**, *7*, 167-172.

209. Swarnkar, A.; Marshall, A. R.; Sanhira, E. M.; Chernomordik, B. D.; Moore, D. T.; Christians, J. A.; Chakrabarti, T.; Luther, J. M., Quantum dot–induced phase stabilization of α -CsPbI₃ perovskite for high-efficiency photovoltaics. *Science* **2016**, *354*, 92-95.

210. Maity, P.; Dana, J.; Ghosh, H. N., Multiple Charge Transfer Dynamics in Colloidal CsPbBr₃ Perovskite Quantum Dots Sensitized Molecular Adsorbate. *J. Phys. Chem. C* **2016**, *120*, 18348-18354.

211. Maity, P.; Debnath, T.; Ghosh, H. N., Ultrafast Hole- and Electron-Transfer Dynamics in CdS–Dibromofluorescein (DBF) Supersensitized Quantum Dot Solar Cell Materials. *J. Phys. Chem. Lett.* **2013**, *4*, 4020-4025.

References

212. Debnath, T.; Maity, P.; Maiti, S.; Ghosh, H. N., Electron Trap to Electron Storage Center in Specially Aligned Mn-Doped CdSe d-Dot: A Step Forward in the Design of Higher Efficient Quantum-Dot Solar Cell. *J. Phys. Chem. Lett.* **2014**, *5*, 2836-2842.
213. Singhal, P.; Ghosh, H. N., Ultrafast Hole/Electron Transfer Dynamics in a CdSe Quantum Dot Sensitized by Pyrogallol Red: A Super-Sensitization System. *J. Phys. Chem. C* **2014**, *118*, 16358-16365.
214. González-Pedro, V.; Xu, X.; Mora-Seró, I.; Bisquert, J., Modeling High-Efficiency Quantum Dot Sensitized Solar Cells. *ACS Nano* **2010**, *4*, 5783-5790.
215. Becker, M. A.; Radich, J. G.; Bunker, B. A.; Kamat, P. V., How Does a SILAR CdSe Film Grow? Tuning the Deposition Steps to Suppress Interfacial Charge Recombination in Solar Cells. *J. Phys. Chem. Lett.* **2014**, *5*, 1575-1582.
216. Lee, H. J.; Bang, J.; Park, J.; Kim, S.; Park, S.-M., Multilayered Semiconductor (CdS/CdSe/ZnS)-Sensitized TiO₂ Mesoporous Solar Cells: All Prepared by Successive Ionic Layer Adsorption and Reaction Processes. *Chem. Mater.* **2010**, *22*, 5636-5643.
217. Lai, C.-H.; Chou, P.-T., All chemically deposited, annealing and mesoporous metal oxide free CdSe solar cells. *Chemical Communications* **2011**, *47*, 3448-3450.
218. Santra, P. K.; Nair, P. V.; George Thomas, K.; Kamat, P. V., CuInS₂-Sensitized Quantum Dot Solar Cell. Electrophoretic Deposition, Excited-State Dynamics, and Photovoltaic Performance. *J. Phys. Chem. Lett.* **2013**, *4*, 722-729.
219. Watson, D. F., Linker-Assisted Assembly and Interfacial Electron-Transfer Reactivity of Quantum Dot–Substrate Architectures. *J. Phys. Chem. Lett.* **2010**, *1*, 2299-2309.
220. Sahasrabudhe, A.; Bhattacharyya, S., Dual Sensitization Strategy for High-Performance Core/Shell/Quasi-shell Quantum Dot Solar Cells. *Chem. Mater.* **2015**, *27*, 4848-4859.

References

221. Rawalekar, S.; Kaniyankandy, S.; Verma, S.; Ghosh, H. N., Ultrafast Charge Carrier Relaxation and Charge Transfer Dynamics of CdTe/CdS Core–Shell Quantum Dots as Studied by Femtosecond Transient Absorption Spectroscopy. *J. Phys. Chem. C* **2010**, *114*, 1460-1466.
222. Wu, K.; Liang, G.; Shang, Q.; Ren, Y.; Kong, D.; Lian, T., Ultrafast Interfacial Electron and Hole Transfer from CsPbBr₃ Perovskite Quantum Dots. *J. Am. Chem. Soc.* **2015**, *137*, 12792-12795.
223. Klenk, R.; Klaer, J.; Scheer, R.; Lux-Steiner, M. C.; Luck, I.; Meyer, N.; Rühle, U., Solar cells based on CuInS₂—an overview. *Thin Solid Films* **2005**, *480*, 509-514.
224. Pons, T.; Pic, E.; Lequeux, N.; Cassette, E.; Bezdetnaya, L.; Guillemin, F.; Marchal, F.; Dubertret, B., Cadmium-Free CuInS₂/ZnS Quantum Dots for Sentinel Lymph Node Imaging with Reduced Toxicity. *ACS Nano* **2010**, *4*, 2531-2538.
225. Tsuji, I.; Kato, H.; Kudo, A., Visible-Light-Induced H₂ Evolution from an Aqueous Solution Containing Sulfide and Sulfite over a ZnS–CuInS₂–AgInS₂ Solid-Solution Photocatalyst. *Angewandte Chemie* **2005**, *117*, 3631-3634.
226. Panthani, M. G.; Stolle, C. J.; Reid, D. K.; Rhee, D. J.; Harvey, T. B.; Akhavan, V. A.; Yu, Y.; Korgel, B. A., CuInSe₂ Quantum Dot Solar Cells with High Open-Circuit Voltage. *J. Phys. Chem. Lett.* **2013**, *4*, 2030-2034.
227. Omata, T.; Nose, K.; Otsuka-Yao-Matsuo, S., Size dependent optical band gap of ternary I-III-VI₂ semiconductor nanocrystals. *J. Appl. Phys.* **2009**, *105*, 073106.
228. Allen, P. M.; Bawendi, M. G., Ternary I–III–VI Quantum Dots Luminescent in the Red to Near-Infrared. *J. Am. Chem. Soc.* **2008**, *130*, 9240-9241.
229. Carey, G. H.; Abdelhady, A. L.; Ning, Z.; Thon, S. M.; Bakr, O. M.; Sargent, E. H., Colloidal Quantum Dot Solar Cells. *Chem. Rev.* **2015**, *115*, 12732-12763.

References

230. Padilha, L. A.; Stewart, J. T.; Sandberg, R. L.; Bae, W. K.; Koh, W.-K.; Pietryga, J. M.; Klimov, V. I., Carrier Multiplication in Semiconductor Nanocrystals: Influence of Size, Shape, and Composition. *Acc. Chem. Res.* **2013**, *46*, 1261-1269.
231. Schaller, R. D.; Klimov, V. I., High Efficiency Carrier Multiplication in PbSe Nanocrystals: Implications for Solar Energy Conversion. *Phys. Rev. Lett.* **2004**, *92*, 186601.
232. Stubbs, S. K.; Hardman, S. J. O.; Graham, D. M.; Spencer, B. F.; Flavell, W. R.; Glarvey, P.; Masala, O.; Pickett, N. L.; Binks, D. J., Efficient carrier multiplication in InP nanoparticles. *Phys. Rev. B* **2010**, *81*, 081303.
233. Stolle, C. J.; Schaller, R. D.; Korgel, B. A., Efficient Carrier Multiplication in Colloidal CuInSe₂ Nanocrystals. *J. Phys. Chem. Lett.* **2014**, *5*, 3169-3174.
234. Klimov, V. I., Spectral and Dynamical Properties of Multiexcitons in Semiconductor Nanocrystals. *Annual Review of Physical Chemistry* **2007**, *58*, 635-673.
235. Debnath, T.; Maiti, S.; Maity, P.; Ghosh, H. N., Subpicosecond Exciton Dynamics and Biexcitonic Feature in Colloidal CuInS₂ Nanocrystals: Role of In–Cu Antisite Defects. *J. Phys. Chem. Lett.* **2015**, *6*, 3458-3465.
236. Zhong, H.; Zhou, Y.; Ye, M.; He, Y.; Ye, J.; He, C.; Yang, C.; Li, Y., Controlled Synthesis and Optical Properties of Colloidal Ternary Chalcogenide CuInS₂ Nanocrystals. *Chem. Mater.* **2008**, *20*, 6434-6443.
237. Castro, S. L.; Bailey, S. G.; Raffaele, R. P.; Banger, K. K.; Hepp, A. F., Synthesis and Characterization of Colloidal CuInS₂ Nanoparticles from a Molecular Single-Source Precursor. *J. Phys. Chem. B* **2004**, *108*, 12429-12435.
238. Nose, K.; Omata, T.; Otsuka-Yao-Matsuo, S., Colloidal Synthesis of Ternary Copper Indium Diselenide Quantum Dots and Their Optical Properties. *J. Phys. Chem. C* **2009**, *113*, 3455-3460.

References

239. Hamanaka, Y.; Kuzuya, T.; Sofue, T.; Kino, T.; Ito, K.; Sumiyama, K., Defect-induced photoluminescence and third-order nonlinear optical response of chemically synthesized chalcopyrite CuInS₂ nanoparticles. *Chemical Physics Letters* **2008**, *466*, 176-180.
240. Uehara, M.; Watanabe, K.; Tajiri, Y.; Nakamura, H.; Maeda, H., Synthesis of CuInS₂ fluorescent nanocrystals and enhancement of fluorescence by controlling crystal defect. *The Journal of Chemical Physics* **2008**, *129*, 134709.
241. Hamanaka, Y.; Ogawa, T.; Tsuzuki, M.; Kuzuya, T., Photoluminescence Properties and Its Origin of AgInS₂ Quantum Dots with Chalcopyrite Structure. *J. Phys. Chem. C* **2011**, *115*, 1786-1792.
242. Binsma, J. J. M.; Giling, L. J.; Bloem, J., Luminescence of CuInS₂. *Journal of Luminescence* **1982**, *27*, 35-53.
243. Ueng, H. Y.; Hwang, H. L., The defect structure of CuInS₂. part I: Intrinsic defects. *Journal of Physics and Chemistry of Solids* **1989**, *50*, 1297-1305.
244. Mao, B.; Chuang, C.-H.; Wang, J.; Burda, C., Synthesis and Photophysical Properties of Ternary I-III-VI AgInS₂ Nanocrystals: Intrinsic versus Surface States. *J. Phys. Chem. C* **2011**, *115*, 8945-8954.
245. Dai, M.; Ogawa, S.; Kameyama, T.; Okazaki, K.-i.; Kudo, A.; Kuwabata, S.; Tsuboi, Y.; Torimoto, T., Tunable photoluminescence from the visible to near-infrared wavelength region of non-stoichiometric AgInS₂ nanoparticles. *J. Mat. Chem.* **2012**, *22*, 12851-12858.
246. Li, L.; Pandey, A.; Werder, D. J.; Khanal, B. P.; Pietryga, J. M.; Klimov, V. I., Efficient Synthesis of Highly Luminescent Copper Indium Sulfide-Based Core/Shell Nanocrystals with Surprisingly Long-Lived Emission. *J. Am. Chem. Soc.* **2011**, *133*, 1176-1179.

References

247. Jara, D. H.; Stampleskoskie, K. G.; Kamat, P. V., Two Distinct Transitions in Cu_xInS_2 Quantum Dots. Bandgap versus Sub-Bandgap Excitations in Copper-Deficient Structures. *J. Phys. Chem. Lett.* **2016**, *7*, 1452-1459.
248. Chen, B.; Zhong, H.; Zhang, W.; Tan, Z. a.; Li, Y.; Yu, C.; Zhai, T.; Bando, Y.; Yang, S.; Zou, B., Highly Emissive and Color-Tunable $CuInS_2$ -Based Colloidal Semiconductor Nanocrystals: Off-Stoichiometry Effects and Improved Electroluminescence Performance. *Advanced Functional Materials* **2012**, *22*, 2081-2088.
249. Redjai, E.; Massé, G., Donor-Acceptor Pair Transitions in $AgInS_2$. *physica status solidi (b)* **1985**, *131*, K157-K159.
250. Krustok, J.; Raudoja, J.; Krunks, M.; Mändar, H.; Collan, H., Nature of the native deep localized defect recombination centers in the chalcopyrite and orthorhombic $AgInS_2$. *J. Appl. Phys.* **2000**, *88*, 205-209.
251. Bose, R.; Ahmed, G. H.; Alarousu, E.; Parida, M. R.; Abdelhady, A. L.; Bakr, O. M.; Mohammed, O. F., Direct Femtosecond Observation of Charge Carrier Recombination in Ternary Semiconductor Nanocrystals: The Effect of Composition and Shelling. *J. Phys. Chem. C* **2015**, *119*, 3439-3446.
252. Bose, R.; Bera, A.; Parida, M. R.; Adhikari, A.; Shaheen, B. S.; Alarousu, E.; Sun, J.; Wu, T.; Bakr, O. M.; Mohammed, O. F., Real-Space Mapping of Surface Trap States in $CIGSe$ Nanocrystals Using 4D Electron Microscopy. *Nano Lett.* **2016**, *16*, 4417-4423.
253. Ogawa, T.; Kuzuya, T.; Hamanaka, Y.; Sumiyama, K., Synthesis of $Ag-In$ binary sulfide nanoparticles-structural tuning and their photoluminescence properties. *J. Mat. Chem.* **2010**, *20*, 2226-2231.
254. Akkerman, Q. A.; Genovese, A.; George, C.; Prato, M.; Moreels, I.; Casu, A.; Marras, S.; Curcio, A.; Scarpellini, A.; Pellegrino, T.; Manna, L.; Lesnyak, V., From Binary Cu_2S to

References

Ternary Cu–In–S and Quaternary Cu–In–Zn–S Nanocrystals with Tunable Composition via Partial Cation Exchange. *ACS Nano* **2015**, *9*, 521-531.

255. Song, W.-S.; Yang, H., Efficient White-Light-Emitting Diodes Fabricated from Highly Fluorescent Copper Indium Sulfide Core/Shell Quantum Dots. *Chem. Mater.* **2012**, *24*, 1961-1967.

256. Kaniyankandy, S.; Rawalekar, S.; Verma, S.; Palit, D. K.; Ghosh, H. N., Charge carrier dynamics in thiol capped CdTe quantum dots. *Phys. Chem. Chem. Phys.* **2010**, *12*, 4210-4216.

257. Knowles, K. E.; McArthur, E. A.; Weiss, E. A., A Multi-Timescale Map of Radiative and Nonradiative Decay Pathways for Excitons in CdSe Quantum Dots. *ACS Nano* **2011**, *5*, 2026-2035.

258. Kraatz, I. T.; Booth, M.; Whitaker, B. J.; Nix, M. G. D.; Critchley, K., Sub-Bandgap Emission and Intraband Defect-Related Excited-State Dynamics in Colloidal CuInS₂/ZnS Quantum Dots Revealed by Femtosecond Pump–Dump–Probe Spectroscopy. *J. Phys. Chem. C* **2014**, *118*, 24102-24109.

259. Sewall, S. L.; Franceschetti, A.; Cooney, R. R.; Zunger, A.; Kambhampati, P., Direct observation of the structure of band-edge biexcitons in colloidal semiconductor CdSe quantum dots. *Phys. Rev. B* **2009**, *80*, 081310.

260. Gdor, I.; Shapiro, A.; Yang, C.; Yanover, D.; Lifshitz, E.; Ruhman, S., Three-Pulse Femtosecond Spectroscopy of PbSe Nanocrystals: 1S Bleach Nonlinearity and Sub-Band-Edge Excited-State Absorption Assignment. *ACS Nano* **2015**, *9*, 2138-2147.

261. El-Ballouli, A. a. O.; Alarousu, E.; Usman, A.; Pan, J.; Bakr, O. M.; Mohammed, O. F., Real-Time Observation of Ultrafast Intraband Relaxation and Exciton Multiplication in PbS Quantum Dots. *ACS Photonics* **2014**, *1*, 285-292.

References

262. Nishijima, Y.; Ueno, K.; Yokota, Y.; Murakoshi, K.; Misawa, H., Plasmon-Assisted Photocurrent Generation from Visible to Near-Infrared Wavelength Using a Au-Nanorods/TiO₂ Electrode. *J. Phys. Chem. Lett.* **2010**, *1*, 2031-2036.
263. Song, H., Metal Hybrid Nanoparticles for Catalytic Organic and Photochemical Transformations. *Acc. Chem. Res.* **2015**, *48*, 491-499.
264. Li, J.; Cushing, S. K.; Zheng, P.; Senty, T.; Meng, F.; Bristow, A. D.; Manivannan, A.; Wu, N., Solar Hydrogen Generation by a CdS-Au-TiO₂ Sandwich Nanorod Array Enhanced with Au Nanoparticle as Electron Relay and Plasmonic Photosensitizer. *J. Am. Chem. Soc.* **2014**, *136*, 8438-8449.
265. Mongin, D.; Shaviv, E.; Maioli, P.; Crut, A.; Banin, U.; Del Fatti, N.; Vallée, F., Ultrafast Photoinduced Charge Separation in Metal–Semiconductor Nanohybrids. *ACS Nano* **2012**, *6*, 7034-7043.
266. Berr, M.; Vaneski, A.; Susha, A. S.; Rodríguez-Fernández, J.; Döblinger, M.; Jäckel, F.; Rogach, A. L.; Feldmann, J., Colloidal CdS nanorods decorated with subnanometer sized Pt clusters for photocatalytic hydrogen generation. *Appl. Phys. Lett.* **2010**, *97*, 093108.
267. Berr, M. J.; Vaneski, A.; Mauser, C.; Fischbach, S.; Susha, A. S.; Rogach, A. L.; Jäckel, F.; Feldmann, J., Delayed Photoelectron Transfer in Pt-Decorated CdS Nanorods under Hydrogen Generation Conditions. *Small* **2012**, *8*, 291-297.
268. Dutta, S. K.; Mehetor, S. K.; Pradhan, N., Metal Semiconductor Heterostructures for Photocatalytic Conversion of Light Energy. *J. Phys. Chem. Lett.* **2015**, *6*, 936-944.
269. Kim, S. M.; Lee, S. J.; Kim, S. H.; Kwon, S.; Yee, K. J.; Song, H.; Somorjai, G. A.; Park, J. Y., Hot Carrier-Driven Catalytic Reactions on Pt–CdSe–Pt Nanodumbbells and Pt/GaN under Light Irradiation. *Nano Lett.* **2013**, *13*, 1352-1358.

References

270. Yu, X.; Shavel, A.; An, X.; Luo, Z.; Ibáñez, M.; Cabot, A., Cu₂ZnSnS₄-Pt and Cu₂ZnSnS₄-Au Heterostructured Nanoparticles for Photocatalytic Water Splitting and Pollutant Degradation. *J. Am. Chem. Soc.* **2014**, *136*, 9236-9239.
271. Deka, S.; Falqui, A.; Bertoni, G.; Sangregorio, C.; Poneti, G.; Morello, G.; Giorgi, M. D.; Giannini, C.; Cingolani, R.; Manna, L.; Cozzoli, P. D., Fluorescent Asymmetrically Cobalt-Tipped CdSe@CdS Core@Shell Nanorod Heterostructures Exhibiting Room-Temperature Ferromagnetic Behavior. *J. Am. Chem. Soc.* **2009**, *131*, 12817-12828.
272. Soni, U.; Tripathy, P.; Sapra, S., Photocatalysis from Fluorescence-Quenched CdSe/Au Nanoheterostructures: A Size-Dependent Study. *J. Phys. Chem. Lett.* **2014**, *5*, 1909-1916.
273. Habas, S. E.; Yang, P.; Mokari, T., Selective Growth of Metal and Binary Metal Tips on CdS Nanorods. *J. Am. Chem. Soc.* **2008**, *130*, 3294-3295.
274. Elmalem, E.; Saunders, A. E.; Costi, R.; Salant, A.; Banin, U., Growth of Photocatalytic CdSe-Pt Nanorods and Nanonets. *Adv. Mater* **2008**, *20*, 4312-4317.
275. Cushing, S. K.; Li, J.; Meng, F.; Senty, T. R.; Suri, S.; Zhi, M.; Li, M.; Bristow, A. D.; Wu, N., Photocatalytic Activity Enhanced by Plasmonic Resonant Energy Transfer from Metal to Semiconductor. *J. Am. Chem. Soc.* **2012**, *134*, 15033-15041.
276. Gao, H.; Liu, C.; Jeong, H. E.; Yang, P., Plasmon-Enhanced Photocatalytic Activity of Iron Oxide on Gold Nanopillars. *ACS Nano* **2012**, *6*, 234-240.
277. Li, P.; Wei, Z.; Wu, T.; Peng, Q.; Li, Y., Au-ZnO Hybrid Nanopyramids and Their Photocatalytic Properties. *J. Am. Chem. Soc.* **2011**, *133*, 5660-5663.

References

278. Steiner, D.; Mokari, T.; Banin, U.; Millo, O., Electronic Structure of Metal-Semiconductor Nanojunctions in Gold CdSe Nanodumbbells. *Phys. Rev. Lett.* **2005**, *95*, 056805.
279. Kobayashi, Y.; Nonoguchi, Y.; Wang, L.; Kawai, T.; Tamai, N., Dual Transient Bleaching of Au/PbS Hybrid Core/Shell Nanoparticles. *J. Phys. Chem. Lett.* **2012**, *3*, 1111-1116.
280. Lee, J.-S.; Shevchenko, E. V.; Talapin, D. V., Au–PbS Core–Shell Nanocrystals: Plasmonic Absorption Enhancement and Electrical Doping via Intra-particle Charge Transfer. *J. Am. Chem. Soc.* **2008**, *130*, 9673-9675.
281. Yang, Y.; Shi, J.; Chen, H.; Dai, S.; Liu, Y., Enhanced off-resonance optical nonlinearities of Au@CdS core-shell nanoparticles embedded in BaTiO₃ thin films. *Chemical Physics Letters* **2003**, *370*, 1-6.
282. Shaviv, E.; Schubert, O.; Alves-Santos, M.; Goldoni, G.; Di Felice, R.; Vallée, F.; Del Fatti, N.; Banin, U.; Sönnichsen, C., Absorption Properties of Metal–Semiconductor Hybrid Nanoparticles. *ACS Nano* **2011**, *5*, 4712-4719.
283. Dreaden, E. C.; Neretina, S.; Qian, W.; El-Sayed, M. A.; Hughes, R. A.; Preston, J. S.; Mascher, P., Plasmonic Enhancement of Nonradiative Charge Carrier Relaxation and Proposed Effects from Enhanced Radiative Electronic Processes in Semiconductor–Gold Core–Shell Nanorod Arrays. *J. Phys. Chem. C* **2011**, *115*, 5578-5583.
284. O'Connor, T.; Panov, M. S.; Mereshchenko, A.; Tarnovsky, A. N.; Lorek, R.; Perera, D.; Diederich, G.; Lambright, S.; Moroz, P.; Zamkov, M., The Effect of the Charge-Separating Interface on Exciton Dynamics in Photocatalytic Colloidal Heteronanocrystals. *ACS Nano* **2012**, *6*, 8156-8165.

References

285. Pandey, A.; Guyot-Sionnest, P., Hot Electron Extraction From Colloidal Quantum Dots. *J. Phys. Chem. Lett.* **2010**, *1*, 45-47.
286. Tisdale, W. A.; Williams, K. J.; Timp, B. A.; Norris, D. J.; Aydil, E. S.; Zhu, X. Y., Hot-Electron Transfer from Semiconductor Nanocrystals. *Science* **2010**, *328*, 1543.
287. Williams, K. J.; Nelson, C. A.; Yan, X.; Li, L.-S.; Zhu, X., Hot Electron Injection from Graphene Quantum Dots to TiO₂. *ACS Nano* **2013**, *7*, 1388-1394.
288. Sippel, P.; Albrecht, W.; Mitoraj, D.; Eichberger, R.; Hannappel, T.; Vanmaekelbergh, D., Two-Photon Photoemission Study of Competing Auger and Surface-Mediated Relaxation of Hot Electrons in CdSe Quantum Dot Solids. *Nano Lett.* **2013**, *13*, 1655-1661.
289. Mukherjee, S.; Zhou, L.; Goodman, A. M.; Large, N.; Ayala-Orozco, C.; Zhang, Y.; Nordlander, P.; Halas, N. J., Hot-Electron-Induced Dissociation of H₂ on Gold Nanoparticles Supported on SiO₂. *J. Am. Chem. Soc.* **2014**, *136*, 64-67.
290. Dong, Y.; Choi, J.; Jeong, H.-K.; Son, D. H., Hot Electrons Generated from Doped Quantum Dots via Upconversion of Excitons to Hot Charge Carriers for Enhanced Photocatalysis. *J. Am. Chem. Soc.* **2015**, *137*, 5549-5554.
291. Yu, P.; Wen, X.; Lee, Y.-C.; Lee, W.-C.; Kang, C.-C.; Tang, J., Photoinduced Ultrafast Charge Separation in Plexcitonic CdSe/Au and CdSe/Pt Nanorods. *J. Phys. Chem. Lett.* **2013**, *4*, 3596-3601.
292. Guijarro, N.; Lana-Villarreal, T.; Mora-Seró, I.; Bisquert, J.; Gómez, R., CdSe Quantum Dot-Sensitized TiO₂ Electrodes: Effect of Quantum Dot Coverage and Mode of Attachment. *J. Phys. Chem. C* **2009**, *113*, 4208-4214.

References

293. Shen, Q. K., J.; Diguna, L. J.; Toyoda, T., Effect of ZnS coating on the photovoltaic properties of CdSe quantum dot-sensitized solar cells. *Journal of Applied Physics* **2008**, *103*, 084304.
294. Exchange of ideas and information on the issue of Competitive Change in the Electric Power Industry. Topic: What are the issues involved in competition? In *Committee on Energy and Natural Resources*, 105th ed.; Bureau of National Affairs: Washington, D.C., 1997; p 17.
295. Zhao, K.; Pan, Z.; Zhong, X., Charge Recombination Control for High Efficiency Quantum Dot Sensitized Solar Cells. *J. Phys. Chem. Lett.* **2016**, *7*, 406-417.
296. Zhang, H.; Bao, H.; Zhong, X., Highly efficient, stable and reproducible CdSe-sensitized solar cells using copper sulfide as counter electrodes. *J. Mater. Chem. A* **2015**, *3*, 6557-6564.
297. Debnath, T.; Parui, K.; Maiti, S.; Ghosh, H. N., An Insight into the Interface through Excited-State Carrier Dynamics for Promising Enhancement of Power Conversion Efficiency in a Mn-Doped CdZnSSe Gradient Alloy. *Chem. Eur. J.* **2017**, *23*, 3755-3763.
298. Hod, I.; González-Pedro, V.; Tachan, Z.; Fabregat-Santiago, F.; Mora-Seró, I.; Bisquert, J.; Zaban, A., Dye versus Quantum Dots in Sensitized Solar Cells: Participation of Quantum Dot Absorber in the Recombination Process. *J. Phys. Chem. Lett.* **2011**, *2*, 3032-3035.
299. Fillinger, A.; Parkinson, B. A., The Adsorption Behavior of a Ruthenium-Based Sensitizing Dye to Nanocrystalline TiO₂ Coverage Effects on the External and Internal Sensitization Quantum Yields. *J. Electrochem. Soc.* **1999**, *146*, 4559-4564.
300. Adachi, M.; Sakamoto, M.; Jiu, J.; Ogata, Y.; Isoda, S., Determination of Parameters of Electron Transport in Dye-Sensitized Solar Cells Using Electrochemical Impedance Spectroscopy. *J. Phys. Chem. B* **2006**, *110*, 13872-13880.

References

301. Fabregat-Santiago, F.; Garcia-Belmonte, G.; Mora-Sero, I.; Bisquert, J., Characterization of nanostructured hybrid and organic solar cells by impedance spectroscopy. *Phys. Chem. Chem. Phys.* **2011**, *13*, 9083-9118.
302. Ben-Shahar, Y.; Scotognella, F.; Kriegel, I.; Moretti, L.; Cerullo, G.; Rabani, E.; Banin, U., Optimal metal domain size for photocatalysis with hybrid semiconductor-metal nanorods. *Nature Communications* **2016**, *7*, 10413.
303. Rühle, S.; Shalom, M.; Zaban, A., Quantum-Dot-Sensitized Solar Cells. *ChemPhysChem* **2010**, *11*, 2290-2304.
304. Hod, I.; Zaban, A., Materials and Interfaces in Quantum Dot Sensitized Solar Cells: Challenges, Advances and Prospects. *Langmuir* **2014**, *30*, 7264-7273.
305. McGuire, J. A.; Joo, J.; Pietryga, J. M.; Schaller, R. D.; Klimov, V. I., New Aspects of Carrier Multiplication in Semiconductor Nanocrystals. *Acc. Chem. Res.* **2008**, *41*, 1810-1819.
306. Huang, X.; El-Sayed, I. H.; Qian, W.; El-Sayed, M. A., Cancer Cell Imaging and Photothermal Therapy in the Near-Infrared Region by Using Gold Nanorods. *J. Am. Chem. Soc.* **2006**, *128*, 2115-2120.
307. Saunders, A. E.; Popov, I.; Banin, U., *J. Phys. Chem. B* **2006**, *110*, 25421.
308. Mokari, T.; Sztrum, C. G.; Salant, A.; Rabani, E.; Banin, U., Formation of asymmetric one-sided metal-tipped semiconductor nanocrystal dots and rods. *Nat Mater* **2005**, *4*, 855-863.
309. Yang, J.; Elim, H. I.; Zhang, Q.; Lee, J. Y.; Ji, W., Rational Synthesis, Self-Assembly, and Optical Properties of PbS–Au Heterogeneous Nanostructures via Preferential Deposition. *J. Am. Chem. Soc.* **2006**, *128*, 11921-11926.

References

310. Huang, J.; Huang, Z.; Yang, Y.; Zhu, H.; Lian, T., Multiple Exciton Dissociation in CdSe Quantum Dots by Ultrafast Electron Transfer to Adsorbed Methylene Blue. *J. Am. Chem. Soc.* **2010**, *132*, 4858-4864.
311. Yang, Y.; Rodríguez-Córdoba, W.; Xiang, X.; Lian, T., Strong Electronic Coupling and Ultrafast Electron Transfer between PbS Quantum Dots and TiO₂ Nanocrystalline Films. *Nano Lett.* **2012**, *12*, 303-309.
312. Robel, I.; Kuno, M.; Kamat, P. V., Size-Dependent Electron Injection from Excited CdSe Quantum Dots into TiO₂ Nanoparticles. *J. Am. Chem. Soc.* **2007**, *129*, 4136-4137.
313. Sykora, M.; Petruska, M. A.; Alstrum-Acevedo, J.; Bezel, I.; Meyer, T. J.; Klimov, V. I., Photoinduced Charge Transfer between CdSe Nanocrystal Quantum Dots and Ru–Polypyridine Complexes. *J. Am. Chem. Soc.* **2006**, *128*, 9984-9985.
314. Huang, J.; Huang, Z.; Jin, S.; Lian, T., Exciton Dissociation in CdSe Quantum Dots by Hole Transfer to Phenothiazine. *J. Phys. Chem. C* **2008**, *112*, 19734-19738.
315. Zhang, Y.; Jing, P.; Zeng, Q.; Sun, Y.; Su, H.; Wang, Y. A.; Kong, X.; Zhao, J.; Zhang, H., Photoluminescence Quenching of CdSe Core/Shell Quantum Dots by Hole Transporting Materials. *J. Phys. Chem. C* **2009**, *113*, 1886-1890.
316. Debnath, T.; Maity, P.; Ghosh, H. N., Super Sensitization: Grand Charge (Hole/Electron) Separation in ATC Dye Sensitized CdSe, CdSe/ZnS Type-I, and CdSe/CdTe Type-II Core–Shell Quantum Dots. *Chem. Eur. J.* **2014**, *20*, 13305-13313.
317. Singhal, P.; Ghosh, H. N., Hot-Hole Extraction from Quantum Dot to Molecular Adsorbate. *Chem. Eur. J.* **2015**, *21*, 4405-4412.
318. Ivanov, S. A.; Achermann, M., Spectral and Dynamic Properties of Excitons and Biexcitons in Type-II Semiconductor Nanocrystals. *ACS Nano* **2010**, *4*, 5994-6000.

References

319. Khon, E.; Hewa-Kasakarage, N. N.; Nemitz, I.; Acharya, K.; Zamkov, M., Tuning the Morphology of Au/CdS Nanocomposites through Temperature-Controlled Reduction of Gold-Oleate Complexes. *Chem. Mater.* **2010**, *22*, 5929-5936.

References
